THE UNIVERSITY OF HULL

Metal Oxide Nanoparticles as Potential MRI Contrast Agents

being a Thesis submitted for the Degree of
Doctor of Philosophy
in the University of Hull

by

Naomi Elizabeth Jones, MChem

June 2015

ABSTRACT

Magnetic resonance imaging (MRI) is a common medical imaging modality that does not require the administration of radiopharmaceuticals, as it relies on the inherent nuclear spin of the protons in the tissues and organs. However, it lacks sensitivity in comparison to imaging techniques such as positron emission tomography (PET) and therefore changes at a cellular level are difficult to detect. To increase the level of information that can be obtained from MR images, contrast agents such as superparamagnetic iron oxide nanoparticles (SPIONs) or gadolinium based chelates can be used. Contrast agents work by making areas of the image where the agent is concentrated either lighter or darker; this is known as T_1 and T_2 relaxation respectively. Typically, gadolinium based chelates influence T_1 relaxation times, and SPION affect T_2 relaxation times of the hydrogen protons within the target organ or tissue. Recently, research has expanded from the use of chelated compounds with an increasing focus on improving and refining the properties of nanoparticles as contrast agents.

The work described here focusses on the preparation of new cation and anion doped SPION-based contrast agents with improved imaging properties for MRI. Specifically, the following series of oxide nanoparticles were prepared: $Fe_{2-x}Dy_xO_3$, $Fe_{2-x}Gd_xO_3$, $Gd_{2-x}Mn_xO_3$, $Gd_{2-x}Fe_xO_3$, $Dy_{2-x}Fe_xO_3$ and $Fe_2O_{3-x}F_{2x}$.

The nanoparticles were prepared *via* either co-precipitation or solid state reactions. Powder X-ray diffraction, ICP-AES, TEM, SEM, XPS, Mössbauer spectroscopy and magnetic measurements were performed to characterise the samples. The potential of selected samples to be developed into contrast agents was tested at the Royal Infirmary in Hull.

The nanoparticles prepared in this work that show the most potential for improving T_1 relaxation rates at 3 T are the $Gd_{2-x}Mn_xO_3$ nanoparticle series. Of these $Gd_{1.98}Mn_{0.02}O_3$, $Gd_{1.90}Mn_{0.10}O_3$, $Gd_{1.79}Mn_{0.21}O_3$ nanoparticles in addition to $Fe_{1.96}Gd_{0.04}O_3$ nanoparticles also show potential for use at 11.7 T as T_1 contrast agents.

$Fe_{1.96}Gd_{0.04}O_3$ and $Fe_{1.99}Dy_{0.01}O_3$ nanoparticles exhibited high T_2 relaxation rates at 11.7 T compared to those of prepared γ-Fe_2O_3 nanoparticles.

$Fe_2O_{3-x}F_{2x}$ nanoparticles exhibited high T_2 relaxation rates at both 3 T and 11.7 T compared against γ-Fe_2O_3 nanoparticles, showing their potential for use both at clinical and higher magnetic field strengths.

ACKNOWLEDGEMENTS

I would like to express my gratitude to my supervisors Dr M. Grazia Francesconi, Prof. Steve J. Archibald and Dr Anne-Marie Seymour for their continuous support during my PhD. The guidance and support provided by Dr M. Grazia Francesconi during my research was invaluable, as was the patience to be a sounding board for my ideas.

I would also like to thank Prof. Dave Evans for kindly providing Mössbauer spectroscopy, Ann Lowry and Tony Sinclair for their assistance with the TEM and SEM, as well as Bob Knight for sample analysis on the ICP-AES. Additionally, thanks go to Soma Salamon at the University of Duisburg-Essen for carrying out magnetic measurements; Dr Peter Gibbs and Dr Martin Pickles at the MRI centre at Hull Royal Infirmary for their assistance with MRI measurements.

Parts of this project could have not have been done with contributions from Connah Burnett and Amy Bradley, who spent lots of hours alongside me tinkering away in the lab as well as having numerous well deserved coffee breaks. I would also like to thank Alicja Kownacka for all her help and patience with the NMR.

My fellow lab colleagues Dr Matthew Simmons, Dr Kreshnik Hoxha and Mr Simon Fellows deserve huge thanks for their help, friendship and tolerance of me staining all the glassware in the lab brown! Their support, along with Matt's creative engineering skills will not be forgotten.

Finally, I would like to thank my family and friends for their love and support over the last few years, I couldn't have done it with you.

TABLE OF CONTENTS

LIST OF ABBREVIATIONS

AAS	Atomic Absorption Spectroscopy
CT	Computed-Tomography
ICP-AES	Inductively Coupled Plasma – Atomic Emission Spectroscopy
MR	Magnetic Resonance
MRI	Magnetic Resonance Imaging
NMR	Nuclear Magnetic Resonance
PET	Positron Emission Spectroscopy
PXRD	Powder X-ray Diffraction
SEM	Scanning Electron Microscopy
SPECT	Single-Photon Emission Computed-Tomography
SPION(s)	Superparamagnetic Iron Oxide Nanoparticles
TEM	Transmission Electron Spectroscopy
USPION(s)	Ultra-small Superparamagnetic Iron Oxide Nanoparticles
XPS	X-ray Photoelectron Spectroscopy

LIST OF MATERIALS

Chemical	Supplier
Iron (II) chloride tetrahydrate, >99%	Sigma Aldrich
Iron(III) chloride, 97%	Sigma Aldrich
Gadolinium(III) chloride hexahydrate, 99%	Alfa Aesar
Manganese(II) chloride tetrahydrate, 99%	Alfa Aesar
Gadolinium(III) hydroxide, >99%	Sigma Aldrich
Dysprosium(III) Nitrate	Sigma Aldrich
Ethylene glycol, 99%	Alfa Aesar
Sodium hydroxide pellets, reagent grade	Fisher Scientific
Citric Acid	Alfa Aesar

1 INTRODUCTION

1.1 BIOMEDICAL IMAGING

The field of biomedical imaging is of great importance in modern day medicine and non-invasive ways to see inside the human body are essential to help diagnose diseases, broken bones or problems with tissues and organs. There are a range of modalities available that are capable of detecting changes in tissues and organs *in vivo,* including X-ray radiography, magnetic resonance imaging (MRI) and positron emission tomography (PET). Whilst PET and SPECT can detect changes in tissue at a cellular level, MRI and ultrasound lack sensitivity and can only provide images at near cellular level.[1, 2] The latter techniques do however have the advantage of providing both physiological and anatomical images at the same time, whereas PET must be combined with other modalities such as computed tomography (CT) in order to determine the anatomical location of the area being imaged (Figure 1-1).

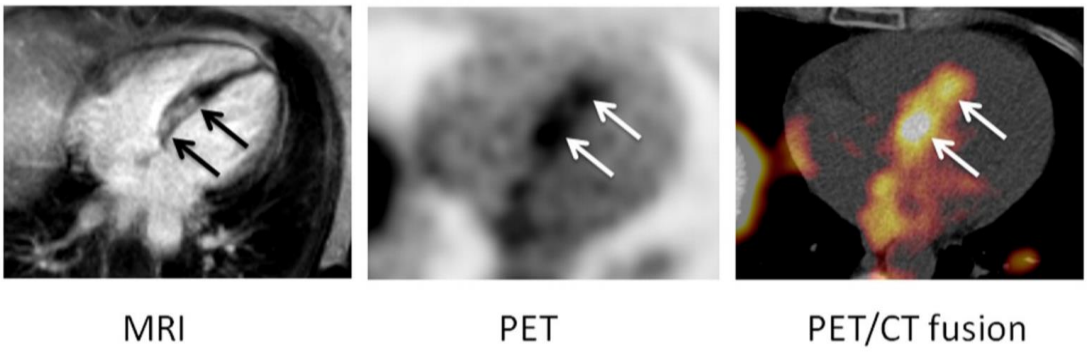

Figure 1-1 A comparison of MRI, PET and PET/CT images of a patient with acute myocarditis. From: Imaging of myocardial inflammation with somatostatin receptor based PET/CT - A comparison to cardiac MRI (2015), Figure 2a.[3]

Unlike PET or SPECT techniques, MRI does not rely on the use of radiopharmaceuticals to highlight areas of the body in order to collect an image. It does however, often require the use of contrast agents: compounds which alter the magnetic environment of water protons in a localised area and enables images to be collected with greater sensitivity and detail. Contrast agents for MRI are typically compounds containing paramagnetic metals such as gadolinium or iron.[2, 4, 5]

The MRI technique is based on the magnetic spin of hydrogen protons within water and fat molecules in the body. When an image is required of a specific area of the body, a contrast agent can be used that targets specific biomarkers in that area. This means that the hydrogen protons in that area have a different environment to the tissue in the rest of the body. Therefore when an MR image is collected the relaxation time for this area will be different, causing it to stand out.[6]

There are two different types of image that can be obtained by MRI, a T_1-weighted image, in which water protons undergo longitudinal relaxation, the RF signal increases and the white areas of an image become brighter; and secondly, a T_2-weighted image where water protons undergo transverse relaxation, the RF signal decreases and contrast is improved by the black areas of the image becoming darker. Both types of imaging method are used, although some are more favoured depending upon the target organ being imaged. The theory of MRI is discussed further in section 2.2.

Commercially used contrast agents for MRI include compounds consisting of superparamagnetic iron oxide nanoparticles (SPIONs), or gadolinium complexes.[7, 8] In both cases the metals are paramagnetic, containing unpaired electrons and have high magnetic moments. The magnetic properties of the compounds are a key factor as they influence the relaxation time experienced by the water protons *in vivo*. Therefore it is

essential to understand the different factors that influence these properties in order to develop new more effective contrast agents that can be tailored to specific applications.

In order to understand the development of MRI contrast agents, first the different types of magnetism need to be understood. This will be covered in the next section followed by a discussion of different metal oxide materials, including their preparation, structure and magnetic properties. Finally this chapter will discuss the preparation of contrast agents for magnetic resonance imaging.

1.2 MAGNETISM

All materials exhibit diamagnetic behaviour due to the movement of paired electrons. However, some materials for example, iron oxides, exhibit other types of magnetism which are more dominant. There are four main types of magnetism that a material can exhibit, detailed below, and one phenomenon known as superparamagnetism, unique to nanosized particles is also described.[5, 9-11]

1.2.1 Ferromagnetism

In ferromagnetism, the spin of the neighbouring electrons align parallel over areas of the material creating domains (Figure 1-2). Ferromagnetic materials are made up of multiple domains each with a different direction of magnetisation (Figure 1-3). When a magnetic field is applied all the domains align parallel, greatly improving the material's magnetism (Figure 1-4). The magnetic susceptibility of ferromagnetic materials is affected by temperature, and obeys the Curie-Weiss law (Equation 1-1)[10]. This states that when the Curie temperature is reached, there is sufficient thermal energy to overcome the alignment caused by the magnetic field, allowing free rotation of the electron spins and resulting in the material becoming paramagnetic (Figure 1-5).

$$\chi = \frac{C}{T-\theta} \qquad \text{Equation 1-1}$$

χ = Magnetic susceptibility C = Curie constant

T = Absolute temperature Θ = Weiss constant

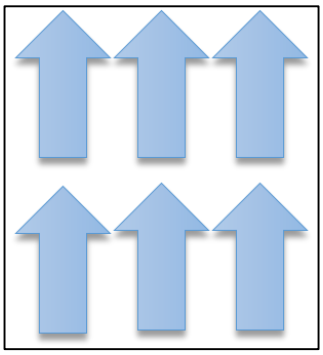

Figure 1-2 Neighbouring electron spins align parallel to create a single domain in a ferromagnetic material. Each arrow represents an electron.

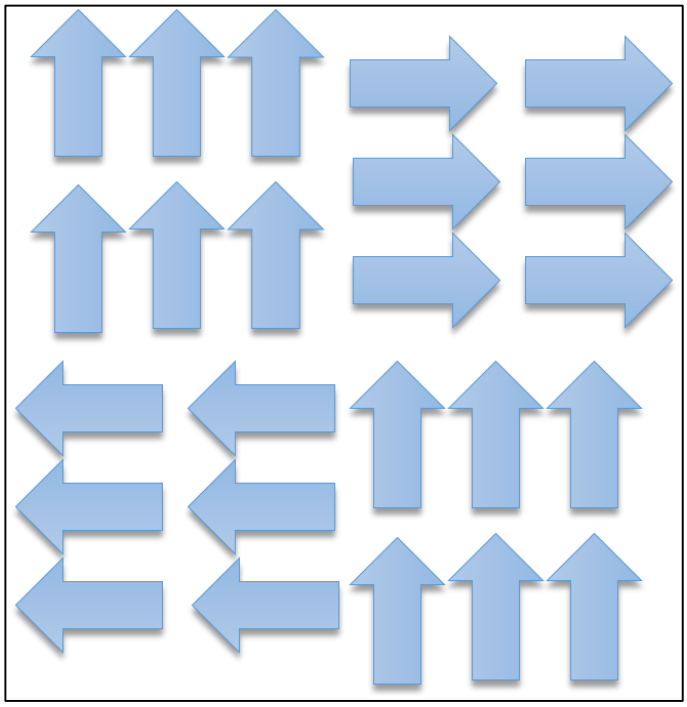

Figure 1-3 Multiple domains exist in ferromagnetic materials. Each arrow represents an electron.

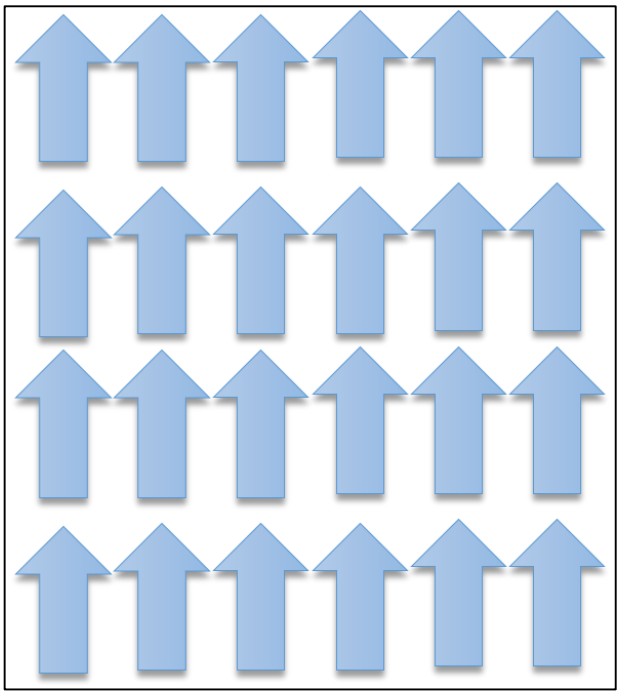

Figure 1-4 In an applied magnetic field, the multiple domains align parallel creating a net magnetic moment. Each arrow represents an electron.

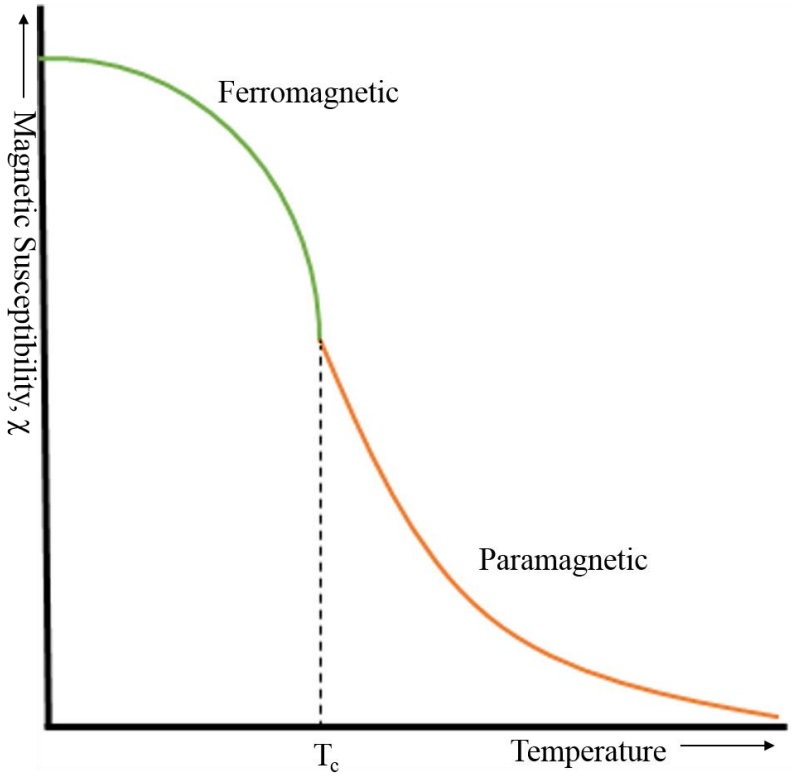

Figure 1-5 As the temperature increases and the Curie temperature is reached, the magnetic susceptibility decreases and the magnetic ordering changes from ferromagnetic to paramagnetic.

1.2.2 Antiferromagnetism

In antiferromagnetic materials, electron spins align anti-parallel causing equal magnetic moments in both directions, leading to an overall magnetic moment of zero. There are three possible ways of ordering electron spins in antiferromagnetic materials, as shown in Figure 1-6. Above the Néel temperature, thermal energy causes some electrons to rotate making the material weakly paramagnetic (Equation 1-2, Figure 1-7). In antiferromagnetic materials, the application of a magnetic field has no effect on the alignment of the electrons.

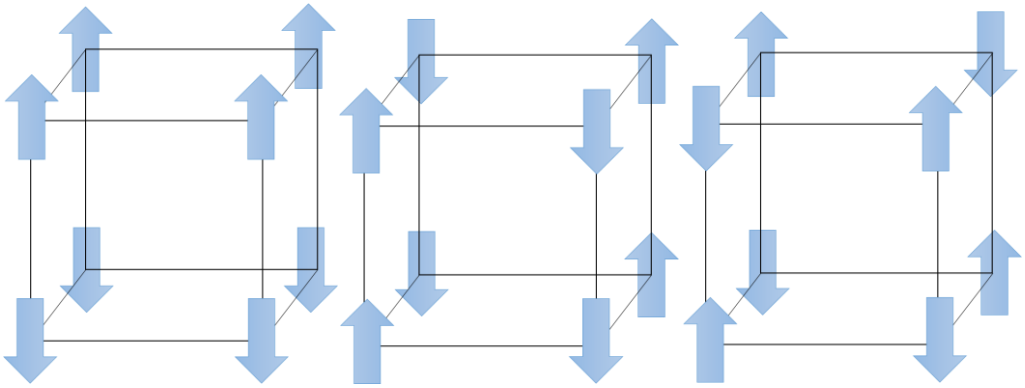

Figure 1-6 Three types of antiferromagnetic ordering, A-type, C-type and G-type from left to right respectively. Each arrow represents an electron.[12]

$$\chi = \frac{C}{T\text{-}T_N} \qquad \text{Equation 1-2}$$

11

χ = Magnetic susceptibility

C = Curie constant

T = Absolute temperature

T_N = Néel temperature

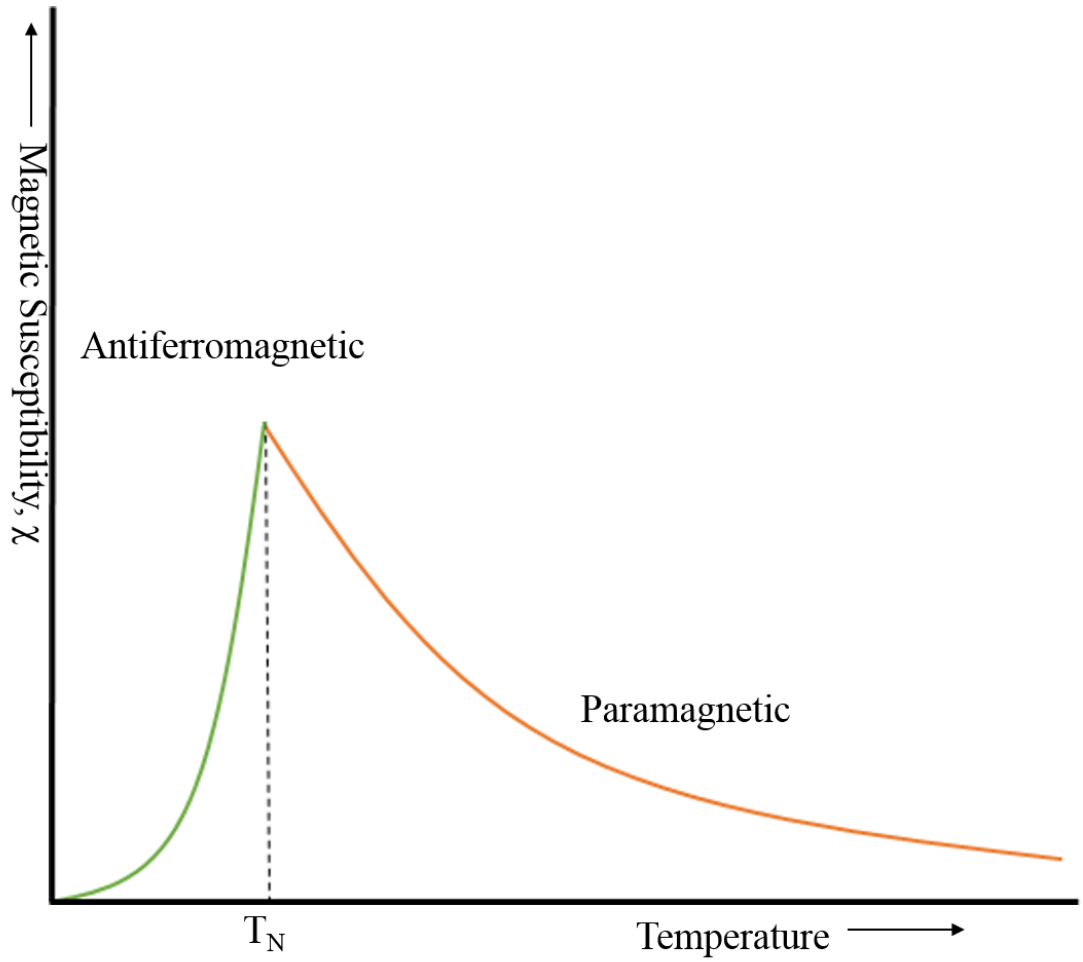

Figure 1-7 As the temperature increases and the Néel temperature is reached, the magnetic susceptibility decreases and the magnetic ordering changes from antiferromagnetic to paramagnetic.

1.2.3 Ferrimagnetism

In ferrimagnetic materials unpaired electrons orientate anti-parallel (Figure 1-8). However, there is a greater net magnetic moment in one direction causing the material to exhibit magnetic properties in the absence of an applied magnetic field. These materials act as permanent magnets, but do become paramagnetic above the critical temperature.

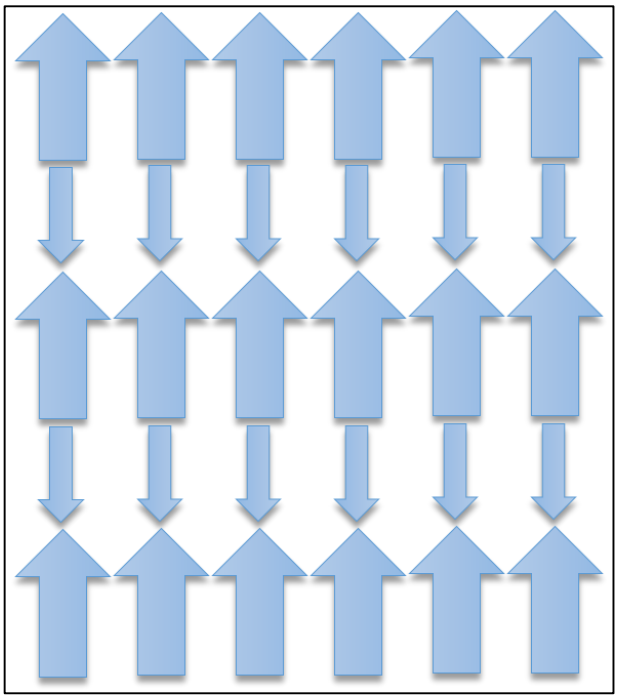

Figure 1-8 Ferrimagnetic ordering results in electron spins aligning antiparallel, with a greater net magnetic moment in one direction. Each arrow represents an electron.

1.2.4 Paramagnetism

Paramagnetism occurs when neighbouring electron spins orientate randomly and do not create domains (Figure 1-9). However, when a magnetic field is applied all the unpaired electrons align in one direction, causing a net magnetic moment in that direction (Figure 1-10). With increasing temperature, the magnetic susceptibility of the material steadily decreases (Figure 1-11).

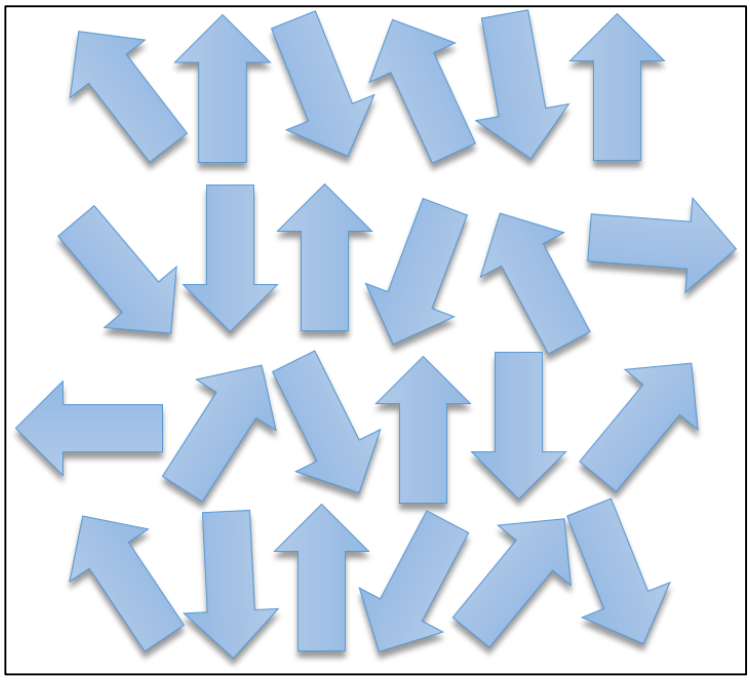

Figure 1-9 In paramagnetic materials, electron spins randomly orientate causing the material to have no net magnetic moment. Each arrow represents an electron.

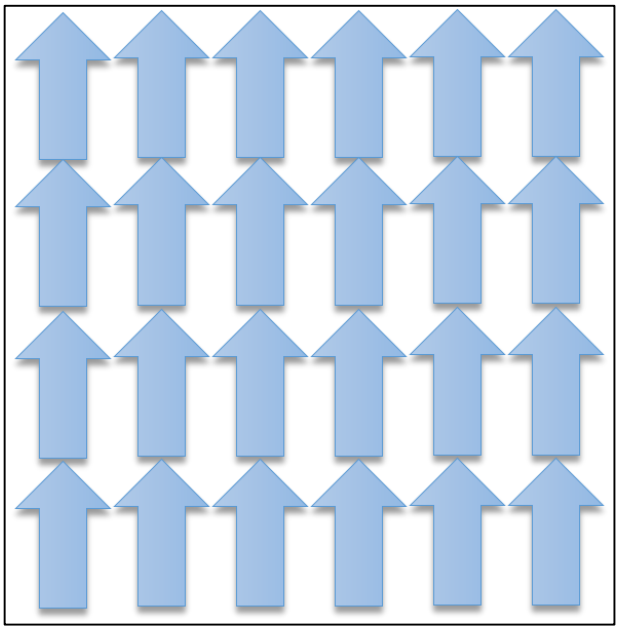

Figure 1-10 In an applied magnetic field, the electron spins in paramagnetic materials align parallel leading to a net magnetic moment. Each arrow represents an electron.

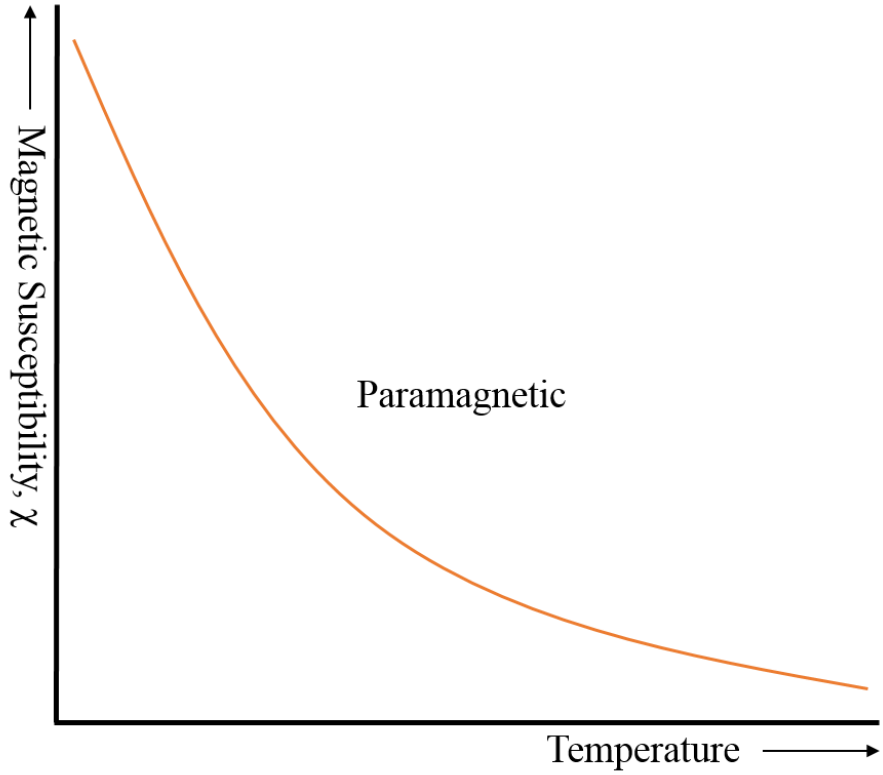

Figure 1-11 In paramagnetic materials, the magnetic susceptibility decreases as temperature increases.

1.2.5 Superparamagnetism

In some materials that display ferromagnetism, a phenomenon known as superparamagnetism occurs when the particle size of that material falls below approximately 50 nm.[11] At this particle size, thermal energy is sufficient to overcome the stabilising forces between neighbouring magnetic domains, leading to small particles with only one magnetic domain. Within this singular domain, all electron spins align causing each particle to have an independent net magnetic moment. Application of an external magnetic field causes all the individual particles to align resulting in a large magnetic moment (Figure 1-12). On removal of the magnetic field all magnetic properties revert to their original state.[10, 11]

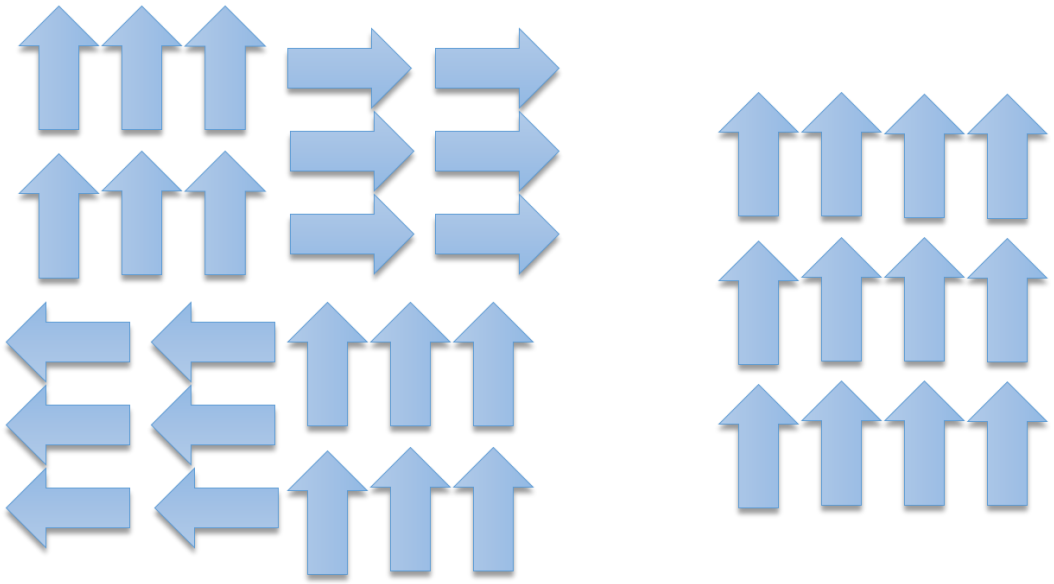

Figure 1-12 Superparamagnetism typically occurs in magnetic materials less than approximately 50 nm diameter, in the absence of an applied magnetic field. In these materials there is only one magnetic domain, compared to multiple domains in materials with larger particle sizes. Each arrow represents an electron.

A magnetic field is usually represented as lines of force that can penetrate an object within the field.[10, 13] The density of these lines is known as the magnetic flux density (B). In diamagnetic materials the flux density decreases, whereas in paramagnetic materials the flux density increases (Figure 1-13). In a vacuum, the relationship between magnetic flux density and the magnetic field (H) is directly related to the permeability of free space (μ_0) (Equation 1-3).

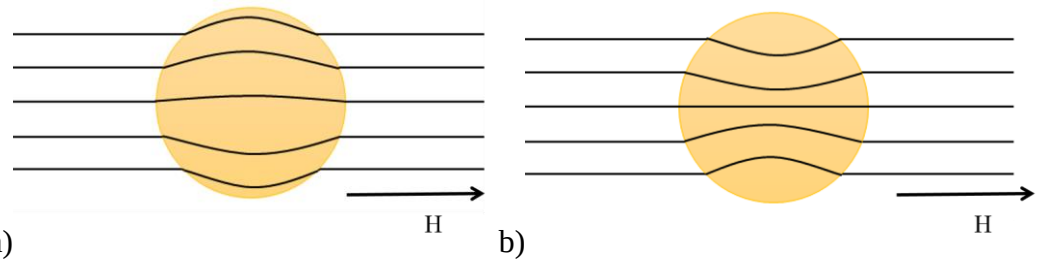

a) b)

Figure 1-13 Changes in flux density in a) diamagnetic materials, b) paramagnetic materials.

$$B=\mu_0 H \qquad \text{Equation 1-3}$$

The field produced by a material in a magnetic field is the material's magnetisation (M). This means the magnetic flux density can be expressed (Equation 1-4):

$$B=\mu_0(H+M) \qquad \text{Equation 1-4}$$

In the case of materials for biomedical imaging, the magnetic property most discussed is the magnetic susceptibility (χ) and relates to the magnetisation of a material (Equation 1-5):

$$\chi=\frac{M}{H} \qquad \text{Equation 1-5}$$

Ferromagnetic materials have a magnetic memory (magnetic remanence), where the magnetic properties initiated by the magnetic field exist for a short time after the magnetic field has been removed. Different ferromagnetic materials exhibit different magnetic remanence times and can be characterised by their hysteresis curves.[10] The highest point on a hysteresis curve indicates the material's magnetisation saturation and limits a materials magnetic remanence, as it is the maximum value of magnetisation for the material when an external magnetic field is applied. This means that continuing to increase the magnetic field will not increase the magnetisation of the material any further.

Superparamagnetic materials have no magnetic memory, however their magnetisation increases with increasing magnetic field strengths, until the magnetisation saturation point is reached.[10]

Figure 1-14 shows hysteresis curves for superparamagnetic and ferromagnetic materials. For superparamagnetic materials in the absence of a magnetic field, each nanoparticle domain is randomly orientated. As the material is exposed to increasing magnetic field

strengths, the magnetic induction steadily increases. Magnetisation saturation is reached when the curve plateaus and further increase of the magnetic field strength has no effect on the magnetic induction and all the spin domains within the nanoparticle are aligned. Reversal of the magnetic field strength results in near identical curves as the magnetic domains align in the opposite direction.

In ferromagnetic materials, the same induction curve is initially seen as the magnetic field strength increases from zero to the magnetisation saturation point. However, due to the magnetic remanence of the material, magnetic induction is still present in the absence of a magnetic field.

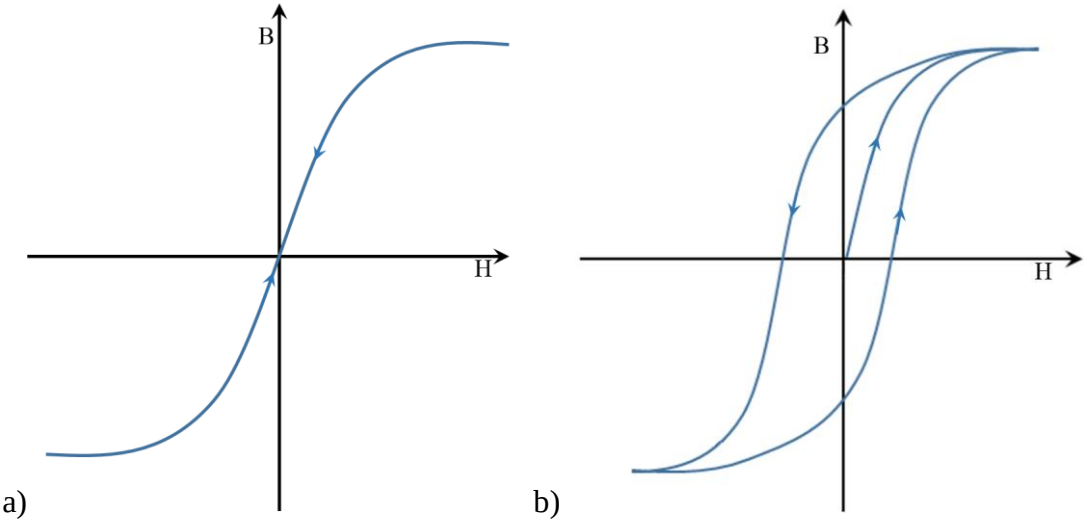

Figure 1-14 Magnetic hysteresis curves for a) superparamagnetic materials and b) ferromagnetic materials. H represents the magnetic field strength and B the magnetic induction (flux).

1.3 METAL OXIDES

Metal oxide solids consist of an oxygen anion lattice with the metal ions filling some of the coordination sites.[9, 13] Depending upon the crystal structure the ordering of the cations and anions can vary. Within these solids, different magnetic properties arise due to the proximity of ions within the unit cell. These are dependent on the coupling interactions and the extent of overlap between atomic orbitals.[14, 15]

There are three types of exchange interactions- direct exchange interactions, superexchange interactions and indirect exchange interactions. These will be discussed below.

1.3.1 Direct Exchange Interactions

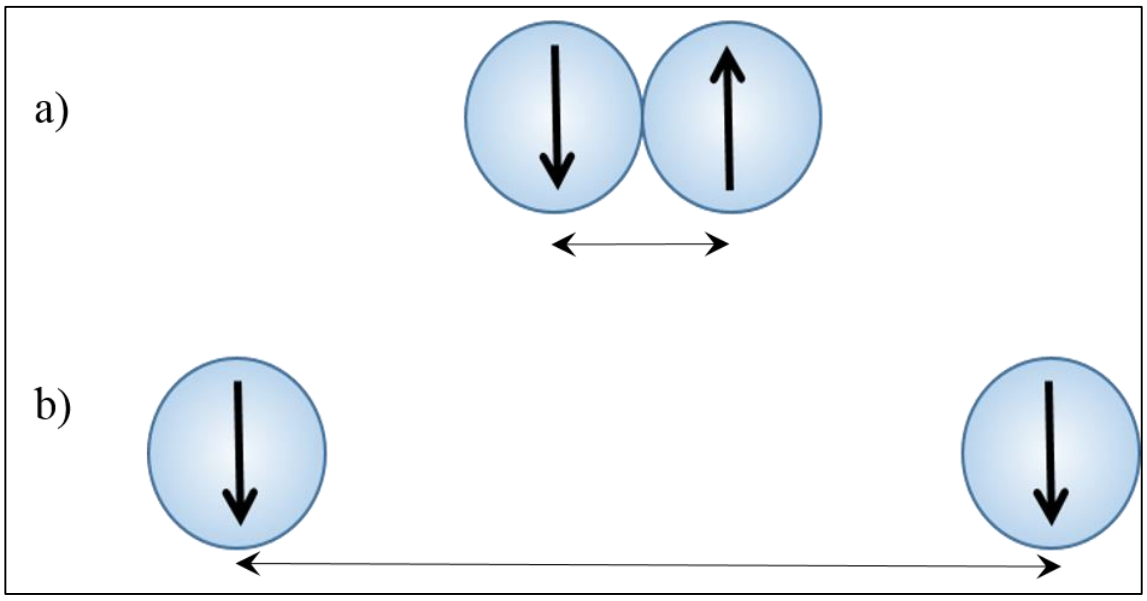

Figure 1-15 Schematic showing direct exchange interactions between metal centres a) close together and b) far apart.

Direct exchange interactions usually occur between two metal centres that are in close proximity to one another (Figure 1-15). Due to the Pauli exclusion principle, the electrons must have opposing spins; however as the two metal centres get further apart the coupling effects get weaker and the electron spins are free to change direction. .[14, 15]

1.3.2 Superexchange interactions

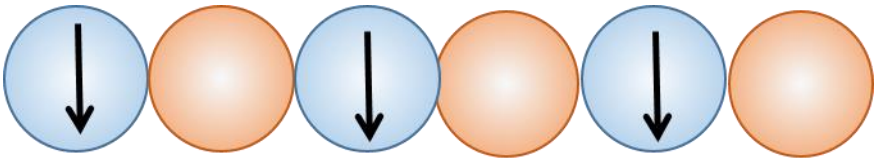

Figure 1-16 Schematic showing superexchange interactions.

Superexchange interactions (Figure 1-16) involve the coupling of electron spins through a non-metal intermediate ion such as oxygen. .[14, 15]

This can result in either:

- Antiferromagnetic coupling (Figure 1-17) where the electron spins on the metal centres align antiparallel.

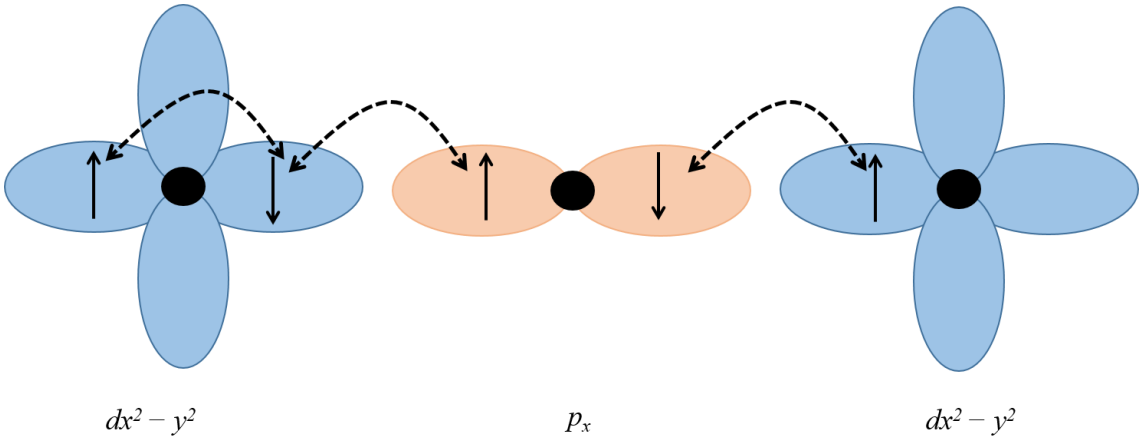

Figure 1-17 Schematic showing the orbital overlap in antiferromagnetic superexchange interactions.

- Ferromagnetic coupling (Figure 1-18) where the electron spins on the metal centres align parallel.

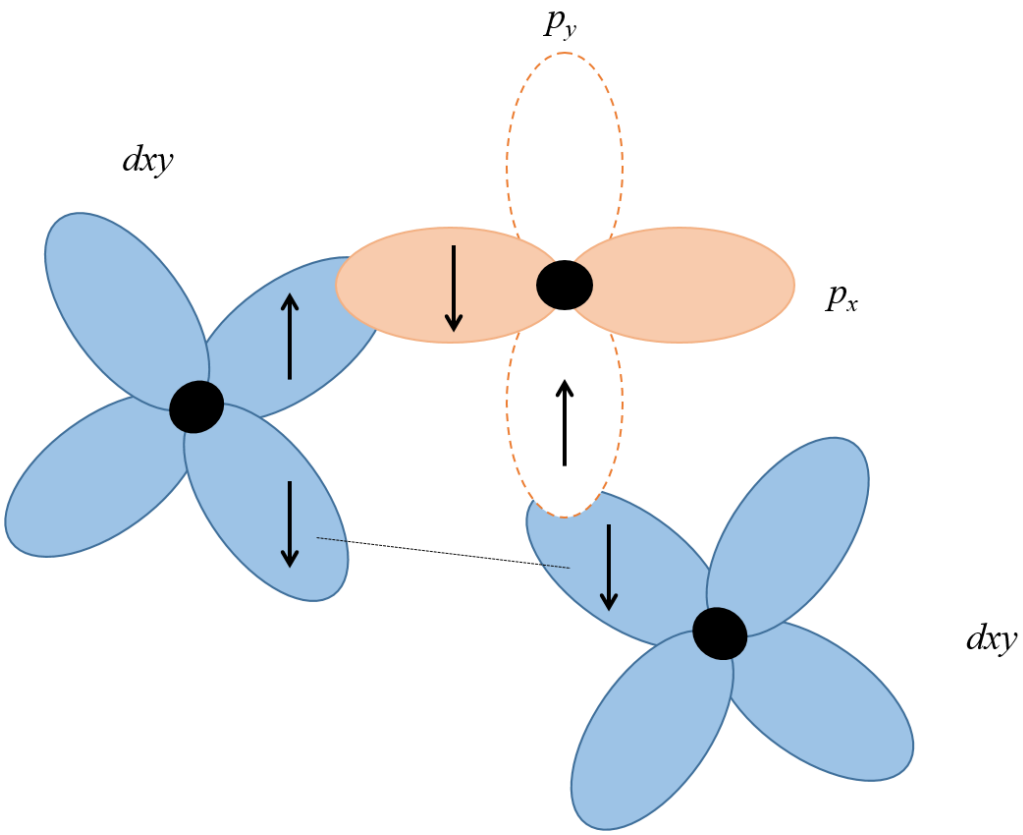

Figure 1-18 Schematic showing the orbital overlap in ferromagnetic superexchange interactions.

1.3.3 Indirect exchange interactions

The third type of coupling is *via* indirect exchange interactions (Figure 1-19), also known as RKKY (Ruderman, Kittel, Kasuya and Yasida) interactions.[14, 15] This occurs where two or more metal centres couple through itinerant electrons. The electron spin on one metal centre causes a nearby spin to align antiparallel, thus causing the next metal centre to align parallel to the first.

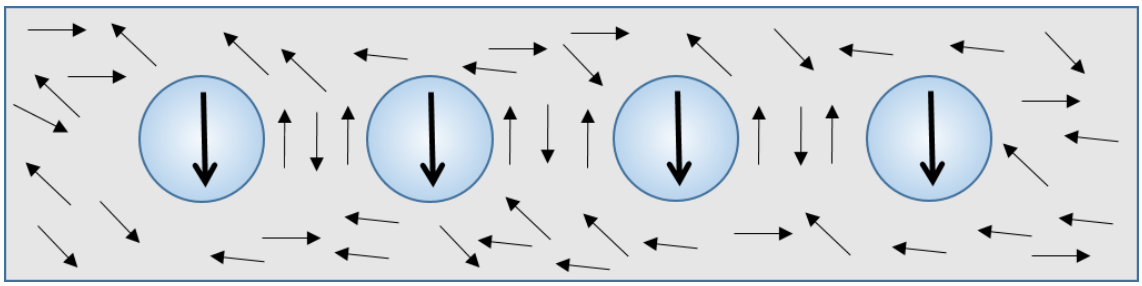

Figure 1-19 Schematic showing indirect exchange interactions.

Transition metal compounds all possess valence *d* shell electrons, so overlap of orbitals is purely reliant on the proximity of the ions. Coupling between transition metal *3d* shell electrons and unpaired lanthanide *4f* electrons is more difficult, as not only are the *f* orbitals at different angles to the *d* orbitals, making overlap difficult, the *4f* electrons are shielded by complete *5s* and *5d* electron shells. Due to this lanthanide – transition metal coupling takes place *via* indirect exchange only.[13, 15]

1.3.4 Iron Oxide

A wide variety of iron oxides exist in nature, each with characteristics unique to that compound. One of the most common forms is magnetite, Fe_3O_4, also known as lodestone and originally used for its natural magnetic properties. Rarer forms of iron oxide such as β-Fe_2O_3 and ε-Fe_2O_3[16, 17] have low natural abundance and successful isolation of these compounds have only been done in the laboratory.

The most stable type of iron oxide is hematite, the alpha form of Fe_2O_3. It is antiferromagnetic at room temperature and paramagnetic above 700°C. [16, 18] Hematite is isostructural with corundum, Al_2O_3, and consists of a hexagonal structure with a = 0.5034 nm and c = 1.375 nm. There are 6 units per unit cells with two thirds of the cation sites occupied by Fe^{3+} ions and regular vacancies on every third site. [16, 19] Hematite is the phase

transition product of maghemite, γ-Fe_2O_3, and is often a product of reactions above temperatures of 350°C. As hematite does not have any useful magnetic properties it will not be discussed in any further detail.

The two main types of magnetic iron oxide investigated are magnetite and maghemite. The structures and magnetic properties are discussed below, as well as methods of characterisation. It is important to know they type of iron oxide produced by a reaction, especially when carrying out cation or anion doping. Different synthetic routes are also discussed for the preparation of Fe_3O_4, γ-Fe_2O_3, $Fe_{3-x}M_xO_4$ and $Fe_{2-x}M_xO_3$, where M is a metal cation.

Magnetite (Fe_3O_4) and maghemite (γ-Fe_2O_3) both possess the inverse spinel structure, and are widely used in biomedical applications including drug delivery[20, 21], magnetic hyperthermia[22, 23] and as contrast agents for techniques such as magnetic resonance imaging (MRI).[2, 5, 24, 25]

$MgAl_2O_4$, is the original spinel mineral and many other oxides have been found showing the same structure, with formula AB_2O_4 (A= M^{2+}; B = M^{3+}) each compound having different electrical and magnetic properties.[26]

The spinel structure (Figure 1-20) consists of 8 formula units with 8A, 16B and 32O atoms, with two distinct arrangements, normal spinel (A)[B_2]O_4 and inverse spinel (B)[AB]O_4, with ( ) denoting cations in tetrahedral sites and [ ] denoting cations in octahedral sites; although depending upon the cations in question there can be a degree of inversion, forming a structure part way between.[9, 13]

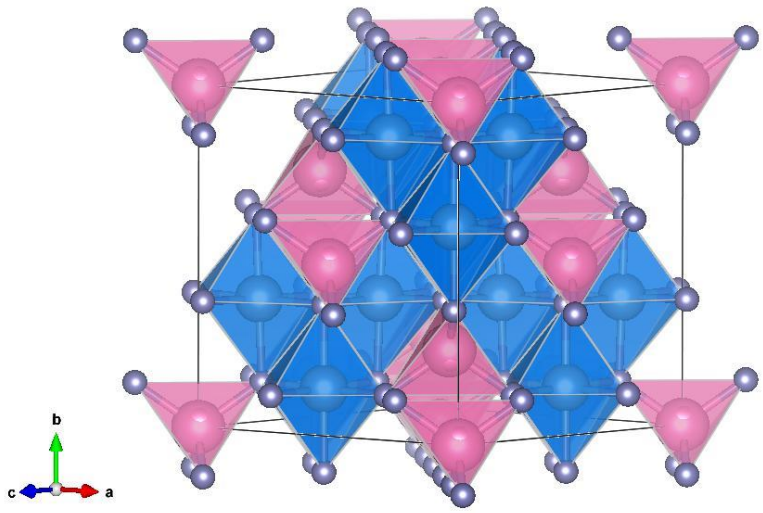

Figure 1-20 Spinel structure; Pink = Mg^{2+} ions, blue = Al^{3+} ions and grey = O^{2-} ions.

Magnetite (Fe_3O_4) has an inverse spinel structure $(Fe^{3+})[Fe^{2+},Fe^{3+}]O_4$ (Figure 1-21). It can be either stoichiometric with twice as many Fe^{3+} cations than Fe^{2+} cations in the unit cell, or non-stoichiometric where the ratio between the two cations can vary and cation vacancies maintain the charge neutrality.[9, 16, 27] Altering the stoichiometry changes the properties of both the bulk material and nanosized particles and allows tailoring to specific applications.[11, 28] However, on a nanoparticulate level, magnetite is chemically unstable and tends to form a core-shell structure with a layer of maghemite (γ-Fe_2O_3) surrounding a Fe_3O_4 core.[29] Magnetite adopts the cubic $Fd\bar{3}m$ space group, with unit cell $(Fe^{3+})_8[Fe^{3+}Fe^{2+}]_{16}O_{32}$.[30]

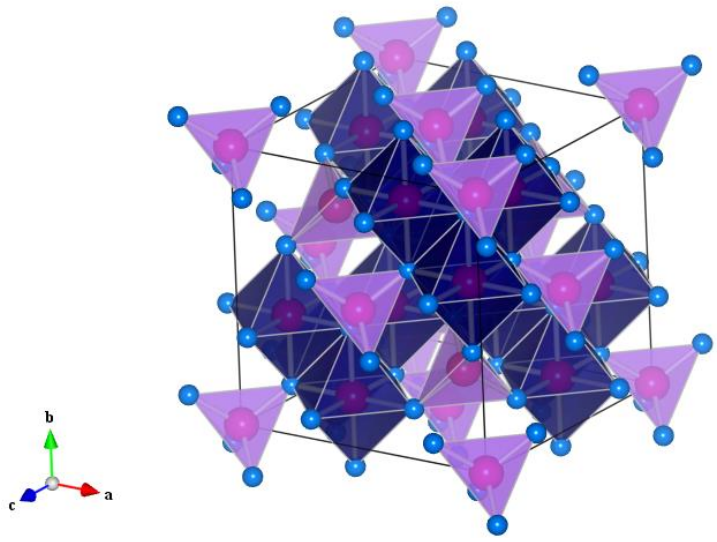

Figure 1-21 Fe_3O_4 unit cell structure with $Fd\bar{3}m$ space group. The dark blue shapes highlight the octahedral holes and the light purple shapes the tetrahedral holes. Pink spheres represent iron atoms and blue oxygen atoms.[31]

Maghemite, γ-Fe_2O_3, is the fully oxidised form of magnetite with only Fe^{3+} cations present in the unit cell (Figure 1-22). The inverse spinel structure is retained with cation vacancies compensating for the greater positive charge.

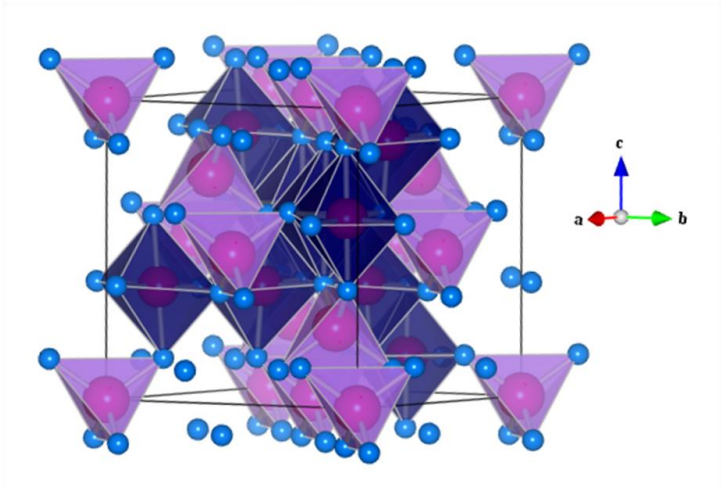

Figure 1-22 γ-Fe_2O_3 unit cell structure with $Fd\bar{3}m$ space group. The dark blue shapes highlight the octahedral holes and the light purple shapes the tetrahedral holes. Pink spheres represent iron atoms and blue oxygen atoms.[32]

For both magnetite and maghemite, the magnetic properties depend upon the arrangement of cations within the structure.[9] Cations in tetrahedral sites align parallel with one another as do those in octahedral sites (Figure 1-23). Between the sites the cations are aligned antiparallel. This usually results in ferrimagnetic properties due to the 2:1 ratio of octahedral sites to tetrahedral sites occupied (8 tetrahedral sites; 16 octahedral sites occupied); hence the magnetic properties can be tailored depending upon the type of cation and its distribution across the unit cell.

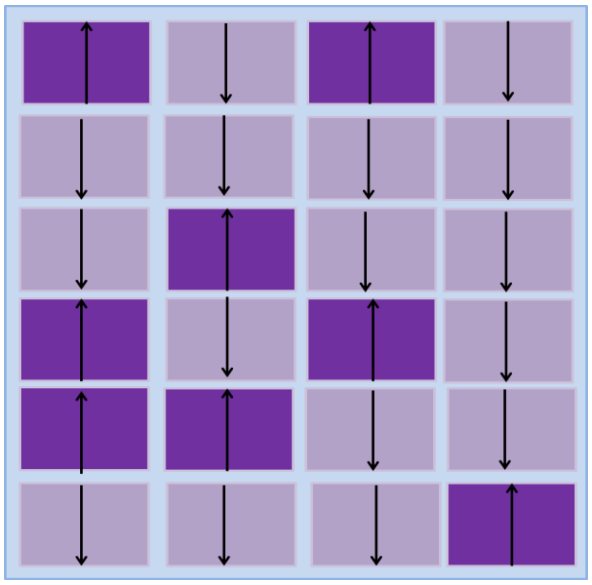

Figure 1-23 Schematic representation of the distribution of cations in spinels. The light squares represent spins of cations in octahedral sites and the dark squares, spins of cations in tetrahedral sites.

Synthetic routes for the preparation of iron oxides are varied and depend upon the size of particles required. Typical solid state calcination methods are one possible route, but high temperatures produce large particles, often micrometre sized.[33, 34] As the temperature reduces, the particle sizes also reduce but obtaining nanoparticles *via* this method can be difficult.

The preparation of iron oxide nanoparticles is often done *via* complex thermal decomposition or hydrothermal routes in which the particles are formed in the presence of a surfactant that protects the surface from oxidation.[35 36] Even though these routes still require temperatures of a few hundred degrees Celsius, the surfactants limit the growth of the particles keeping them in the nanometre range. Particles produced in this way tend to be hydrophobic, and so require ligand exchange in order to become hydrophilic and more biocompatible.

Alternative routes include soft chemistry techniques such as co-precipitation which can be used to produce magnetite or maghemite nanoparticles at low temperature. This route was initially proposed by Massart in 1981,[37] where iron oxide nanoparticles were prepared from ferric and ferrous chloride salts, following addition of ammonia solution.

Due to the nature of the reaction and lack of surfactants, when synthesising magnetite it is highly likely a mixture of magnetite and maghemite nanoparticles are produced. This is due to the chemical instability of magnetite on the nanoscale, and pure magnetite is difficult to produce even in anaerobic conditions.[38]

Multiple studies have shown that the magnetic properties of magnetite and maghemite nanoparticles vary with size and often the method of synthesis or surface coating impacts upon the final characteristics of the nanoparticles prepared.[39-42]

1.3.5 Cation doping of iron oxides

New cation doped iron oxide nanoparticles have been extensively investigated.[43-48] Most research conducted in these areas focus on cation doping of magnetite with divalent cations, forming the cubic unit cell, $Fd\bar{3}m$.

Cation substitution is used frequently in solid state chemistry to tailor the properties of inorganic solids. In most cases, cation substitution is typically dependent on the size of the substituting ion compared to the size of the available holes within the unit cell. If cation substitution occurs in iron oxide nanoparticles, coupling interactions between the iron cations across both octahedral and tetrahedral holes are either altered or entirely disrupted depending upon the nature of the substituting cation. This directly affects the magnetic anisotropy of the nanoparticle which in turn impacts the magnetic susceptibility, altering the properties of the nanoparticles as a whole.

A wide range of cation doped iron oxide nanoparticles have been proposed as effective contrast agents for MRI applications.[49, 50] One extensively researched cation for doping of iron oxide nanoparticles is Mn^{2+}. The metal induces T_1 relaxation increasing the positive contrast of the MR image. It is therefore anticipated that by doping manganese cations into magnetite or maghemite, a dual contrast probe exploiting both T_1 and T_2 relaxation properties can potentially be produced.

Both co-precipitation and thermal decomposition methods are used for the preparation of $MnFe_2O_4$ type compounds. Lu *et al.* [45] prepared Mn^{2+} doped Fe_3O_4 nanoparticles by thermal decomposition of iron(III) acetylacetonate and manganese(II) acetylacetonate in the presence of 1,2-hexadecanediol, oleic acid, oleylamine and benzyl ether. The hydrophilic nanoparticles produced were coated with methoxy-poly(ethylene glycol)-b-poly(3-caprolactone) or (mPEG-b-PCL) and measured their size to be approximately 8 nm. The polymer bound nanoparticles formed a micelle with the nanoparticles in the hydrophobic centre. Analysis by AAS determined a Fe:Mn ratio of 1.995 suggesting one third of the iron ions in Fe_3O_4 had been substituted with manganese. Furthermore, characterisation by XRD showed a match to the JCPDS card for bulk manganese ferrite

indicating that the Mn^{2+} ions had successfully substituted all the Fe^{2+} ions in the tetrahedral holes.

For a more tailored formula Kim *et al.* prepared partially Mn^{2+} substituted Fe_3O_4 using a co-precipitation method mixing Fe^{2+}/Fe^{3+} chloride salts with $MnCl_2$ in water. [51] Surface adsorption of lecithin was used to improve solubility and form a ferrofluid. [51] Due to the ratio of reactants the expected formula for the nanoparticles produced was $Fe_{2.9}\ Mn_{0.1}O_4$ however further work is required to determine the presence of manganese in the compound.

One other dopant for Fe_3O_4 nanoparticles is Zn^{2+}, which forces oxidation of Fe^{2+} to Fe^{3+}. Oxidation to maghemite would more than likely result in zinc being expelled from the unit cell rather than change oxidation state. Interestingly, zinc doped magnetite can form both regular spinel, mixed spinel and inverse spinel structures depending upon the extent of zinc doping.[52, 53]

Bárcena *et al.*[50] investigated the preparation of zinc doped magnetite by the hot injection method, and looked at the difference in magnetic properties when zinc is doped into spinel and inverse spinel structures. It was stated that in regular spinel structures the Zn^{2+} ions occupy the tetrahedral holes resulting in antiferromagnetic properties, which decrease a contrast agent's effectiveness due to the decrease in the materials magnetic moment. However, when doped into an inverse spinel structure such as magnetite the magnetic properties can be significantly improved, so a new, more superior contrast agent can be synthesised.

The magnetic properties of zinc doped iron oxide nanoparticles have also been investigated by Liu *et al.* [54] and Hochepeid *et al.*[55] Whilst not specifically directed towards MRI applications, the research provides a great insight to how changes in the cation distribution across the unit cell affects the overall magnetic properties of the

nanoparticles. Liu *et al.* found that when doping Fe_3O_4 with Zn^{2+} the magnetisation values of the nanoparticles increased from 19.8 emu g^{-1} when x = 0 to 54.1 when x = 0.34, however when x = 0.76 the magnetisation values reduced to 30 emu g^{-1}. This reduction is due to the Zn^{2+} ions substituting the Fe^{3+} ions on the A sites and causing a redistribution of the remaining Fe^{3+} ions across the A and B sites. This affects the coupling between the Fe^{3+} ions and in turn affects the magnetic moment. Similarly Hochepied *et al.* investigated the magnetisation values of magnetite in relation to particle size. It was found that as particle size decreased so did the magnetisation value due to an increase in the surface area:volume ratio increasing disorder of magnetic moments in the sublattices. Addition of Zn^{2+} ions into the lattice produced a similar effect, agreeing with the results presented by Liu *et al*.[54]

Most recently, lanthanide (Gd^{3+}, Eu^{3+}) doped iron oxide nanoparticles have emerged as a new multimodal contrast agent that can be used for both optical and magnetic resonance imaging.[56, 57] Furthermore, there has been an increase in the use of cation doped iron oxide nanoparticles toward combined MRI/PET/SPECT imaging in recent years.[58, 59]

More traditional contrast agents for MRI are gadolinium based coordination complexes affecting mainly T_1 relaxation times. Significant amounts of research has been carried out into the effects different ligands have on the contrast agent as a whole, with more recent research looking into using gadolinium based nanoparticles instead as a way to further improve the sensitivity of contrast agents.[60-63]

Kim *et al.* [51] attempted cation doping of Fe_3O_4 with gadolinium to produce $Fe_{2.8}Gd_{0.2}O_4$ and PXRD patterns shows shift to lower 2 theta angles

Further research of gadolinium doped iron oxide nanoparticles as contrast agents is limited, although there have been some investigation into preparation by co-precipitation for other medical uses, such as hyperthermia treatments.[23]

Drake *et al*[23] synthesised $Gd_{0.02}Fe_{2.98}O_4$ nanoparticles for use as hyperthermia treatments in tumour therapy. The nanoparticles were prepared using a co-precipitation method and the size measured to be 13 nm. Characterisation by PXRD and ICP-OES confirms the spinel structure is maintained and gadolinium is present in the sample. The magnetic properties were also investigated *via* vibrating sample magnetometer (VSM) and a magnetisation value of 67.65 emu g^{-1} determined. Furthermore, the group studied the specific power absorption rate (SAR) for a known concentration of nanoparticles and found that the gadolinium doped magnetite nanoparticles achieved significantly larger SAR values than those of magnetite, currently used for this application.

1.3.6 Anion Doping of iron oxides

Anionic substitution is an excellent alternative to cation doping for tuning the properties of inorganic solids and has been widely researched for the modification of electronic properties in superconductors [64-68]and photocatalysts.[69, 70] However, very little research has been carried out into anion doping of any form of iron oxide, especially the more chemically stable maghemite nanoparticles. Due to this, little is known about how modification on the anionic site will affect the materials magnetic properties.

Anion doping of compounds used for superconductors and photocatalysts modifies the structure of the solid and alters its magnetic properties. Hence, this research can be translated to the field of biomedical imaging as high magnetisation values are essential for MRI contrast agents.[2] Anion doping of metal oxide compounds such as maghemite or gadolinium oxide, allows the study of super-exchange interactions whilst excluding any metal-metal interactions exhibited. This means the magnetic exchange interactions can be investigated and modified to improve the overall magnetic properties of the solid.

1.3.7 Gadolinium Oxide and Dysprosium Oxide

Gadolinium oxide and dysprosium oxide both adopt the bixbyite structure with the space group $IA\bar{3}$ (Figure 1-24).[71] This unit cell is derived from the fluorite structure, with the cations occupying the 8a and 24d sites and anions occupying the 48e sites, leaving the 16c anion sites unoccupied.[72] The FCC sublattices are formed by the metal cations, with an ordered arrangement of oxygen anions.[73, 74] Anion vacancies show ordering across two unit cell lengths (2*a*).

Gadolinium oxide nanoparticles are often prepared by low temperature co-precipitation techniques, where a base, such as sodium hydroxide or tetramethylammonium hydroxide (TMAH) is added to a gadolinium salt, producing gadolinium oxide particles less than 5 nm in diameter.[62, 75] Often, polyols are added to help avoid the formation of metal hydroxide compounds as well as to control the particle size and reduce particle agglomeration.[76]

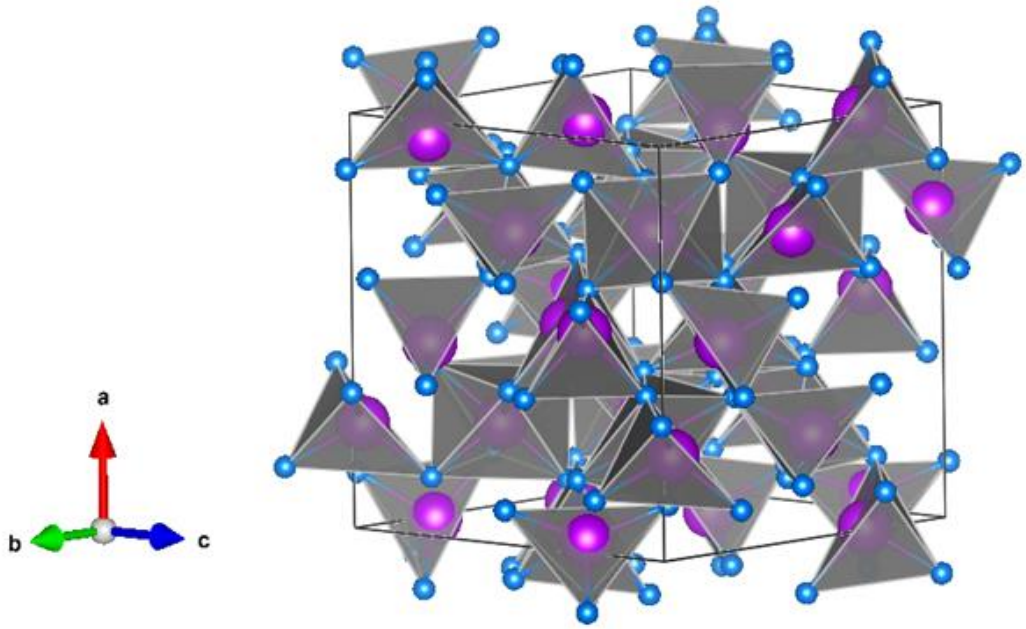

Figure 1-24 The bixbyite unit cell structure of Gd_2O_3 and Dy_2O_3 with space group $IA\bar{3}$. Oxygen atoms are marked in blue, gadolinium/dysprosium atoms are marked in purple.

Similar precipitation methods are also employed for the preparation of dysprosium oxide nanoparticles, however in some cases it has been reported that in order to achieve single phase Dy_2O_3 nanoparticles the precipitate produced must also be calcined at high temperatures.[77, 78]

1.4 MRI AND CONTRAST AGENTS

MRI is a popular biomedical technique for taking images of the body's organs and tissues.[2, 6] Unlike PET scans MRI does not use harmful gamma radiation, however it lacks sensitivity hence minute cellular changes are difficult to detect.[79] To overcome this problem and improve the detail of MR images, contrast agents such as superparamagnetic iron oxide nanoparticles (SPIONs) or gadolinium based chelates are used.

Two types of contrast agent exist, those that predominantly affect longitudinal, or T_1, relaxation rates of water protons and those that affect transverse, or T_2, relaxation rates of water protons. Typically, when a T_1 contrast agent is used, the signal in the area that the agent is present increases, causing white areas of an image to become brighter. T_2 contrast agents have the opposite effect, causing a decrease in signal and darkening of black areas of an image. The precessional frequency of each MR active nucleus varies with magnetic field strength according to the Larmor equation; with T_1 relaxation rates decreasing with increasing magnetic field strengths. The theory of MRI is discussed further in section 2.2.

T_2 SPIO contrast agents cause local inhomogeneities in the magnetic field produced during MR, which in turn causes water protons in the vicinity to undergo relaxation at a different rate to the rest of the tissue, allowing more detailed images to be collected. Typically, gadolinium based chelates affect T_1 relaxation times and SPION affect T_2 relaxation times.[2, 5, 80]

1.4.1 Components of a contrast agent

Typically, a contrast agent is comprised of the following key components (Figure 1-25):

Chelate based contrast agent -	**Nanoparticle based contrast agents -**
Metal centre	Nanoparticle core
Chelating ligand	Surface coating
Targeting agent (optional)	Targeting agent (optional)

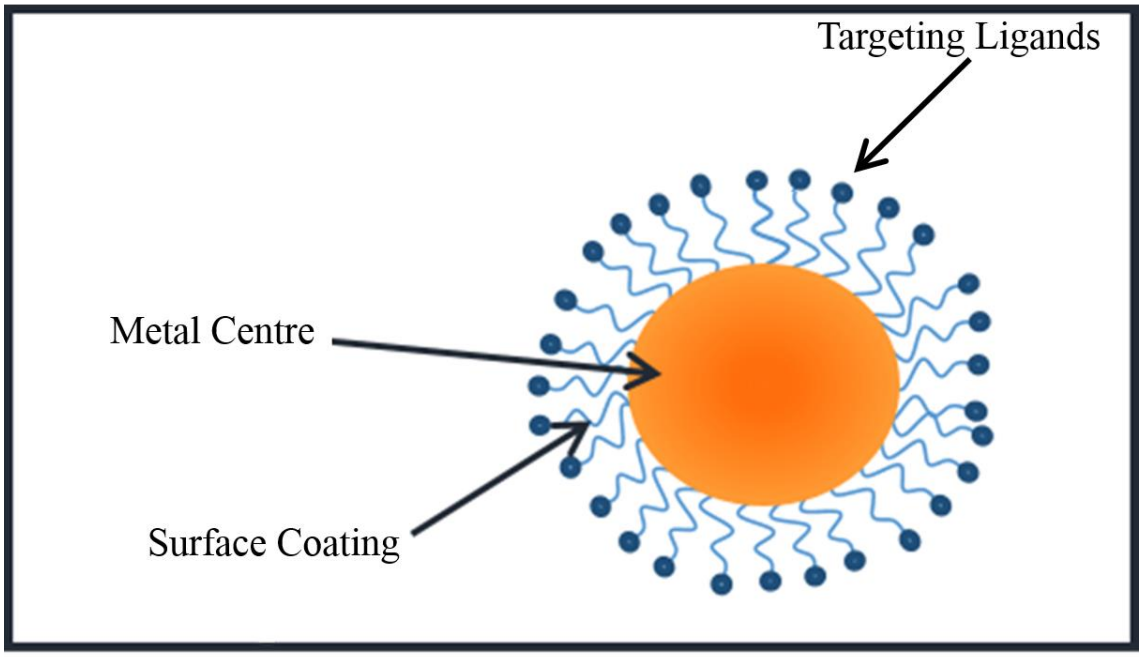

Figure 1-25 Components of a contrast agent typically include a metal centre, surface coating and targeting ligands.

The individual components that make up MRI contrast agents are discussed in the following section.

The most common metal centres are gadolinium or iron. Gd^{3+} is used because it has an isotropic S state and is paramagnetic due to the seven unpaired electrons in the valence shell, which give the largest magnetic moments of the lanthanide series.[81] SPION possess

a unique phenomenon known as superparamagnetism at room temperature due to their small size and the multiple iron ions per particle cause large magnetic moments.

Surface coatings and chelating ligands provide biocompatibility through either capping the surface of a nanoparticle or stabilising a metal centre, limiting the toxic effect of the contrast agent within the body.[82, 83] Surface coatings also have the added property of helping to mask the contrast agent from the body's defences. The size of the nanoparticles has a major effect on how well the contrast agent is tolerated by the body, and different sized nanoparticles can be used to image different areas. For example gadolinium chelate complexes are used to image vascular and interstitial areas of the body,[84] and large hydrodynamic diameter iron oxide nanoparticles tend to be used to image the liver.[85] The size and biocompatibility of the chelate complexes can be altered by using different ligands bonded to the metal centre. In these cases it is important to choose a ligand that allows water molecules to enter the coordination sphere and undergo relaxation.[4]

Targeting agents are beneficial components as they allow contrast agents to be selective to a chosen area of the body. For example, targeting the biomarkers expressed on cancer cells can lead to easy identification of a tumour on a MR image.[86]

With the first two components a generic contrast agent can be prepared by functionalising the surface of the nanoparticles for different biomarkers a multitude of different and useful contrast agents can be formulated.

It is difficult to directly compare the magnetic properties of chelated complexes and solid nanoparticles as the nature of the nanoparticle structure allows for other interactions to occur between the various cations that are not present in chelated complexes.

It was previously stated that iron oxide nanoparticles are the most commonly used T_2 contrast agents, and as yet there is little competition for this title. Nevertheless, research into how to improve the characteristics of iron oxide to induce a greater T_2 effect has been carried out over the last decade, with studies on size, surface coatings and chemical composition.[41, 56, 60, 87-90]

Research has also been carried out into improving T_1 contrast agents, with a recent focus on the use of gadolinium oxide nanoparticles as T_1 contrast agents and gadolinium labelled iron oxide nanoparticles for use as dual probe contrast agents at 1.5 T, 3.0 T and 7.0 T.[63, 91-93]

One major advantage of using SPIONs as MRI contrast agents is their superparamagnetic properties.[2, 5, 94] Another benefit is that the nanoparticle surface can be modified, allowing specific biomarkers to be targeted. This means that the nanoparticles can highlight the presence or absence of a tumour, and can also be used to determine the extent and progression of a specific illness. Typically, SPIONs are composed of either Fe_3O_4 (magnetite), or γ-Fe_2O_3 (maghemite). Commercial iron oxide nanoparticles (Endorem/Feridex, manufactured by Guerbet SA, and Resovist manufactured by Schering AG) have already been clinically approved and have found multiple uses in the biomedical world.[95]

It has been proven in many cases that magnetic susceptibilty is one of the major factors affecting the use of specific nanoparticles as contrast agents. The higher the magnetic susceptibility, the greater the nanoparticle's relaxation effect and the better the contrast agent. Therefore it is critical that the unit cell structure is well defined in order to be able to tailor properties appropriately.[47, 96, 97]

When choosing the metals used in nanoparticulate contrast agents for MRI, the distribution, metabolism and elimination of the agents needs to be considered. To work effectively as contrast agents the nanoparticle must be able to evade the body's reticulo-endothelial system (RES) and stay in circulation long enough to reach the targeted destination.[85]

When larger particle sized (< 200 nm hydrodynamic radii) contrast agents enter the body intravenously, they trigger an immune response from the RES and are taken up by macrophages.[2, 5] The circulation time around the body before this typically depends upon the surface coating of the particles, with coatings such as polyethylene glycol (PEG) being favoured for longer circulation times.[98]

Large hydrodynamic diameter iron based nanoparticles collect in the liver and spleen after collection by the RES, one of the reasons they are used to image these organs.[5] However, elimination of smaller hydrodynamic radii (< 6 nm) nanoparticles is done by the kidneys,[85] with the contrasts agents being excreted mostly unchanged in the urine within a few hours of administration.[99] Nanoparticle contrast agents with hydrodynamic radii between these two values do undergo opsonisation by the RES, however due to their small surface area this process takes longer. This results in these nanoparticles having extended circulation times compared to other particles.[85]

Biocompatibility is an essential property of any compound to be used in a biological environment. Surface coating of nanoparticles helps to improve stability, solubility and circulation times, improving the viability and efficacy as a contrast agent.[98] A wide variety of coatings have been used to improve the biocompatibility of nanoparticles for an array of biomedical applications, with widely used coatings including polysaccharides such as dextran or chitosan, polymers, or amino acids. SPIONS without any surface coating tend to aggregate in water and in some cases are chemically unstable when

exposed to air. This is a problem in vivo as large agglomerations form and uncoated particles react with proteins in the serum, reducing circulation of the particles and therefore the effectiveness for MRI. A variety of polysaccharides and polymers have been investigated as potential surface coatings including chitosan,[100, 101] dextran[100, 102] and PEG.[7, 24, 100] Surface coatings offer a range of properties that can be added to SPIONS.[2, 5] Chitosan is a natural polymer that has been shown to facilitate movement of particles into cells and binds easily to iron oxide nanoparticles, leaving positively charged amino groups open for further reactions.[100]

PEG is another common coating for SPIONS that improves their hydrophilicity and extends circulation time of the contrast agent, by enabling easier evasion of the RES.[88, 103]

Dextran is a commonly used surface coating in current commercial iron oxide based MRI contrast agents.[41, 104, 105] Dextran improves the hydrophilicity of the nanoparticles although research by Li *et al* [106] suggests it is susceptible to detachment from the nanoparticles in vivo. To overcome this, other forms of dextran such as carboxymethyl dextran have been investigated as they provide a more rigid structure with stronger attachments.

All of these polymers can be further modified for the reaction with targeting agents.[100] This allows the contrast agent to be specific to a particular cell type or region, improving image contrast in that area only. For example, Veiseh *et al.* developed dual function optical/MRI nanoprobes for targeting brain tumours.[107] The nanoprobe was based on an iron oxide nanoparticle core, coated with PEGylated chitosan attached to targeting agent chlorotoxin.

1.5 AIMS

The aim of this research is to design and prepare new contrast agents for use with MRI. This will be done in three ways:

- Investigation into how current contrast agents e.g. iron oxide nanoparticles can be improved, through the synthesis and characterisation of Gd^{3+} and Dy^{3+} doped iron oxide nanoparticles.

- Preparation and testing of alternative metal oxide nanoparticles for potential use as MRI contrast agents, such as gadolinium oxide and dysprosium oxide.

- Investigation of the effect of exchange interactions on the magnetic properties of nanoparticles through anion substitution of iron oxide nanoparticles.

2 ANALYTICAL METHODS AND CHARACTERISATION TECHNIQUES

2.1 XRD

X-ray diffraction is a widely used technique for the analysis of the crystal structure of solids. Patterns can be collected from samples that are either a single crystal or a multicrystallite sample such as powder. For single crystal, the diffraction spots can be used to determine the structure of the crystal analyzed.[108] For powder samples, the data collected shows the diffraction peaks that can be matched to peaks calculated for the same unit cells with similar lattice parameters. For this method to be useful, knowledge of the possible composition of the powder sample is required.

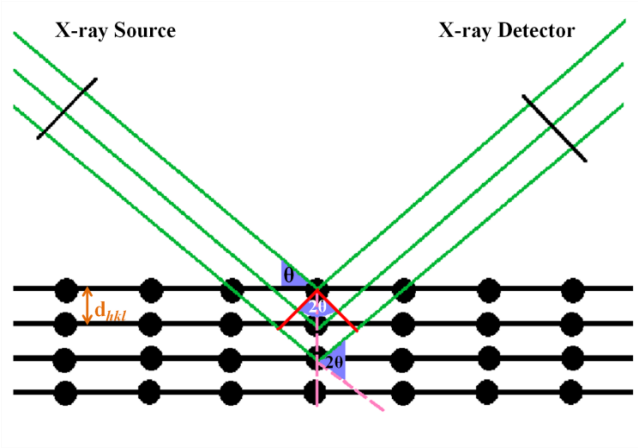

Figure 2-1- Bragg conditions for X-ray difraction.

The technique is based on the Bragg law: stating that when X-rays hit the surface of a crystal they are diffracted by the atoms within the crystal. For the reflected signal to be strong enough to be detected all the reflections need to be in phase with one another (Figure 2-1).[108]

For this to occur there must be an integral spacing between the path lengths of the reflected X-rays (Equation 2-1). This is shown by the Bragg equation (Equation 2-2) and determines the interplanar spacing within the crystal.[13]

$$\text{difference in pathlength} = 2d_{hkl}\sin\theta_{hkl} \qquad \text{Equation 2-1}$$

Thus, for an integral number of wavelengths (n) the Bragg equation can be formed:

$$n\lambda = 2d_{hkl}\sin\theta_{hkl} \qquad \text{Equation 2-2}$$

λ= wavelength of X-rays

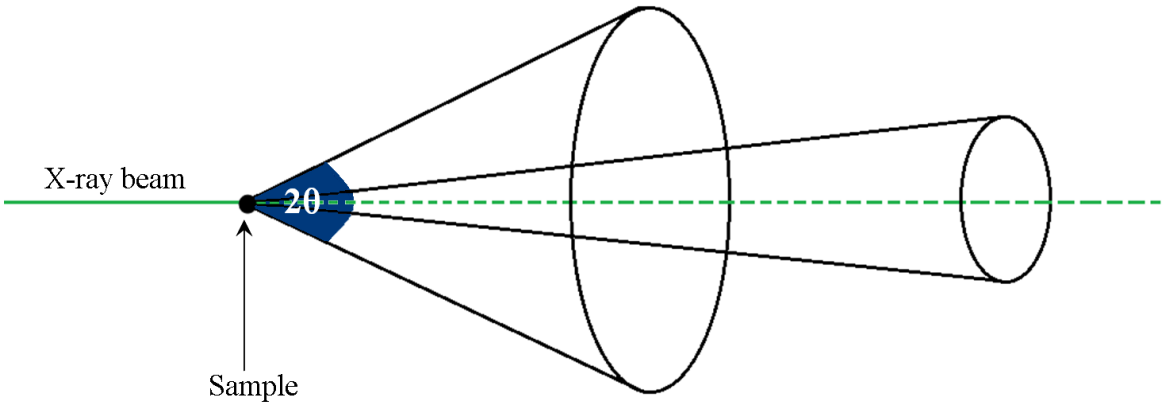

Figure 2-2 Diffraction cone observed in powder samples.

In the case of powder X-ray diffraction, when X-rays hit the sample it will scatter in all directions giving rise to a cone of scattering (Figure 2-2). The X-ray detector moves around the sample and measures the cone scattering at different angles (°2θ) (Figure 2-3).

Each cone represents a plane of diffraction and this data can then be used to identify the sample structure and composition.[109, 110]

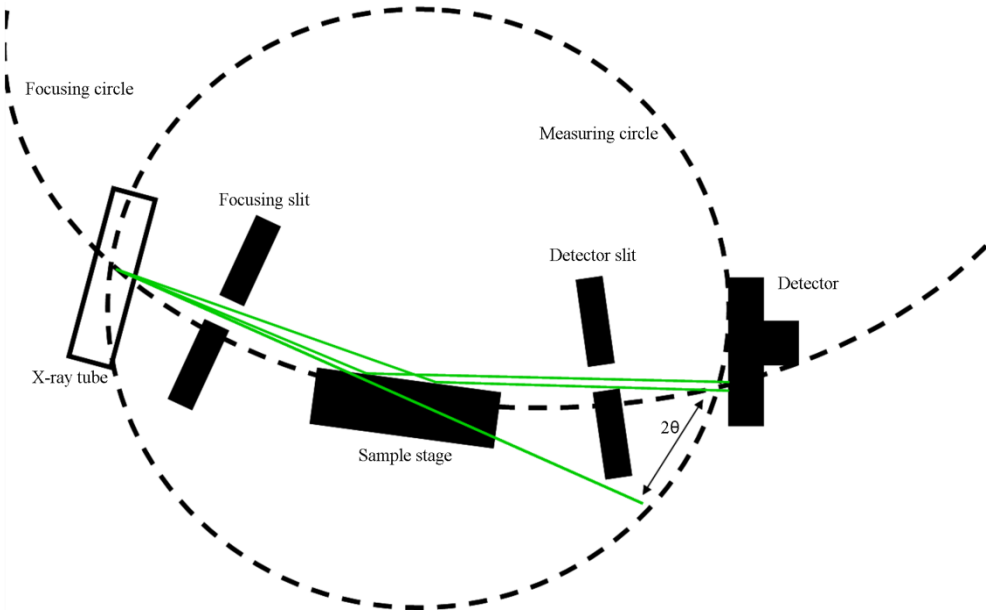

Figure 2-3 X-ray diffractometer setup. The detector can rotate around the sample stage allowing scattering to be measured at different angles.

X-rays are generated by a beam of electrons striking a metal target. This strike causes electrons close to the nucleus of the metal atom to fall out of orbit, forming a vacancy which is filled from electrons moving down from higher energy levels. The energy difference caused by the movement of electrons from higher energy levels to lower energy levels is emitted as an X-ray.[108]

2.2 NUCLEAR MAGNETIC RESONANCE (NMR) AND MAGNETIC RESONANCE IMAGING (MRI)

Magnetic resonance imaging (MRI) and nuclear magnetic resonance (NMR) are similar techniques used to measure the relaxation rates of different materials. The main difference between the two techniques is that NMR measures relaxation against a fixed frame reference point, whereas in MRI it is possible to move the gradient coils and relaxation measurements can be taken within a rotating frame of reference.[6] Typically, MRI refers to proton relaxation in the form of an image, with areas of the body containing protons relaxing at different rates showing up as darker or lighter parts of an image. NMR is usually used to measure proton relaxation as a function of time, and is commonly used as a way of testing compounds with the potential for use as contrast agents.[99]

In order to be MR active, atoms must possess angular momentum, caused by an odd number of protons or neutrons in an atoms nucleus. Laws of electromagnetism state that movement of a charged particle causes a magnetic field and therefore MR active nuclei possess a magnetic moment. The most commonly used element is hydrogen due to its abundance in the human body, but other MR active nuclei include carbon-13, fluorine-19 and phosphorus-31.[6]

The magnetic moments of MR active nuclei are usually randomly orientated due to thermal energy, but align parallel or antiparallel when an external magnetic field is applied. The population of magnetic moments aligned in the parallel or antiparallel state is dependent upon the strength of the magnetic field and its ability to overcome the thermal energy level of the nuclei. Nuclei with low thermal energy tend to align parallel to the magnetic field, whilst nuclei with high thermal energy align antiparallel. The population of the antiparallel state is lower than that of the parallel state and so there is a net magnetic moment aligned parallel with the magnetic field. The energy gap between

the two energy states is directly proportional to the magnetic field strength, increasing field strength increases the amount of energy required to produce resonance *via* excitation.[110, 111]

When observing an electron spinning around its own axis, a further spin can be introduced through the application of an external magnetic field (Figure 2-4). This second spin causes the magnetic moment of the nucleus to rotate around the magnetic field axis in a circular motion at a speed known as the precessional frequency.

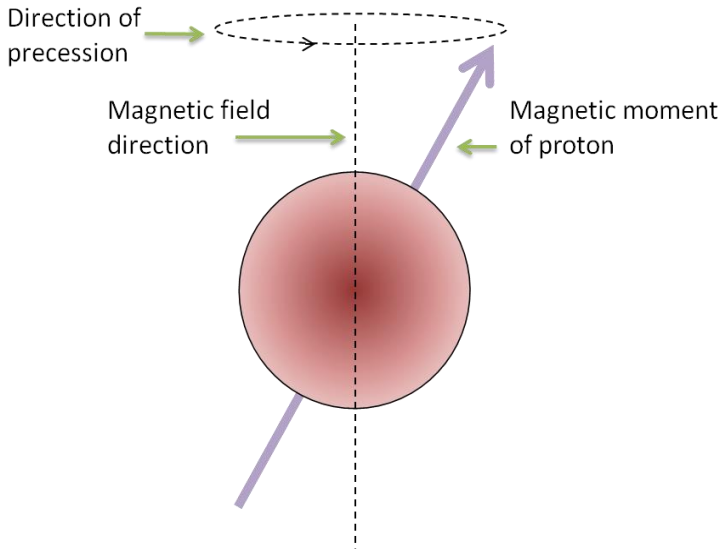

Figure 2-4 A hydrogen nucleus in the presence of a magnetic field.

Precessional frequency is directly related to magnetic field strength *via* the Lamor equation (Equation 2-3) and is specific to each set of nuclei. Different nuclei precess at different frequencies allowing specific nuclei to be measured without interference from others. Each MR active nuclei has its own gyro-magnetic ratio, expressed in mHz/ T.[99]

$$\omega_0 = B_0 \times \lambda \qquad \text{Equation 2-3}$$

ω_0 = Precessional frequency

B_0 = Magnetic field strength

λ = gyro-magnetic ratio

If a radio frequency (RF) pulse ($10^6 – 10^8$ Hz) is applied to hydrogen nuclei at the same frequency as their precessional frequency, resonance occurs and the nucleus gains energy. This leads to excitation of some nuclei from the low energy state to the high energy state. This causes the overall magnetic moment to change direction away from the direction of the magnetic field to an angle called the flip angle (Figure 2-5). The magnitude of the flip angle is dependent upon the strength of the RF pulse applied and is most commonly 90˚, flipping the magnetic moment of the nuclei from the longitudinal plane into the transverse plane. Application of an RF pulse at the correct frequency and the corresponding excitation forms the basis of the relaxation mechanisms that are used to collect MR images.[112]

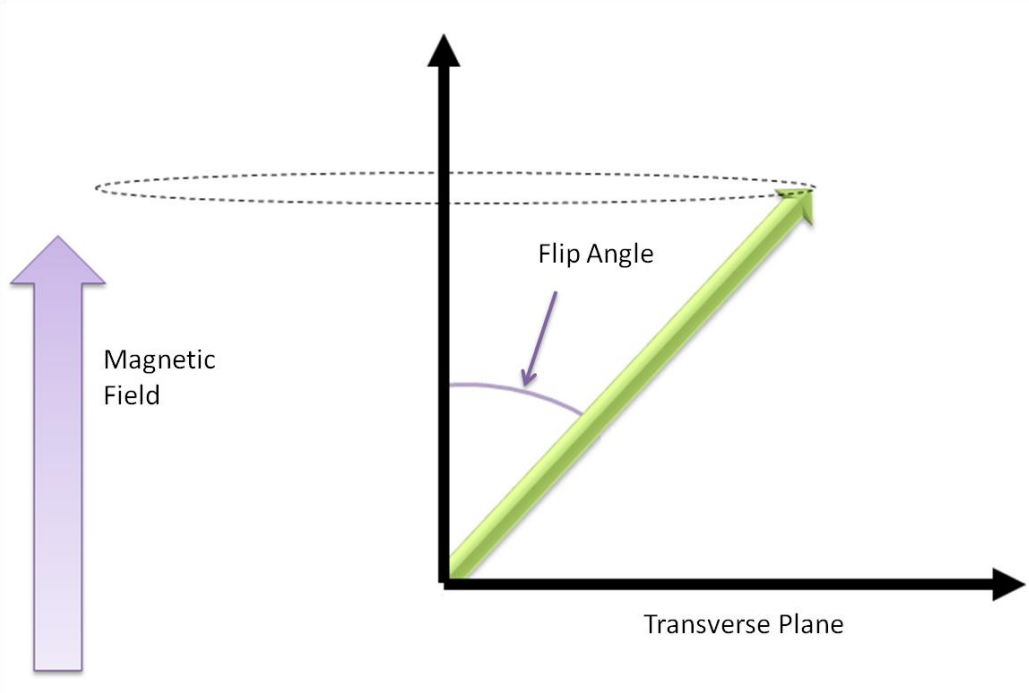

Figure 2-5 When an RF pulse is applied to hydrogen nuclei the magnetic moment changes direction away from the magnetic field, at an angle known as the flip angle.

2.2.1 Relaxation

Once the RF pulse is removed the magnetic moments of the nuclei try to realign parallel with the magnetic field. In order to do this the nuclei must lose the energy gained by application of the RF pulse, this process is termed relaxation. During this process some of the high energy state nuclei return to the lower energy state, known as free induction decay (FID) and it is this signal that is measured by the NMR/MRI.[111, 112]

There are two types of relaxation mechanisms, depending on the plane that is affected, known as T_1 and T_2. Both these mechanisms come about due to the hydrogen nuclei losing their absorbed energy and returning to the lower energy state. At the same time, although totally exclusively, the magnetic moments of the hydrogen nuclei lose coherence and magnetisation decays from the transverse plane back to the longitudinal plane.[113]

T_1 relaxation is also known as spin lattice, or longitudinal relaxation and is caused by nuclei releasing energy to the surrounding environment (Figure 2-6). This causes the magnetic moments of the hydrogen nuclei to recover their longitudinal magnetisation and is an exponential process.[113]

T_2 relaxation is an exponential decay process caused by nuclei transferring energy to other nuclei that are close by (Figure 2-7). This exchange is due to the interaction of magnetic fields on neighboring nuclei and gives the T_2 relaxation process its alternative name of spin-spin, or transverse relaxation. The T_2 relaxation mechanism is the decay of the transverse magnetisation and is due to the dephasing and rephasing of the magnetic moments in the transverse plane.[113]

In both cases the measured T_1 and T_2 times are the time it takes for 63% of the longitudinal magnetisation to recover or 63% of the transverse magnetisation to be lost, respectively.

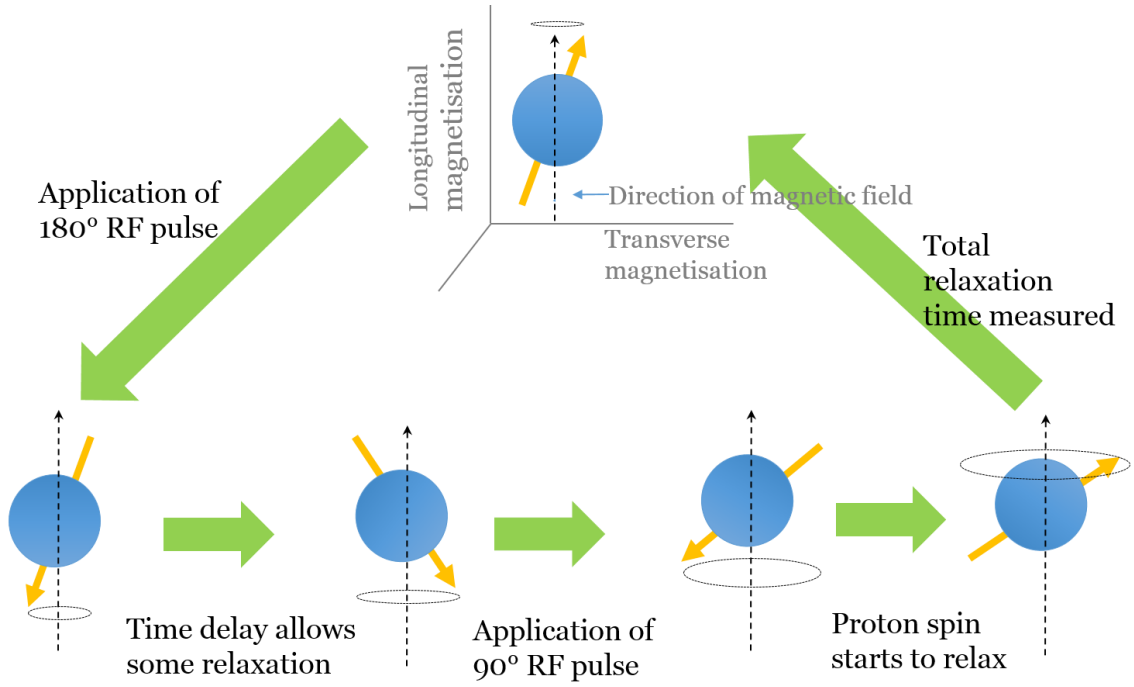

Figure 2-6 Schematic showing the T_1 relaxation of a proton.

T_2* decay is another minor relaxation pathway caused by the external magnetic field not being entirely homogenous. When different areas of the field are stronger or weaker the nuclei in those areas precess faster or slower. This means that they have slightly different relaxation times to the bulk tissue as there is a different rate of dephasing of the nuclei. In most cases T_2 processes produce a rapid loss of signal and have to be compensated for in order to measure T_1 and T_2 processes accurately. This is typically done by using a spin-echo pulse sequence, which uses an additional RF pulse to a flip angle of 180°.[112, 113]

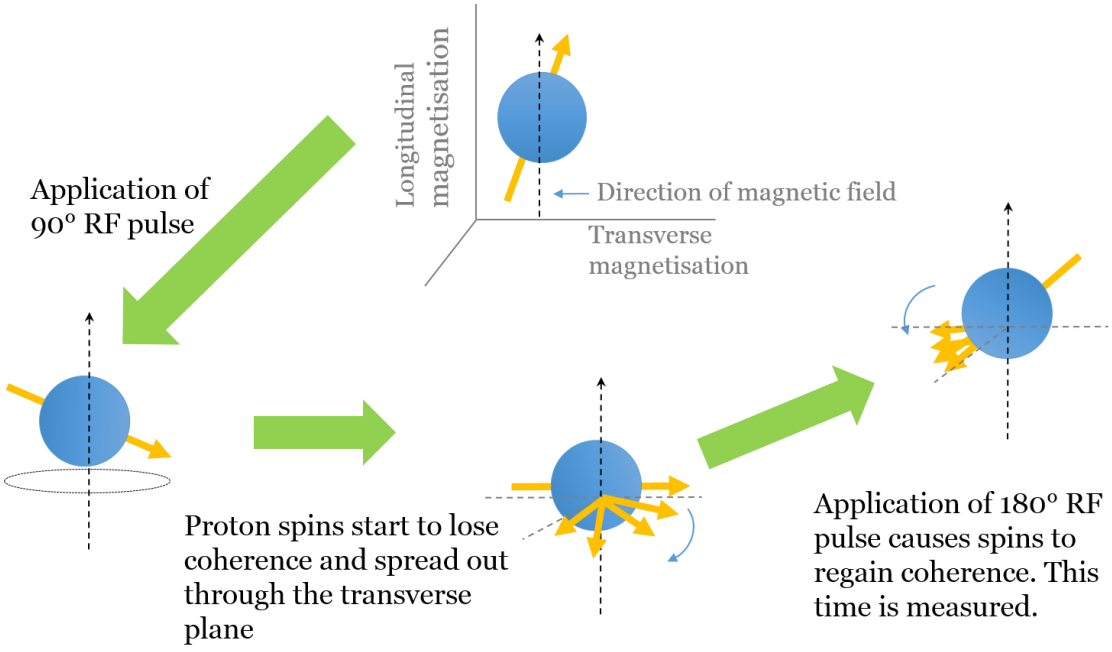

Figure 2-7 Schematic showing the T_2 relaxation of a proton.

Gadolinium based complexes are paramagnetic due to the presence of seven unpaired electrons. One of the most common complexes is Gd-DTPA (diethylenetriaminepenta-acetic acid), commercially known as Magnevist.[7] When in an external magnetic field

these complexes cause inhomogeneities in the magnetic field, causing relaxation to occur between the Gd^{3+} complexes and water molecules in a co-ordination sphere (Figure 2-8). Water molecules close to the contrast agent enter the inner coordination sphere and transfer energy gained from the RF pulse onto the Gd complex, they then leave the coordination sphere 'relaxed' allowing more water molecules to complete the process.[4]

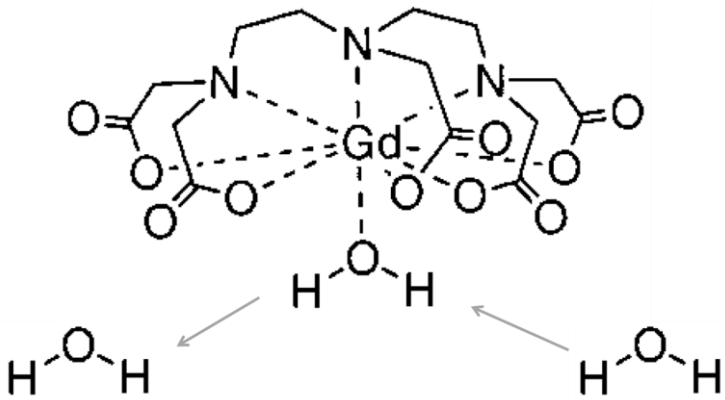

Figure 2-8 A gadolinium based chelate complex with water molecule bound in the inner co-ordination sphere.[114]

When a magnetic field is applied to an area of the body containing SPIONs, the particles align causing a magnetic dipole and a localised magnetic field around the particle (Figure 2-9). Nearby water protons that diffuse into the localised magnetic field experience a greater magnetic effect and therefore have shorter relaxation times.[6, 29, 99, 115]

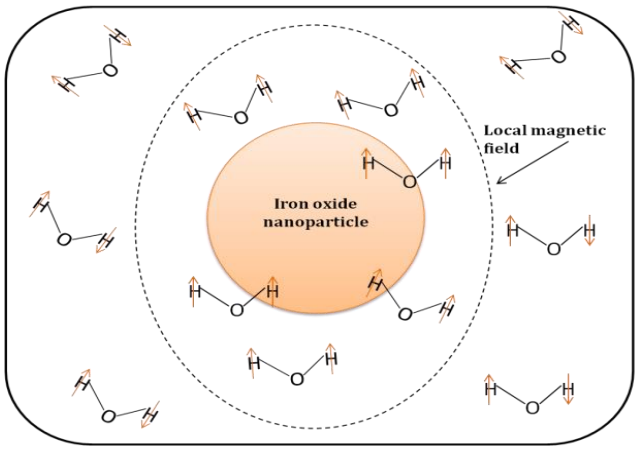

Figure 2-9 Proton relaxation in the presence of iron oxide contrast agents.

2.3 MÖSSBAUER SPECTROSCOPY

The Mössbauer effect, originally discovered in 1957, allows detection of minute variations in the energy between nuclei interacting with their electrons, known as hyperfine interactions. It is used as part of Mössbauer spectroscopy in the measurement of magnetism, bond structure, relaxation processes and electronic and molecular structure. It is based upon the absorption and emission of γ-rays causing energy level transitions in nuclei. Both the splitting and energy associated with the orbital levels are affected by the electronic and magnetic environment. It is these changes that provide information about the atoms local environment.[116]

In free nuclei, absorption or emission of γ-rays causes the nuclei to undergo recoil due to conservation of momentum and has a recoil energy E_R. Therefore to get the magnitude of energy required for nuclear transitions to take place and achieve resonance, the energy of the γ-ray must be the sum of the both the transition energy to achieve resonance and the recoil energy of the absorbing nucleus. In order to do this, loss of energy by recoil events needs to be resolved.[117]

Rudolph Mössbauer discovered that atoms in solid matrices have a greater effective mass than that of a single free nucleus, making the recoil energy, E_R, very small. If the emitted and absorbed γ-ray is the same energy and the nucleus is part of a solid matrix, resonance is achieved.

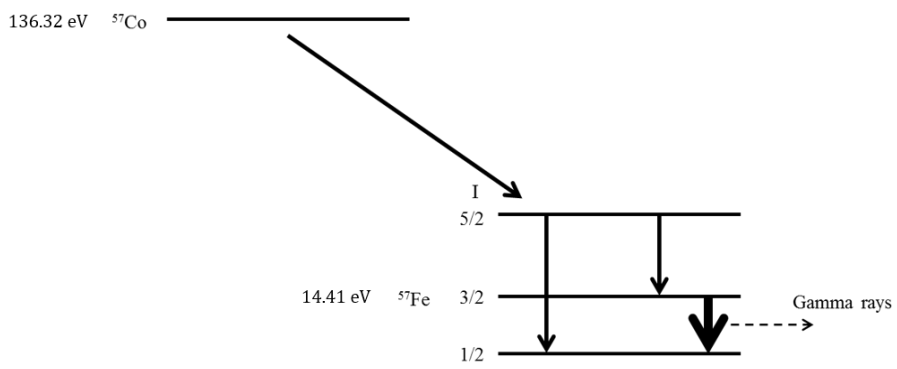

Figure 2-10 The generation of ^{57}Fe γ-rays in Mössbauer spectroscopy.

Production of γ-rays with the same energy as the absorbing nuclei is essential for this technique to work. For example, to analyse a sample containing ^{57}Fe a source with equal energy would need to be used. To produce this energy a ^{57}Co source is used which undergoes decay to a ^{57}Fe excited state. This can then emit a γ-ray of the correct energy to analyse the sample (Figure 2-10).[110]

If the source of the γ-ray and absorbing nuclei are the same energy, a Mössbauer spectrum will show as single absorption line, see Figure 2-11.

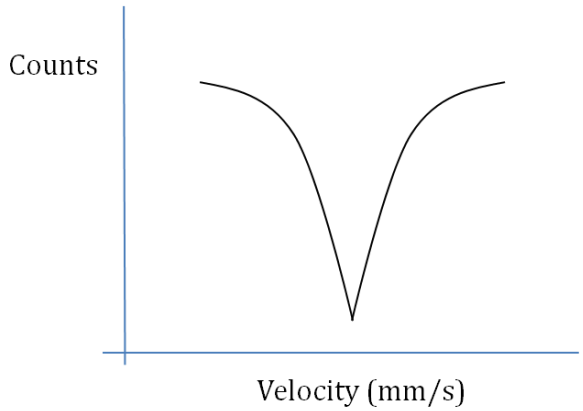

Figure 2-11 A single absorption line is produced when the γ–ray and absorbing nuclei have the same energy.

The Mössbauer effect is limited to specific isotopes as the emitting and absorbing energy must match the nuclear energy level transitions to achieve resonance. Furthermore, the energy of the γ-ray is important to achieve recoil-free events and so the Mössbauer effect is only present in isotopes with low energy excited states. The resolution of Mössbauer spectroscopy is limited by the lifetime of the nuclear excited states before decay and emission of γ-rays, again limiting the number of isotopes that can be used. The most common Mössbauer isotope is ^{57}Fe; Figure 2-12 shows the other isotopes suitable for this type of spectroscopy.[118]

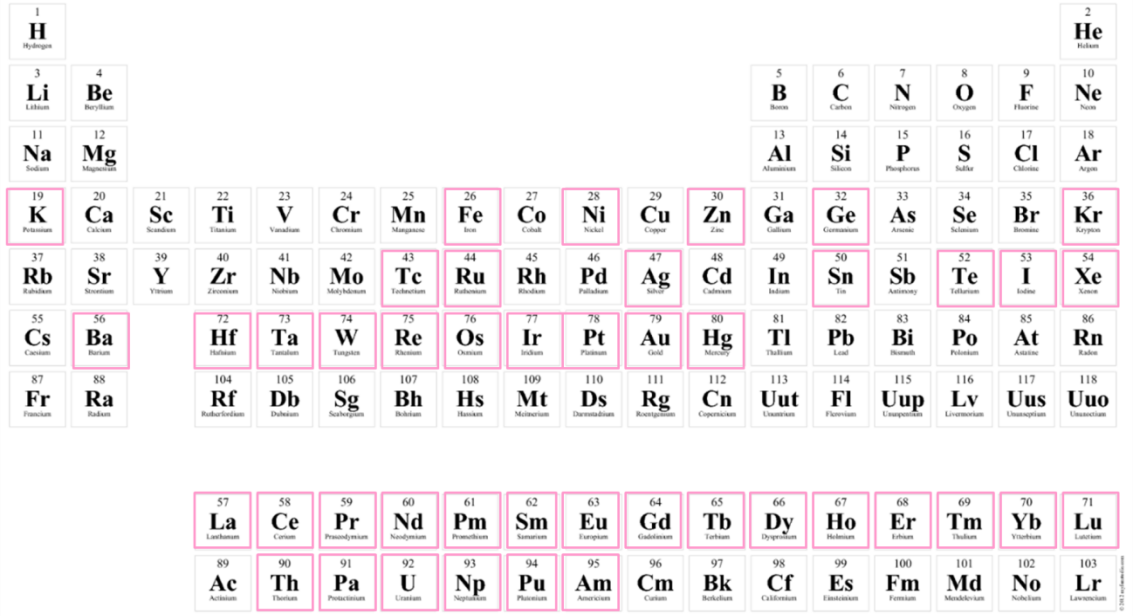

Figure 2-12 Possible isotopes for use in Mössbauer spectroscopy (highlighted in pink).

In order to measure the hyperfine interactions the γ-ray source is oscillated at a few mm/s to cause minute changes in the energy. Where the γ-ray energy matches the energy of a nuclear transition in the absorbing nuclei a peak is seen on the spectrum. The nuclear energy levels are affected by their environment in three ways, the isomer shift, the quadrupole splitting and the magnetic splitting.[117]

2.3.1 Isomer Shift

Isomer shift is useful for the determination of oxidation states, ligand bonding states, electron shielding and the electronegativity of specific groups. It arises due to the nucleus having a non-zero volume and is also affected by the number of s electrons present. A difference in the number of s electrons between the absorber and γ-ray source causes a shift in the resonance energy and thus the whole Mössbauer spectrum is shifted.[118]

2.3.2 Quadrupole Splitting

This is caused by the presence of nuclei with angular momentum I>1/2 having an uneven charge distribution, producing a nuclear quadrupole moment. Splitting of the nuclear energy levels by an electric field is caused by asymmetrical electron charge distribution characterised by the electric field gradient (EFG), see Figure 2-13.[116]

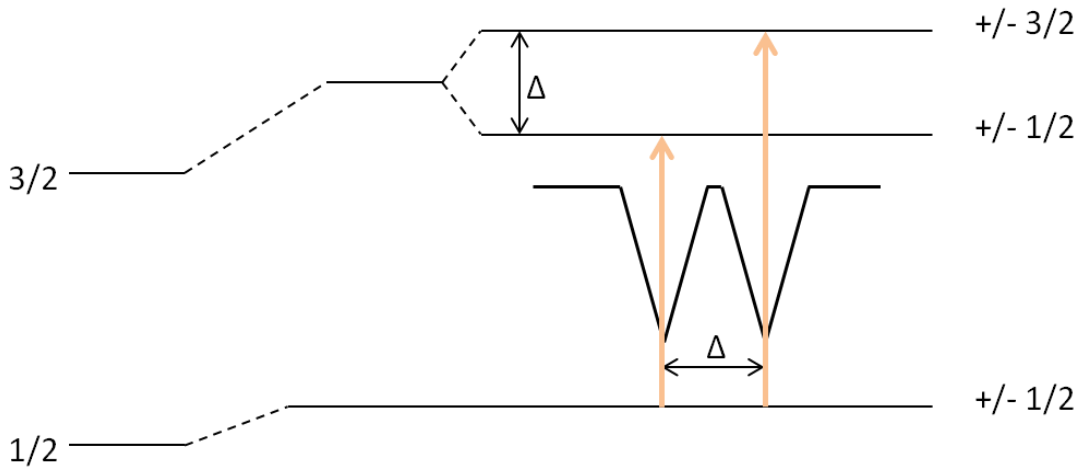

Figure 2-13 Quadrupole splitting of the nuclear energy levels.

2.3.3 Magnetic Splitting

Magnetic splitting occurs when the nuclei experience dipolar interactions with a magnetic field, splitting energy levels into 2I+1 substates, where I is the spin of the energy level.

As transitions can only occur when M_I changes by 0 or 1, for ^{57}Fe there are six possible transitions giving a sextet (Figure 2-14).[118]

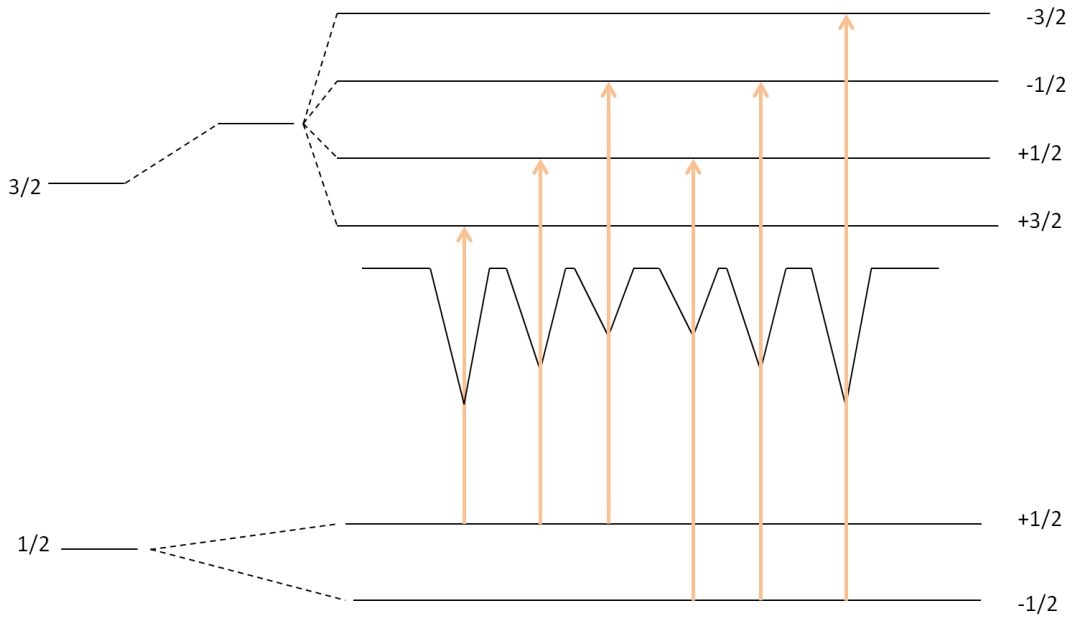

Figure 2-14 Magnetic splitting of nuclear energy levels for ^{57}Fe.

The positions of the lines in the spectra are due to the splitting of the energy levels and the intensities are due to the angle between the γ-ray and the nuclear spin moment. The outer and inner spectral line intensities are always in a 3:1 ratio but the middle line intensity has a range of 0-4 depending upon the angle between the γ-ray and nuclear spin moment. Typically, in polycrystalline samples this value is 2 however other samples and in the presence of an applied magnetic field this number can provide information about the nuclear moment orientation and magnetic ordering.[116]

2.4 ELECTRON MICROSCOPY

Electron microscopy is a useful technique for imaging solids at the micro- and nano-scale. The two main methods are scanning electron microscopy (SEM), mainly used for imaging the external morphology of samples, and transmission electron microscopy (TEM), which is capable of imaging at higher magnification and can provide detailed images of the internal structure. Additionally these methods can be combined with energy dispersive X-ray spectroscopy (EDX) which is capable of providing the elemental composition of the sample being analysed.

2.4.1 Transmission Electron Microscopy

A TEM consists of an electron emission source, typically tungsten or lanthanum hexaboride which emits electrons once an electric field is applied. The electrons then travel through a vacuum and are focused by various optical lenses onto the sample. The electrons interact with the sample as they pass. This allows grayscale images to be collected of the samples, providing detailed information on the size and shape of the solid analyte.

2.4.2 Scanning Electron Microscopy

In a similar manner to TEM, an electron beam is formed from the application of current to a tungsten or lanthanum hexaboride source and accelerated through a vacuum. In this case the electrons are scattered by the surface of the sample and measured by a detector. One key point to note about SEM is that non conducting samples require a coating before analysis, often gold or carbon, otherwise the images collected will be blurred due to electrons absorbing to the sample surface and interacting with the electron beam.

3 LANTHANIDE SUBSTITUTED IRON OXIDE NANOPARTICLES (LN= GD, DY)

Over the last decade a substantial amount of research has been conducted in biomedical imaging, drug delivery and theragnostics, where the properties and characteristics of modified iron oxide nanoparticles are of major interest[2, 5, 25, 119, 120]. Fine adjustment of the chemical composition has a direct impact on the properties of a solid and can result in the development of new and exciting compounds with unique attributes, leading the way to new applications.

In MRI, one major advantage of using SPIONs (superparamagnetic iron oxide nanoparticles) is their unique superparamagnetic properties.[5, 121] In bulk iron oxide the material is split into a number of magnetic domains. Within each domain there is a net magnetic moment caused by alignment of neighbouring unpaired electrons. Adjoining domains have different directions of net magnetisation until a magnetic field is applied and all domains align. In iron oxide nanoparticles, due to their small size all magnetic domains align even in the absence of a magnetic field, a phenomenon known as superparamagnetism.[11] This phenomenon is exploited when iron oxide nanoparticles are used as MRI contrast agents. Each nanoparticle behaves as one large paramagnet, each containing multiple metal centres exhibiting a large magnetic moment. The higher the magnetic moment, the stronger the relaxation effects of MRI contrast agents on water protons in the body, causing a large difference in signal and increased sensitivity.

Another benefit of using SPIONs for biomedical applications is that the nanoparticle surface can be modified, allowing specific biomarkers, such as those expressed on tumour cells, to be targeted.[21] This means that the nanoparticles can highlight the presence or absence of a tumour, and determine the extent and progression of a specific illness.

Typically, SPIONs are composed of either Fe_3O_4 (magnetite), or γ-Fe_2O_3 (maghemite); other types of iron oxide exist but do not possess the magnetic properties conducive to biomedical applications.

It has been established that iron oxide nanoparticles, whether magnetite or maghemite, can provide much improved T_2 relaxation times, enhancing the negative contrast of an MR image.[122] In order to further the development of new, superior contrast agents, tailoring of iron oxide nanoparticles through cation doping has been extensively investigated.

Magnetite and maghemite possess slightly different magnetic properties, with magnetite having a larger magnetic moment than maghemite. However, synthesising single phase magnetite on the nanoparticle scale is difficult and often results in particles with a magnetite core and maghemite shell.[123, 124] For bulk material, PXRD shows the same set of peaks, that shift to lower angles for Fe_3O_4 and it is hence used to distinguish between the two polymorphs. However, for nanoparticles the two sets of PXRD peaks are broad and overlap significantly; this makes it difficult to distinguish one phase from another effectively.

Magnetite (Fe_3O_4) has an inverse spinel structure $B[AB]O_4$, relating to $Fe^{3+}[Fe^{2+}Fe^{3+}]O_4$ with the tetrahedral holes occupied by the Fe^{3+} and the octahedral holes divided between the remaining Fe^{3+} and Fe^{2+} ions. Cation substitution is typically dependent on the size of the substituting ion compared to the size of the tetrahedral and octahedral holes combined with the crystal field stabilisation energy. If cation substitution occurs, magnetic coupling interactions between the iron cations across both octahedral and tetrahedral holes are either altered or entirely disrupted depending upon the nature of the substituting cation. This impacts the magnetic susceptibility, altering the properties of the nanoparticles as a whole.

It has been proven in many cases that magnetisation saturation needs to be one of the major factors in designing nanoparticles for use as contrast agents.[49, 125, 126] The higher the magnetisation saturation, the greater the nanoparticle's relaxation effect and the better the contrast agent. Therefore it is critical that the unit cell structure is well defined in order to be able to tailor properties appropriately.

In vivo detection of larger nanoparticles by the reticulendothelial system (RES) and excretion from the body through the liver means that larger iron oxide nanoparticles started out as blood pool contrast agents.[6] However, progression in control of both nanoparticle size and biocompatibilty have become top priorities. These advancements mean the nanoparticles can more easily evade the RES increasing circulation times and improving MR images of target areas.[89, 105, 127] Multiple studies have shown that the magnetic properties of magnetite and maghemite vary with size and often the method of synthesis or surface coating also influences the final magnetic characteristics of the materials.[39, 40, 42]

A wide range of cation doped iron oxide nanoparticles have been proposed as good contrast agents for MRI. One extensively researched area is manganese ferrite nanoparticles.[44, 49, 60] In commercially used MnO nanoparticles, the metal induces T_1 relaxation and so by doping manganese cations into magnetite, a contrast agent with dual T_1 and T_2 relaxation properties can potentially be produced.

Determination of the parent structure is essential in order to know the unit cell structure (spinel or inverse spinel) and also the doping mechanism i.e. substitution, intercalation, formation of vacancies, which will greatly affect the chemical and magnetic properties of the nanoparticles as well as their stability.

There are a wide variety of synthetic routes for the preparation of $MnFe_2O_4$ type compounds, with both co-precipitation and thermal decomposition methods being equally popular. Lu *et al*.[45] prepared Mn doped Fe_3O_4 nanoparticles by thermal decomposition of iron(III) acetylacetonate and manganese(II) acetylacetonate in the presence of 1,2-hexadecanediol, oleic acid, oleylamine and benzyl ether. The hydrophilic nanoparticles produced were coated with methoxy-poly(ethylene glycol)-b-poly(3-caprolactone) or (mPEG-b-PCL) and measured to be approximately 8 nm. The polymer bound nanoparticles formed a micelle with the nanoparticles in the hydrophobic centre. Analysis by AAS determined a Fe/Mn ratio of 1.995 suggesting one third of the iron ions have been substituted with manganese. Furthermore, characterisation by XRD showed a match to the JCPDS card for bulk manganese ferrite indicating that the Mn^{2+} ions had successfully substituted all the Fe^{2+} ions in the tetrahedral holes.

For a more tailored approach, Kim *et al*.[44] prepared partially substituted Mn doped Fe_3O_4 using a co-precipitation method mixing Fe^{2+}/Fe^{3+} chloride salts with $MnCl_2$ in water. Surface adsorption of lecithin was used to improve solubility and form a ferrofluid. Due to the ratio of reactants the expected formula for the nanoparticles produced was $Fe_{2.9}Mn_{0.1}O_4$ however further work is required to determine the presence of manganese in the unit cell.

One other common dopant for magnetite nanoparticles is zinc. Due to zinc preferring a 2+ oxidation state, the structure of the substituted iron oxide must be magnetite and cannot be maghemite. Further oxidation to maghemite would more than likely result in zinc being expelled from the unit cell rather than oxidise.

Bárcena *et al.*[50] investigated the preparation of zinc doped magnetite by hot injection method, and looked at the difference in magnetic properties when zinc is doped into spinel and inverse spinel structures. [54] It was stated that in regular spinel structures the Zn^{2+}

ions occupy the tetrahedral holes resulting in antiferromagnetic properties, which decrease a contrast agent's effectiveness. On the other hand, when doped into an inverse spinel structure, such as magnetite, the magnetic properties can be significantly improved, so a new, superior contrast agent can be synthesised.

The magnetic properties of zinc doped iron oxide nanoparticles have also been investigated by Liu *et al.*[54] and Hochepeid *et al.*[55] Whilst not specifically directed towards MRI applications, this research provides a great insight to how changes in the cation distribution across the unit cell affects the magnetic properties of the nanoparticles overall to a great extent.

Most recently, lanthanide doped iron oxide nanoparticles have emerged as exciting new multimodal contrast agents that can be used for both optical and magnetic resonance imaging.[56, 57] Lanthanide doped magnetite and lanthanide labelled magnetite nanoparticles have been reported as potential MRI contrast agents, and research of gadolinium doped iron oxide nanoparticles prepared by co-precipitation for other medical uses, such as hyperthermia treatments has also been reported.[23]

Xiao *et al.*[128] have reported the preparation of gadolinium doped iron oxide nanoparticles as T_1-T_2 dual-modal MRI contrast agents. The 4.74 nm nanoparticles were prepared by thermal decomposition and obtained r_1 and r_2 values of 73.9 $mM^{-1}s^{-1}$ and 65.9 $mM^{-1}s^{-1}$ respectively.

Yang *et al.*[129] reports dual T_1-T_2 contrast agents based on gadolinium labelled iron oxide nanoparticles prepared by thermal decomposition similarly to Xiao *et al.*[128]. The prepared magnetite nanoparticles were coated with silicon oxide and labelled with Gd-DTPA. Longitudinal relaxation rates of the nanoparticles at 3 T were 3.7 $mM^{-1}s^{-1}$, 3.2 $mM^{-1}s^{-1}$ and 4.2 $mM^{-1}s^{-1}$ for Gd:Fe molar ratios of 0, 0.1 and 0.3 respectively. Transverse relaxation rates for the same molar ratios were reported at 27.9 $mM^{-1}s^{-1}$, 22.7 $mM^{-1}s^{-1}$

and 17.4 $mM^{-1}s^{-1}$ respectively. Cytotoxicity testing of the prepared nanoparticles against two cell lines, U87MG and MCF-7, indicated low toxicity after 24 hour exposure to concentrations up to 200 μg/mL.

The preparation of gadolinium doped iron oxide nanoparticles for use as magnetic hyperthermia agents has been reported by Drake *et al.*[23] The nanoparticles, prepared by a co-precipitation route, had an average diameter of 13 nm and PXRD diffraction peaks matched those of the spinel structure. The gadolinium: iron atomic ratio was determined to be 0.007:1, leading to the formula $Gd_{0.02}Fe_{2.98}O_3$.

As can be seen, SPIONs and cation doped SPIONs have many uses in medical areas. Doped nanoparticles can affect both T_1 and T_2 relaxation pathways providing essential data and improved images.

Recent literature has suggested that whilst particles on the nanometre scale exhibit excellent T_2 relaxation properties, particles of iron oxide approximately 4 nm or less may be used for T_1 type imaging.[36, 130] This is due to the small particle size and surface coating resulting in particles with smaller magnetic moments than equivalent iron oxides in larger particles, combined with *in vivo* distribution resulting in weaker localised magnetic fields, and thus relaxation occurs by the slower T_1 pathway.

This chapter focuses on the development of single phase iron oxide nanoparticles by soft chemistry techniques, and studies the magnetic properties of the resulting nanoparticles. It then continues to look at the development of lanthanide doped γ-Fe_2O_3 nanoparticles, and the effect of cation doping on the magnetic properties and potential application as MRI contrast agents.

3.1 EXPERIMENTAL

This section describes the method used to prepare single phase γ-Fe_2O_3 nanoparticles as well as the $Fe_{2-x}Gd_xO_3$ $0 \leq x \leq 0.05$ and $Fe_{2-x}Dy_xO_3$ $0 \leq x \leq 1$ nanoparticle series. The lanthanide based starting reagents used were $GdCl_3.6H_2O$ and $Dy(NO_3)_3$ respectively. All nanoparticles were prepared following the method below:

$FeCl_2.4H_2O$ (0.01045 moles), $FeCl_3$ and 'lanthanide starting reagent' (see Table 3-1, Table 3-2 and Table 3-3 for molar ratios) were mixed in 50 mL ethylene glycol and heated to 80˚C. 5M NaOH solution was added dropwise until the pH of the solution reached 10. The temperature was then increased to 120˚C and stirred. After 1 hour, the heat was removed. The mixed solution was exposed to an oxygen rich atmosphere by connecting a separate flask of decomposing H_2O_2 (30%, 100 volumes; 25 mL) to the main reaction vessel and left overnight. The nanoparticles were collected magnetically and washed with warm water before being dried in an oven.

The dried nanoparticles were dispersed in an aqueous solution of hydrochloric acid at pH 4, and citric acid added in a 1:1.2 $Fe_{2-x}M_xO_3$ (M= Fe, Gd, Dy) : citric acid molar ratio. The mixture was stirred for 2 hours before magnetic decantation and the collected nanoparticles were washed with deionised water and the pH adjusted to pH 7. These solutions were then used for MRI and NMR measurements.

Table 3-1 Moles of $FeCl_3$ used in the synthesis of γ-Fe_2O_3.

%Molar Cation Substitution	**Moles $FeCl_3$**	**Moles 'Lanthanide Starting Reagent'**
0	0.00209	0

Table 3-2 Moles of $FeCl_3$ and $GdCl_3.6H_2O$ used in the synthesis of $Fe_{2-x}Gd_xO_3$ ($0 \leq x \leq 0.05$).

%Molar Cation Substitution	**Moles $FeCl_3$**	**Moles $GdCl_3.6H_2O$**
0.67	0.0020691	0.0000209
1.33	0.0020482	0.0000418
2.00	0.0020273	0.0000627
2.67	0.0020064	0.0000836
3.33	0.0019855	0.0001045
6.67	0.001881	0.000209
16.67	0.0015675	0.0005225
23.33	0.0013585	0.0007315
33.33	0.001045	0.001045

Table 3-3 Moles of $FeCl_3$ and $Dy(NO_3)_3$ used in the synthesis of $Fe_{2-x}Dy_xO_3$ ($0 \leq x \leq 0.05$).

%Molar Cation Substitution	**Moles of $FeCl_3$**	**Moles of $Dy(NO_3)_3$**
0.67	0.02069	0.000209
3.33	0.01986	0.001045
6.67	0.01881	0.00209
16.67	0.01568	0.005225
33.33	0.01045	0.01045

3.2 RESULTS

3.2.1 γ-Fe_2O_3 nanoparticles

The preparation of γ-Fe_2O_3 (maghemite) nanoparticles was carried out *via* a co-precipitation method from the iron (II) chloride and iron(III) chloride salts. The resulting nanoparticles were characterised by powder X-ray diffraction (PXRD), Mössbauer spectroscopy, X-ray photoelectron spectroscopy (XPS) and transmission electron microscopy (TEM). Magnetic data was also collected *via* a superconducting quantum interference device (SQUID). Relaxation measurements measured by both an 11.7T nuclear magnetic resonance (NMR) instrument set up for imaging and a 3T magnetic resonance imaging (MRI) scanner can be found in Chapter 6.

The PXRD patterns (Figure 3-1) show that the diffraction peaks match those of γ-Fe_2O_3, however due to the broadening of the diffraction peaks a match with Fe_3O_4 was also determined.[9, 131]The percentage of Fe_3O_4 and γ-Fe_2O_3 was determined from PXRD data using a peak deconvolution method.[38] These calculations showed that over 98 weight % of the iron oxide sample has the γ-Fe_2O_3 structure (Table 3-4). The lattice parameter for the prepared nanoparticles was calculated using HighScore Plus software using the Jørgensen $Fd\bar{3}M$ model for γ-Fe_2O_3.[132]

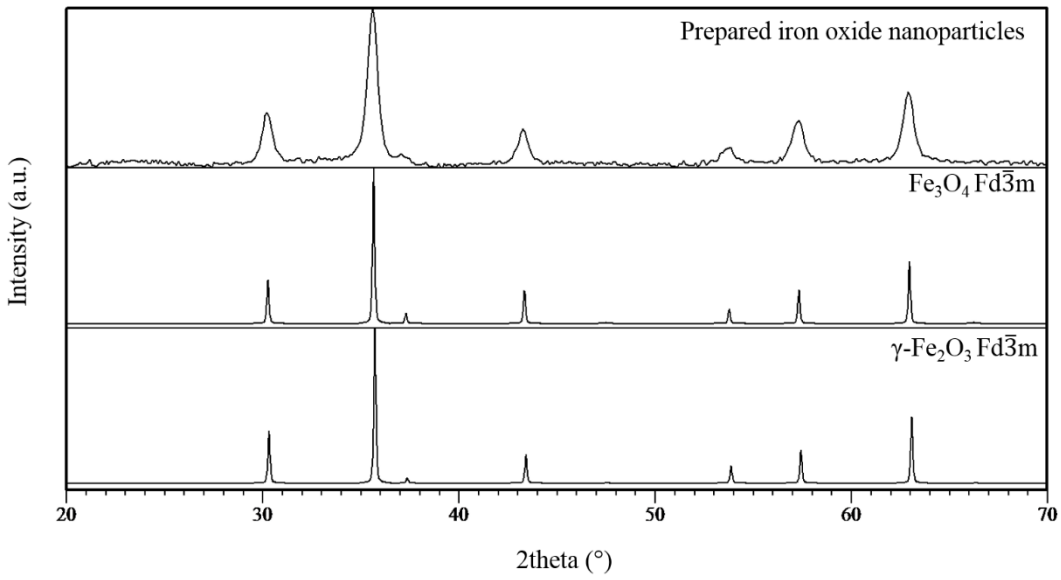

Figure 3-1 PXRD pattern for the prepared iron oxide nanoparticles (top) compared against Fe_3O_4 and γ-Fe_2O_3 simulated PXRD patterns.

This result was further consolidated by XPS data (Figure 3-2). The XPS spectrum shows three peaks corresponding to Fe^{3+} and a peak corresponding to O^{2-} (Table 3-5). The peak at 286 eV can be assigned to carbon and the peak at 784 eV can be assigned to an Fe auger.[133] If the sample also contained Fe_3O_4 nanoparticles, the spectrum would also show peaks for Fe^{2+} at the positions indicated in Table 3-5. As this is not the case, it can be reasonably concluded that only γ-Fe_2O_3 nanoparticles are present.

Table 3-4 Component peak intensity of resolved 440 peak in iron oxide PXRD pattern

440 Peak Intensity from Peak Deconvolution Process (a.u.)		**Calculated content (Weight %)**	
Fe_3O_4	**γ-Fe_2O_3**	**Fe_3O_4**	**γ-Fe_2O_3**
0	848.4805	1.545	98.46

Therefore, based on the PXRD and XPS data collected it can be reasonably assumed that single phase γ-Fe_2O_3 nanoparticles have been prepared.

Table 3-5 Tabulated XPS binding energies for Fe_3O_4 and γ-Fe_2O_3.[9]

Compound	**Fe (*2p*$_{3/2}$)**	**Fe (*3p*$_{3/2}$)**	**Fe (*3s*)**	**O (*1s*)**
Fe_3O_4	708.3 (doublet)	53.9	-	530.2
γ-Fe_2O_3	711.0 (doublet)	55.7	93.6	530.0

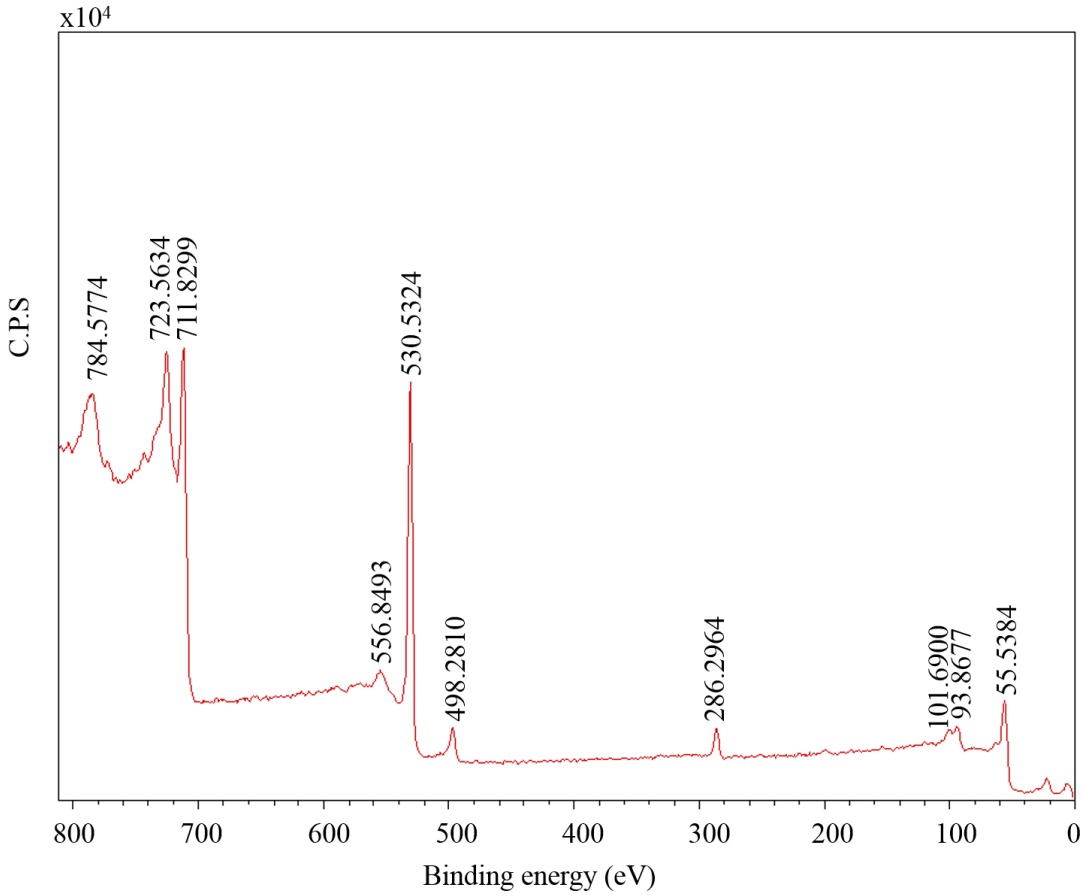

Figure 3-2 XPS spectrum for iron oxide nanoparticles prepared in this work.

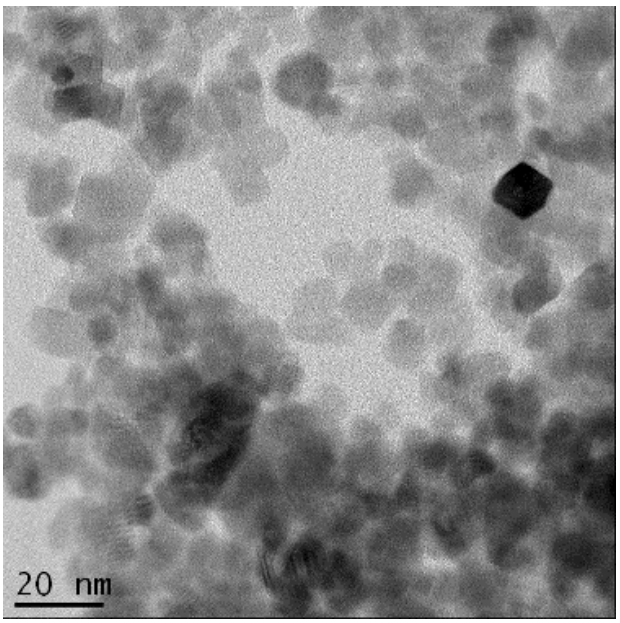

Figure 3-3 TEM image of γ-Fe_2O_3 nanoparticles prepared in this work.

The particle size could not be determined from TEM images (Figure 3-3) due to agglomeration. However, applying the Scherrer equation (Equation 3-1) to the PXRD data estimated the particle size of the prepared γ-Fe_2O_3 nanoparticles, to be 13.1 nm.

The Scherrer equation is:

$$\tau = \frac{K\lambda}{\beta\cos\theta} \qquad \text{(Equation 3-1)}$$

Where:

T = mean crystallite diameter (Å)

K = shape constant, 0.89 for spherical crystallites

λ = 1.542 nm diffraction wavelength (Cu)

B = full peak width at half maximum, FWHM (radians)

Θ = theta (radians)

Mössbauer spectroscopy was also carried out on the prepared maghemite nanoparticles at both 80 K and 298 K (Figure 3-4 and Figure 3-5). The spectrum collected at 80 K shows 6 well defined peaks, following a typical 3:2:1 ratio. This sextet formation is associated with γ-Fe_2O_3 materials and is well documented and relates to the magnetic splitting of the Fe^{3+} ions at low temperature.[116, 118]

At 298 K the spectrum still shows 6 peaks, however the percentage transmission of the 4 central peaks of the sextet are roughly equal (99.28%), with the 2 outer peaks of the sextet having slightly higher percent transmission values (99.34%). Peak broadening can be attributed to the small particle size.

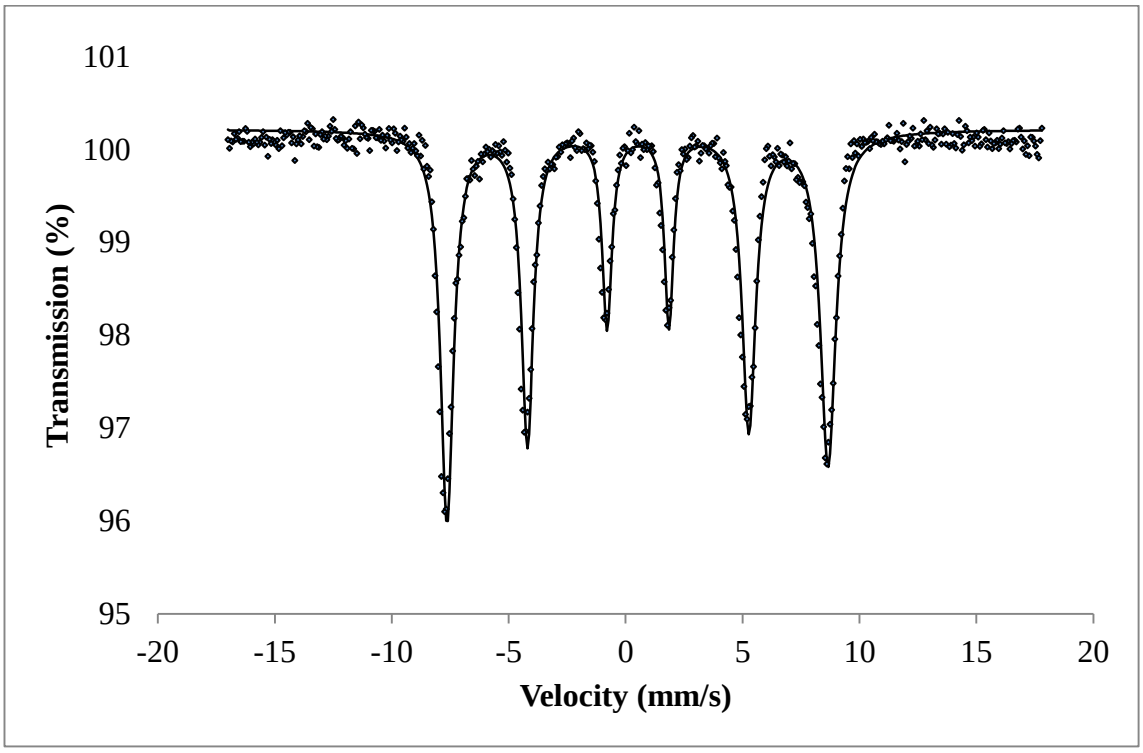

Figure 3-4 Mössbauer spectrum of the prepared γ-Fe_2O_3 nanoparticles collected at 80 K

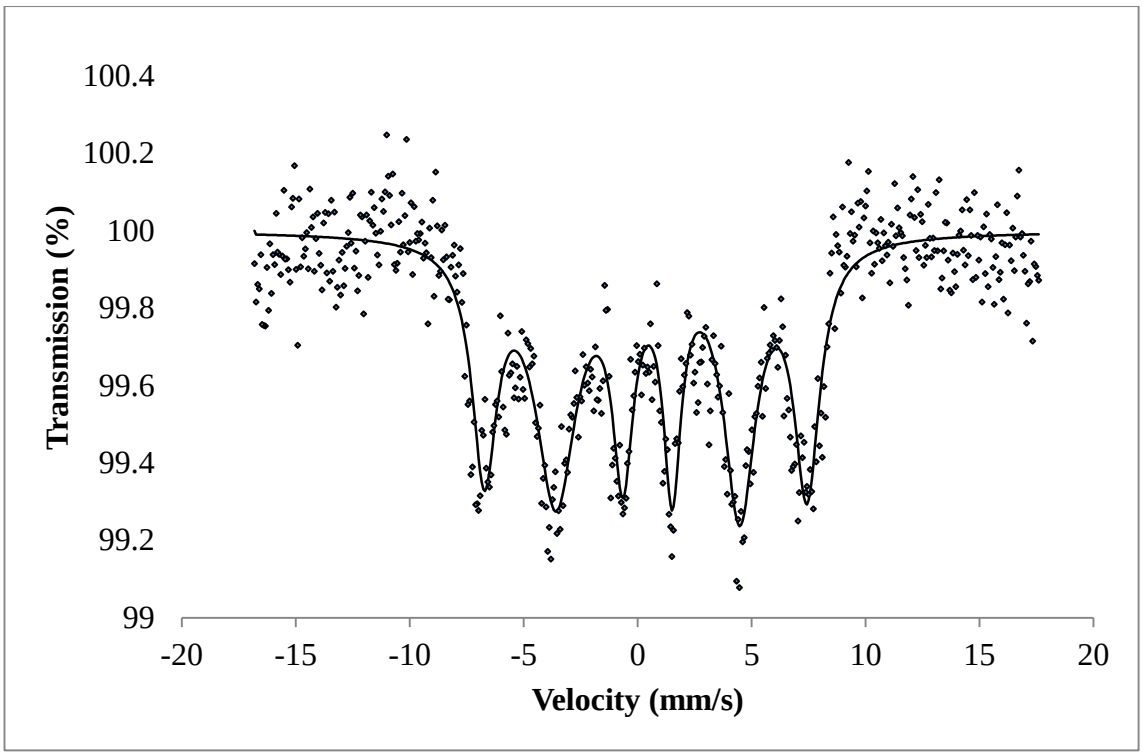

Figure 3-5 Mössbauer spectrum of the prepared γ-Fe_2O_3 nanoparticles collected at 298 K

SQUID analyses of the nanoparticles are shown in Figure 3-6 and Figure 3-7. Magnetic saturisation data has been collected in the form of hysteresis loops and ZFC-FC curves.

The hysteresis loop (Figure 3-6) shows two sets of data collected as the magnetic field strength increases then decreases. Both sets follow closely together, directly overlapping at 0 gauss, indicating superparamagnetic behaviour. Data from ideal superparamagnets would follow the exact same path in both directions. The slight splitting observed indicates that this material is not a perfect superparamagnetic material however the difference between the lines is negligible, and so the material will still exhibit superparamagnetic behaviour. The hysteresis loop indicates that the magnetic susceptibility value for the nanoparticles is 57.6 emu/g at 300 K.

ZFC-FC magnetisation data (Figure 3-7) was also collected. The ZFC curve initially increases as temperature increases, followed by a gradual decrease until 300 K is reached.

The FC curve shows a gradual decrease in magnetisation as temperature increases. The temperature at which the two curves diverge is known as the blocking temperature, and above this temperature superparamagnetic behaviour is observed. In the case of the prepared γ-Fe_2O_3 nanoparticles this temperature is 38 K.

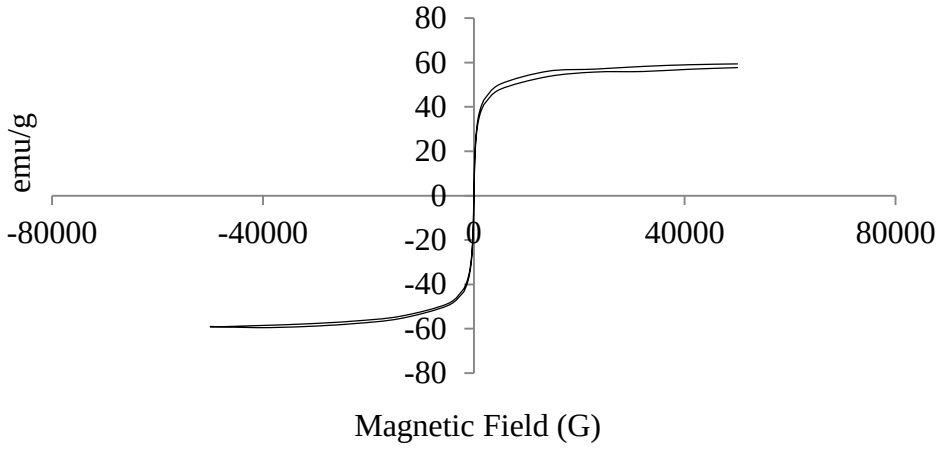

Figure 3-6 Hysteresis curve for the γ-Fe_2O_3 nanoparticles prepared in this work.

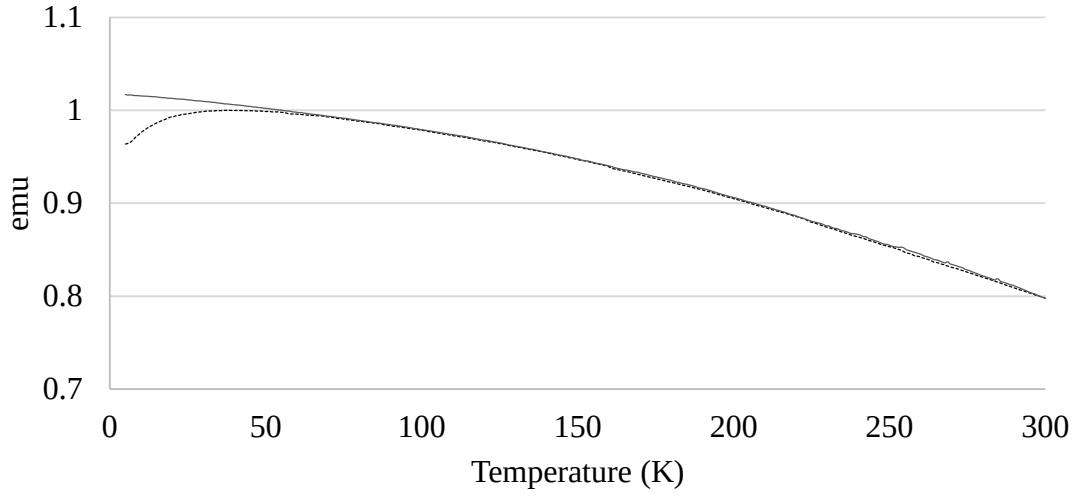

Figure 3-7 Magnetisation curve for the γ-Fe_2O_3 nanoparticles prepared in this work.

3.2.2 $Fe_{2-x}Gd_xO_3$ solid solution nanoparticle series $0 \leq x \leq 0.05$

The synthesis of the $Fe_{2-x}Gd_xO_3$ solid solution nanoparticle series $0 \leq x \leq 0.27$ was carried out by the same co-precipitation method used to prepare single phase maghemite nanoparticles and the same characterisation methods were used. In addition, ICP-AES was used to determine the formulae of the solid solutions in the series. Table 3-6 shows the theoretical molar % compared against the actual molar % achieved.

Table 3-6 The theoretical % compared against the actual molar % of Gd^{3+} $Fe_{2-x}Gd_xO_3$ solid solutions

Theoretical molar %	Actual molar % obtained by ICP-AES	Calculated Formula
0.66	0.48	$Fe_{1.99}Gd_{0.01}O_3$
2.00	2.0	$Fe_{1.96}Gd_{0.04}O_3$
2.67	2.62	$Fe_{1.95}Gd_{0.05}O_3$
3.33	2.62	$Fe_{1.95}Gd_{0.05}O_3$
6.67	6.04	$Fe_{1.88}Gd_{0.12}O_3$
16.67	13.65	$Fe_{1.73}Gd_{0.27}O_3$
23.33	9.59	$Fe_{1.81}Gd_{0.19}O_3$
33.33	No precipitate obtained.	N/A

The results show increasing amounts of Gd^{3+} cation substitution has been achieved in γ-Fe_2O_3 for increasing $GdCl_3$ in the reagents mixture, ranging from x=0.01 up to x=0.27 although a consistent doping pattern can not be observed. For the two samples with a molar percentage of 2.62 %, the calculated formula is $Fe_{1.95}Gd_{0.05}O_3$. One possible cause for both compounds to have the same formula may be loss of gadolinium during the reaction, potentially in the form of non-magnetic gadolinium hydroxide. However the

exact cause is unknown. Further characterisation of the two $Fe_{1.95}Gd_{0.05}O_3$ compounds has been carried out, detailed below. For clarity purposes these compounds have been named $Fe_{1.95}Gd_{0.05}O_3$ (2.67 %) and $Fe_{1.95}Gd_{0.05}O_3$ (3.33 %).

The first four samples shown in Table 3-6 have been characterised by various techniques. $Fe_{1.73}Gd_{0.27}O_3$ and $Fe_{1.81}Gd_{0.19}O_3$ were characterised by PXRD as they were prepared only to determine the upper solubility limit of Gd^{3+} in γ-Fe_2O_3 for the preparation of single phase $Fe_{2-x}Gd_xO_3$ solid solutions. Preparation of $FeGdO_3$ solid solution nanoparticles was attempted, however under these reaction conditions no precipitate formed.

Characterisation of $Fe_{2-x}Gd_xO_3$ solid solutions ($x \leq 0.05$) by PXRD is shown in Figure 3-8. The figure shows a comparison of each $Fe_{2-x}Gd_xO_3$ solid solution starting with γ-Fe_2O_3 and ascending with increasing Gd^{3+} content. The diffraction patterns for all the $Fe_{2-x}Gd_xO_3$ solid solutions show the same diffraction peaks as γ-Fe_2O_3, indicating the spinel structure has been maintained after cation substitution has taken place.

Figure 3-8 shows the PXRD patterns for $Fe_{2-x}Gd_xO_3$ solid solutions where x=0,0.12,0.19,0.27. Once again all the $Fe_{2-x}Gd_xO_3$ solid solutions prepared follow the spinel structure, although additional diffraction peaks start to emerge in the $Fe_{1.73}Gd_{0.27}O_3$ diffraction pattern, indicated by the arrows (Figure 3-9). Due to the small amount of this phase, it is not possible to identify it. The lattice parameters have been calculated from the PXRD patterns (Table 3-7) and show variations in the unit cell parameters with increasing Gd^{3+} content.

The particle size of the $Fe_{2-x}Gd_xO_3$ solid solutions has been estimated using the Scherrer equation (Equation 3-1). Compared against the γ-Fe_2O_3 nanoparticles that have a mean particle diameter of 13.16 nm, the particles in the $Fe_{2-x}Gd_xO_3$ solid solution series have smaller diameters. Between x=0.01 and x=0.04, the mean particle diameter is 9.37 nm,

and for x=0.05 the mean particle diameter is 10.93 nm. When x= 0.12 the mean particle diameter is 16.39 nm, and x=0.19 and x=0.27 the particle diameter increases further to 21.85 nm.

Figure 3-10 shows the XPS spectrum for $Fe_{1.96}Gd_{0.04}O_3$. The XPS binding energies are shown in Table 3-8. Peaks can be attributed to the presence of Fe^{3+} in γ-Fe_2O_3 and the presence of gadolinium in the sample is confirmed by the peaks at 1188 eV and 1223 eV.

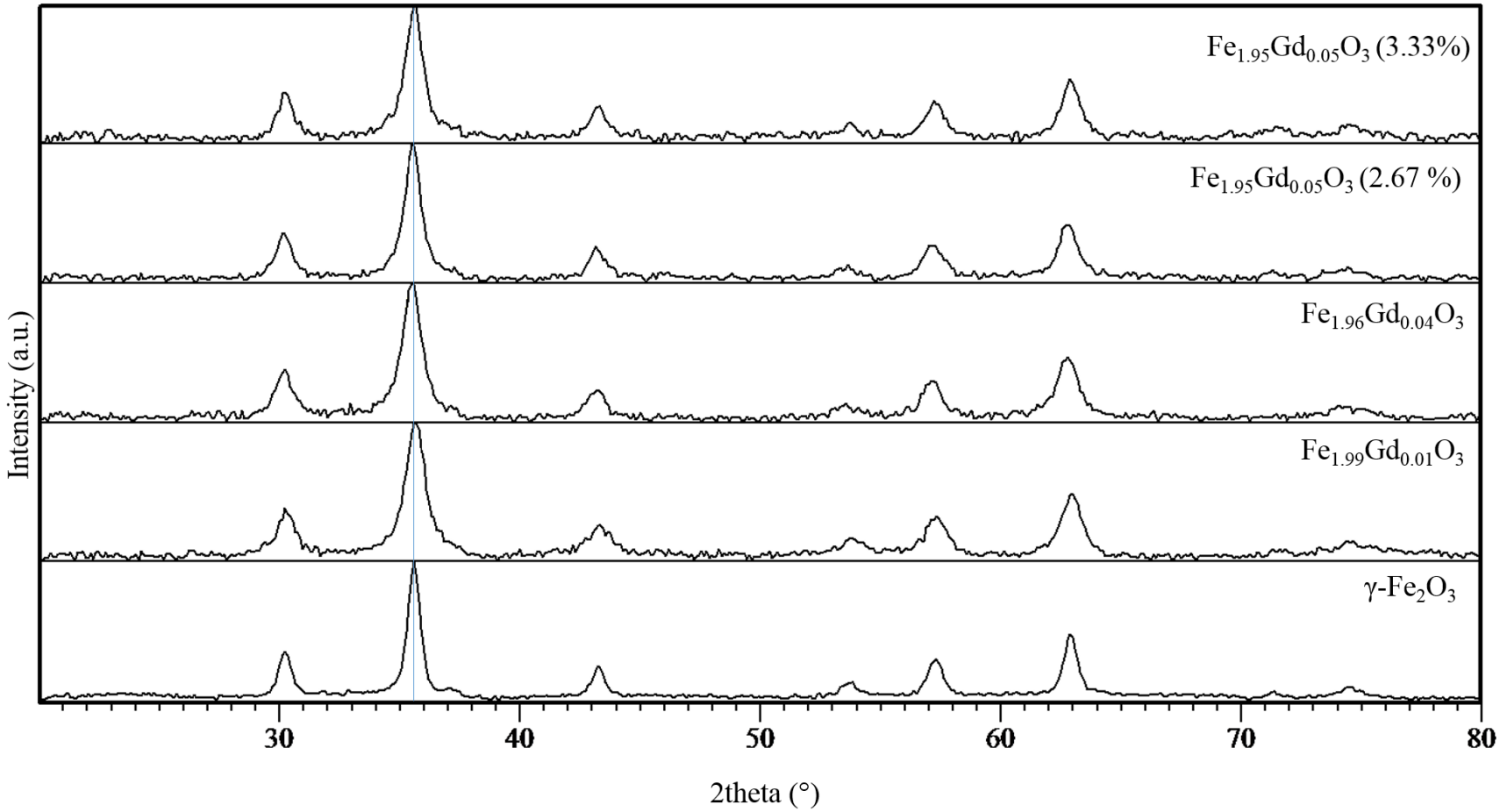

Figure 3-8 PXRD patterns for $Fe_{2-x}Gd_xO_3$ solid solution series $x \leq 0.05$.

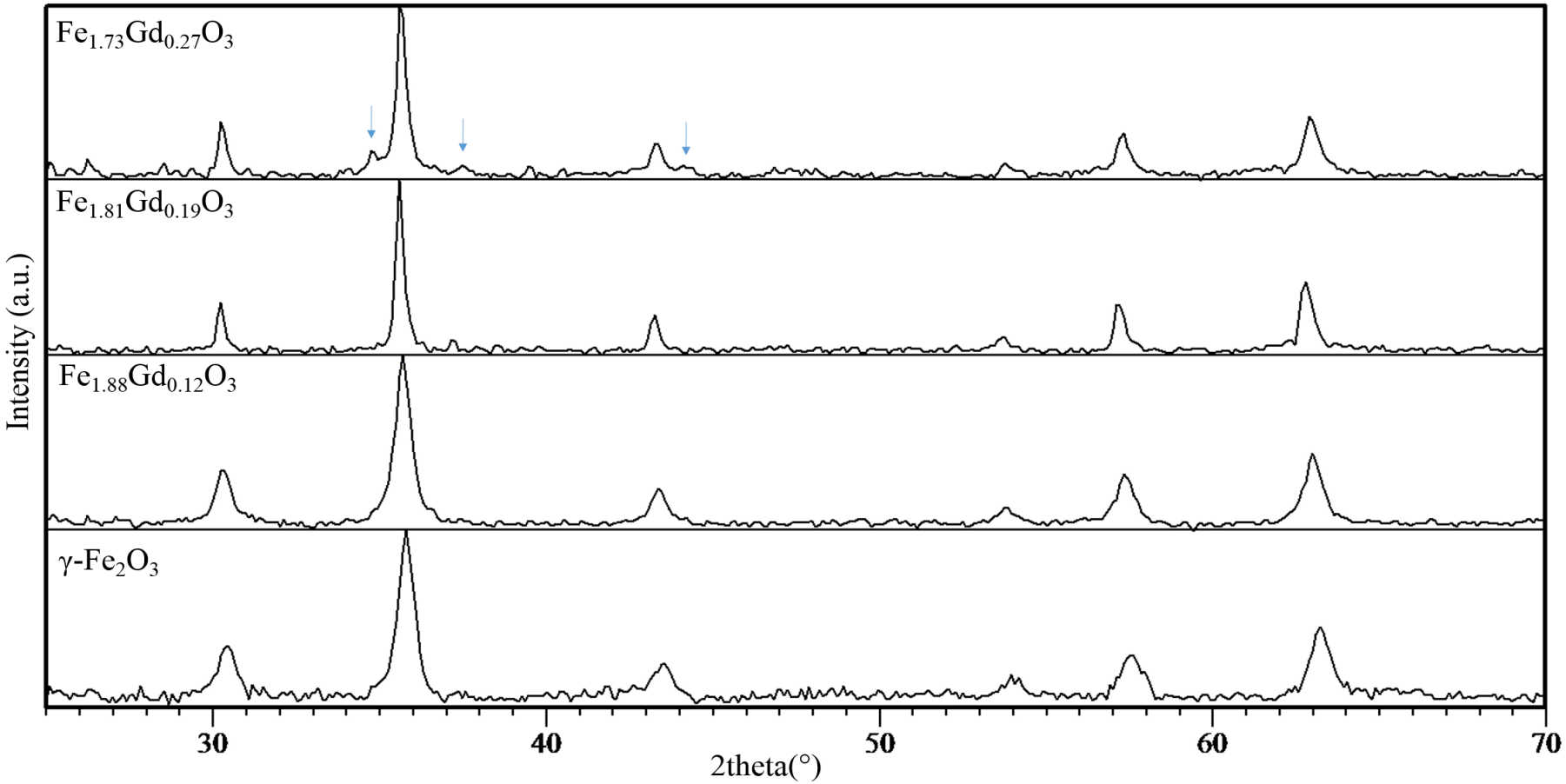

Figure 3-9 PXRD patterns for Fe2−xGdxO3 solid solution series for x=0,0.12,0.19,0.2. Impurities are indicated by the blue arrows.

Table 3-7 Lattice parameters for the $Fe_{2-x}Gd_xO_3$ nanoparticle series $0 \leq x \leq 0.05$, calculated using HighScore Plus software using the Jørgensen $Fd\bar{3}M$ model for γ-Fe_2O_3.[132]

$Fe_{2-x}Gd_xO_3$ nanoparticle series	**Lattice parameters (Å)**
γ-Fe_2O_3	8.320(7)
$Fe_{1.99}Gd_{0.01}O_3$	8.309(4)
$Fe_{1.96}Gd_{0.04}O_3$	8.334(3)
$Fe_{1.95}Gd_{0.05}O_3$ (2.67 %)	8.327(5)
$Fe_{1.95}Gd_{0.05}O_3$ (3.33 %)	8.329(3)

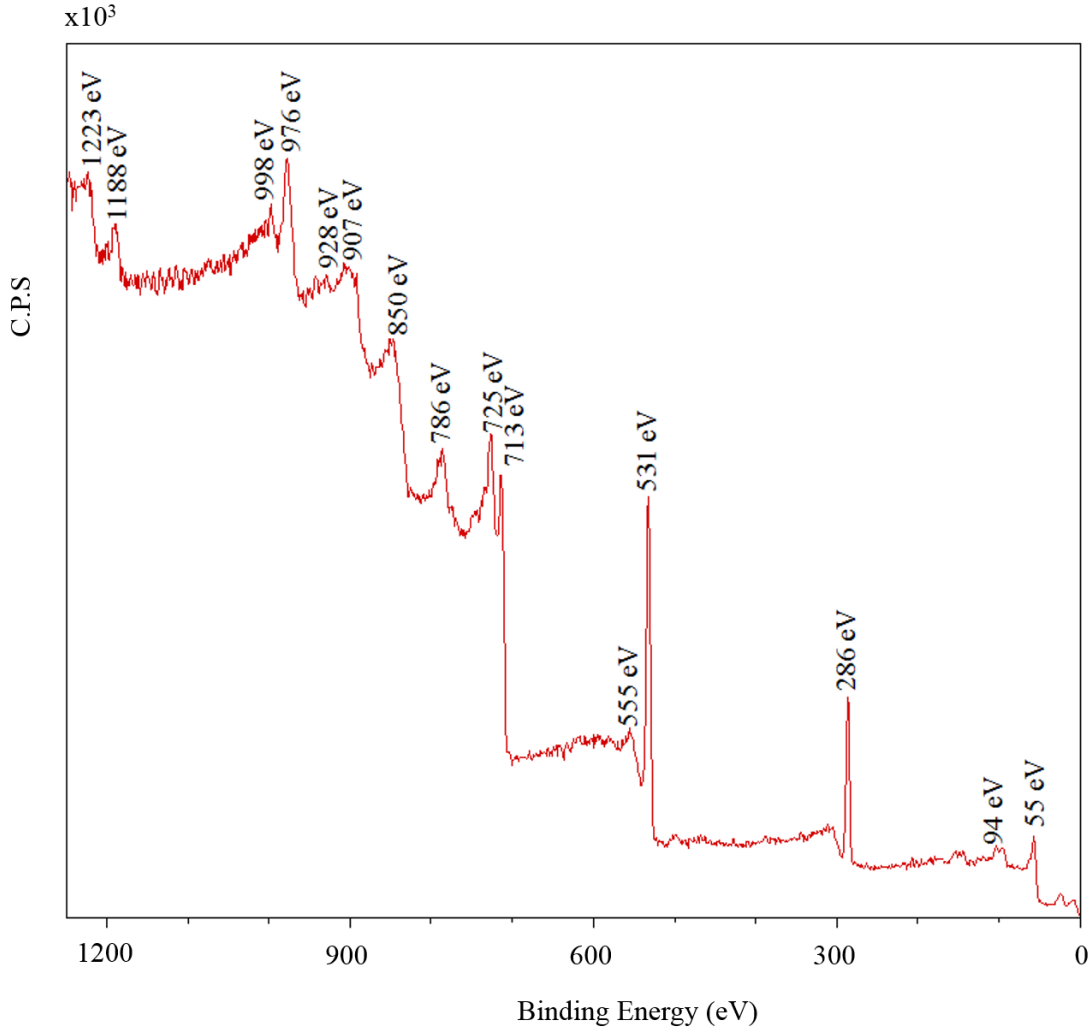

Figure 3-10 XPS survey for $Fe_{1.96}Gd_{0.04}O_3$ prepared in this work.

Table 3-8 Assignment of the XPS binding energies for $Fe_{1.96}Gd_{0.04}O_3$.

Binding Energy (eV)	**Element**
55	Fe $3P_{3/2}$
94	Fe *3s*
286	C
531	O *1s*
555	Fe $3P_{3/2}$
713	Fe $2p_{3/2}$
725	Fe $2p_{3/2}$
786	Fe auger
850	Fe auger
976	O auger
998	O auger
1188	Gd $3d^5$
1223	Gd $3d^3$

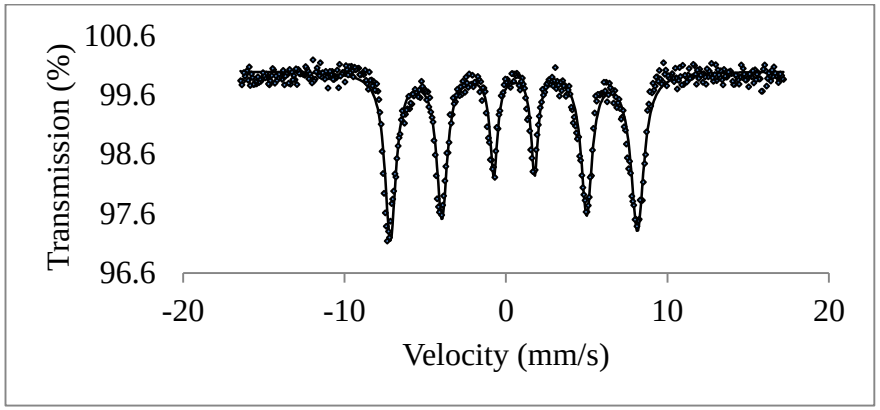

Figure 3-11 Mössbauer spectrum of $Fe_{1.99}Gd_{0.01}O_3$ collected at 80 K.

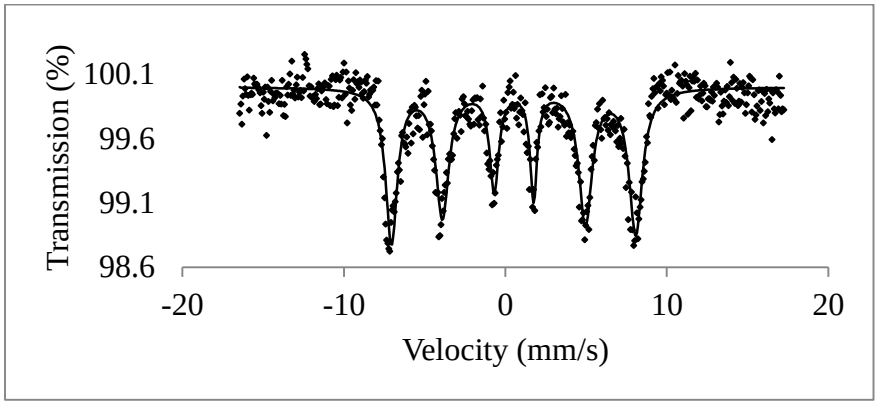

Figure 3-12 Mössbauer spectrum of $Fe_{1.96}Gd_{0.04}O_3$ collected at 80 K.

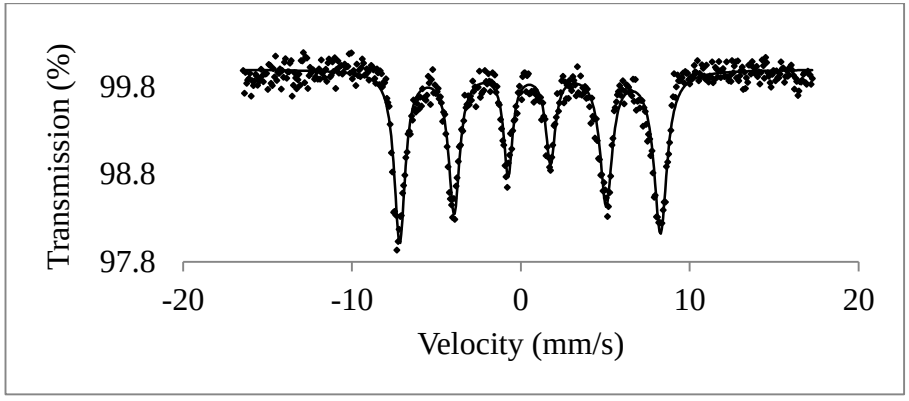

Figure 3-13 Mössbauer spectrum of $Fe_{1.95}Gd_{0.05}O_3$ (2.67 %) collected at 80 K.

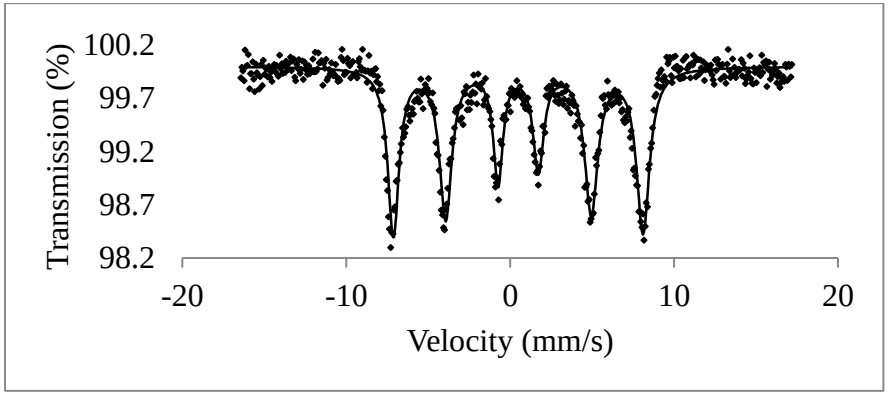

Figure 3-14 Mössbauer spectrum of $Fe_{1.95}Gd_{0.05}O_3$ (3.33 %) collected at 80 K.

At 80 K Mössbauer spectra (Figure 3-11 to Figure 3-14) for all the $Fe_{2-x}Gd_xO_3$ ($0.1 \leq x \leq 0.05$) series show a sextet of peaks indicating the magnetic ordering of Fe dominates at low temperatures. At 298 K the spectrum for $Fe_{1.99}Gd_{0.01}O_3$ (Figure 3-15 to Figure 3-18) also shows a sextet of peaks. However, for $Fe_{2-x}Gd_xO_3$ with $x \geq 0.04$ each spectrum shows 5 peaks with the central peak being most dominant. When compared to the spectrum for $Fe_{1.99}Gd_{0.04}O_3$ there is a decrease in the percentage transmission in $Fe_{2-x}Gd_xO_3$ with $x \geq 0.04$. It is likely that the sextet of peaks due to $Fe^{3+}$is hidden by the broad central peak due to the increasing Gd^{3+} content.

For all the $Fe_{2-x}Gd_xO_3$ solid solutions, magnetic data were collected. The M-H curves (Figure 3-19 to Figure 3-22) all exhibit similar behaviour; two overlapping curves are observed as the magnetic field strength is varied. In all cases, at 0 gauss there is no remanance or coercivity, indicating superparamagnetic behaviour.

The ZFC-FC magnetisation curves (Figure 3-23 to Figure 3-26) for the $Fe_{2-x}Gd_xO_3$ series all follow the same trend. For the ZFC curve, the magnetisation rapidly increases as temperature increases, followed by a gradual decline in magnetisation between the blocking temperature and 300 K. The FC magnetisation curves show a gradual increase in magnetisation as the temperature decreases. The blocking temperature for each solid solution has been determined and is shown in Table 3-9

The magnetic susceptibility data is shown in Table 3-10. The magnetic susceptibility increases when Gd^{3+} is added in small amounts to γ-Fe_2O_3, as shown by the change in susceptibility from 57.6 emu/g to 61.9 emu/g. However, increasing the Gd^{3+} content further to $Fe_{1.96}Gd_{0.04}O_3$ causes the susceptibility to decrease. Increasing the Gd^{3+} content further, as for $Fe_{1.95}Gd_{0.05}O_3$ (2.67 %) and $Fe_{1.95}Gd_{0.05}O_3$ (3.33 %) shows a decrease in susceptibility and an increase in susceptibility respectively. Considering the irregular

behaviour of the magnetic susceptibility and blocking temperatures across the series, it is difficult to discuss the influence of gadolinium on the magnetic properties of γ-Fe_2O_3.

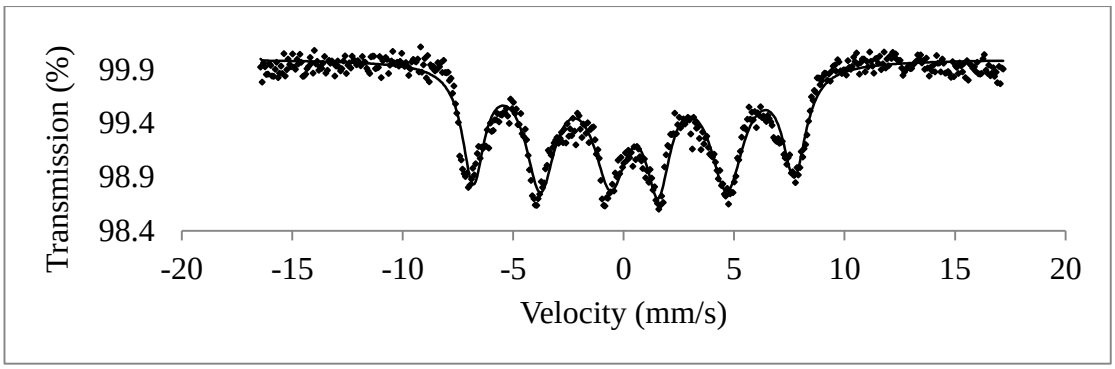

Figure 3-15 Mössbauer spectrum of $Fe_{1.99}Gd_{0.01}O_3$ collected at 298 K.

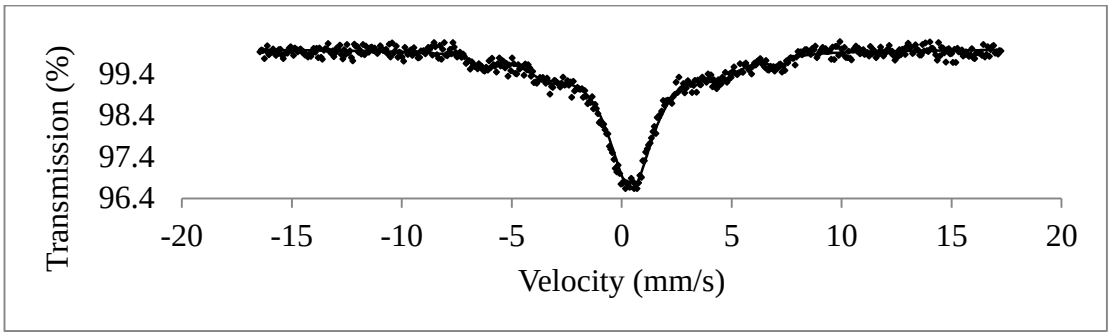

Figure 3-16 Mössbauer spectrum of $Fe_{1.96}Gd_{0.04}O_3$ collected at 298 K.

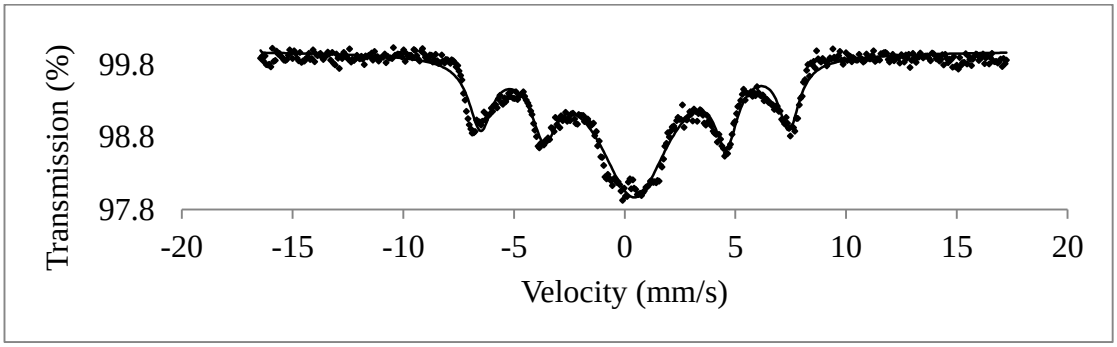

Figure 3-17 Mössbauer spectrum of $Fe_{1.95}Gd_{0.05}O_3$ (2.67%) collected at 298 K

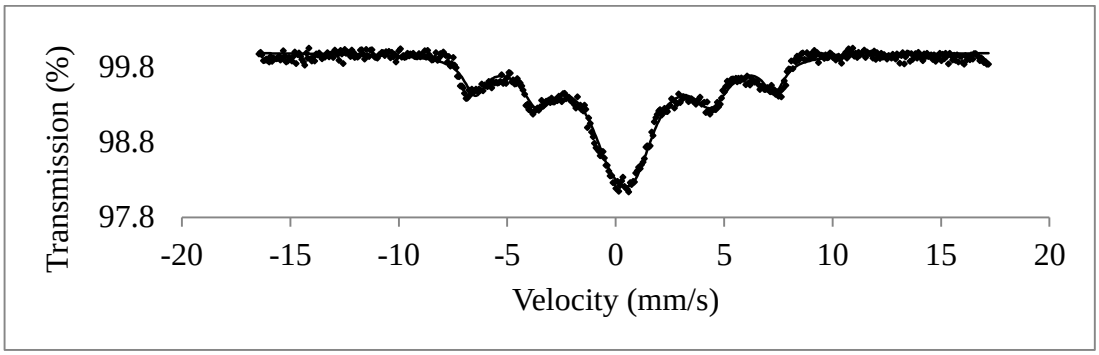

Figure 3-18 Mössbauer spectrum of $Fe_{1.95}Gd_{0.05}O_3$ (3.33 %) collected at 298 K

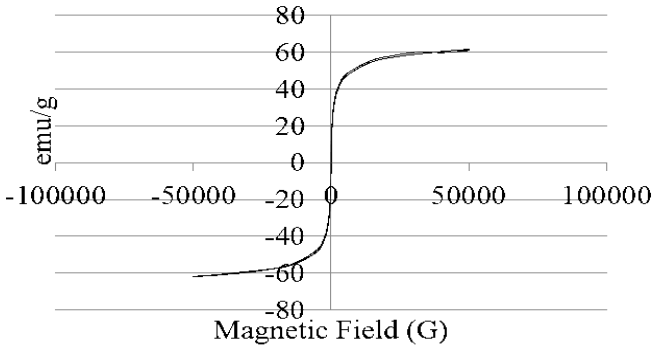

Figure 3-19 Magnetic hysteresis loop for $Fe_{1.99}Gd_{0.01}O_3$.

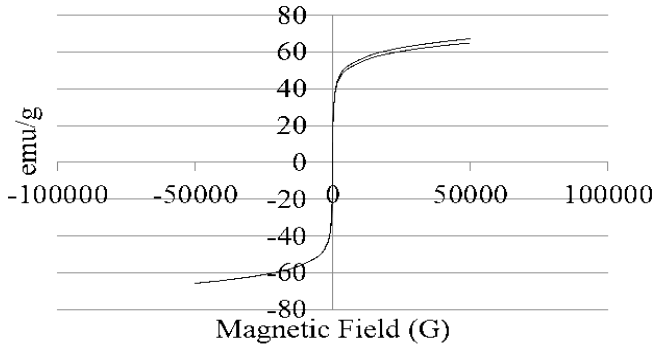

Figure 3-20 Magnetic hysteresis loop for $Fe_{1.96}Gd_{0.04}O_3$.

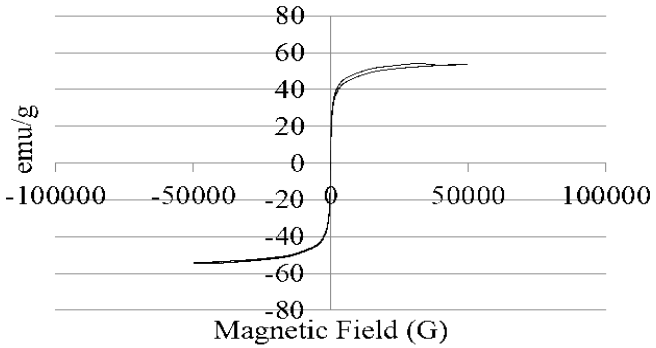

Figure 3-21 Magnetic hysteresis loop for $Fe_{1.95}Gd_{0.05}O_3$ (2.67%).

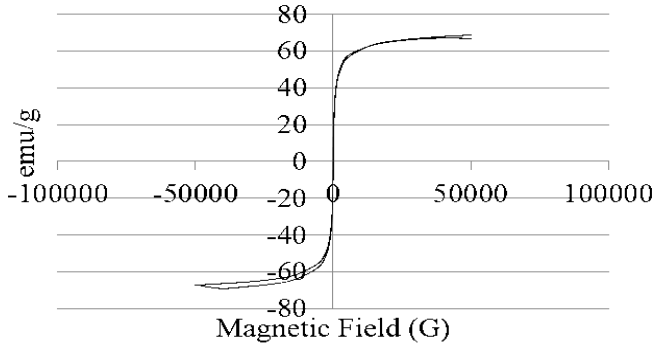

Figure 3-22 Magnetic hysteresis loop for $Fe_{1.95}Gd_{0.05}O_3$ (3.3%).

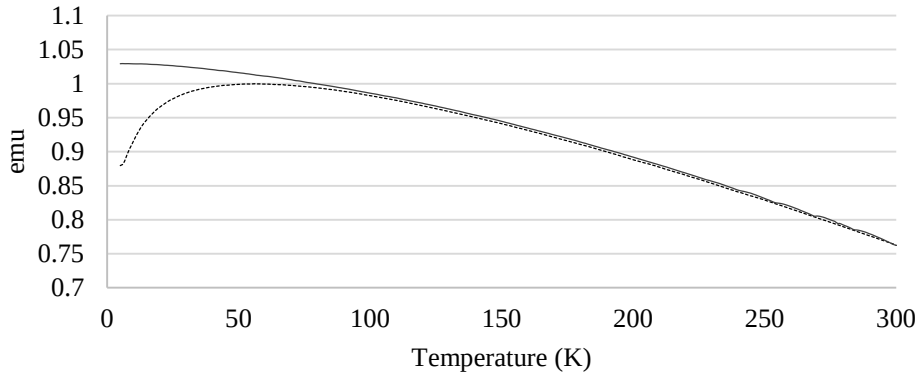

Figure 3-23 ZFC-FC curves for $Fe_{1.99}Gd_{0.01}O_3$.

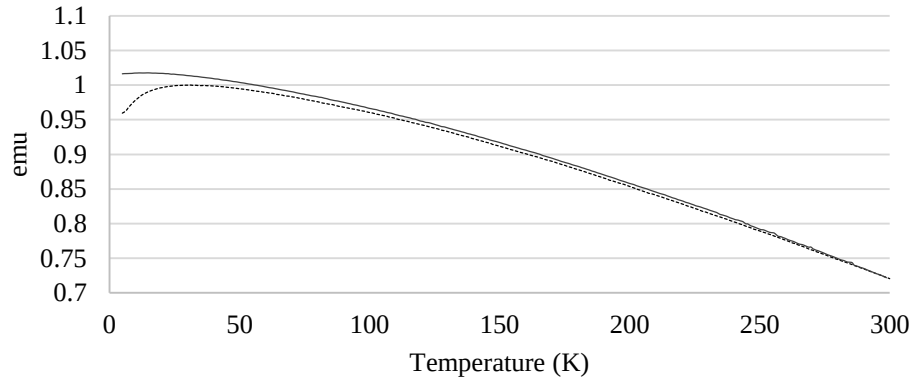

Figure 3-24 ZFC-FC curves for $Fe_{1.96}Gd_{0.04}O_3$.

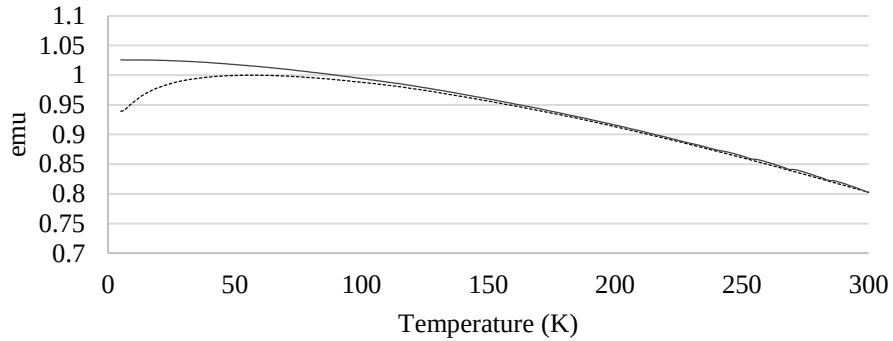

Figure 3-25 ZFC-FC curves for $Fe_{1.95}Gd_{0.05}O_3$ (2.67%)

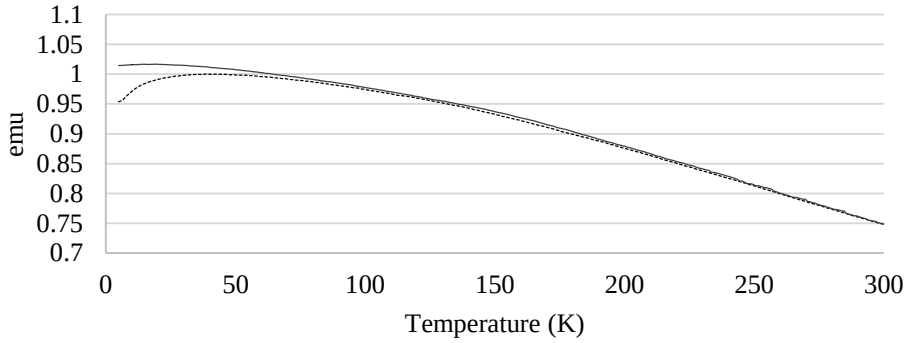

Figure 3-26 ZFC-FC curves for $Fe_{1.95}Gd_{0.05}O_3$ (3.3%)

Table 3-9 Blocking temperature for $Fe_{2-x}Gd_xO_3$ series.

Compound	Blocking Temperature (K)
γ-Fe_2O_3	38.28
$Fe_{1.99}Gd_{0.01}O_3$	56.17
$Fe_{1.96}Gd_{0.04}O_3$	31.30
$Fe_{1.95}Gd_{0.05}O_3$ (2.67%)	55.16
$Fe_{1.95}Gd_{0.05}O_3$ (3.3%)	38.33

Table 3-10 Magnetisation susceptibility values for the $Fe_{2-x}Gd_xO_3$ series.

Compound	300K (emu/g)	5K (emu/g)
Fe_2O_3	57.64677	70.38226
$Fe_{1.99}Gd_{0.01}O_3$	61.92842	74.63158
$Fe_{1.96}Gd_{0.04}O_3$	52.19533	64.87757
$Fe_{1.95}Gd_{0.05}O_3$ (2.67%)	43.90687	56.50076
$Fe_{1.95}Gd_{0.05}O_3$ (3.33%)	68.68155	89.99418

3.2.3 $Fe_{2-x}Dy_xO_3$ solid solution nanoparticle series $0 \leq x \leq 1$

The synthesis of the $Fe_{2-x}Dy_xO_3$ solid solution nanoparticle series with $0 \leq x \leq 0.06$ was carried out by the same co-precipitation method used to prepare single phase maghemite nanoparticles and the same characterisation methods were used. In addition, ICP-AES was used to determine the formulae of the different nanoparticle solid solutions in the series. Table 3-11 shows the theoretical molar % compared against the actual molar % achieved.

Table 3-11 Theoretical molar % and actual molar % obtained by ICP-AES for $Fe_{2-x}Dy_xO_3$ solid solutions.

Theoretical molar %	Actual % obtained by ICP-AES	Calculated Formula
0.66	0.56	$Fe_{1.99}Dy_{0.01}O_3$
3.33	2.94	$Fe_{1.94}Dy_{0.06}O_3$
6.6	6.06	$Fe_{1.88}Dy_{0.12}O_3$
16.66	12.39	$Fe_{1.75}Dy_{0.25}O_3$
33.33	43.81	$Fe_{1.12}Dy_{0.88}O_3$

Solid solutions with the formule $Fe_{1.99}Dy_{0.01}O_3$ and $Fe_{1.94}Dy_{0.06}O_3$ have been prepared as single phase, whereas PXRD indicated that above x= 0.06, the materials were not single phase. The PXRD patterns for $Fe_{1.99}Dy_{0.01}O_3$ and $Fe_{1.94}Dy_{0.06}O_3$ are shown in Figure 3-28. The diffraction patterns for all the $Fe_{2-x}Dy_xO_3$ solid solutions show very broad peaks and, for up to x = 0.06, the PXRD patterns indicate the spinel structure has been maintained after cation substitution has taken place. A small shift to lower 2 theta angles as the Dy^{3+} content increases is visible from the comparison of the PXRD patterns. This indicates a slight enlargement of the unit cell, though calculation of the lattice parameters was made unreliable by the broadness of the peaks.

The particle size of the $Fe_{2-x}Dy_xO_3$ solid solutions has been estimated using the Scherrer equation and is shown in

Table 3-12. Compared against the γ-Fe_2O_3 nanoparticles that have a mean particle diameter of 13.16 nm, the particles in the $Fe_{2-x}Dy_xO_3$ solid solution series have much smaller diameters at 4.64 nm and 2.32 nm for x = 0.01 and x = 0.06 respectively. TEM

images (Figure 3-27) show the particles to be spherical, however agglomeration makes it difficult to use the images to obtain particle size.

Table 3-12 Particle diameter estimated using the Scherrer equation for $Fe_{2-x}Dy_xO_3$ nanoparticles series.

Compound	**Particle diameter (nm) as determined by the Scherrer equation**
γ-Fe_2O_3	13.16
$Fe_{1.99}Dy_{0.01}O_3$	4.64
$Fe_{1.94}Dy_{0.06}O_3$	2.32

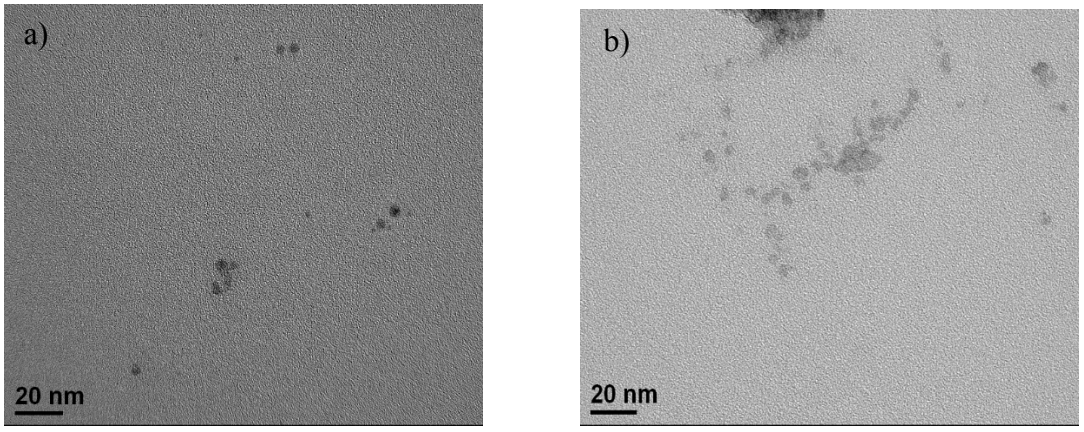

Figure 3-27 TEM images for a) $Fe_{1.99}Dy_{0.01}O_3$; b) $Fe_{1.94}Dy_{0.06}O_3$

At 80 K the Mössbauer spectrum for $Fe_{1.99}Dy_{0.0.1}O_3$ (Figure 3-29) shows 5 peaks and the spectrum for $Fe_{1.94}Dy_{0.06}O_3$ (Figure 3-30) shows one central peak of similar percentage transmission. It is likely that the spectrum for $Fe_{1.99}Dy_{0.0.1}O_3$, the sextet of peaks expected for Fe^{3+} is hidden by the broad central peak due to the increasing Dy^{3+} content.

The singlet peak for $Fe_{1.94}Dy_{0.0.6}O_3$ shows superparamagnetic behaviour is dominant at 80 K and may be related to the small particle size. At 298 K both spectra (Figure 3-31 and Figure 3-32) show a doublet indicating superparamagnetic behaviour at that temperature.

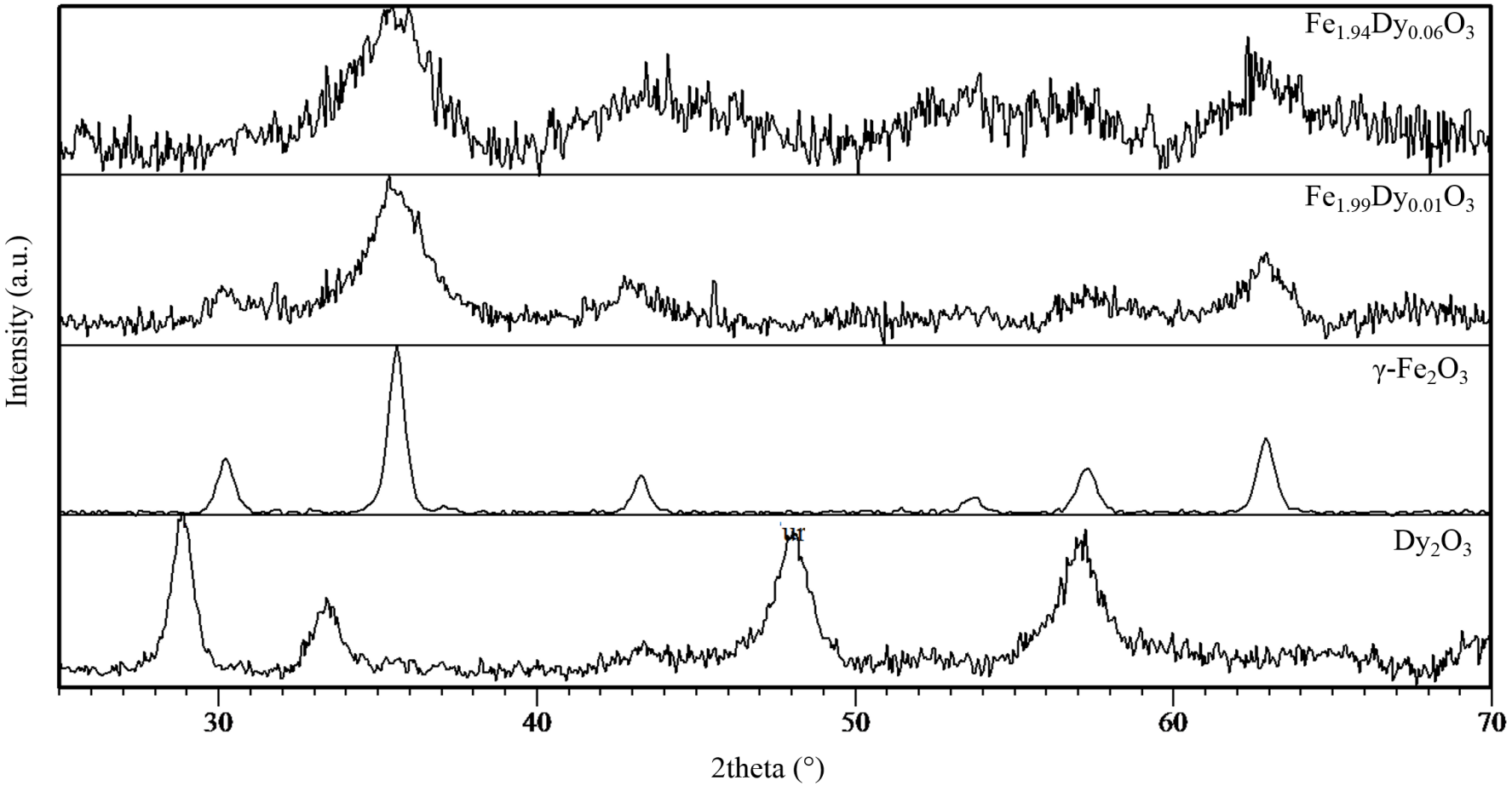

Figure 3-28 PXRD patterns for $Fe_{1.99}Dy_{0.01}O_3$ and $Fe_{1.94}Dy_{0.06}O_3$ solid solution nanoparticles compared against the PXRD patterns for γ-Fe_2O_3 and Dy_2O_3.

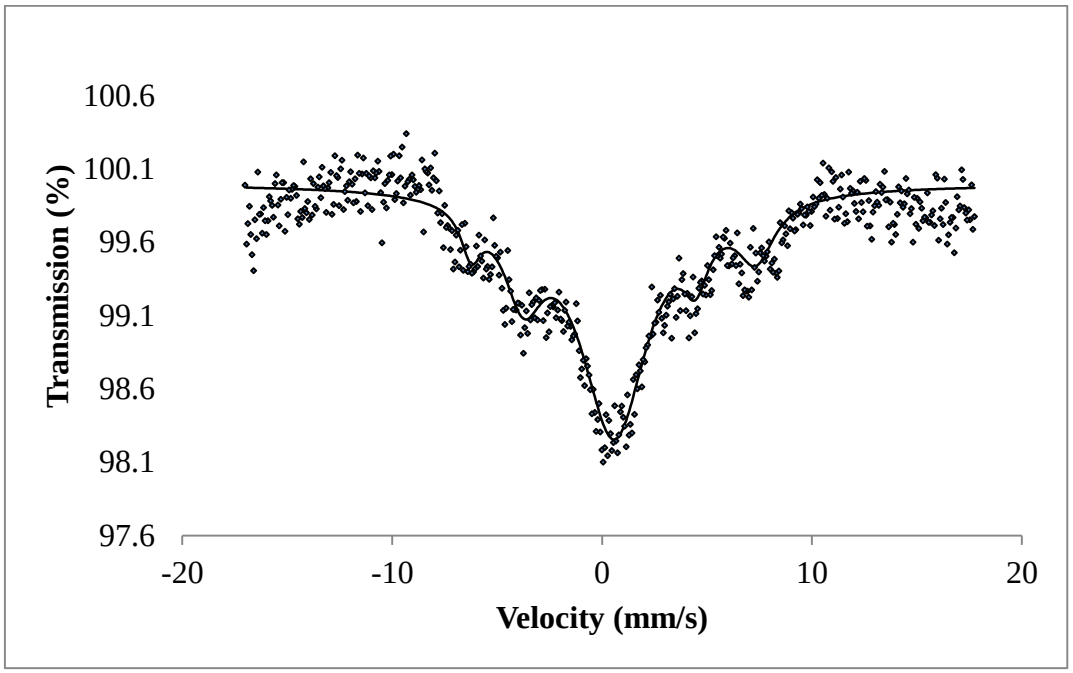

Figure 3-29 Mössbauer spectrum for $Fe_{1.99}Dy_{0.01}O_3$ collected at 80 K.

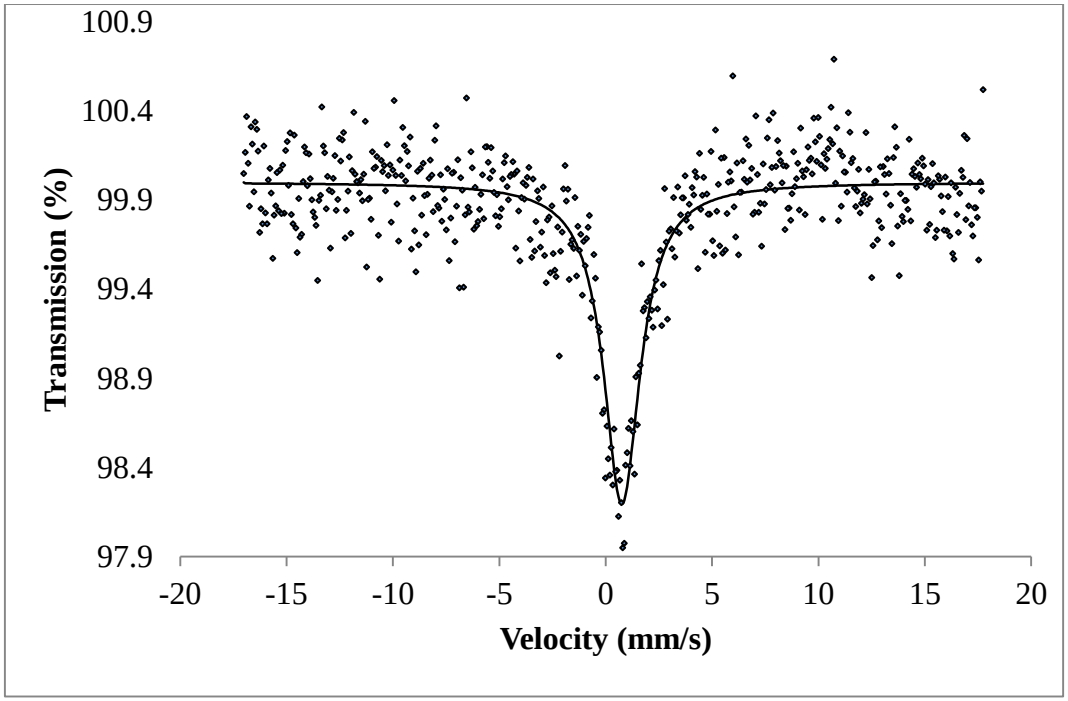

Figure 3-30 Mössbauer spectrum for $Fe_{1.94}Dy_{0.06}O_3$ collected at 80 K.

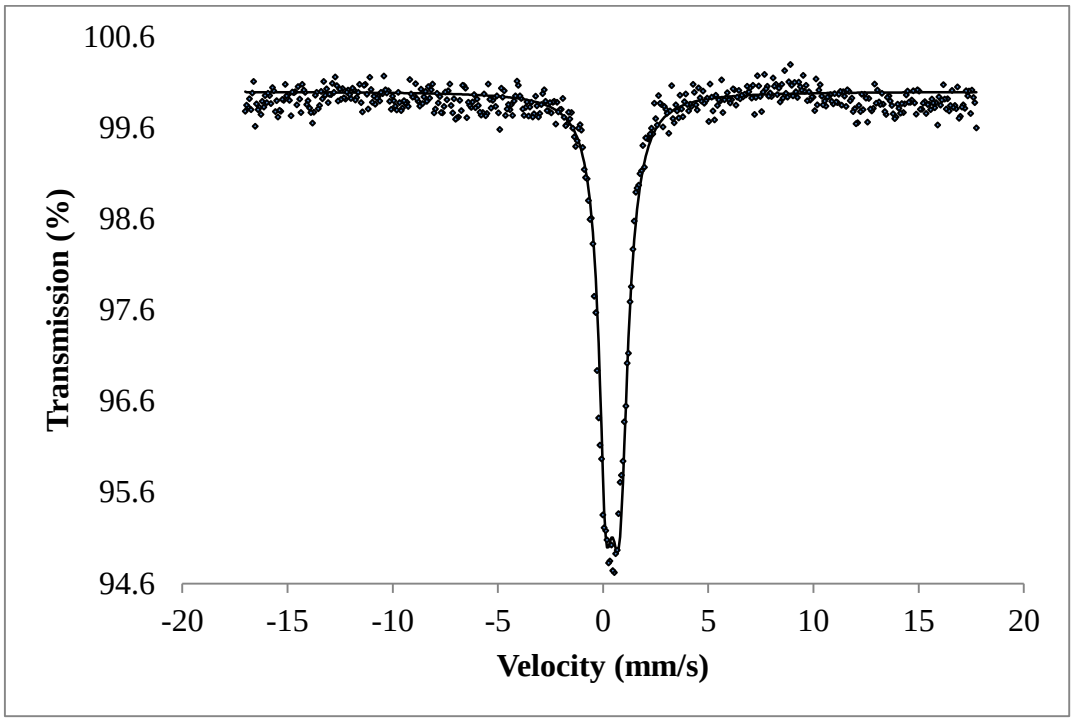

Figure 3-31 Mössbauer spectrum for $Fe_{1.99}Dy_{0.01}O_3$ collected at 298 K.

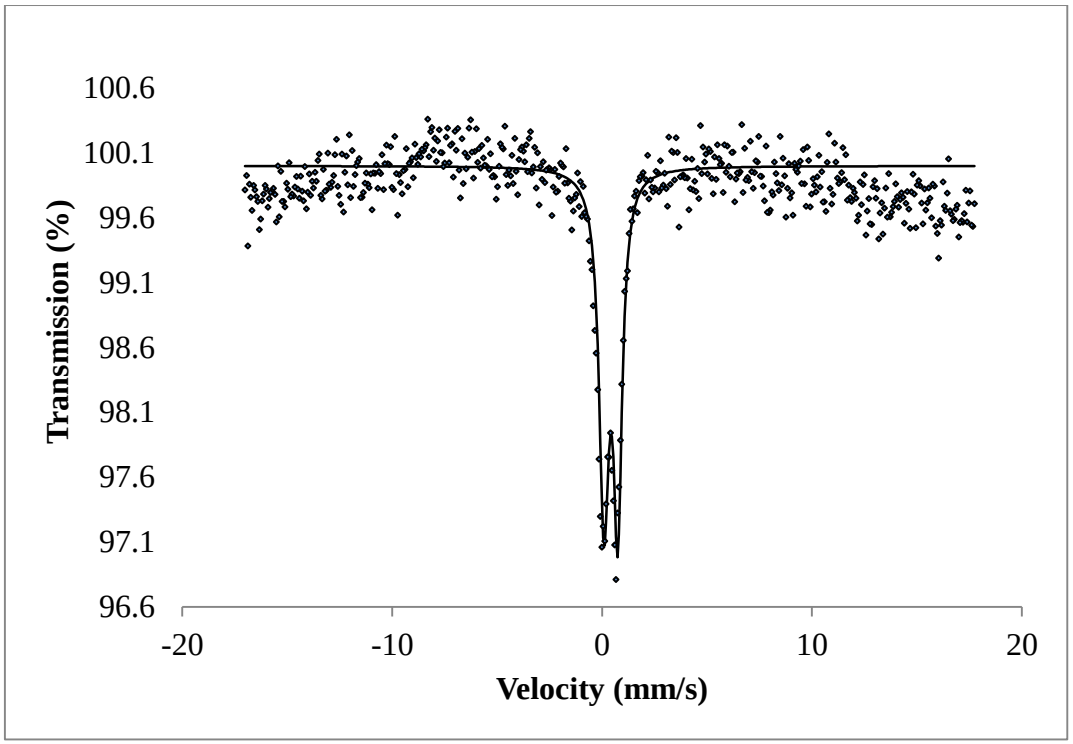

Figure 3-32 Mössbauer spectrum for $Fe_{1.94}Dy_{0.06}O_3$ collected at 298 K.

3.3 DISCUSSION

The synthesis of γ-Fe_2O_3 nanoparticles was carried out by a co-precipitation reaction method similar to the method originally reported by Massart *et al.* in 1981.[37] In accordance with the reported method, a 2:1 ratio of Fe^{3+}:Fe^{2+} iron salts was used and mixed with a base to precipitate nanoparticles. The Fe^{2+}/Fe^{3+} mixture is necessary as the synthetic route requires Fe_3O_4 as an intermediate, which then undergoes oxidation to produce γ-Fe_2O_3. The following step includes addition of H_2O_2, which ensures that the oxidation of $Fe^{2+}$to Fe^{3+} proceeds to completion.

γ-Fe_2O_3 and Fe_3O_4 both show the inverse spinel structure with γ-Fe_2O_3 differing from Fe_3O_4 because it only contains iron in its +3 oxidation state and it contains iron vacancies. γ-Fe_2O_3 has a face centred cubic unit cell with 32 octahedral sites and 64 tetrahedral sites, of which 16 octahedral sites and 8 tetrahedral sites are occupied by cations.[9] Typically in the inverse spinel structure, Fe^{3+} ions occupy half the 16 available octahedral sites and all of the 8 available tetrahedral sites, leaving half of the octahedral sites vacant. Due to these vacancies γ-Fe_2O_3 does not possess a magnetic moment in the absence of a magnetic field as both octahedral and tetrahedral sites are equivalent and align antiparallel. In Fe_3O_4, Fe^{2+} ions occupy these vacant octahedral sites and cause a permanent magnetic moment. Due to the different properties of the various types of iron oxide nanoparticles it is important to establish first whether γ-Fe_2O_3, Fe_3O_4 or a mixture is present in the samples.

PXRD diffraction patterns show broad peaks that can be attributed to the small crystallite size. Due to this peak broadening, the diffraction peaks match both magnetite and maghemite standard diffraction patterns. This is caused by magnetite and maghemite both having cubic unit cells with a = 8.39 Å and 8.34 Å respectively.[9] The PXRD data collected

in this work was analysed by a peak deconvolution method, originally reported by Kim *et al.*[38] to determine the percentage composition of Fe_3O_4 and γ-Fe_2O_3 in the product. A series of known mixtures were prepared using magnetite and maghemite nanoparticles purchased from Sigma Aldrich and the PXRD data for each mixture collected (Appendix 1). The two calibration graphs of integrated peak intensity against percentage Fe_3O_4 and percentage γ-Fe_2O_3 in the original mixture were plotted. The diffraction peak used in each case was the 440 reflection.[38] From the calibration graphs (Appendix 1) it was then possible to determine the percentage composition in iron oxide samples prepared in this work. PXRD data for the nanoparticles prepared by the method presented in section 3.1 were analysed and it was determined that the sample composition was 98.5 % γ-Fe_2O_3.

From the diffraction pattern it can be determined that the nanoparticles prepared match the diffraction peaks associated with the $Fd\bar{3}m$ space group. This indicates that the unit cell is a face centred cubic lattice, and investigation by Jorgensen *et al.* has shown that the cations are distributed randomly across their respective sites.[32] Cation ordering is only achieved by tripling the unit cell along the *c* axis, which would result in either of the enatiomeric space groups $P4_12_12$ or $P4_32_12$. Both of these space groups have super-lattice peaks at low 2θ angles. The absence of these in the experimental data shows that the cubic $Fd\bar{3}m$ is the correct space group for the prepared nanoparticles. The PXRD data were then used to determine the unit cell size for these γ-Fe_2O_3 nanoparticles as a = 8.320(7) Å, in agreement with data reported by Jorgensen *et al.*[32]

Further corroboration of the elemental composition and oxidation state of the iron ions in the prepared nanoparticles was obtained by X-ray Photoelectron Spectroscopy (XPS). This technique is typically used to determine the elemental composition of the surface of materials, however, in the case of nanoparticles the beam penetrates through the entire

particle, yielding a reasonably accurate analysis. The technique is very sensitive to changes in oxidation state, reflected by shifts in binding energy for the same ions. When XPS was applied to the prepared iron oxide nanoparticles, peaks were observed at 55.5384 eV, 93.8677 eV, 530.5324 eV, 711.8299 eV, and 723.5634 eV and can all be attributed to the presence of γ-Fe_2O_3.

Mössbauer spectroscopy uses hyperfine interactions to determine the electronic and magnetic environment of the different ions within a compound, and can be used to indicate whether magnetite or maghemite has been synthesized.

Due to the magnetic splitting of Fe ions when exposed to a ^{57}Co source, a Mössbauer spectrum shows a sextet of peaks. Yang *et al.* studied 150-200 nm diameter nanoparticles of Fe_3O_4, γ-Fe_2O_3 and $Fe_{3-\delta}O_4$ nanoparticles with intermediate amounts of vacancies, *via* Mössbauer spectroscopy at room temperature.[134] The spectra show the splitting of peaks for $Fe_{3-\delta}O_4$ nanoparticles relating to differently charged ions being distributed across the octahedral and tetrahedral sites. In this case, Fe^{3+} ions occupy the tetrahedral sites and the remaining Fe^{2+} and Fe^{3+} ions occupy octahedral sites. If all sites contained the same ion, no difference in charge would exist and no splitting would occur. In γ-Fe_2O_3 no peak splitting is observed as there is only Fe^{3+} in both the octahedral and tetrahedral sites.[118, 135]

As discussed by Salazar *et al.*, when nanoparticles are less than approximately 20 nm diameter, this hyperfine splitting can be difficult to observe due to peak broadening effects.[136]

The experimental data for γ-Fe_2O_3 nanoparticles at 298 K is still a sextet, although the peaks are broader than at 80 K. The presence of the sextet between −10 mm/s and 10 mm/s can be explained by the magnetic behaviour of the nanoparticles at different

temperatures. Typically at room temperature, there is enough thermal energy to overcome any coupling interactions between neighbouring ions, hence each ion within a nanoparticle behaves as a paramagnet. This should result in a Mössbauer spectrum with a doublet peak close to zero, corresponding to the superparamagnetic behaviour. However, in this case a sextet is observed instead of a doublet. One possible explanation is that the experimental observation time for Mössbauer spectroscopy is approximately 10 ns, which may be shorter than the relaxation time of the magnetic nanoparticles. This means that Mössbauer spectroscopy will show the nanoparticles as ferrimagnetic instead of superparamagnetic hence a sextet is observed and instead a doublet.[137]

One way to overcome this problem is to analyse the nanoparticles *via* SQUID which has longer experimental observation times, allowing the magnetic moment of the superparamagnetic nanoparticle to undergo relaxation during the measurement, and superparamagnetism can be observed.[137]

Two sets of magnetic data were collected *via* SQUID in the form of a magnetisation curve and an M-H plot for the prepared γ-Fe_2O_3 nanoparticles (Figure 3-6 and Figure 3-7). The magnetisation curve shows how the magnetic moment of the nanoparticles varies with temperature in the presence and absence of a magnetic field. The zero field cooled (ZFC) curve is obtained by cooling the nanoparticles in the absence of a magnetic field and recording changes in the magnetisation. In this case, it is observed that as the temperature decreases the magnetisation increases until the blocking temperature is reached at 38.28 K. After this point the magnetisation decreases rapidly. The blocking temperature is the temperature at which the nanoparticles have the highest magnetisation in ZFC conditions. Above the blocking temperature there is enough thermal energy to overcome the coupling forces between magnetic domains leading to superparamagnetic behaviour. This results

in the magnetisation of the particles steadily decreasing as the temperature increases (Figure 3-7). For the field cooled (FC) curve the particles magnetisation at high temperature fluctuates due to thermal energy. As the temperature decreases, these fluctuations reduce and more particles align with the magnetic field causing the magnetisation to rise steadily.[138]

The M-H curve shows the hysteresis of the prepared γ-Fe_2O_3 nanoparticles (Figure 3-6). The data shows two almost identical curves that have no magnetic remanence in the absence of a magnetic field, shown by 0 emu/g magnetisation at 0 Oe magnetic field confirming the superparamagnetic behaviour of the nanoparticles. It also shows that the magnetic saturation of these particles is 57.64 emu/g, indicated by the levelling of the hysteresis line at high magnetic field strengths.

The data collected for the prepared iron oxide nanoparticles conclusively shows that single phase γ-Fe_2O_3 nanoparticles have been achieved under these synthetic conditions. The size of the nanoparticles has been estimated by the Scherrer equation to be 13.1 nm which is in agreement with data reported in the literature for nanoparticles produced by the same method. Magnetic and relaxivity measurements were also collected, and can be used as a base line for comparison with the cation substituted $Fe_{2-x}M_xO_3$ solid solutions (M= Gd, Dy).

The TEM images collected for the prepared nanoparticles show the particles are very agglomerated (Figure 3-3). The method of synthesis has a large impact on the monodispersity of the nanoparticles produced. Methods that involve hydrophobic surfactants typically produced very monodisperse samples. The aqueous route used here led to samples with reduced monodispersity, due to hydrophilic characteristics. One other reason for the agglomeration could be that the citric acid used to functionalise the

nanoparticles may not coat each particle separately but form clumps of particles within one layer of coating, increasing the agglomeration between the magnetic particles.

3.3.1 $Fe_{2-x}Gd_xO_3$ solid solution nanoparticle series $0 \leq x \leq 1$

Iron oxide nanoparticles synthesised by the co-precipitation method are typically prepared in aqueous solution. In order to synthesise $Fe_{2-x}Gd_xO_3$ solid solutions, $GdCl_3$ was used as a starting reagent, however this readily forms $Gd(OH)_3$ in aqueous solutions and so an alternative solvent was sought. Ethylene glycol was chosen as it has a similar polarity to water so that the impact on the hydrophilicity of the nanoparticles could be minimised, and it has a high boiling point allowing reactions to be carried out at higher temperatures than in water. When considering the reaction process the amount of energy required to make and break bonds during Gd^{3+}/Fe^{3+} substitution would be larger than the energy required for the formation of γ-Fe_2O_3 due to the greater size of Gd^{3+} ions (r= 0.938 Å, octahedral coordination)[139] compared to that of Fe^{3+} ions (r= 0.645 Å, octahedral coordination).[139] Therefore a higher boiling point solvent meant that more energy could be provided to the reaction system.

In order to determine whether Gd^{3+}/Fe^{3+} substitution occurred or whether the Gd^{3+} ions where retained in the prepared samples or were washed away during the reaction, ICP-AES analysis was carried out. The data confirmed the presence of gadolinium in all the $Fe_{2-x}Gd_xO_3$ solid solution nanoparticles and indicates a maximum x value of 0.27, which is higher than any reported in literature to the best of the author's knowledge.

The ICP-AES data shows when 0.66 molar % Gd^{3+} ions were added to the reaction at the start, only 0.48 molar % Gd^{3+} ions actually remained in the sample after the reaction was completed. Yet, when 2.0 molar % Gd^{3+} ions were added to the starting reagents, 2.0 molar % Gd^{3+} ions remained in the sample. The difference between the theoretical molar

% and actual molar % obtained is not consistent across the series. This may be due to water being produced by the reaction, causing the formation of $Gd(OH)_3$ which would not have been collected magnetically at the end and therefore would have been lost.

Substitution of Fe^{3+} by Gd^{3+} ions will maintain the charge neutrality of the compounds but the size difference between Fe^{3+} and Gd^{3+} ions would cause a change in the unit cell size, indicated by a shift in the PXRD diffraction peaks (Gd^{3+} r = 0.938 Å, octahedral co-ordination; Fe^{3+} r = 0.654 Å, octahedral co-ordination).[139] This shift increases as the extent of doping increases.

The PXRD data for the $Fe_{2-x}Gd_xO_3$ solid solution nanoparticles shows that, even at x=0.19, the spinel structure is maintained. However, at x = 0.27 extra diffraction peaks that do not belong to the spinel structure start to appear. These peaks could not be identified.

The γ-Fe_2O_3 structure is therefore maintained, after gadolinium substitution, similar to the finding reported by Drake *et al.*[23] who also found that the spinel structure was maintained after gadolinium substitution in Fe_3O_4 nanoparticles.[23] Drake *et al.* prepared Fe_3O_4 type nanoparticles *via* a similar co-precipitation route, forming $Fe_{2.98}Gd_{0.02}O_4$ nanoparticles of 13.2 nm diameter and a magnetisation value of 65.67 emu/g. In comparison, the $Fe_{2-x}Gd_xO_3$ solid solution series presented here had particle diameters of 9.4-10.9 nm and a magnetisation from 61.9 emu/g down to 43.9 emu/g as the Gd^{3+} content increased. The slightly lower magnetisation values of the prepared nanoparticles can be explained by the smaller particle size and the absence of the extra Fe^{2+} cations γ-Fe_2O_3 compared to Fe_3O_4.

Cation doping of spinel structures has previously been reported by Chakrabarti *et al* who studied the magnetic properties of cobalt doped maghemite nanoparticles.[140] Other studies reported have included manganese doped magnetite and zinc doped magnetite.[28,

[50, 55, 141] The common theme is the dopant metal, which is a transition metal like iron, hence the existing co-operative magnetic interactions such as superexchange and double exchange interactions between the *d* orbitals on the transition metals are not disrupted.

However, in this case the cation dopant is a lanthanide, hence it is necessary to question whether the same exchange interactions are maintained as lanthanides have a *4f* valence shell.

In the γ-Fe_2O_3 unit cell two types of exchange interactions take place. Within the A sublattice double exchange occurs between the Fe^{3+} ions on different A sites due to the close proximity of the *d* orbitals and the spins of the Fe^{3+} cations all align parallel. The same occurs between the Fe^{3+} ions on the B sites, however the alignment of electrons on the B sites is anti-parallel to those on the A sites. A second type of exchange interaction occurs between the A and B sublattices, superexchange, in which coupling between Fe^{3+} ions occurs *via* the oxide anion, whose *p* orbitals overlap with the Fe^{3+} ions *d* orbitals.

However, when some Fe^{3+} ions are replaced with Gd^{3+} ions, there is potential for these coupling interactions to be disrupted. Based on size, the Gd^{3+} ions would occupy the larger octahedral holes as reported by Kim *et al.*[142]

Tahar *et al* investigated $CoFe_2O_4$ nanoparticles partially substituted with lanthanide ions (Ln^{3+}) such as La, Nd, Gd etc. to learn how the magnetic properties of the nanoparticles changed *via* magnetic coupling interactions.[143] The nanoparticles were prepared by refluxing the iron and lanthanide salts with sodium acetate in diethylene glycol.

The calculated formula, determined by ICP was $CoFe_{1.90}Ln_{0.1}O_4$. PXRD patterns show for all cases of Fe^{3+} substitution with Ln^{3+} ions the spinel structure was maintained, with the exception of Gd^{3+}, whose pattern and ICP data was not shown. However, a study of

the $CoFe_{2-x}Gd_xO_4$ samples using the EELs technique showed that when x= 0.1 the Gd^{3+} distribution is homogenous throughout the particle, but when x = 0.2 Gd^{3+} ions are concentrated closer to the surface of the nanoparticles.

This study suggested an increase in unit cell size as Fe^{3+} was substituted by Ln^{3+} ions, compared against $CoFe_2O_4$ particles, but also a decreasing unit cell size trend as the Ln^{3+} ions changed from lanthanum, across the group to holmium, due to the lanthanide contraction, although the results in this case varied, between 8.401 Å and 8.407 Å. The paper suggested the migration of the smaller Co^{2+} ions from the octahedral sites to the tetrahedral sites and vice versa the migration of the Fe^{3+} ions would reduce the lattice strain caused by having large Ln^{3+} ions in the octahedral interstices. This would mask any changes in the unit cell parameters, in agreement with the observations in this work (Table 3-7).

All the $CoFe_2O_4$ nanoparticles behaved superparamagnetically, and in all cases the blocking temperature decreased after substitution, compared to the unsubstituted $CoFe_2O_4$ nanoparticles. All the substituted samples with the exception of $CoFe_{2-x}Ho_xO_4$ had higher magnetisation saturation values than the original $CoFe_2O_4$ material.[143]

As Tahar *et al.* described, if the material adopts a pure inverse spinel structure with all the Co^{2+} ions in octahedral sites, then it is possible to determine the theoretical magnetic moment per formula unit for each $CoFe_{2-x}Ln_xO_4$. However, a lack of correlation was observed between the theoretical and experimental magnetic moments. Tahar *et al.* attributed the discrepancies to a decrease in Fe^{3+}- Fe^{3+} ions coupling interactions due to Ln^{3+} ion doping, and only weak coupling interactions taking place between both Ln^{3+}–Fe^{3+} ions (*4f-3d)* and Ln^{3+} –Ln^{3+} ions (*4f-5d-4f)*, resulting in lower magnetic moment contributions. In addition, the migration of Co^{2+} ions into the tetrahedral sites

and Fe^{3+} ions into the octahedral sites would result in a greater amount of Fe^{3+} contribution from octahedral sites than accounted for in theoretical calculations, although this would lead to an increase in the magnetisation saturation, which was not observed.[143]

Panda *et al.* studied the magnetic properties of Pr- and Gd- substituted $CoFe_2O_4$ nanoparticles prepared by the thermal decomposition of mixed metal citrate gels at different temperatures.[47] Analysis of the prepared materials by PXRD indicated that in all cases the spinel structure was maintained, although $CoGd_xFe_{2-x}O_4$ samples with $x>0.2$ were amorphous.

The magnetic properties of the lanthanide doped cobalt ferrite materials were studied, showing that doping with lanthanide ions at any temperature reduced the magnetisation saturation and magnetic moment of the resulting material. This was attributed to the lanthanide ions having localized *4f* electrons and essentially acting in the same way as non-magnetic ions, occupying the octahedral sites of the spinel unit cell. This would cause a reduction in the magnetic moment of the material as the net magnetic moment is dependent upon the number of magnetic ions in the material. This aligns with the observations of this study; as the value of x in $CoFe_{2-x}Ln_xO_4$ increased, the magnetic moment decreased.

XPS spectroscopy was carried out on one of the $Fe_{2-x}Gd_xO_3$, $Fe_{1.96}Gd_{0.04}O_3$. The spectrum shows the presence of Fe^{3+} ions and the absence of peaks relating to Fe^{2+} ions. Once again, this supports the conclusion that γ-Fe_2O_3 type nanoparticles have formed. Unfortunately, the main peak assigned to Gd^{3+} overlaps with the peak for carbon making it difficult to distinguish and therefore this data cannot be used to calculate the Fe^{3+}:Gd^{3+} ratio and confirm the chemical formula previously calculated from the ICP-AES data. However, comparison of the carbon peak in this spectrum with the carbon peak observed in the

single phase γ-Fe_2O_3 sample shows a greater intensity in this case, which it is reasonable to assume is caused by the presence of Gd^{3+} ions. The main Gd 3d peaks can be observed at 1188 eV and 1223 eV.

Similar spectra are seen by Xiao *et al.* who also observed peaks for Fe, Gd, C and O, however they note the absence of the satellite peak for Fe at 94 eV. This peak can be assigned to Fe *3s* and is associated with the presence of γ-Fe_2O_3. The satellite peak at 94 eV is observed for the nanoparticles prepared in this work indicating the presence of γ-Fe_2O_3 nanoparticles.[128]

Additionally, for the $Fe_{2-x}Gd_xO_3$ solid solutions the Mössbauer spectra at 298 K show the sextet contribution from the Fe^{3+} ions as well as a central peak that can be attributed to the presence of Gd^{3+} ions (Figure 3-15 to Figure 3-17). The intensity of this central peak varies with Gd^{3+} concentration, however the peak broadening could also be influenced by particle size.[144] Although, the spectra at 80 K still show the sextet relating to the Fe^{3+} ions, showing that at low temperatures magnetic ordering is favoured (Figure 3-11 to Figure 3-14)

The blocking temperatures shown by the ZFC-FC curves for the $Fe_{2-x}Gd_xO_3$ solid solution nanoparticles suggest that the Gd^{3+} content has no discernible effect on the transition temperature. The blocking temperature varies between 31.30 K and 56.17 K across the series with no obvious relationship to Gd^{3+} content (Table 3-9).

The M-H curves collected *via* SQUID shows all the $Fe_{2-x}Gd_xO_3$ solid solution nanoparticles exhibit superparamagnetic behaviour, with magnetisation values ranging between 43.91 emu/g and 68.68 emu/g at 300 K depending upon the gadolinium content with a similar pattern observed for measurements at 5 K. However, the increase in magnetisation saturation values is not linear. Initially the magnetisation saturation

increases from 57.65 emu/g for γ-Fe_2O_3 to 61.93 emu/g for $Fe_{1.99}Gd_{0.01}O_3$ nanoparticles, suggesting the substitution of iron ions with gadolinium ions improves the magnetisation saturation. Yet further substitution with gadolinium ions causes the magnetisation saturation to reduce, with the notable exception of $Fe_{1.95}Gd_{0.05}O_3$ (3.33%). The reduction in magnetic moment and magnetisation saturation values agrees with the findings of Panda *et al.* and Tahar *et al.* who investigated lanthanide doped iron oxide nanoparticles, and also agrees with the findings of Bae *et al.* who studied the magnetic properties of gadolinium labelled magnetite nanoparticles.[47, 91, 143] However the increase in the magnetic moment in $Fe_{1.99}Gd_{0.01}O_3$ and $Fe_{1.95}Gd_{0.05}O_3$ (3.33%) must indicate that the Gd^{3+} ions are coupling with other ions in the nanoparticles cooperatively, leading to an increased in magnetic moment and magnetisation saturation.

3.3.2 $Fe_{2-x}Dy_xO_3$ solid solution nanoparticle series $0 \leq x \leq 1$

The lanthanide ion Dy^{3+} has a larger magnetic moment than Gd^{3+} ions, at 10.60 BM. Recent literature suggests that this ion may influence T_2 relaxation properties, suggesting that the incorporation of Dy^{3+} ions into γ-Fe_2O_3 nanoparticles could result in an improved T_2 contrast agent. The preparation of $Fe_{2-x}Dy_xO_3$ solid solution nanoparticles was carried out by the same co-precipitation method used to the prepare $Fe_{2-x}Gd_xO_3$ solid solution nanoparticles, but starting with dysprosium nitrate instead of chloride. Dy^{3+} ions are smaller than Gd^{3+} ions and so it was expected that the maghemite nanoparticles may accept more dysprosium into the lattice than in the $Fe_{2-x}Gd_xO_3$ series. There is no literature available relating to dysprosium doped- or dysprosium labelled- iron oxides and so only comparisons between the $Fe_{2-x}Gd_xO_3$ series and the $Fe_{2-x}Dy_xO_3$ series can be drawn.

The PXRD patterns collected for the $Fe_{2-x}Dy_xO_3$ series (Figure 3-28) indicated that above x=0.06, the prepared nanoparticles were not single phase and so no further characterisation was carried out for these samples. However for x=0.1 and x= 0.06, the PXRD patterns indicated that the spinel structure had been maintained.

ICP-AES was used to confirm the presence of dysprosium in the newly prepared materials. The formulae have been calculated at $Fe_{1.99}Dy_{0.01}O_3$ and $Fe_{1.94}Dy_{0.06}O_3$, are based on the general formula $Fe_{2-x}Dy_xO_3$. In comparison to the $Fe_{2-x}Gd_xO_3$ solid solution nanoparticle series, the initial amount of cation substitution is the same, resulting in $Fe_{1.99}M_{0.01}O_3$ (M=Gd, Dy) in both cases. However, for sample $Fe_{1.94}Dy_{0.06}O_3$, the equivalent gadolinium doped iron oxide nanoparticle has the formula $Fe_{1.95}Gd_{0.05}O_3$, showing from the same molar amounts of starting reagent, more cation substitution has occurred with the smaller Dy^{3+} ion, as expected.

Comparison of the 311 peak position for the $Fe_{1.99}Dy_{0.01}O_3$ and $Fe_{1.94}Dy_{0.06}O_3$ and pure maghemite nanoparticles, shows a shift of the diffraction peak to lower angles. This indicates an increase in the unit cell size and would suggest the substitution of Fe^{3+} ions with Dy^{3+} ions, as the latter have a larger ionic radius (Fe^{3+}= 0.785 Å, Dy^{3+}= 1.052 Å).[139]

The particle size for the $Fe_{2-x}Dy_xO_3$ solid solution nanoparticle series was calculated by the Scherrer equation from the collected PXRD patterns. Similarly to the $Fe_{2-x}Gd_xO_3$ series, the particle diameters are much smaller than the pure maghemite nanoparticles, prepared by the same method. This may be due to strain of the lattice as the lattice distorts to accommodate the larger lanthanide ions,[142] considering that the particle size decrease as the dysprosium content increases. TEM images of the particles show spherical morphology (Figure 3-27), however due to agglomeration, there are not enough singular particles to accurately determine the particle diameter.

The Mössbauer spectra for γ-Fe_2O_3 shows the collapse of the sextet spectrum as the temperature increases. At 80 K, a trend can be seen in the Mössbauer spectra as the Dy^{3+} content increases. Moving from γ-Fe_2O_3 to $Fe_{1.99}Dy_{0.01}O_3$ the sextet reduces and a main central peak is observed, due to the presence of paramagnetic dysprosium.[118] As the dysprosium content increases further the sextet disappears entirely and just the paramagnetic component is observed. At 298 K, both $Fe_{1.99}Dy_{0.01}O_3$ and $Fe_{1.94}Dy_{0.06}O_3$ show a doublet, indicating that the material is superparamagnetic at this temperature (Figure 3-31 and Figure 3-32). This phenomenon can be attributed to the small particle size of the $Fe_{1.99}Dy_{0.01}O_3$ and $Fe_{1.94}Dy_{0.06}O_3$ particles.

3.4 CONCLUSIONS

The preparation of both $Fe_{2-x}Gd_xO_3$ and $Fe_{2-x}Dy_xO_3$ solid solution nanoparticles has been carried out. In both cases single phase materials for $x \leq 0.27$ and $x \leq 0.06$ respectively were prepared and PXRD confirmed that the spinel structure of the host γ-Fe_2O_3 compound was maintained.

For the $Fe_{2-x}Gd_xO_3$ solid solution, cation doping was achieved up to x=0.27, which is the highest reported substitution of γ-Fe_2O_3 nanoparticles with any lanthanide ion, to the best of the authors knowledge. The magnetic moments of the $Fe_{2-x}Gd_xO_3$ nanoparticles varied with varying Gd^{3+} content suggesting the distribution and magnetic coupling effects of the Gd^{3+} ions within the γ-Fe_2O_3 lattice plays an important role. Preparation of dysprosium substituted iron oxide materials was carried out, yielding novel compounds with the formulae $Fe_{1.99}Dy_{0.01}O_3$ and $Fe_{1.94}Dy_{0.06}O_3$. Mössbauer spectra indicate that these substituted particles are superparamagnetic at room temperature, similar to the $Fe_{2-x}Gd_xO_3$ solid solutions and also have similar particle sizes.

4 CATION DOPED GADOLINIUM OXIDE AND DYSPROSIUM OXIDE NANOPARTICLES

The field of nanoparticles for MRI contrast agents is expanding rapidly following the realisation that nanoparticles can provide increased MRI sensitivity compared to chelate based complexes.[92, 145] Gadolinium complexes are widely used as contrast agents due to their large magnetic moment and excellent T_1 relaxation properties. Recent studies have, hence, focussed on gadolinium oxide nanoparticles, and take into account both size of the nanoparticle and the surface coating's influence on their toxicity and biocompatibility. Furthermore, nanoparticles that contain other metals as well as gadolinium may provide stronger T_1 relaxation signals in MRI, increasing the techniques sensitivity.

A range of methods have been reported for the preparation of gadolinium oxide nanoparticles including mechanochemical and hydrothermal.[146, 147] However, the most commonly used method is co-precipitation in the presence of diethylene glycol (DEG).[63 93, 148]

Azizian *et al.*[148] synthesized diethylene glycol (DEG) coated gadolinium oxide nanoparticles by refluxing gadolinium chloride, sodium hydroxide and DEG followed by filtration to remove any free gadolinium or excess DEG. The resulting particles had a hydrodynamic diameter of 5.9 ± 0.13 nm and r_1 and r_2 relaxivities of 13.31 $mM^{-1}s^{-1}$ and 11.81 $mM^{-1}s^{-1}$ respectively per Gd^{3+} at 1.5 T. Similarly, Park *et al.*[92] synthesized approximately 1 nm Gd_2O_3 nanoparticles by refluxing gadolinium chloride, gadolinium acetate or gadolinium acetylacetonate in tripropylene glycol for 24 hours, washing the resulting precipitate with water and refluxing twice more for 24 hours each. The formation of Gd_2O_3 nanoparticles was confirmed by HRTEM to be cubic, with a lattice

parameter of 3.13 Å. The r_1 and r_2 relaxivities of the prepared Gd_2O_3 nanoparticles coated with D-glucuronic acid, were 9.9 $mM^{-1}s^{-1}$ and 10.5 $mM^{-1}s^{-1}$ respectively at 1.5 T.

The luminescence property of the lanthanides is well known and doping of gadolinium oxide nanoparticles with other lanthanides has been carried out to improve these luminescent properties. In particular, Zhou *et al.*[147] describes doping of gadolinium oxide nanoparticles with ytterbium, thulium and erbium to produce dual modal compounds for use with both optical and magnetic resonance imaging. These particles were prepared using the metal nitrate salts, urea and glycerol. The mixture was treated hydrothermally to produce a metal carbonate precursor, which was then calcined at 500 °C for 3-4 hours to form the oxide. The size of the nanoparticles could be tuned by adjusting the glycerol content, resulting in particles ranging from 10 -270 nm.

Dy^{3+} chelate compounds as well as Dy_2O_3 nanoparticles have been investigated as potential T_2 MRI contrast agents due to the high magnetic moment and fast electronic relaxation times of dysprosium,[15] especially at higher magnetic field strengths. One drawback of current MRI techniques is low sensitivity, which leads to low quality images. This can be overcome by utilising MRI scanners with higher magnetic field strengths and higher signal to noise ratios. Currently, this requires high doses of contrast agents to provide adequate relaxation effects for images to be obtained. One advantage of dysprosium oxide nanoparticles is the high concentration of metal centres with a high combined magnetic moment leading to fast T_2 relaxation even at low doses.[149, 150]

Synthesis of Dy_2O_3 particles is commonly carried out by thermal decomposition methods, with more recent reports of soft chemistry methods such as co-precipitation being used.

Tok *et al.*[151] used a co-precipitation method followed by annealing of the precipitate at 700 °C. Analysis of the precipitate before heating indicated amorphous dysprosium

oxides and carbonates had formed. Only after further annealing of the precipitate it was possible to obtain pure dysprosium oxide nanoparticles, approximately 30 nm diameter.

Das *et al.*[152] reported synthesis of Dy_2O_3:Tb^{3+} nanocrystals by thermal decomposition of a Tb-Dy oleate complex. The method yielded 2.8 nm diameter particles with the cubic bixbyite Dy_2O_3 structure (Figure 1-24) confirmed by X-ray diffraction. From a 1:19 ratio of Tb^{3+}:Dy_2O_3 of starting reagents it was determined by EDX that 6.1 molar % Tb^{3+} doped into the Dy_2O_3:Tb^{3+} nanocrystals prepared, and have a relaxivity of 2.17 $mM^{-1}s^{-1}$ per nanocrystal at 7 T.

Kattel *et al.*[150] also reported a thermal decomposition approach to prepare both Dy_2O_3 nanoparticles and $Dy(OH)_3$ nanorods, from $Dy(NO)_3$ starting reagents. The preparation of Dy_2O_3 nanoparticles was carried out at 200 °C, and $Dy(OH)_3$, at 80 °C. Both the nanoparticles and nanorods were then functionalised with glucuronic acid. The Dy_2O_3 nanoparticles prepared had an average physical particle diameter of 3.2 nm and average hydrodynamic particle diameter of 6.2 nm. Relaxivity measurements for Dy_2O_3 nanoparticles indicate relaxivity values of r_1 = 0.008 $mM^{-1}s^{-1}$ and r_2 = 65.04 $mM^{-1}s^{-1}$ at 1.5 T.

Cation doping of gadolinium oxide and dysprosium oxide nanoparticles for use as MRI contrast agents has not been previously reported, to the best of the author's knowledge. This chapter discusses cation doping of Gd_2O_3 nanoparticles with both manganese and iron ions as well as the preparation of Dy_2O_3 nanoparticles, and iron doped Dy_2O_3 nanoparticles. All the $Gd_{2-x}Mn_xO_3$, $Gd_{2-x}Fe_xO_3$ and $Dy_{2-x}Fe_xO_3$ solid solutions were prepared by solid state reactions.

Manganese and iron ions have been previously reported as MRI contrast agents. Specifically, manganese oxide nanoparticles, due to the paramagnetic properties and T_1

relaxation properties of the Mn^{2+} ions.[106, 153] Additionally, multiple studies of manganese ferrite compounds have also been reported, looking at the combination of iron and manganese on MRI relaxation rates.[44, 60, 154]

Choi *et al.*[155] reported the preparation of gadolinium oxide nanoparticles, surface doped with manganese oxide for use as MRI contrast agents. The study found that surface doping with manganese improved both T_1 and T_2 relaxation rates when compared against Gd_2O_3 and MnO nanoparticles.

No cation doping of Dy_2O_3 nanoparticles has been reported, however dysprosium and iron ions both exhibit T_2 relaxation properties. The development of a $Dy_{2-x}Fe_xO_3$ nanoparticle series has been carried out to study the magnetic properties and relaxation characteristics at both 3 T and 11.7 T.

4.1 EXPERIMENTAL

This section describes the method used to prepare the $Gd_{2-x}Fe_xO_3$ $0 \leq x \leq 0.08$, $Gd_{2-x}Mn_xO_3$ $0 \leq x \leq 0.21$ and $Dy_{2-x}Fe_xO_3$ $0 \leq x \leq 0.08$ nanoparticle series. The nanoparticles were prepared by the following methods:

$Gd_{2-x}Mn_xO_3$ nanoparticles

$Gd(OH)_3$ and $MnCl_2$ were ground together, placed in an alumina crucible and heated in a furnace for 24 hours at 900 °C. The molar ratios of the two reagents are shown in Table 4-1.

$Gd_{2-x}Fe_xO_3$ nanoparticles

$Gd(OH)_3$ and $FeCl_3$ were ground together, placed in an alumina crucible and heated in a furnace for 24 hours at 600 °C. The molar ratios of the two reagents are shown in Table 4-1.

$Dy_{2-x}Fe_xO_3$ nanoparticles

$Dy(NO_3)_3$ and $FeCl_3$ were ground together, placed in an alumina crucible and heated in a furnace for 8 hours at 500 °C. The molar ratios of the two reagents are shown in Table 4-1.

Surface coating

The nanoparticles were dispersed in an aqueous solution of hydrochloric acid at pH 4, and citric acid added in a 1:1.2 $Ln_{2-x}M_xO_3$: citric acid molar ratio (Ln = Gd^{3+}, Dy^{3+}; M= Mn^{2+}, Fe^{3+}). The mixture was stirred for 2 hours before centrifugation and the collected nanoparticles were washed with deionised water and the pH adjusted to pH 7. These solutions were then used for MRI and NMR measurements.

Table 4-1 Molar ratios for the preparation of $Gd_{2-x}Fe_xO_3$, $Gd_{2-x}Mn_xO_3$and $Dy_{2-x}Fe_xO_3$ nanoparticle series.

%Molar Cation Substitution	**Moles $Gd(OH)_3$/ $Dy(NO_3)_3$ Starting Reagent**	**Moles $FeCl_3$ or $MnCl_2$ Starting Reagent**
0	2.76×10^{-3}	0
1	2.73×10^{-3}	0.0000276
5	2.62×10^{-3}	0.0001378
10	2.48×10^{-3}	0.000276
25	2.07×10^{-3}	0.000689
50	1.38×10^{-3}	0.001378

For ICP-AES analyses, the samples were added to aqua regia and dissolved in a microwave (CEM MARS Xpress) at 200 °C. The samples were then diluted by weight to 15.0g (+/-0.05g) with purified water. Analysis was carried out using a Perkin Elmer Optima 5300DV instrument against calibration at 0 and 10 ppm Gd, Fe, Mn or Dy.

Powder X-ray diffraction patterns were collected on a Panalytical Empyrean Diffractometer with Cu $K_{\alpha 1}$ radiation (1.54 Å) at 30 mA, 40 kV with a step size of 0.05 degrees 2 theta and a 0.5 ° fixed divergence slit.

TEM images were obtained using a Gatan US4000 digital camera mounted onto a JEOL 2010 transmission electron microscope.

4.2 RESULTS

4.2.1 Gd_2O_3 Nanoparticles

From the two series of cation doped Gd_2O_3 nanoparticles prepared two sets of Gd_2O_3 nanoparticles were synthesized for comparison, by dehydrating $Gd(OH)_3$ at 900 °C and 600 °C respectively. At 900 °C, the PXRD diffraction peaks can be matched to those of Gd_2O_3 with the space group $I\,2_1\,3$ (Figure 4-1). At 600 °C, the diffraction peaks indicate the primary phase to be Gd_2O_3, however asymmetric peak broadening can be observed suggesting the presence of impurities. The particle diameter was estimated using the Scherrer equation, with Gd_2O_3 nanoparticles synthesized at 900 °C having a particle diameter of 27.44 nm.

4.2.1 $Gd_{2-x}Mn_xO_3$ nanoparticle series

The synthesis of Mn^{2+} doped Gd_2O_3 nanoparticles was carried out by solid state reaction of $Gd(OH)_3$ and $MnCl_2$ at 900 °C. ICP-AES results (Table 4-2) show increasing cation doping occurs with increasing amounts of starting reagent, however there is no direct correlation between starting amounts and the final amount doped into the compound. Additionally, the latter two compounds in the table (28.3%, 85.42%) show a higher molar % obtained in the final samples than was expected suggesting either the samples are not single phase or there has been a loss of Gd^{3+} ions, causing the Mn:Gd molar ratio to increase.

Table 4-2 ICP-AES data for $Gd_{2-x}Mn_xO_3$ nanoparticle series

Theoretical molar % Mn ions	**Actual molar % Mn ions obtained by ICP-AES**	**Calculated Formula**
1	0.83	$Gd_{1.98}Mn_{0.02}O_3$
5	4.98	$Gd_{1.90}Mn_{0.1}O_3$
10	10.52	$Gd_{1.79}Mn_{0.21}O_3$
25	28.31	$Gd_{2-x}Mn_xO_3$, Mn_2O_3, $Gd(OH)_3$
50	85.42	$Gd_{2-x}Mn_xO_3$, Mn_2O_3, $Gd(OH)_3$

The PXRD patterns (Figure 4-2 and Figure 4-3) for the $Gd_{2-x}Mn_xO_3$ nanoparticle series show diffraction peaks matching those for Gd_2O_3 and indicate that the prepared nanoparticles have a single phase bixbyite structure for $0 \leq x \leq 0.21$. The $Gd_{2-x}Mn_xO_3$ compounds prepared with the theoretical molar percentage of 25 % and 50 % show both secondary and tertiary phases of that can be matched to Mn_2O_3 and $Gd(OH)_3$ in addition to Gd_2O_3.

The particle diameters shown in Table 4-3 for the $Gd_{2-x}Mn_xO_3$ nanoparticle series for $0 \leq x \leq 0.21$ have been estimated using the Scherrer equation. The table indicates an increase in the particle diameter as the x value increases, from 21.25 nm for x = 0.02, up to 40.21 nm for x = 0.21.

.

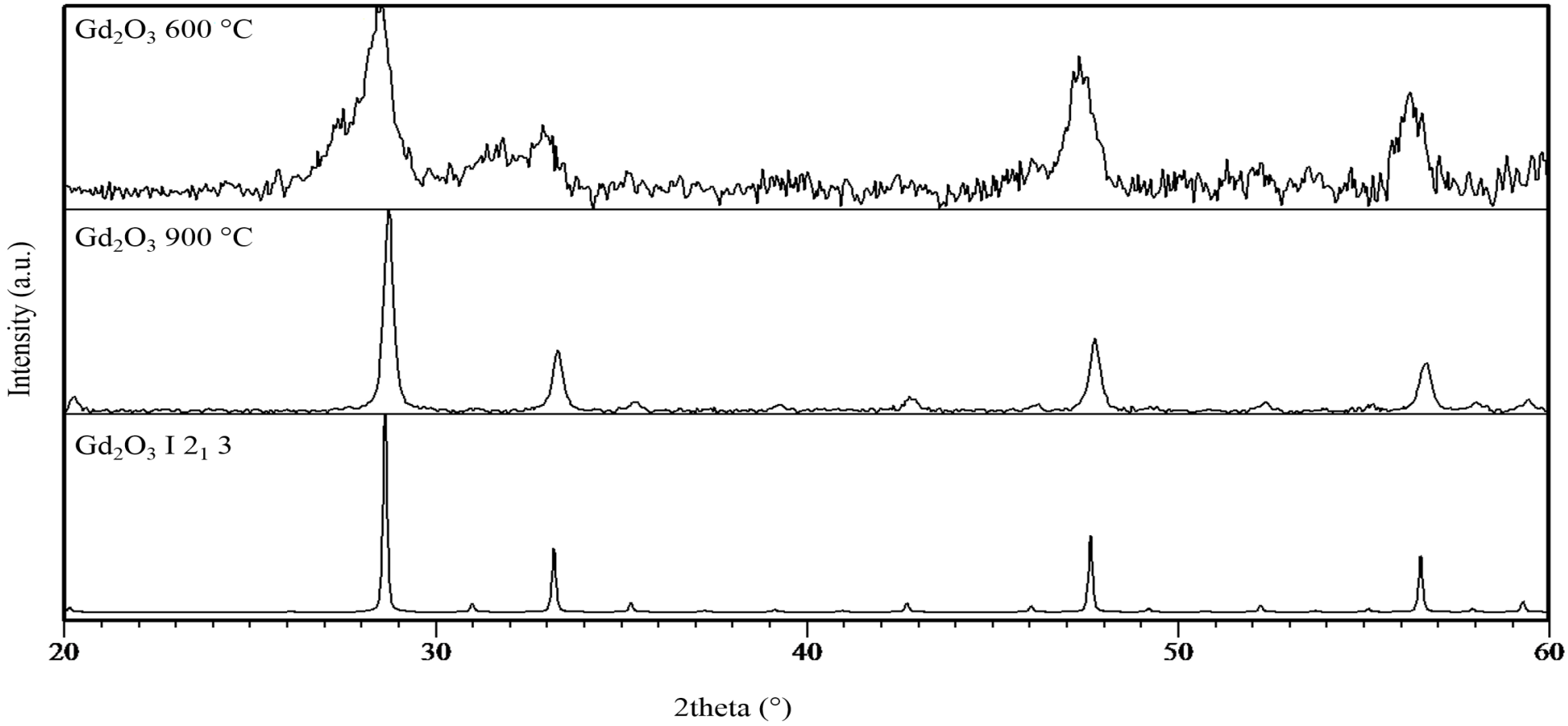

Figure 4-1 PXRD patterns for Gd_2O_3 nanoparticles synthesized at 600 °C and 900 °C.

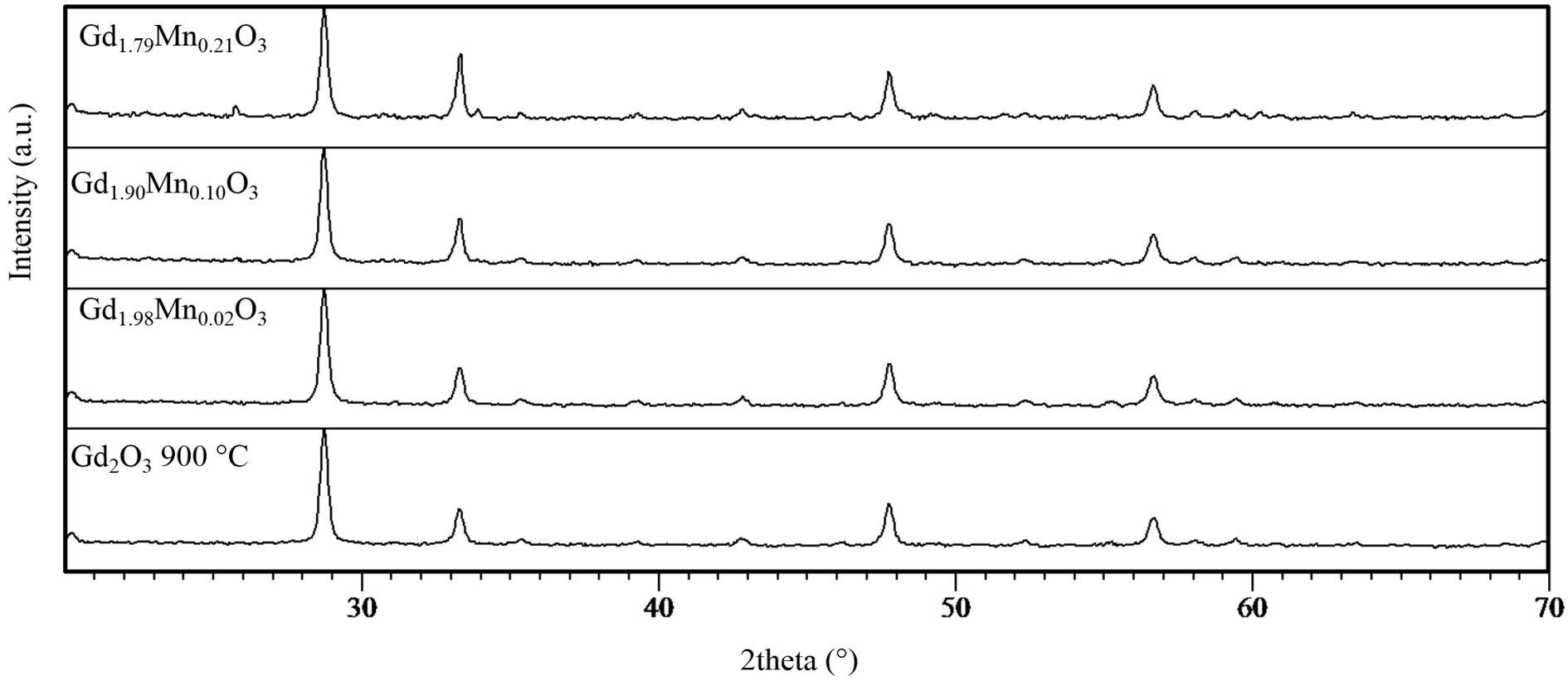

Figure 4-2 PXRD patterns for $Gd_{2-x}Mn_xO_3$ nanoparticle series for $0 \leq x \leq 0.21$

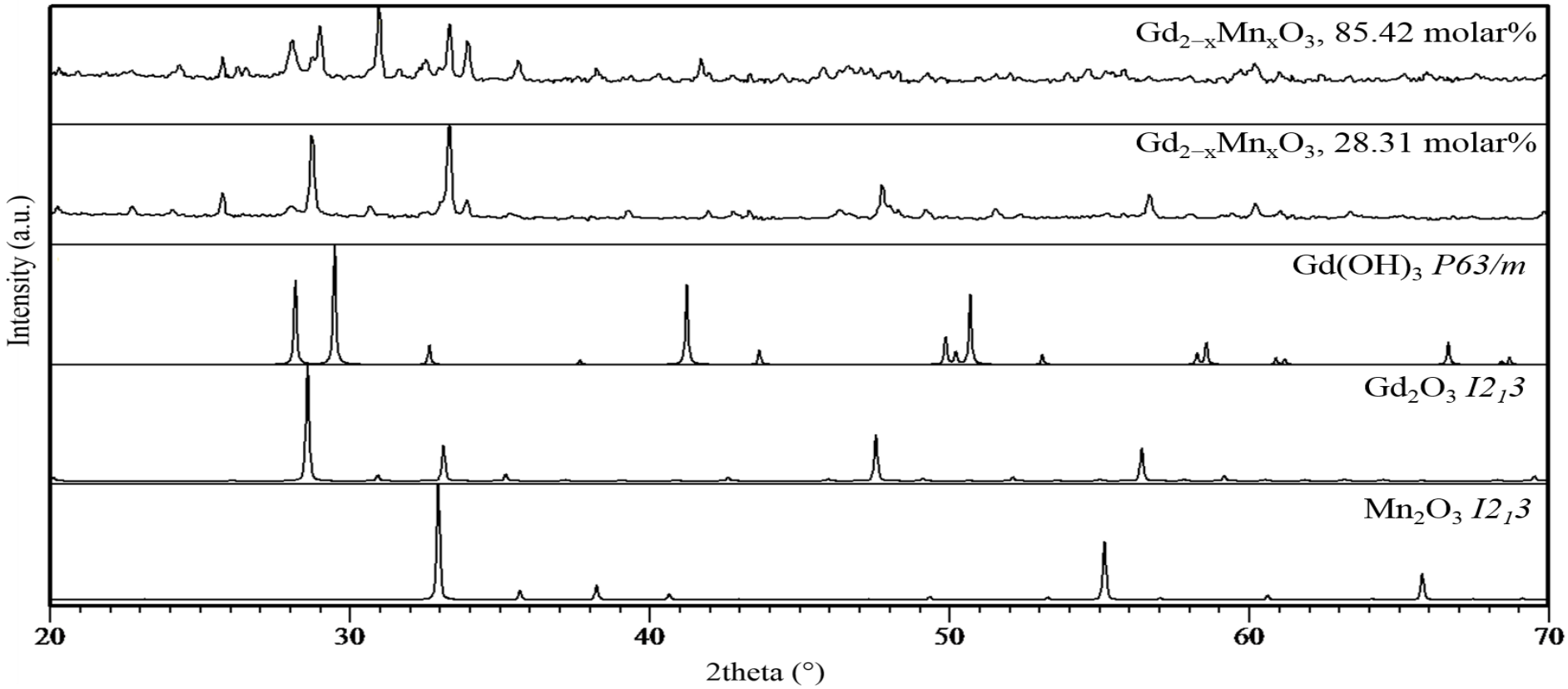

Figure 4-3 PXRD patterns for $Gd_{2-x}Mn_xO_3$ nanoparticle series for $0.57 \leq x \leq 0.71$.

Table 4-3 Particle diameter for $Gd_{2-x}Mn_xO_3$ nanoparticle series estimated by the Scherrer equation.

Compound	Particle Diameter (nm) as determined by the Scherrer equation
Gd_2O_3	27.4
$Gd_{1.98}Mn_{0.02}O_3$	21.3
$Gd_{1.90}Mn_{0.1}O_3$	28.9
$Gd_{1.79}Mn_{0.21}O_3$	40.2

4.2.1 $Gd_{2-x}Fe_xO_3$ nanoparticle series

The synthesis of Fe^{3+} doped Gd_2O_3 nanoparticles was carried out by solid state reaction of $Gd(OH)_3$ and $FeCl_3$ at 600 °C. ICP-AES results (Table 4-4) show increasing cation doping occurs with increasing amounts of starting reagent, however there is no direct correlation between starting amounts and the final amount doped into the compound.

Table 4-4 ICP-AES data for $Gd_{2-x}Fe_xO_3$ nanoparticles.

Theoretical molar % of Fe ions	Actual molar % of Fe obtained by ICP-AES
1	0.61
5	2.22
10	4.20
25	19.42
50	40.07

The PXRD patterns (Figure 4-4) for the $Gd_{2-x}Fe_xO_3$ nanoparticle series show diffraction peaks matching those for Gd_2O_3, however in all cases there are additional peaks that cannot be identified. The compounds with 19.42 % and 40.07 % molar content of Fe show a secondary phase that can be matched to GdOCl.

The particle diameters shown in Table 4-5 for the $Gd_{2-x}Fe_xO_3$ nanoparticle series up to 4.20 molar percent, have been estimated using the Scherrer equation. A trend can be observed: as the Fe^{3+} ion content increases, the particle diameters decrease, suggesting the presence of iron influences the resulting particle size.

A TEM image of the nanoparticles is shown in Figure 4-6. The image shows roughly spherical particles however they are too agglomerated to be able to measure the particle size.

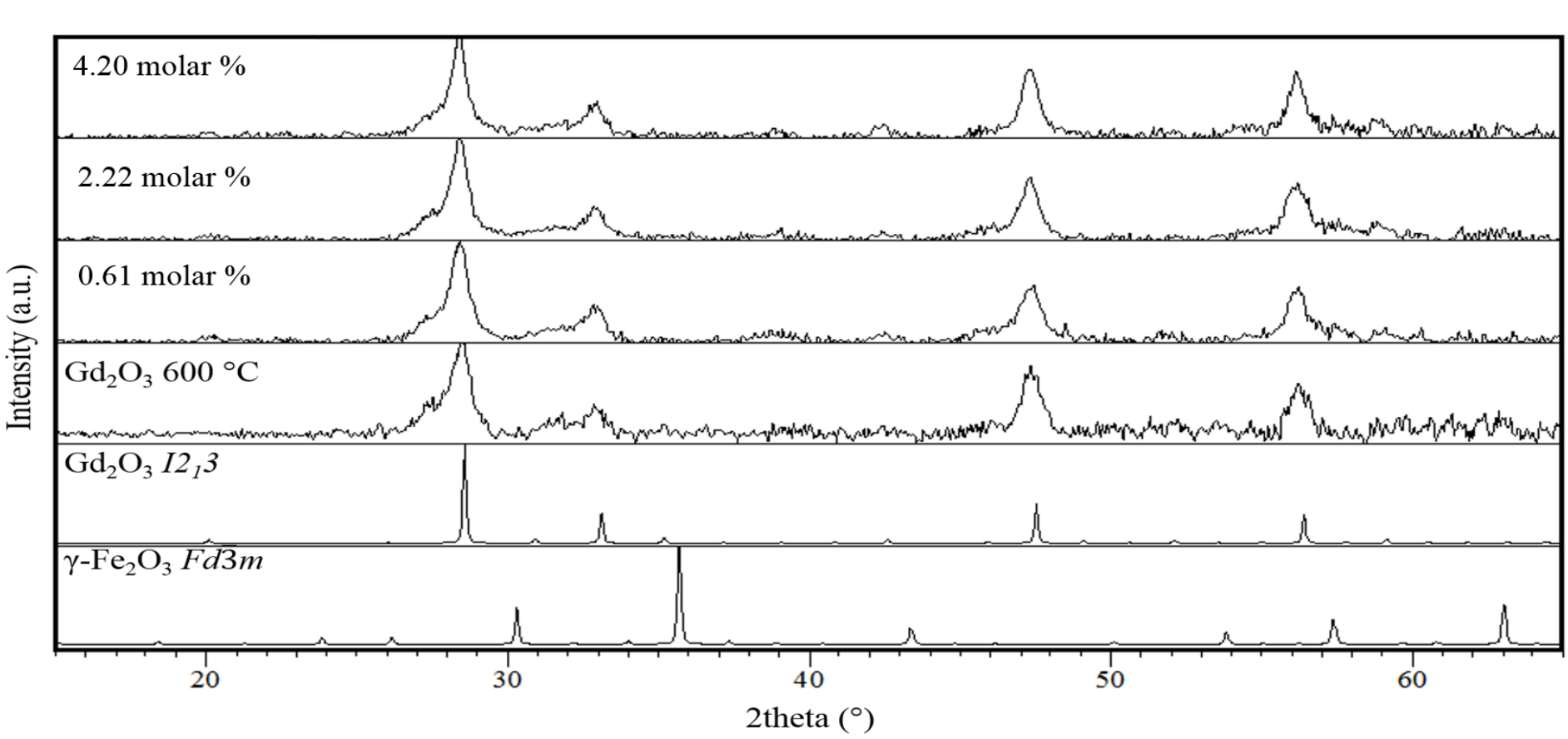

Figure 4-4 PXRD patterns for $Gd_{2-x}Fe_xO_3$ up to 4.20 molar percent.

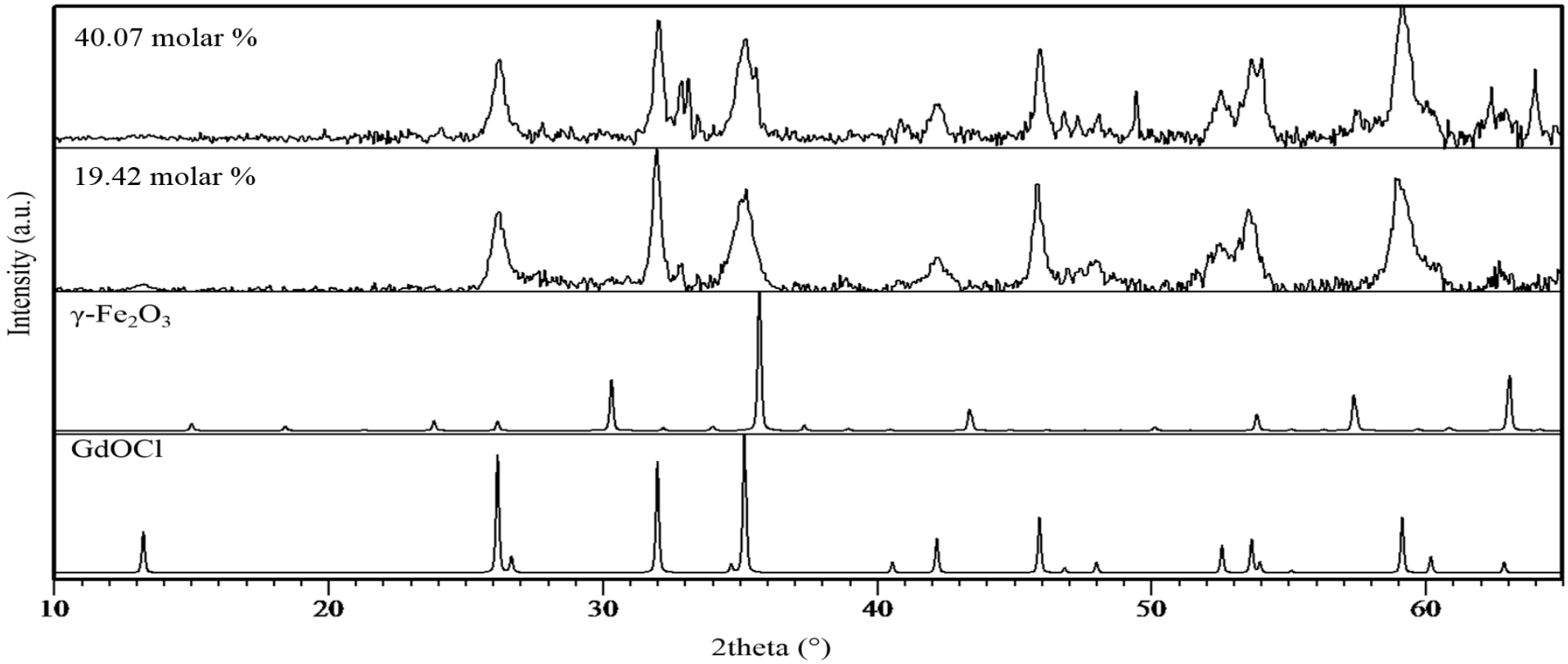

Figure 4-5 PXRD patterns for $Gd_{2-x}Fe_xO_3$ for 19.42 molar percent and 40.07 molar percent matched against GdOCl and γ-Fe_2O_3.

Table 4-5 Particle diameter for the $Gd_{2-x}Fe_xO_3$ nanoparticle series calculated via the Scherrer equation.

Compound	Particle Diameter (nm) as determined by the Scherrer equation
Gd_2O_3	9.4
$Gd_{2-x}Fe_xO_3$, 0.61 molar %	11.4
$Gd_{2-x}Fe_xO_3$, 2.22 molar %	8.6
$Gd_{2-x}Fe_xO_3$, 4.20 molar %	7.8

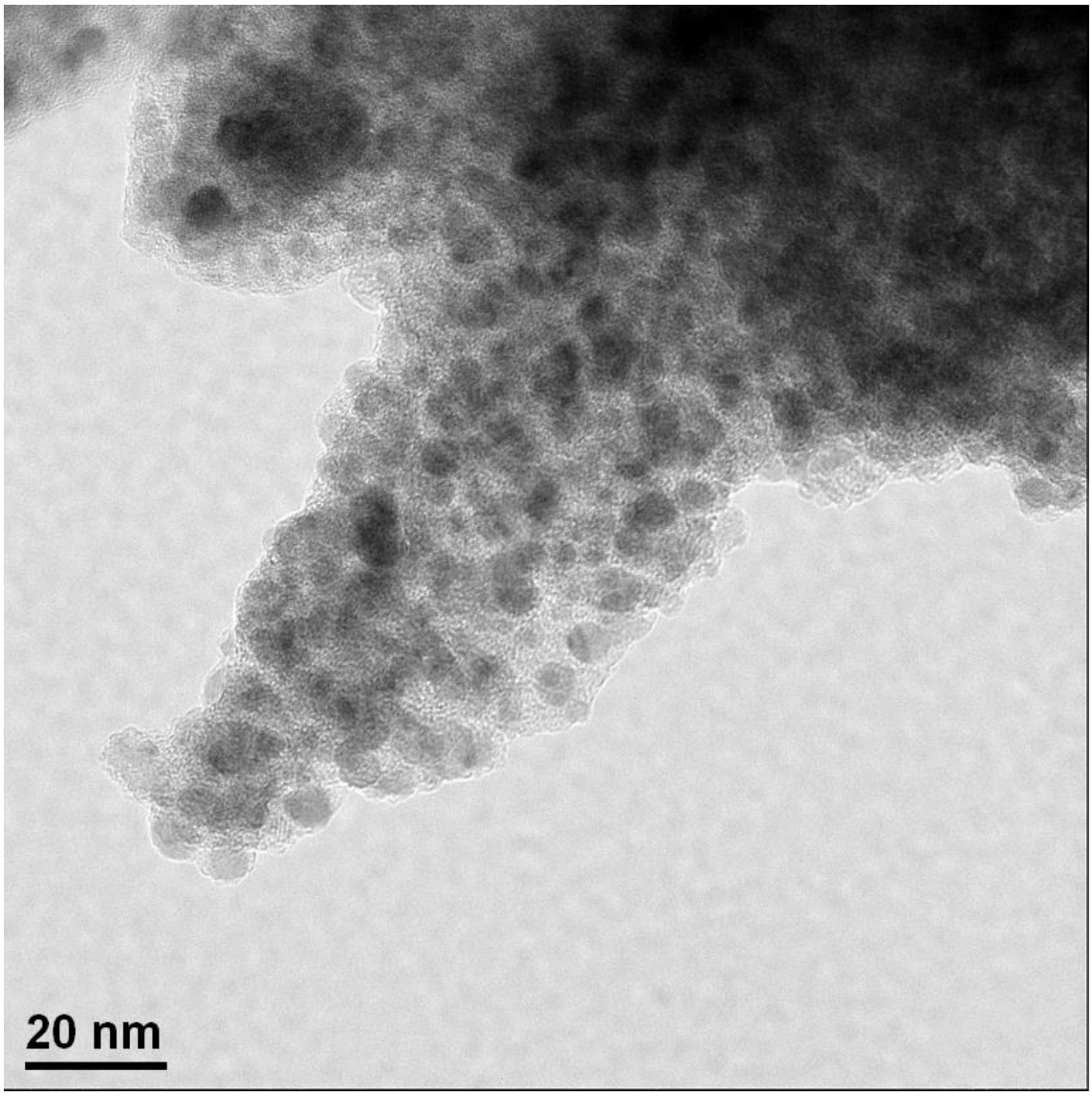

Figure 4-6 A TEM image of $Gd_{1.96}Fe_{0.04}O_3$ nanoparticles coated with citric acid.

4.2.2 $Dy_{2-x}Fe_xO_3$ nanoparticle series

Table 4-6 ICP-AES data for $Dy_{2-x}Fe_xO_3$ nanoparticles.

Theoretical molar % Fe	**Actual molar % Fe obtained by ICP-AES**	**Calculated Formula**
1	1.14	$Dy_{1.98}Fe_{0.02}O_3$
5	4.72	$Dy_{1.91}Fe_{0.09}O_3$
10	10.77	$Dy_{1.78}Fe_{0.22}O_3$
25	34.47	$Dy_{2-x}Fe_xO_3$
50	112.43	$Dy_{2-x}Fe_xO_3$

Dy_2O_3 nanoparticles were prepared by calcination of $Dy(NO_3)_3$ at 500 °C for 8 hours. The PXRD pattern (Figure 4-7) indicates single phase Dy_2O_3 nanoparticles were produced. The PXRD diffraction peaks can be matched to those of Dy_2O_3 with the space group *I* a 3, and the lattice parameter was calculated at a = 10.663(9) Å. The particle diameter was estimated using the Scherrer equation to be 10.16 nm.

The synthesis of Fe^{3+} doped Dy_2O_3 nanoparticles was carried out by the same method used to produce Dy_2O_3 nanoparticles, calcining $Dy(NO_3)_3$ and $FeCl_3$ at 500 °C. ICP-AES results (Table 4-6) show increasing cation doping occurs with increasing amounts of starting reagent.

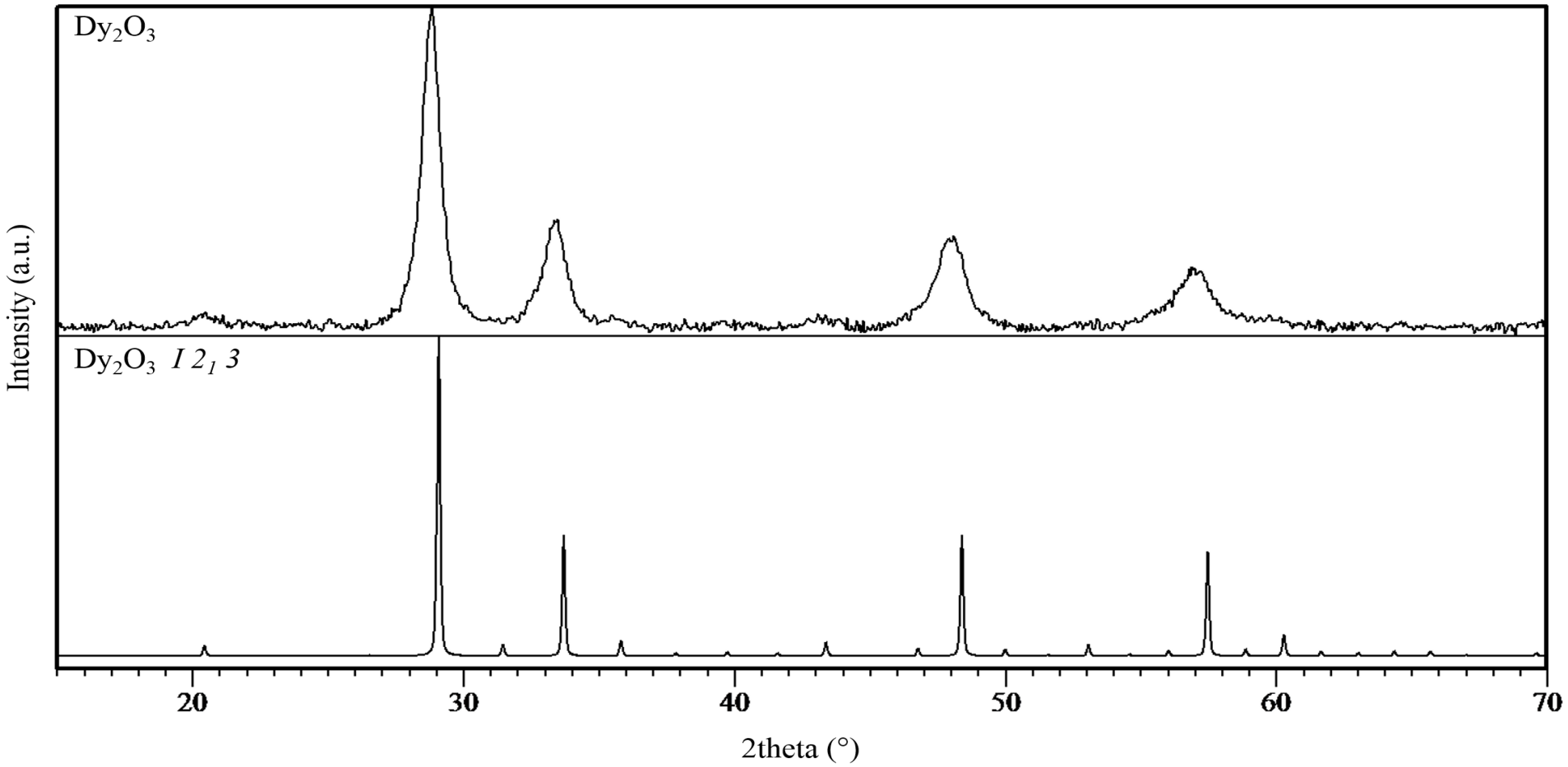

Figure 4-7 PXRD patterns for Dy_2O_3 nanoparticles prepared in this work.

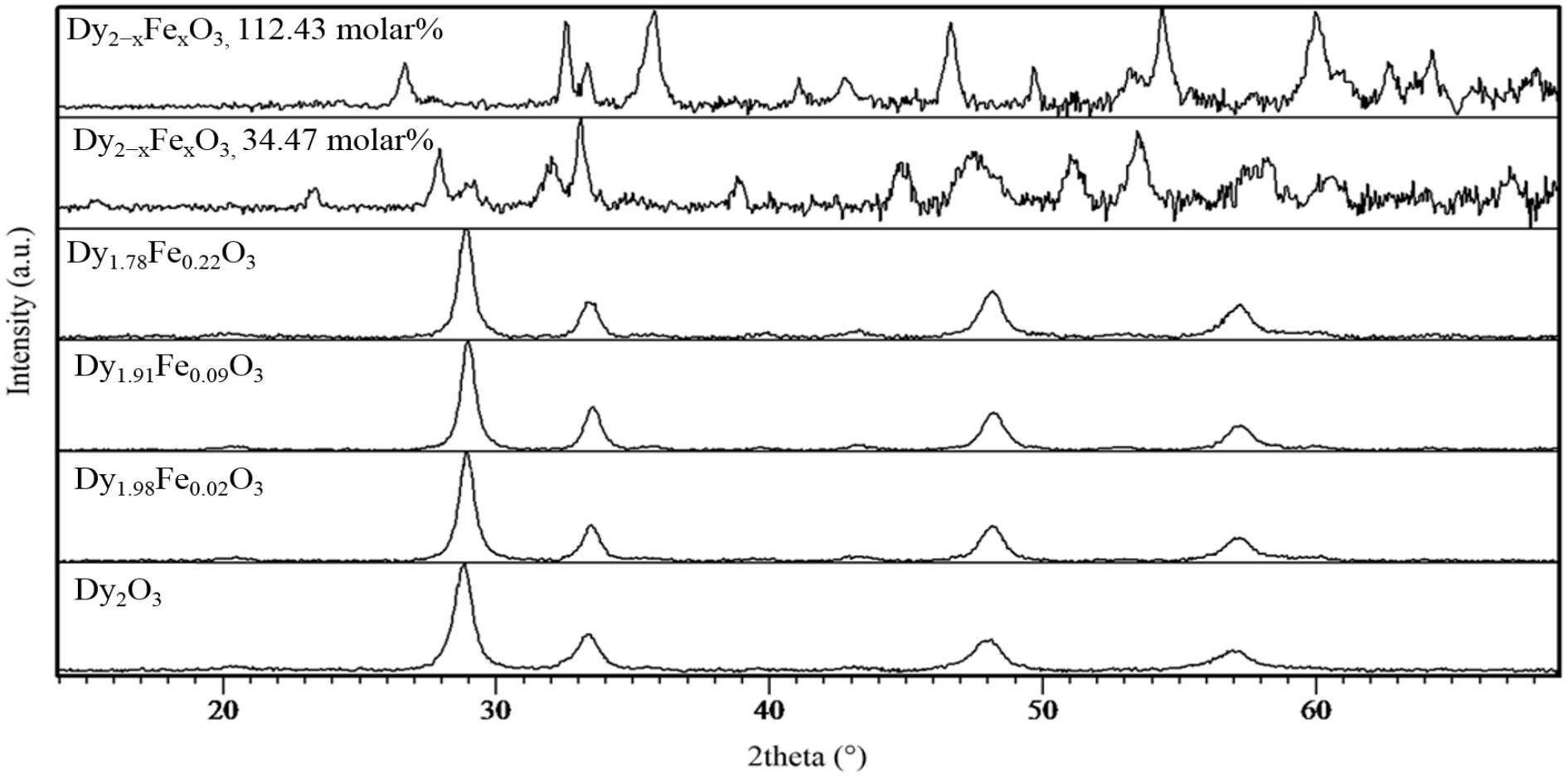

Figure 4-8 PXRD patterns for $Dy_{2-x}Fe_xO_3$ nanoparticle series.

Table 4-7 Particle diameter for the $Dy_{2-x}Fe_xO_3$ nanoparticle series estimated via the Scherrer equation.

Compound	**Particle Diameter (nm) as determined by the Scherrer equation**
Dy_2O_3	10.16
$Dy_{1.98}Fe_{0.02}O_3$	12.20
$Dy_{1.91}Fe_{0.09}O_3$	13.40
$Dy_{1.78}Fe_{0.22}O_3$	13.12

The PXRD patterns (Figure 4-8) for the $Dy_{2-x}Fe_xO_3$ nanoparticle series show diffraction peaks matching those for Dy_2O_3 indicating the prepared nanoparticles have a single phase bixbyite structure for $0 \leq x \leq 0.22$. The compounds with molar percentage of iron of 34.47 % and 112.43 % determined by ICP-AES are not single phase, however the impurities cannot be identified. Further optimisation of the reaction conditions is required to produce single phase nanoparticles containing high molar percentages of iron.

The particle diameters shown in Table 4-7 for the $Dy_{2-x}Fe_xO_3$ nanoparticle series for $0 \leq x \leq 0.22$ have been estimated using the Scherrer equation and show similar particle sizes across the series, ranging between 10.16 – 13.40 nm.

4.3 DISCUSSION

4.3.1 Gd_2O_3 Nanoparticle Series

The synthesis of Gd_2O_3 nanoparticles was achieved by calcination of $Gd(OH)_3$ at both 600 °C and 900 °C. Previously trialled reactions for the preparation of Gd_2O_3 nanoparticles by co-precipitation had been carried out, however resulted in amorphous

material. Due to this preparation of the Gd_2O_3 nanoparticles was pursued *via* the solid state route.

The resulting nanoparticles were characterised by Powder X-ray Diffraction (PXRD). Relaxation measurements measured by both an 11.7T nuclear magnetic resonance (NMR) instrument set up for imaging and a 3T magnetic resonance imaging (MRI) scanner can be found in Chapter 6. The two sets of Gd_2O_3 nanoparticles were prepared as control samples for comparison with the $Gd_{2-x}Fe_xO_3$ and $Gd_{2-x}Mn_xO_3$ nanoparticle series

PXRD patterns for both sets of Gd_2O_3 nanoparticles have diffraction peaks that correspond to the cubic bixbyite Gd_2O_3 structure, similar to that reported by Xiao *et al.*[156] However, diffraction peaks for the particles prepared at 600 °C are asymmetrical indicating the presence of impurities.

The particle size, estimated by the Scherrer equation, indicates that increasing the temperature of the reaction causes an increase in the particle size, from 9.36 nm to 27.4 nm at 600 °C and 900 °C respectively.

4.3.2 $Gd_{2-x}Mn_xO_3$ Nanoparticle Series

A series of $Gd_{2-x}Mn_xO_3$ nanoparticle compounds were prepared by calcination of varying molar ratios of $Gd(OH)_3$ and $MnCl_2$ at 900 °C. This temperature was chosen after trialling reactions at different temperatures, as it was the lowest temperature to produce single phase $Gd_{2-x}Mn_xO_3$ nanoparticles. The nanoparticles were characterised by powder X-ray diffraction (PXRD) and ICP-AES. Relaxation measurements measured by both an 11.7T nuclear magnetic resonance (NMR) instrument set up for imaging and a 3T magnetic resonance imaging (MRI) scanner can be found in Chapter 6.

ICP-AES confirms the presence of Mn^{2+} in all prepared samples, and PXRD patterns indicate single phase nanoparticles were obtained for $0 \leq x \leq 0.21$. For $x > 0.21$ impurities of $Gd(OH)_3$ and Mn_2O_3 were also obtained, again suggesting a solubility limit for the cation doped Gd_2O_3 nanoparticles. Similarly, to the $Gd_{2-x}Fe_xO_3$ nanoparticles, the Mn^{2+} doped Gd_2O_3 nanoparticles also retain the bixbyite structure.

When compared against the $Gd_{2-x}Fe_xO_3$ nanoparticles, greater substitution is achieved with Mn^{2+} than Fe^{3+} ions. This could be due to the higher reaction temperature for this series. Calcination at 600 °C had been attempted for the preparation of $Gd_{2-x}Mn_xO_3$ nanoparticles however, was unsuccessful. The particle size for the $Gd_{2-x}Mn_xO_3$ nanoparticle series ranged from 21.25 nm up to 40.21 nm, much larger than the maximum size obtained for $Gd_{2-x}Fe_xO_3$ nanoparticles at 11.39 nm, and can be explained by the higher reaction temperature causing increased grain growth.

4.3.3 $Gd_{2-x}Fe_xO_3$ Nanoparticle Series

Novel $Gd_{2-x}Fe_xO_3$ compounds were prepared by calcination of varying molar ratios of $Gd(OH)_3$ and $FeCl_3$ at 600 °C. The resulting nanoparticles were characterised by powder X-ray diffraction (PXRD), ICP-AES and Transmission Electron Microscopy (TEM). Relaxation measurements measured by both an 11.7T nuclear magnetic resonance (NMR) instrument set up for imaging and a 3T magnetic resonance imaging (MRI) scanner can be found in Chapter 6.

ICP-AES confirms the presence of $Fe^{2+/3+}$ in all prepared samples, and PXRD patterns indicate single phase nanoparticles were obtained for nanoparticles up to 4.20 molar percent. For molar percentages above 4.20 %, impurities of GdOCl were also obtained, suggesting a solubility limit for the cation doped Gd_2O_3 nanoparticles.

4.3.4 $Dy_{2-x}Fe_xO_3$ Nanoparticle Series

The synthesis of Dy_2O_3 nanoparticles and novel $Dy_{2-x}Fe_xO_3$ nanoparticles was achieved by calcination of varying molar ratios of $Dy(NO_3)_3$ and $FeCl_3$ at 500 °C. The resulting nanoparticles were characterised by powder X-ray diffraction (PXRD) and ICP-AES. Relaxation measurements measured by both an 11.7T nuclear magnetic resonance (NMR) instrument set up for imaging and a 3T magnetic resonance imaging (MRI) scanner can be found in Chapter 6.

ICP-AES confirms the presence of Fe in all prepared samples for $x \neq 0$, and PXRD patterns indicate single phase nanoparticles were obtained for nanoparticles with $0 \leq x \leq 0.22$. Analysis of the PXRD diffraction patterns indicate the diffraction peaks of the prepared $Dy_{2-x}Fe_xO_3$ nanoparticles match those of the cubic Dy_2O_3 bixbyite structure up to $x = 0.22$.[157]

Furthermore, comparison between the $Dy_{2-x}Fe_xO_3$ and $Gd_{2-x}Mn_xO_3$ nanoparticle series suggest similar structural properties, as ICP-AES results for $Gd_{2-x}Mn_xO_3$ show a similar upper limit of stability for the bixbyite structure under Mn substitution, with x= 0.08 before the formation of impurities, which is very similar to that of $Dy_{2-x}Fe_xO_3$ at $x = 0.22$.

However, the estimated particle size for the $Dy_{2-x}Fe_xO_3$ nanoparticle series is reasonably consistent at 10.16 nm (x = 0), 12.20 nm (x = 0.01), 13.40 nm (x = 0.06) and 13.12 nm (x = 0.11), similar to those for the $Gd_{2-x}Fe_xO_3$ nanoparticle series at 9.36 nm (x = 0), 11.39 nm (x = 0.01), 8.57 nm (x = 0.04) and 7.81 nm (x = 0.08).

Due to the different magnetic characteristics of dysprosium and gadolinium however, it would be expected that the magnetic properties of the nanoparticles would be different. This requires further study to be determined.

4.4 CONCLUSIONS

Two novel series of transition metal doped gadolinium oxide nanoparticles, $Gd_{2-x}Fe_xO_3$ and $Gd_{2-x}Mn_xO_3$, have been successfully prepared *via* calcination methods at high temperatures.

In both cases the cubic bixbyite structure was retained, and single phase cation doped Gd_2O_3 nanoparticles were prepared up to 4.20 molar %, for Fe^{3+}, and x = 0.21 for Mn^{2+}.

A novel nanoparticle series of iron doped dysprosium oxide nanoparticles, $Dy_{2-x}Fe_xO_3$, have been successfully prepared *via* calcination methods at 500 °C. For $0 \leq x \leq 0.22$ the cubic bixbyite structure was obtained, and single phase cation doped Dy_2O_3 nanoparticles were prepared.

Further work is required to determine the magnetic properties of these new nanoparticles as well as optimise the reaction conditions to determine the upper limit of cation doping of both the Gd_2O_3 and Dy_2O_3 bixbyite structure.

5 ANION DOPED IRON OXIDE NANOPARTICLES

Successful development of cation modified iron oxide nanoparticles has been achieved on many occasions with a wide range of metal ions. Modification of the chemical composition of iron oxide allows the magnetic properties of the compound to be tuned, targeting a variety of applications, such as drug delivery carriers or contrast agents.[158, 159,22, 136]

Cobalt, nickel, and manganese are just a few of the metal cations that have been used to substitute iron ions and alter the magnetic properties of the material.[43, 48, 50, 141, 160] Anionic substitution is an excellent alternative to cation doping for tuning the properties of inorganic solids and has been widely researched for the modification of electronic properties in superconductors[64, 65, 161, 162] and photocatalysts.[69] However, very little research has been carried out into anion doping of any form of iron oxide, especially the more chemically stable maghemite. To the best of the author's knowledge no anion substitutions in iron oxide nanoparticles have been reported to date. Due to this, little is known about how modification on the anionic site will affect the materials magnetic properties.

^{18}F is well known as a radiolabelling agent for use with imaging techniques such as positron emisssion tomography (PET) and therefore development of a fluorine modified iron oxide nanoparticle could have a potential as a dual MRI/PET probe.[163]

Typical synthetic methods of anionic substitution follow solid state chemistry techniques with a variety of compounds used as the anion source.[70, 164] In the case anionic substitution with fluorine (fluorination), ammonium fluoride, xenon fluoride or copper fluoride are common fluorinating agents. Other methods include the use F_2 gas, PTFE and PVF and for some compounds soft chemistry routes can be applied.[67, 164, 165]

One of the main problems with fluorinating iron oxide nanoparticles is the substitution mechanism between oxygen and fluorine. O^{2-} ions are larger than F^- ions (r = 124 pm and 117 pm respectively) and they show different charges. [67, 164] This means that one of the following mechanisms will occur:

- Substitution of F^- ions with O^{2-} ions in a 1:1 ratio. Due to the difference in charge on the ions some iron cations will reduce oxidation state to compensate for the greater positive charge and maintain the unit cell neutrality.

- Substitution of F^- ions with O^{2-} ions in a 2:1 ratio. This would maintain the charge balance across the unit cell but would cause the unit cell to expand in order to accommodate the F^- ions that do not sit on the oxygen sites and instead may fill interstitial sites.

- Insertion of F^- ions into the interstitial sites of iron oxide lattice. The iron ions will increase oxidation state to compensate for the extra negative charge introduced and the unit cell size will expand to accommodate the extra ions.

The mechanism of fluorination can be controlled to a certain extent by the choice of fluorinating agent and method used.[67]

5.1 EXPERIMENTAL

0.5g of the as prepared γ-Fe_2O_3 was ground in a pestle and mortar with NH_4F powder in different ratios and heated at 250˚C for 8 hours in air. The following ratios were used (NH_4F: γ-Fe_2O_3)1:1, 2:1, 3:1.

Powder X-ray diffraction patterns were collected on a Siemens D5000 Diffractometer with Cu $K_{\alpha 1}$ radiation (1.54 Å) at 30 mA, 40 kV with a step size of 0.02 degrees 2 theta and a 0.5 ° fixed divergence slit.

Surface coating

The nanoparticles were dispersed in an aqueous solution of hydrochloric acid at pH 4, and citric acid added in a 1:1.2 $Fe_2O_{3-x}F_{2x}$: citric acid molar ratio. The mixture was stirred for 2 hours before magnetic decantation and the collected nanoparticles were washed with deionised water and the pH adjusted to pH 7. These solutions were then used for MRI and NMR measurements.

5.2 RESULTS

PXRD of the fluorinated compounds (Figure 5-1) show reflections corresponding to γ-Fe_2O_3 as well a gradual rise in impurities as the ratio of NH_4F:Fe_2O_3 is increased. These impurities can be assigned to hematite, α-Fe_2O_3, the high temperature polymorph. The γ-Fe_2O_3 to α-Fe_2O_3 transformation is well-documented, however is usually expected at temperatures much above 250˚C. These finding suggest that increasing amounts of NH_4F present in the reactions promotes hematite formation. A shift of the diffraction peaks to lower 2 theta angles is seen in the PXRD patterns between the three fluorinated samples as the NH_4F:Fe_2O_3 ratio increases.

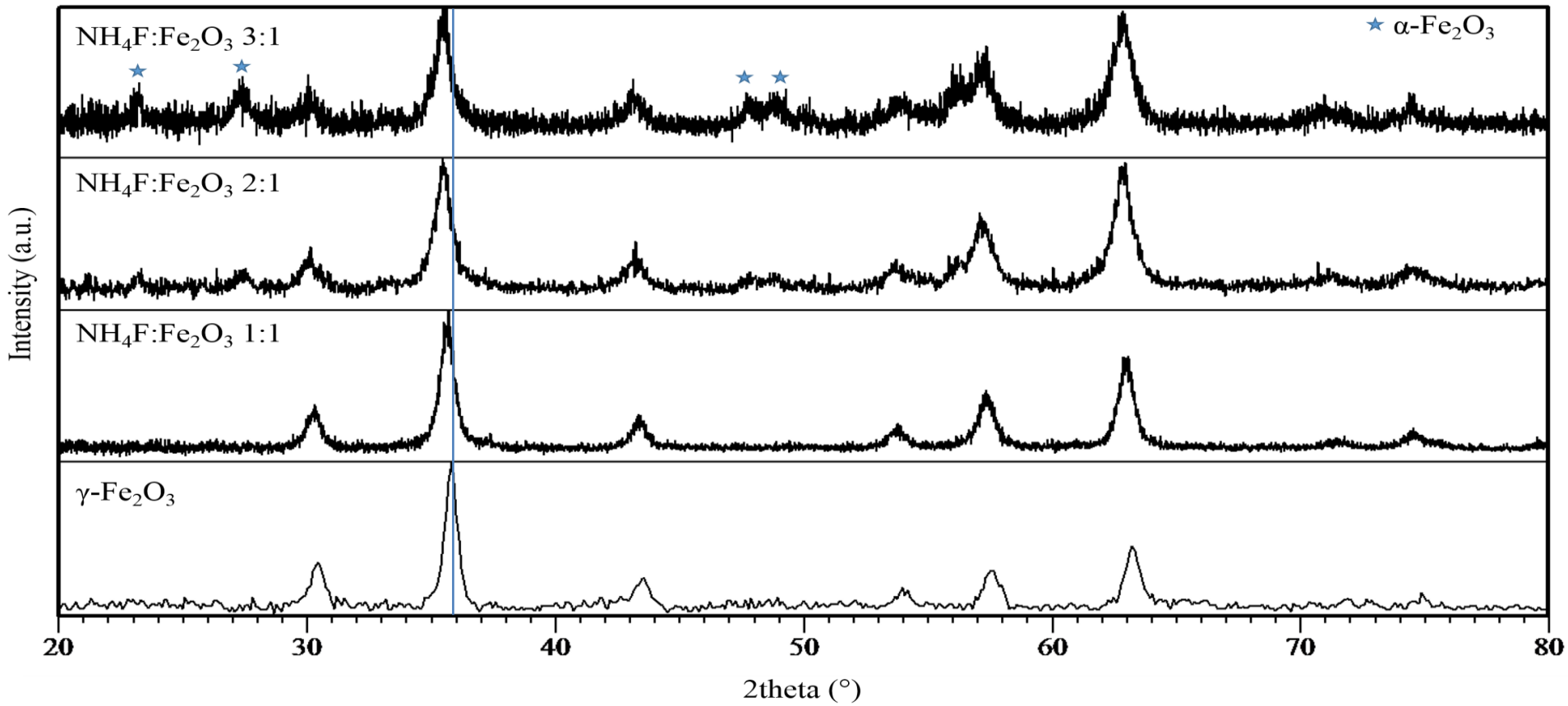

Figure 5-1 PXRD patterns for fluorinated iron oxide nanoparticles with increasing fluoride content. The blue line highlights the shift of the reflections towards lower 2 theta angles with increasing fluoride content.

TEM analysis (Figure 5-2) shows both the spherical γ-Fe_2O_3 and plate-like hematite structures are present in the samples with higher ratios of ammonium fluoride. It is not possible to determine the particle size from the TEM images due to particle agglomeration.

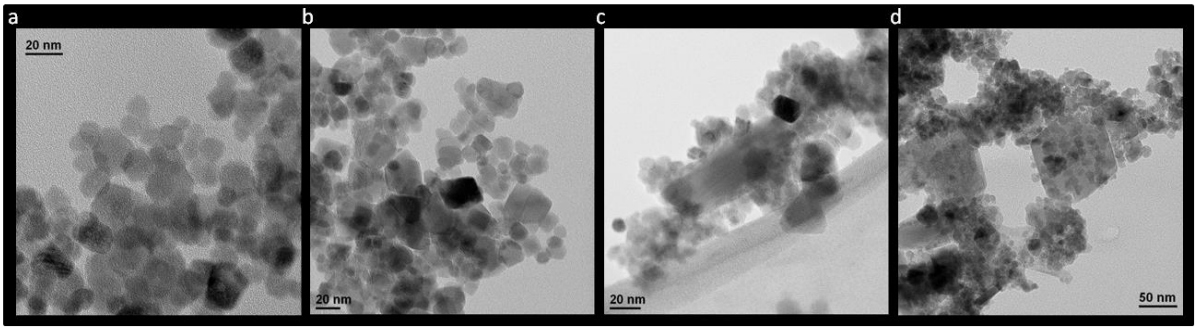

Figure 5-2 TEM images of a) maghemite nanoparticles and Fe_2O_3 nanoparticles reacted with NH_4F in the following ratios b) 1:1 c) 2:1 d) 3:1.

SEM-EDX analysis can be seen in Table 5-1. The weight percentage of fluorine in the nanoparticles increases from 7.47 % up to 33.34 % as the ratio of NH_4F:Fe_2O_3 increases. This suggests fluorine was successfully inserted into the structure. Additionally, the wt% of oxygen decreases as the NH_4F:Fe_2O_3 ratio increases. Furthermore, the graph presented in Figure 5-3 shows that the wt% of fluoride ions in the nanoparticles increases linearly at double the rate that the wt% of oxygen ions decreases, shown by the gradient for fluoride insertion at 6.39 compared to the gradient of oxygen loss at 12.94.

Table 5-1 Elemental analysis results by SEM-EDX.

Sample	**Fe (wt%)**	**O (wt%)**	**F (wt%)**
1:1 NH_4F:Fe_2O_3	58.43	29.87	7.47
2:1 NH_4F:Fe_2O_3	50.99	22.49	21.81
3:1 NH_4F:Fe_2O_3	43.81	17.09	33.34

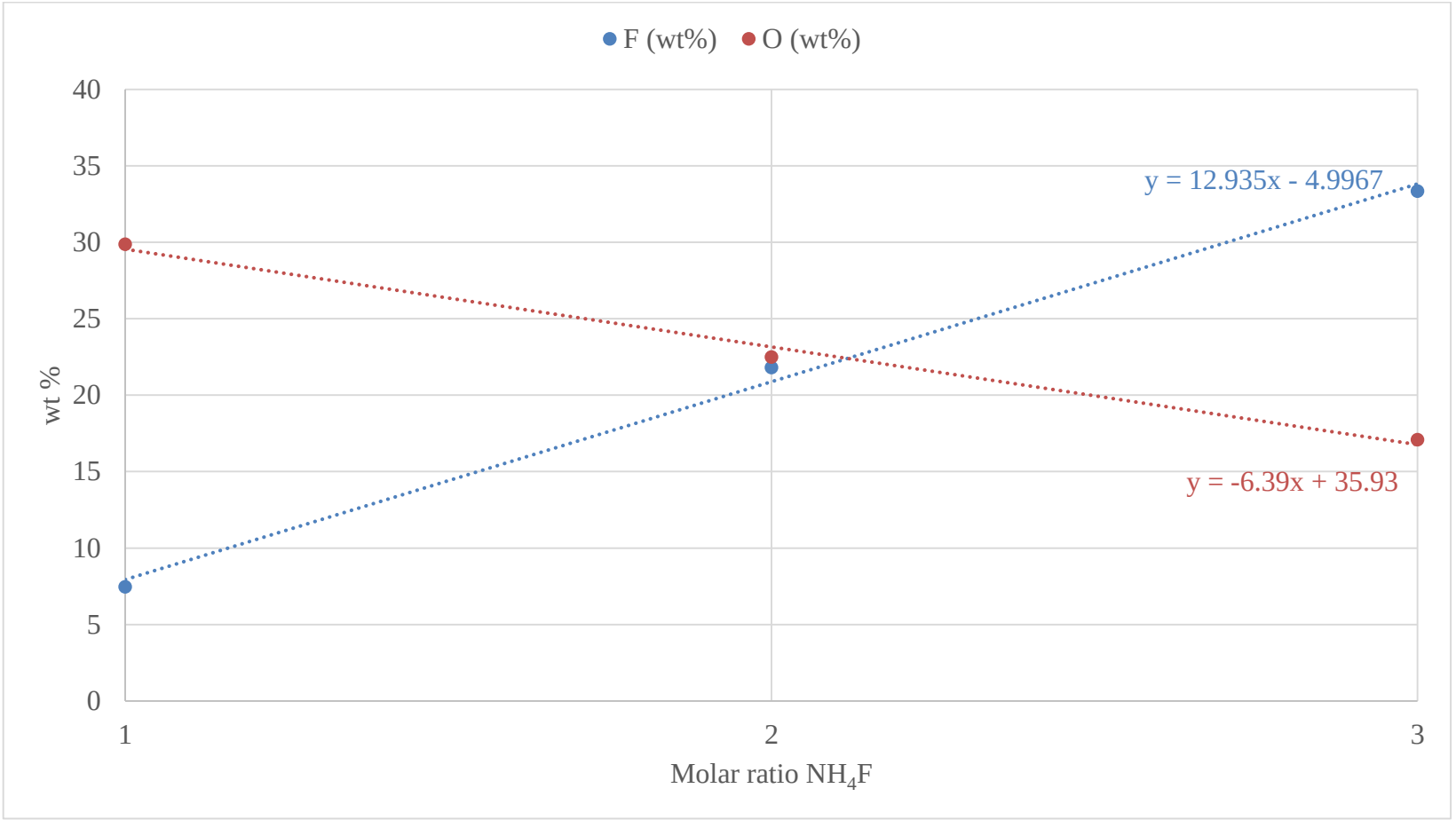

Figure 5-3 Graph showing the change of oxygen and fluorine content for increasing excess' of fluorinating agent.

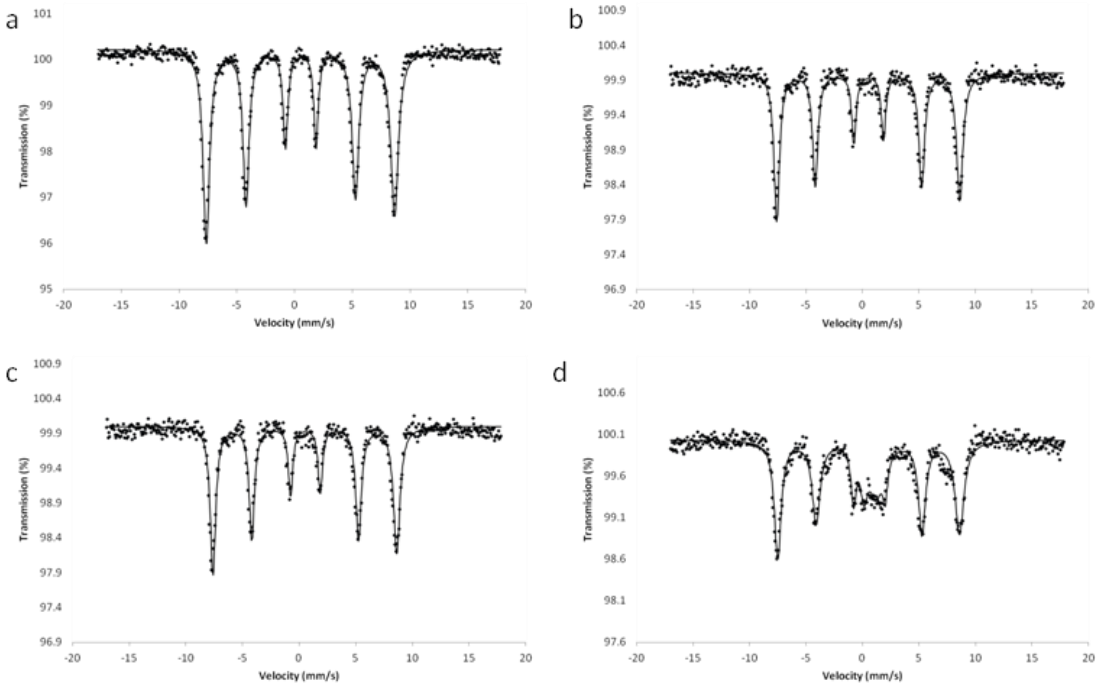

Figure 5-4 Mössbauer spectra for the fluorinated iron oxide nanoparticle series at 80 K of a) maghemite nanoparticles, and Fe_2O_3 nanoparticles reacted with NH_4F in the following ratios b) 1:1 c) 2:1 d) 3:1.

Figure 5-4 shows the Mössbauer spectra for the 3 nanoparticle compounds prepared. For the 1:1 NH_4F:γ-Fe_2O_3 ratio at 80 K, a sextet is observed, matching the spectrum typically seen for γ-Fe_2O_3. As the ratio increases, additional peaks can be seen around 0 mm/s and can be associated with the formation of hematite, α-Fe_2O_3.

5.3 DISCUSSION

The PXRD data shows that the predominant phase in all cases is spinel maghemite, with impurities appearing at higher NH_4F:γ-Fe_2O_3 ratios. Additionally there is a shift in the diffraction peak positions to lower 2 theta angles, indicating an increase in the unit cell size. This can be accounted for by the EDX data which shows increasing amounts of

fluorine present in the compounds as the ratio increases. Figure 5-3 shows that there is a correlation between oxygen loss and fluorine insertion, with twice as much fluorine inserting per oxygen lost. This will maintain charge neutrality across the unit cell, and will cause an increase in unit cell size as indicated by the PXRD data in Figure 5-1.

With this mechanism in mind it is then possible to determine a general formula for the family of compounds, in the form of $Fe_2O_{3-x}F_{2x.}$ Furthermore, the actual formula for 2:1 NH_4F:γ-Fe_2O_3 can be calculated at $Fe_2O_{2.7}F_{0.66}$. Calculating the actual formula for the remaining samples is difficult due to unquantifiable amounts of hematite present in each sample.

The relaxivity data for $Fe_2O_{3-x}F_{2x}$ is shown in Chapter 6. Substitution of oxygen with fluorine in iron oxide nanoparticles has a large impact on both T_1 and T_2 relaxation properties. The results indicate these nanoparticles are excellent T_2 contrast agents at 3 T, and exhibit high T_2 relaxation rates at 11.7 T, showing their potential for use as MRI contrast agents at high magnetic field strengths.

5.4 CONCLUSION

Fluoride doped maghemite nanoparticles with a size range of 12-18 nm have been successfully prepared through solid state reactions of maghemite nanoparticles and ammonium fluoride in varying ratios. Mössbauer spectroscopy and PXRD patterns indicated the spinel type unit cell was maintained after fluorination, with the most likely mechanism a 2:1 fluoride ion:oxygen ion substitution. Formation of hematite occurred in samples with a higher ratio of ammonium fluoride at much lower temperatures than previously reported and further investigation into this needs to be carried out. SEM-EDX

data supports the 2:1 substitution mechanism with a general formula determined as $Fe_2O_{3-x}F_{2x}$, and the exact stoichiometry has been calculated at $Fe_2O_{2.7}F_{0.66}$ for 2:1 NH_4F:γ-Fe_2O_3 prepared by solid state reaction.

6 SURFACE FUNCTIONALISATION OF NANOPARTICLES

Surface functionalisation of nanoparticles improves their stability under physiochemical conditions, reduces toxicity and enables the evasion of the reticuloendothelial system resulting in longer circulation times *in vivo*.

According to literature two of the most common ways to coat iron oxide nanoparticles involves using either polysaccharides such as dextran, or long chain polymers such as polyethylene glycol (PEG). PEG has been closely studied due to its potential to enhance the relaxation properties of the particle it is bound to. It is available with a variety of chain terminations, allowing further conjugation to targeting agents to be carried out.[166, 167]. An alternative functionalising agent, citric acid, $C_6H_8O_7$, is a small chain organic acid that can be used to functionalise the surface of nanoparticles to improve their hydrophillic properties. [41, 88, 103, 168-174]

All three materials were studied as possibilities for surface functionalisation of the nanoparticles prepared in this work.

6.1 EXPERIMENTAL

6.1.1 Simultaneous co-precipitation and functionalisation of nanoparticles:

$FeCl_3$ and dextran/ PEG-MEMA/ citric acid was added to 50 mL ethylene glycol and stirred until homogenous. $FeCl_2$ was added and the mixture heated to 80°C. 5M NaOH was added dropwise until pH 10 was reached and the temperature was increased to 120°C. After stirring for 2 hours the precipitate was collected magnetically and redispersed in water and stirred for an hour. This washing step was repeated 3 times to remove any excess functionalising agent.

6.1.2 Surface functionalisation post synthesis:

Dextran M_r~6000 was used to coat pre-prepared nanoparticles by stirring the nanoparticles with dextran solution for 2 hours at room temperature.

6.1.3 Surface functionalisation post synthesis with sonication:

Dextran M_r~6000 was used to coat pre-prepared nanoparticles by stirring the nanoparticles with dextran solution for 2 hours at room temperature, followed by sonication for 30 minutes.

6.1.4 Post synthesis surface functionalisation using citric acid solution

25 mL of 0.25 M solution of citric acid aqueous solution was added to 0.005225 moles of γ-Fe_2O_3 nanoparticles and stirred for 2 hours. The particles were then collected magnetically and washed before drying in an oven.

Characterisation will be carried out by FTIR spectroscopy and TEM imaging.

6.2 RESULTS

FTIR spectroscopy will be used to determine whether the coating agent is present on the surface of the nanoparticles and TEM will indicate whether the particles have been coated individually in a core-shell approach or whether a cluster of nanoparticles have been coated together (Figure 6-1).

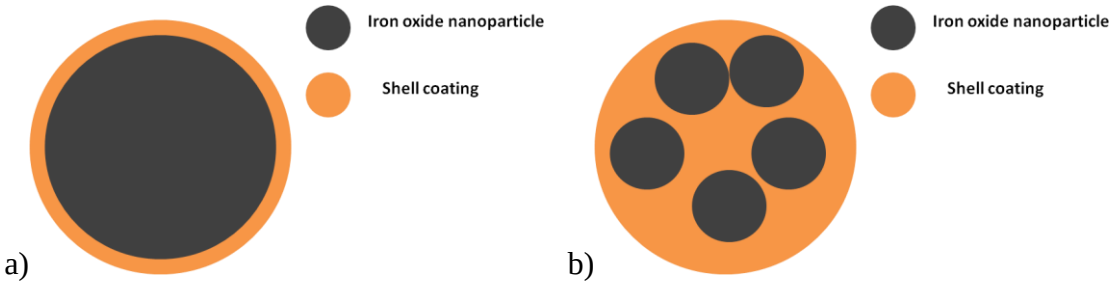

Figure 6-1 a) each nanoparticle is coated individually. b) Multiple nanoparticles are coated together making one large particle.

Initially, the surface functionalisation was investigated using PEG, dextran and citric acid, by precipitating the nanoparticles directing in the presence of the functionalising agent (6.1.1).

It was found that for the nanoparticles coated with dextran Mr ~6000, the coating tended to encapsulated multiple nanoparticles rather than functionalise singular particles, see Figure 6-2.

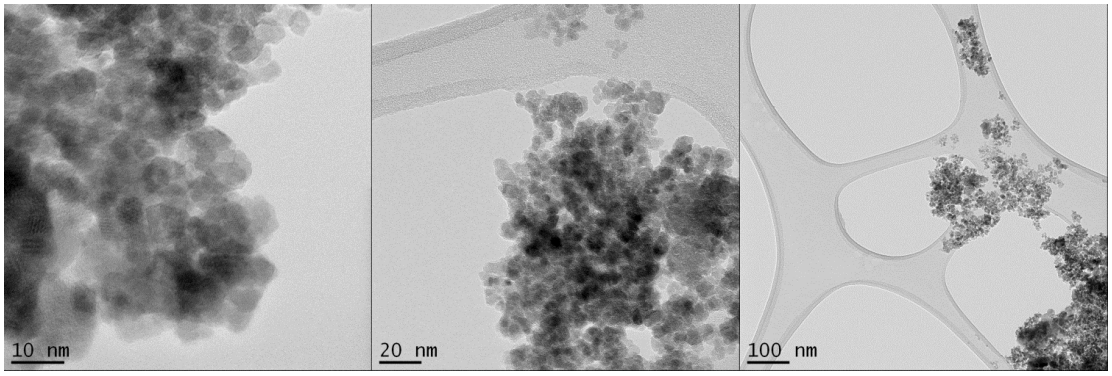

Figure 6-2 TEM images for nanoparticles coated with Dextran Mr~6000 in-process

The FTIR spectrum (Figure 6-3) for the uncoated iron oxide nanoparticles has absorption peaks at 3445 cm^{-1} due to -OH stretching, and 1652 cm^{-1} due to H-O-H bending, most likely from residual moisture on the surface. The absorption band at 2335 cm^{-1} can be associated with -CH stretching. [168, 175]

The dextran functionalised iron oxide nanoparticle FTIR spectrum shows the same absorption bands at 3445 cm^{-1} and 2335 cm^{-1}, however a shift to lower wavenumbers is seen for the -OH band, at 1615 cm^{-1}. [168, 175]

The two spectra are very similar and the absence of any peaks associated with the C-O-C glycoside linkage, suggests dextran has not grafted to the surface of the nanoparticle effectively. This also explains the high degree of agglomeration seen in the TEM images above.

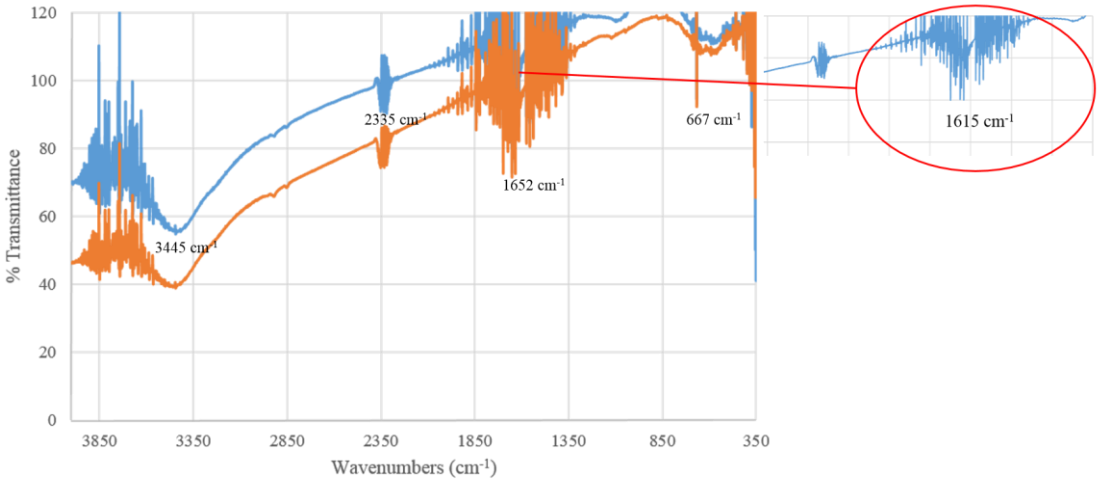

Figure 6-3 FTIR spectra of uncoated γ-Fe_2O_3 nanoparticles (Orange), and dextran coated γ-Fe_2O_3 nanoparticles (blue), prepared by the method described in 6.1.1.

By increasing the amount of dextran Mr~6000 in the starting solution, two things happen. The first is the formation of very small particles, approx. 2-3 nm and the second is the formation of larger particles or agglomerated particles around 10 nm diameter. The TEM (Figure 6-4) shows good dispersion of these nanoparticles.

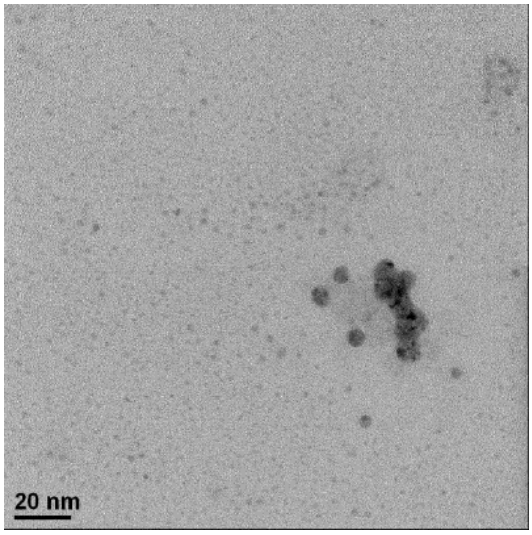

Figure 6-4 TEM image of nanoparticles functionalised using dextran Mr~6000

Nanoparticles functionalised with poly ethylene glycol methyl ether methacrylate (PEG-MEMA). The TEM images shown in Figure 6-5 show very agglomerated nanoparticles that are < 20 nm. However, due to the agglomeration the exact size cannot be determined. In comparison to the dextran Mr~6000 functionalised nanoparticles this method appears to produce less uniform, more agglomerated particles.

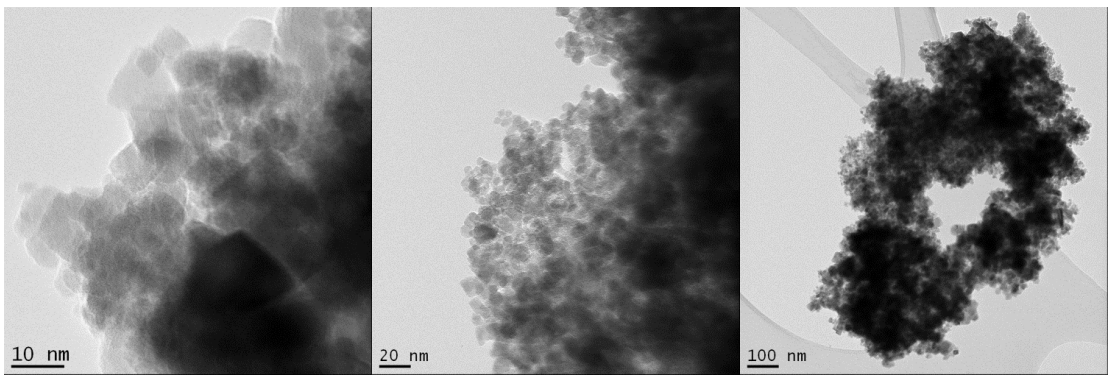

Figure 6-5 TEM images for PEG-MEMA coated γ-Fe_2O_3 nanoparticles in process

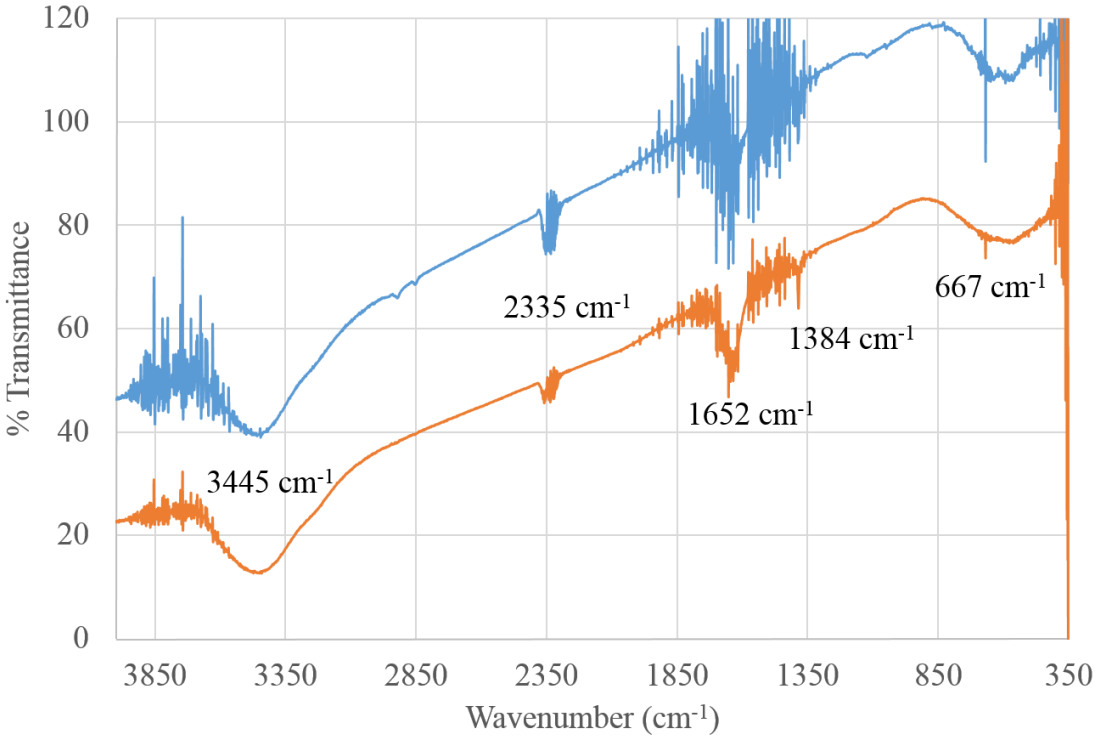

Figure 6-6 FTIR spectra of uncoated γ-Fe_2O_3 nanoparticles (blue), and PEG coated γ-Fe_2O_3 nanoparticles (orange), prepared by the method described in 6.1.1

The FTIR spectra for the both the uncoated iron oxide nanoparticles (blue) and the PEG-MEMA coated nanoparticles (orange) have absorption peaks at 3445 cm^{-1} due to -OH stretching, and 1652 cm^{-1} due to H-O-H bending, again most likely from residual moisture on the surface. The absorption band at 2335 cm^{-1} can be associated with -CH stretching. [168, 175]

The two spectra are very similar and the absorbance in the-CH stretching frequency is almost identical, indicating that PEG may not have attached to the surface of the nanoparticle during the functionalisation process.

The TEM images for the nanoparticles produced under the conditions described in section 6.1.1 are shown in Figure 6-6. The particles are reasonably well separated compared to the results from previous surface functionalization methods, and show almost uniform,

spherical nanoparticles less than 20 nm diameter. Due to the close proximity of the nanoparticles, measurement of the particle size is difficult.

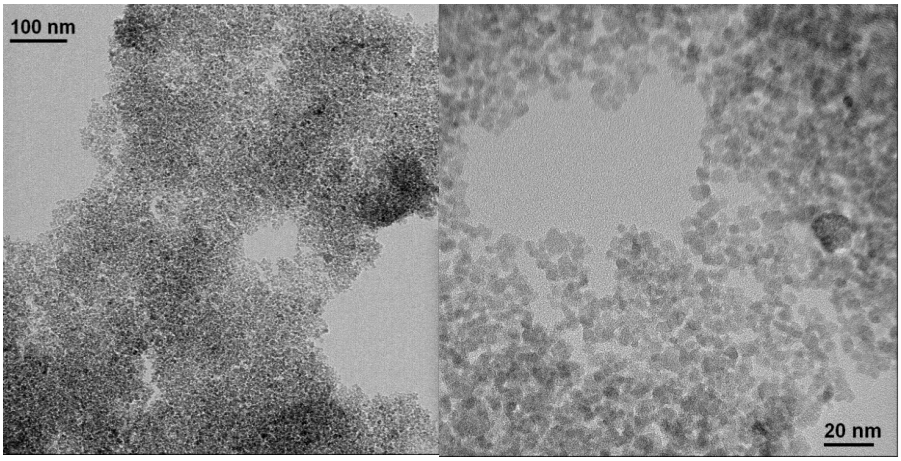

Figure 6-7 TEM images of citric acid functionalised γ-Fe_2O_3 nanoparticles prepared by the method described in 6.1.1

As these results have shown, the best coating method to provide the least agglomerated nanoparticles has been in-process coating with citric acid. However, some of the nanoparticles that been prepared via calcination instead of co-precipitation cannot benefit from this coating technique. Therefore, other methods were investigated that could be applied to the nanoparticles post-synthesis.

Firstly, dextran M_r~6000 was used to coat pre-prepared nanoparticles by stirring the nanoparticles with dextran solution (6.1.2). The resulting TEM images show lots of small particles clumped together. There are multiple small agglomerates instead of one large agglomerate as previously observed with other techniques, suggesting that the dextran functionalization does aid in the dispersion of the particles. Unfortunately, this method does not separate individual particles.

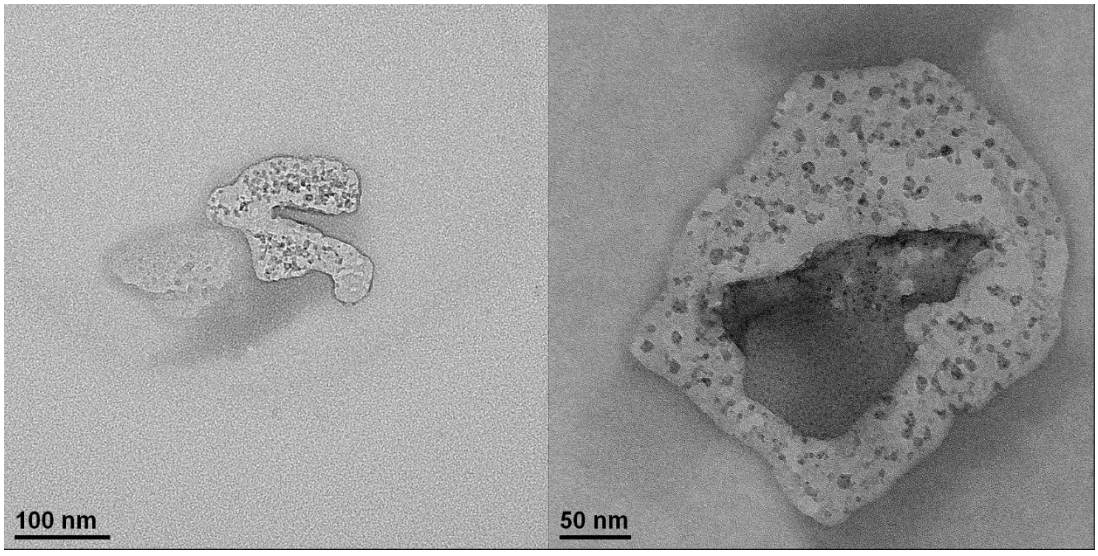

*Figure 6-8 TEM images for nanoparticles prepared according to the method described in 6.1.2**Error! Reference source not found.**.*

However, when this method is followed by sonication, more homogeneously coated nanoparticles are produced (6.1.3).

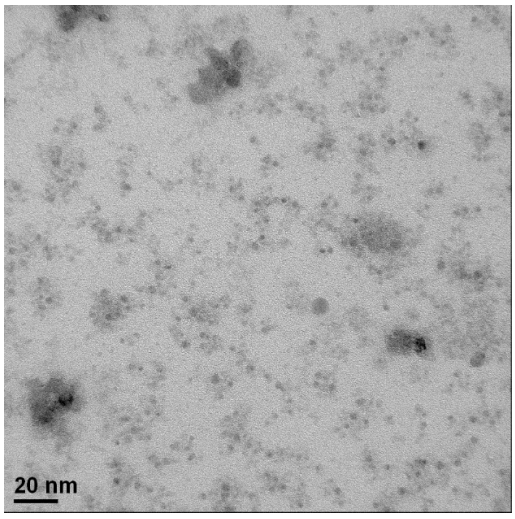

Figure 6-9 TEM images of particles coated with dextran Mr~6000 post synthesis

A similar approach was tested with citric acid, as detailed in 6.1.4. The TEM images show reasonable separation of individual particles by this method (Figure 6-10).

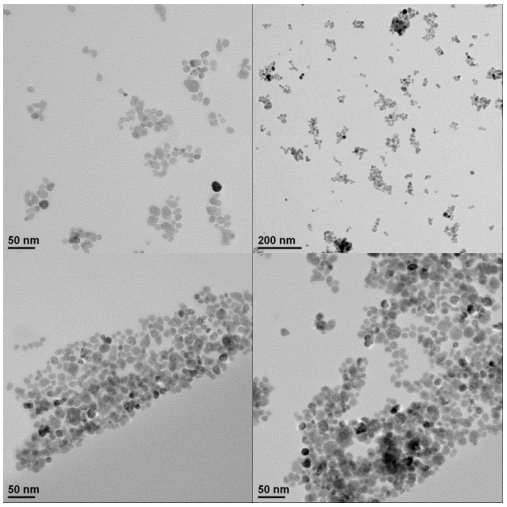

Figure 6-10 TEM images of particles coated with citric acid as described in 6.1.4

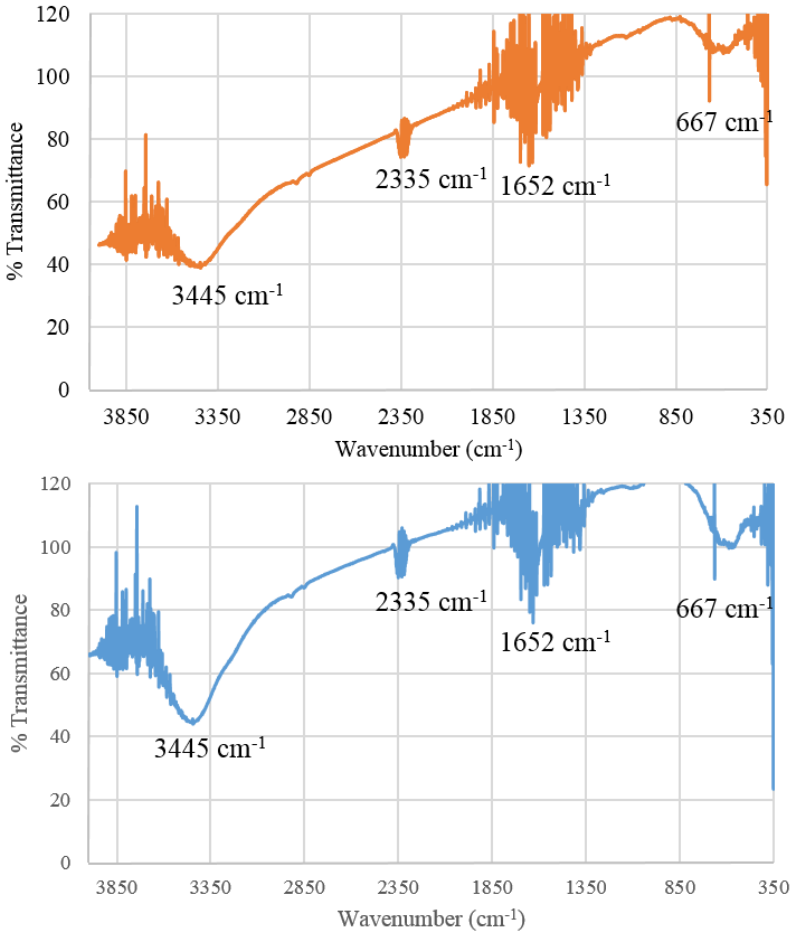

Figure 6-11 FTIR spectra of uncoated iron oxide nanoparticles (orange) and citric acid coated iron oxide nanoparticles (blue), prepared by the method as described in 6.1.4

The FTIR spectra shown in Figure 6-9, once again show similar absorption peaks relating to -OH stretching (3445 cm^{-1}), H-O-H bending (1652 cm^{-1}) and -CH stretching (2335 cm^{-1}).[168, 175] However, in this case the -OH band is stronger and broader indicating an increased presence of -OH associated with carboxylic acid groups, such as those present in citric acid.

In conjunction with the TEM images, this result suggests successful coating of the nanoparticles with citric acid.

6.3 FUNCTIONALISED NANOPARTICLE STABILITY

The stability of these nanoparticles in an aqueous environment was studied. The nanoparticles were initially completely suspended in water, however after 10 minutes the particles started aggregating and settling out of solution (Figure 6-10). To improve this suspension time, the pH at which the functionalisation step occurred was adjusted.

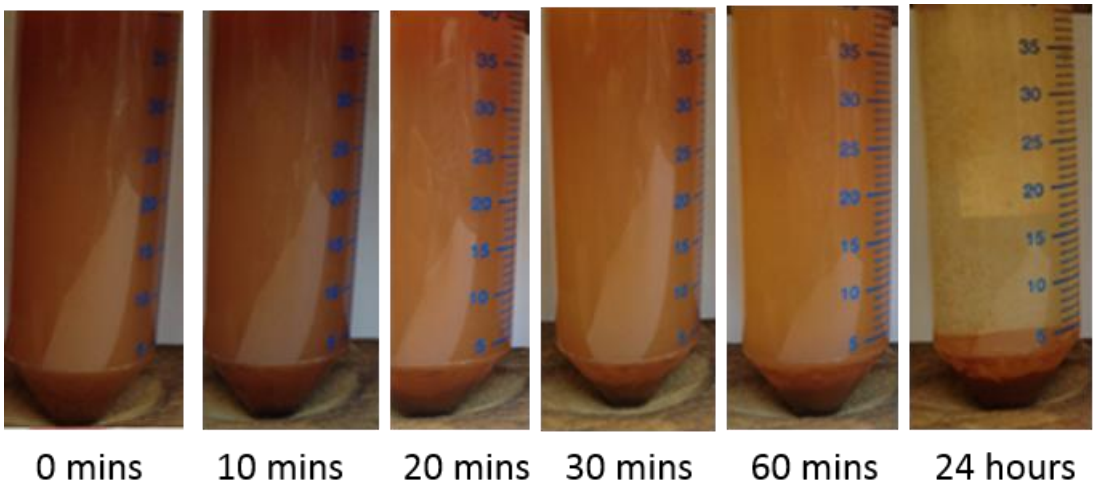

Figure 6-12 Aqueous suspensions of citric acid coated γ-Fe_2O_3

Solutions were prepared at pH 3,4, 5 and 6. It was found that adding the functionalising agent, citric acid, to an aqueous solution of nanoparticles at pH 4 gave the most stable suspension, when re-dispersed in a pH 7 aqueous solution after coating (Figure 6-11).

Therefore, this method was applied to all nanoparticles prior to characterisation by NMR and MRI

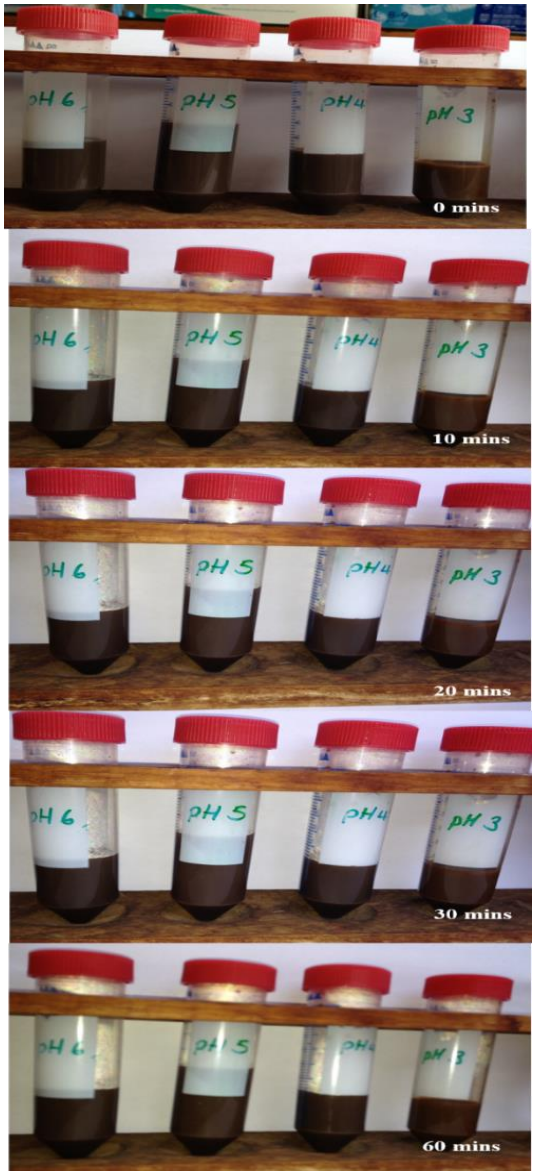

Figure 6-13 Aqueous suspensions of γ-Fe_2O_3 coated with citric acid, prepared at different pH.

7 APPLICATION OF MATERIALS AS MRI CONTRAST AGENTS

In Chapters 3, 4 and 5 the synthesis of cation substituted γ-Fe_2O_3, Gd_2O_3, and Dy_2O_3 and anion doped γ-Fe_2O_3 solid solution nanoparticles was described. In addition to the pure metal oxide nanoparticles, seventeen new, single phase compounds have been prepared based around the general formulae $Fe_{2-x}Gd_xO_3$, $Fe_{2-x}Dy_xO_3$, $Gd_{2-x}Mn_xO_3$, $Gd_{2-x}Fe_xO_3$, $Dy_{2-x}Fe_xO_3$ and $Fe_2O_{3-x}F_{2x}$. All solid solution nanoparticles have been functionalised with citric acid to improve the hydrophilic and biocompatibility properties.

Current clinical magnetic field strengths for MRI are 1.5 T or 3 T, however there is a trend towards the use of higher magnetic field strengths to improve image detail and signal sensitivity. The longitudinal relaxivity of nanoparticles typically decreases at higher magnetic field strengths due to the difference between the resulting tumbling rate and the larmor frequency.[176] Additionally, T_1 relaxation rates are affected by particle diameter, typically decreasing at higher magnetic field strengths. This is due to the decrease in surface:volume ratio.[177]

The next stage of this research is to determine the efficacy of the prepared nanoparticles as MRI contrast agents.

7.1 EXPERIMENTAL

A series of aqueous suspensions were prepared for each compound at concentrations of 0.1 mM, 0.2 mM, 0.3 mM, 0.4 mM and 0.5mM. Each solution was sonicated for 30 minutes before relaxivity measurements were made at 3 T and 11.7 T field strengths.

For Gd_2O_3 nanoparticles, aqueous solutions at concentrations of 1 mM, 2 mM, 3 mM, 4 mM and 5 mM were prepared for the relaxivity measurements at 11.7 T. Different concentrations were required at different field strengths in order to observe a strong signal during MRI measurements.

7.2 RESULTS

In order to determine the performance of the nanoparticles as MRI contrast agents, relaxivity measurements were made and are shown below. The sections are divided into the three 'host' lattices, followed by a section dedicated to each type of cation or anion doped metal oxide nanoparticle.

In each case, the relaxation time of the compound was measured over a range of concentrations. From this data a graph could be plotted; the gradient of which is the relaxivity value of the compound (r_1 or $r_{2)}$, measured in $mM^{-1}s^{-1}$. The graphs are shown for a few example compounds (Figure 7-1 to Figure 7-4) in order to illustrate the process, with the remaining graphs are shown in appendix II. The complete set of relaxivity data is shown in Table 7-1 through to Table 7-11.

7.2.1 Fe_2O_3, Gd_2O_3 and Dy_2O_3 nanoparticle relaxivity

Figure 7-1 shows the r_1 and r_2 relaxivity for γ-Fe_2O_3 nanoparticles prepared by the co-precipitation technique described in Chapter 3. Relaxation measurements were carried out at 3 T across 5 concentrations resulting in an r_1 of 0.52 $mM^{-1}s^{-1}$ and an r_2 of 8.14 $mM^{-1}s^{-1}$. However, the reliability of the latter r_2 value is poor, due to the poor fit of the trend line, from which the relaxivity value is taken, to the data.

At 11.7 T, the r_1 and r_2 values are 3.19 $mM^{-1}s^{-1}$ and 11.44 $mM^{-1}s^{-1}$ per γ-Fe_2O_3 particle. These are both higher than the r_1 and r_2 values obtained at 3 T suggesting the magnetisation saturation point is not reached at the lower field strength of 3 T.

The relaxivity data for Gd_2O_3 nanoparticles are shown in Figure 7-2 and Figure 7-3. For these nanoparticles the data has been presented both by concentration of Gd_2O_3 and by concentration of Gd^{3+} ions. This allows easier comparison with literature relaxivity values for both nanoparticle type contrast agents as well as chelate complex based contrast agents.

Figure 7-2 shows the relaxivity data for Gd_2O_3 nanoparticles measured as a function of Gd^{3+} ion concentration. At 3 T, lower concentrations were sufficient to yield T_1 and T_2 relaxation times, however at 11.7 T the concentration needed to be higher in order to register a signal.

The r_1 and r_2 values obtained at 3 T were 1.69 $mM^{-1}s^{-1}$ and 2.85 $mM^{-1}s^{-1}$ respectively. Increasing the field strength to 11.7 T yielded r_1 and r_2 relaxivities of 0.74 $mM^{-1}s^{-1}$ and 1.79 $mM^{-1}s^{-1}$ respectively. In contrast to the results for the T_2 classified γ-Fe_2O_3 nanoparticles, both the relaxivity values for the Gd_2O_3 nanoparticles decreased by more than 30 %. As would be expected, the same trend is observed for the relaxivity values based on the concentration of Gd_2O_3. The r_1 and r_2 values at 3 T are 3.38 $mM^{-1}s^{-1}$ and 5.70 $mM^{-1}s^{-1}$ respectively. At 11.7 T, the r_1 and r_2 values are 1.49 $mM^{-1}s^{-1}$ and 3.58 $mM^{-1}s^{-1}$ respectively.

The third parent metal oxide compound studied was Dy_2O_3 nanoparticles. Similarly to Gd_2O_3 different concentrations were required for 3 T and 11.7 T measurements. At 3 T, r_1 and r_2 relaxivities were 0.82 $mM^{-1}s^{-1}$ and 4.36 $mM^{-1}s^{-1}$respectively (Figure 7-4). In

comparison to Gd_2O_3 nanoparticles the r_1 is much lower, but can be attributed to Dy^{3+} ions having a predominant T_2 effect. Increasing the field strength to 11.7 T roughly triples the r_1 relaxivity to 2.62 $mM^{-1}s^{-1}$ and doubles the r_2 relaxivity, to 8.27 $mM^{-1}s^{-1}$.

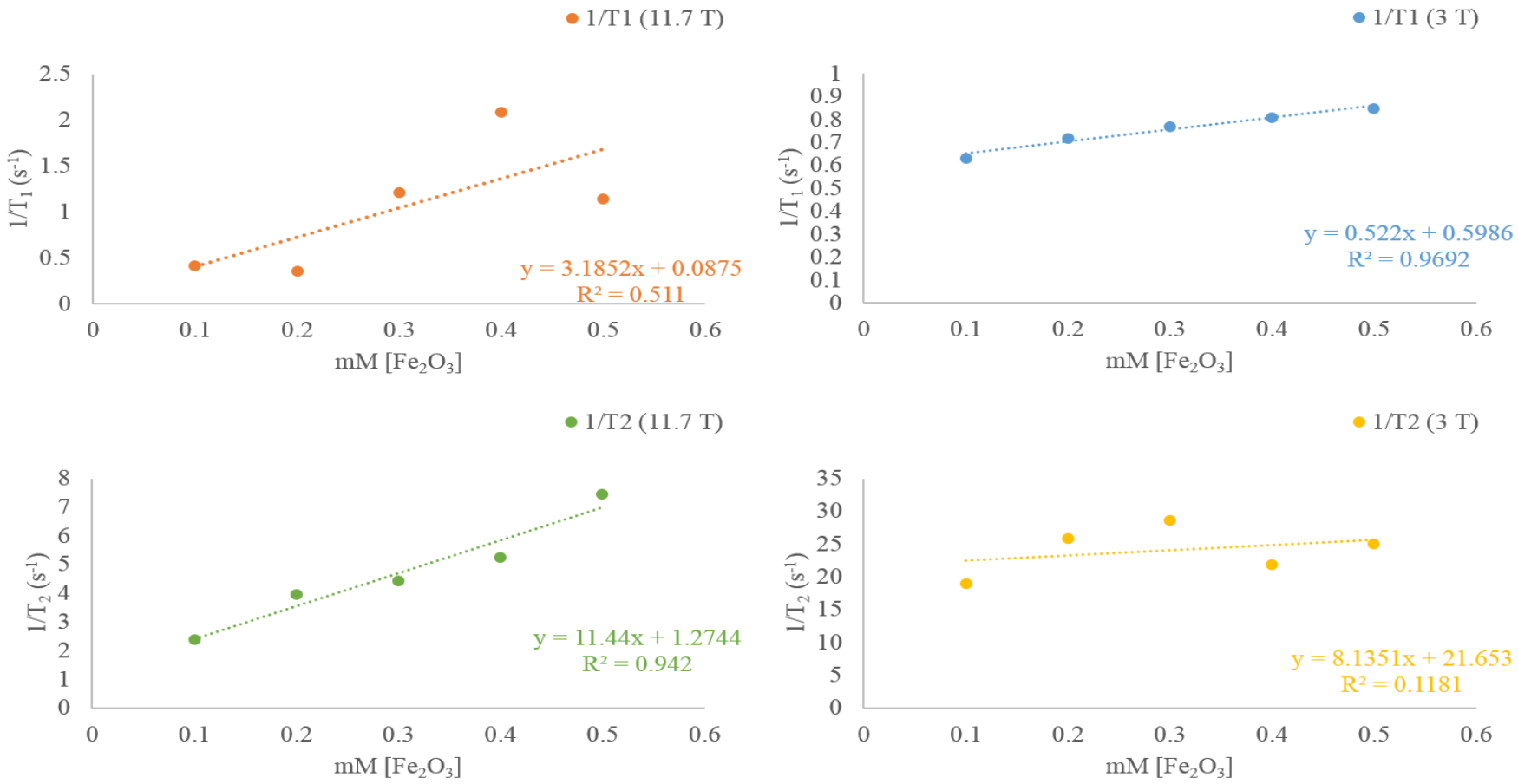

Figure 7-1 T_1 and T_2 relaxation rates per mmol of γ-Fe_2O_3 nanoparticles at 3 T and 11.7 T magnetic field strengths.

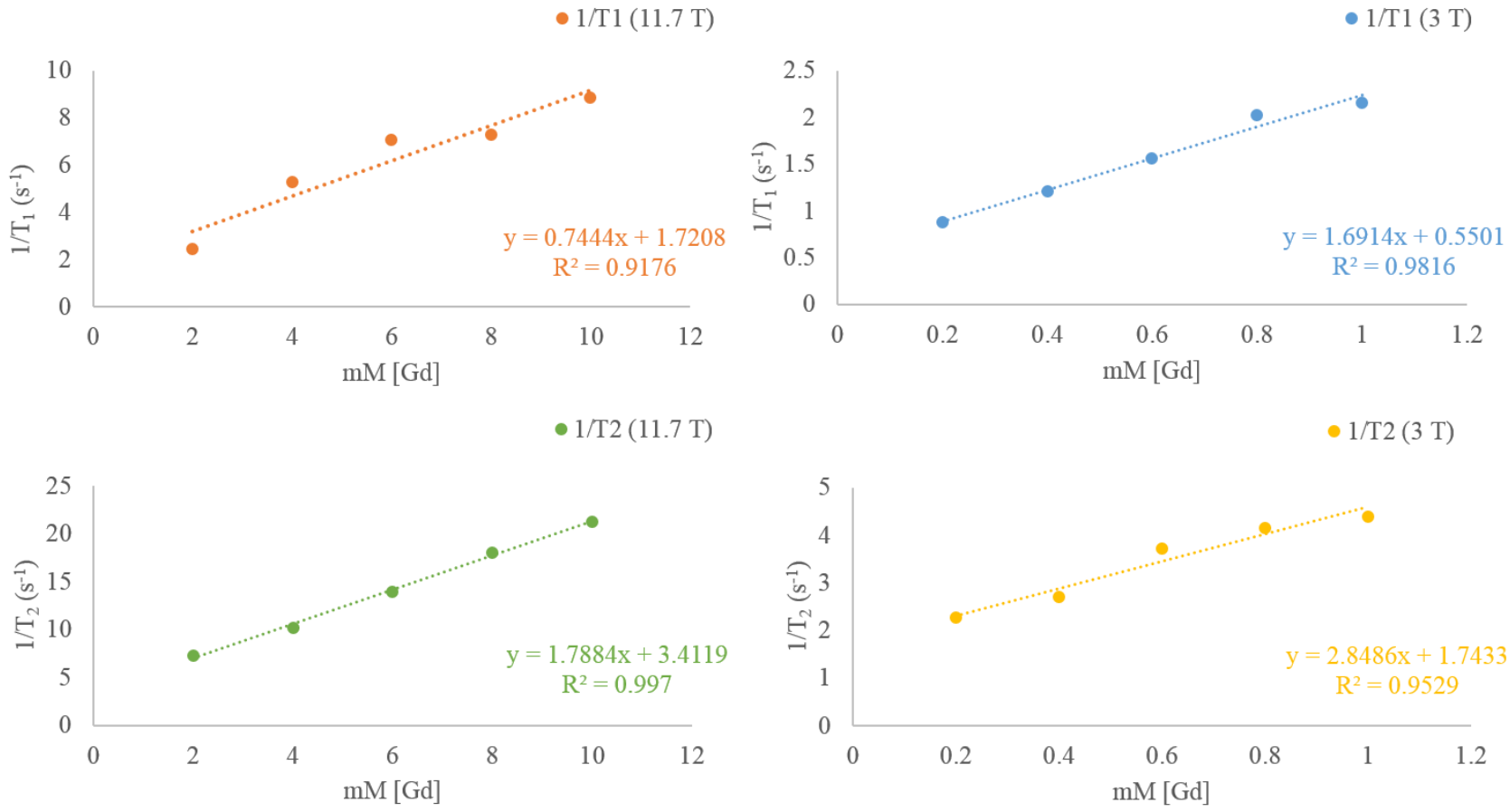

Figure 7-2 T_1 and T_2 relaxation rates per mmol of Gd^{3+} ions in Gd_2O_3 nanoparticles at 3 T and 11.7 T magnetic field strengths.

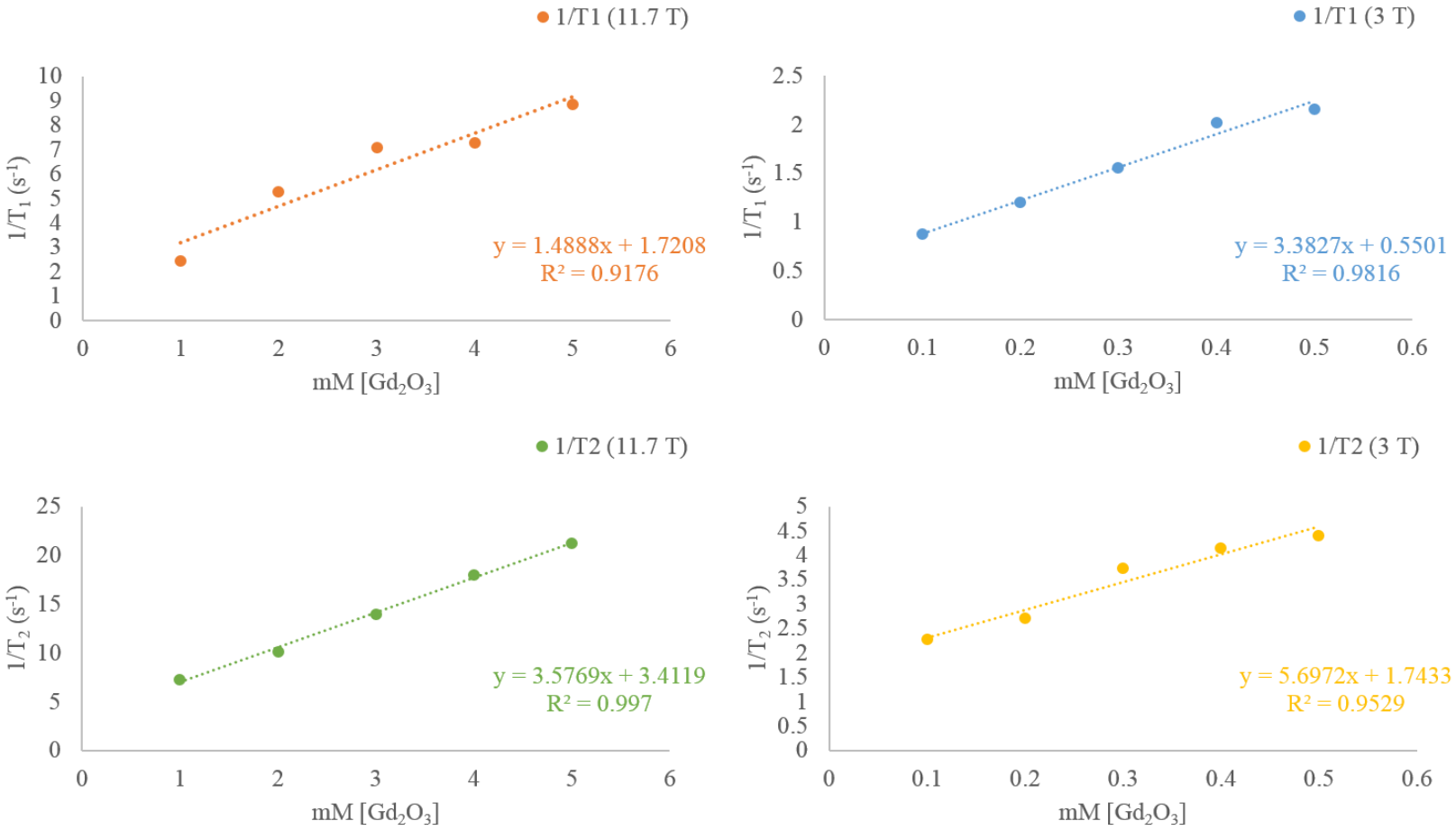

Figure 7-3 T_1 and T_2 relaxation rates per mmol of Gd_2O_3 nanoparticles at 3 T and 11.7 T magnetic field strengths.

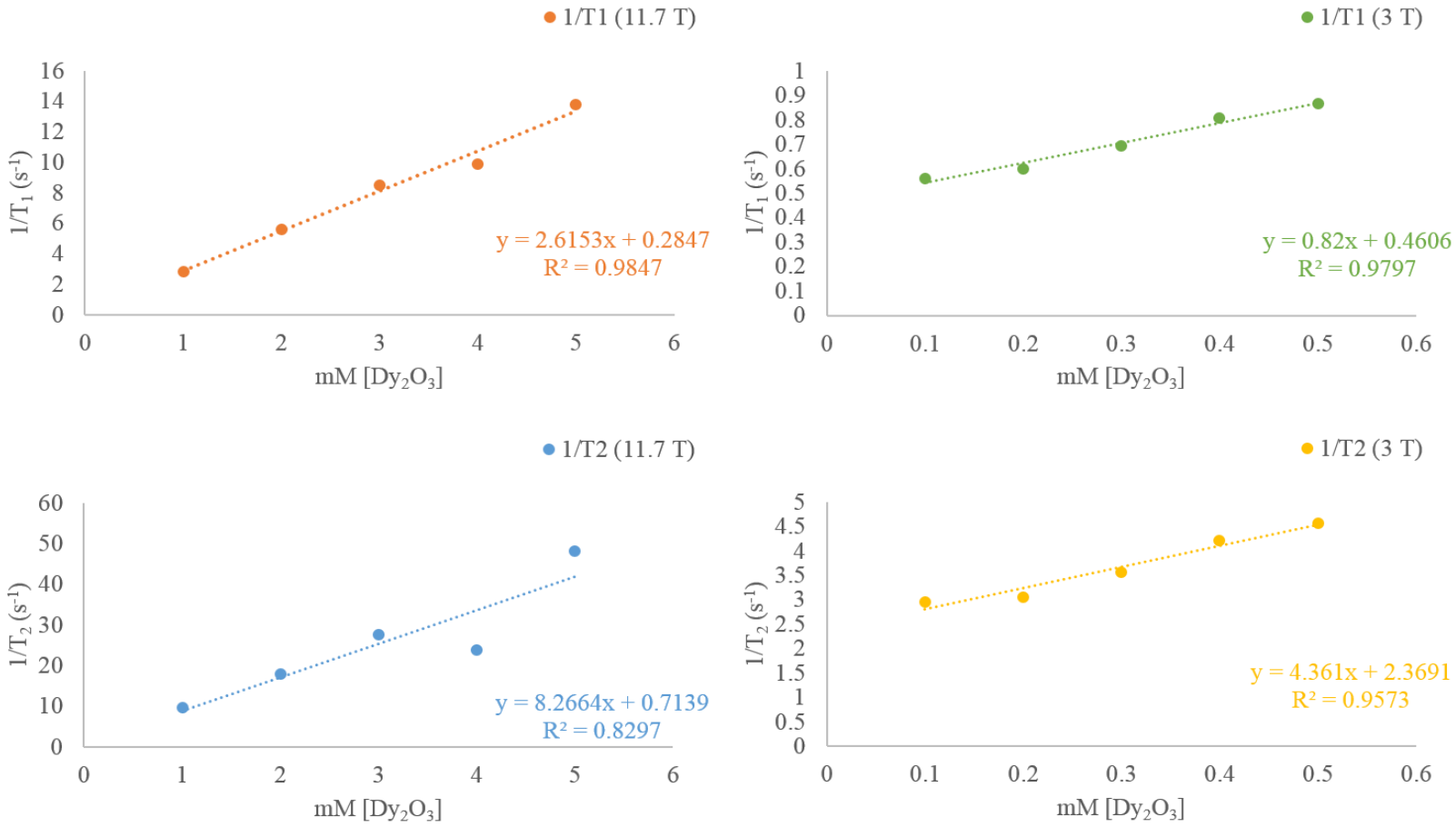

Figure 7-4 T_1 and T_2 relaxation rates per mmol of Dy_2O_3 nanoparticles at 3 T and 11.7 T magnetic field strengths.

Table 7-1 Relaxivity data for Fe_2O_3, Gd_2O_3 and Dy_2O_3 nanoparticles per mmol of compound at 3 T and 11.7 T magnetic field strengths.

Compound	Particle size estimated by the Scherrer equation from PXRD data (nm)	r_1 3T ($mM^{-1}s^{-1}$) Per mmol Metal Oxide	R-squared value	r_1 11.7 T ($mM^{-1}s^{-1}$) Per mmol Metal Oxide	R-squared value	r_2 3T ($mM^{-1}s^{-1}$) Per mmol Metal Oxide	R-squared value	r_2 11.7 T ($mM^{-1}s^{-1}$) Per mmol Metal Oxide	R-squared value
γ-Fe_2O_3	13.12	0.522	0.969	3.185	0.511	8.135	0.118	11.44	0.942
Gd_2O_3	27.44	3.3827	0.9816	1.489	0.918	5.6972	0.9529	3.577	0.997
Dy_2O_3	10.16	0.82	0.980	2.615	0.985	4.361	0.957	8.266	0.830

Table 7-2 Relaxivity data for Gd_2O_3, per mmol of Gd^{3+} ions at 3 T and 11.7 T magnetic field strengths.

Compound	**Particle size estimated by the Scherrer equation from PXRD data (nm)**	**r_1 3T ($mM^{-1}s^{-1}$) Per mmol Gd^{3+}**	**R-squared value**	**r_1 11.7 T ($mM^{-1}s^{-1}$) Per mmol Gd^{3+}**	**R-squared value**	**r_2 3T ($mM^{-1}s^{-1}$) Per mmol Gd^{3+}**	**R-squared value**	**r_2 11.7 T ($mM^{-1}s^{-1}$) Per mmol Gd^{3+}**	**R-squared value**
Gd_2O_3	27.44	1.691	0.9182	0.744	0.918	2.849	0.953	1.788	0.997

7.2.2 $Fe_{2-x}Gd_xO_3$ nanoparticle relaxivity

Table 7-3 and Table 7-4 show the relaxivity data for the $Fe_{2-x}Gd_xO_3$ nanoparticle series at 3 T and 11.7 T. The tables have been split to the relaxivity as a function of Gd^{3+} ion concentration, for comparison with Gd-chelate complexes; and as a function of the $Fe_{2-x}Gd_xO_3$ compound concentration for comparison with the control γ-Fe_2O_3 and Gd_2O_3 nanoparticles prepared.

From Table 7-3, it can be seen that at 3 T the r_1 measurements for the $Fe_{2-x}Gd_xO_3$ nanoparticles fluctuate with increasing Gd^{3+} ion content, however no discernible trend can be observed. Interestingly, increasing the magnetic field strength to 11.7 T does not seem to affect each compound in the same manner. For example, at 3 T, $Fe_{1.99}Gd_{0.01}O_3$ has an r_1 relaxivity of 32.11 $mM^{-1}s^{-1}$ and $Fe_{1.96}Gd_{0.04}O_3$ has a very similar r_1 relaxivity of 32.19 $mM^{-1}s^{-1}$. When these two compounds are placed in a higher strength magnetic field the r_1 values show considerable variation, with the r_1 for the former compound 1551.7 $mM^{-1}s^{-1}$ and the latter compound only 739.71 $mM^{-1}s^{-1}$. At both 3 T and 11.7 T the r_2 relaxivities for the $Fe_{2-x}Gd_xO_3$ series varies widely with no obvious correlation to Gd^{3+} ion content.

Based on the r_1 relaxivity data per mmol Gd^{3+} ion content, the highest r_1 relaxivities are exhibited by $Fe_{1.99}Gd_{0.01}O_3$ and $Fe_{1.96}Gd_{0.04}O_3$ nanoparticles at both 3 T and 11.7 T. Furthermore, the same two compounds also exhibit the highest r_2 relaxivities of the series for both magnetic field strengths. One other compound of note is $Fe_{1.95}Gd_{0.05}O_3$ (3.33 %). At 3 T the r_1 and r_2 values are low in comparison with the rest of the $Fe_{2-x}Gd_xO_3$ series but they increase dramatically at the higher magnetic field strength.

Table 7-4 shows the r_1 and r_2 relaxivity data for the $Fe_{2-x}Gd_xO_3$ series measured as a function of compound concentration. This data has been provided to compare the prepared $Fe_{2-x}Gd_xO_3$ nanoparticles against γ-Fe_2O_3 and Gd_2O_3 nanoparticles

There is a lack of any obvious trend between the relaxivity values and increasing Gd^{3+} ion concentration. In this case the compound with the highest r_1 and r_2 relaxivities is $F_{1.96}Gd_{0.04}O_3$ nanoparticles, at 1.29 $mM^{-1}s^{-1}$ and 144.56 $mM^{-1}s^{-1}$ respectively in a 3 T magnetic field, and 29.59 $mM^{-1}s^{-1}$ and 225.93 $mM^{-1}s^{-1}$ respectively in an 11.7 T magnetic field.

Figure 7-5 shows the r_1 and r_2 relaxivity trend with increasing x value for the $Fe_{2-x}Gd_xO_3$ nanoparticle series. The graph shows that from the series of nanoparticles prepared, the compound with the formula $Fe_{1.96}Gd_{0.04}O_3$ has the strongest relaxation effect in all cases, achieving an r_2 relaxivity of 144.56 $mM^{-1}s^{-1}$ at 3 T, and r_1 and r_2 relaxivities of 29.52 $mM^{-1}s^{-1}$ and 225.93 $mM^{-1}s^{-1}$ respectively at 11.7 T.

Table 7-3 Relaxivity data for $Fe_{2-x}Gd_xO_3$ nanoparticle series per mmol of Gd^{3+} ions at 3 T and 11.7 T magnetic field strengths.

Compound	Particle size estimated by the Scherrer equation from PXRD data (nm)	r_1 3T ($mM^{-1}s^{-1}$) Per mmol Gd^{3+}	R-squared value	r_1 11.7 T ($mM^{-1}s^{-1}$) Per mmol Gd^{3+}	R-squared value	r_2 3T ($mM^{-1}s^{-1}$) Per mmol Gd^{3+}	R-squared value	r_2 11.7 T ($mM^{-1}s^{-1}$) Per mmol Gd^{3+}	R-squared value
$Fe_{1.99}Gd_{0.01}O_3$	9.37	32.105	0.792	1551.7	0.916	827.85	0.6032	7459.5	0.8883
$Fe_{1.96}Gd_{0.04}O_3$	9.37	32.193	0.987	739.71	0.913	3613.9	0.9846	5648.3	0.9812
$Fe_{1.95}Gd_{0.05}O_3$ (2.67 %)	10.93	4.058	0.440	77.657	0.123	72.795	0.1203	321.54	0.0347
$Fe_{1.95}Gd_{0.05}O_3$ (3.33 %)	10.93	3.030	0.925	554.75	0.8055	22.875	0.0208	3679.3	0.976
$Fe_{1.88}Gd_{0.12}O_3$	16.39	10.375	0.994	65.091	0.734	349.4	0.996	112.32	0.8463
$Fe_{1.73}Gd_{0.27}O_3$	21.85	4.641	0.989	5.127	0.917	91.796	0.9241	63.475	0.9185

Table 7-4 Relaxivity data for $Fe_{2-x}Gd_xO_3$ nanoparticle series per mmol of $Fe_{2-x}Gd_xO_3$ compound at 3 T and 11.7 T magnetic field strengths.

Compound	Particle size estimated by the Scherrer equation from PXRD data (nm)	r_1 3T ($mM^{-1}s^{-1}$) Per mmol Compound	R-squared value	r_1 11.7 T ($mM^{-1}s^{-1}$) Per mmol Compound	R-squared value	r_2 3T ($mM^{-1}s^{-1}$) Per mmol Compound	R-squared value	r_2 11.7 T ($mM^{-1}s^{-1}$) Per mmol Compound	R-squared value
$Fe_{1.99}Gd_{0.01}O_3$	9.37	0.321	0.792	15.517	0.916	8.2785	0.6032	74.595	0.888
$Fe_{1.96}Gd_{0.04}O_3$	9.37	1.288	0.987	29.588	0.913	144.56	0.985	225.93	0.981
$Fe_{1.95}Gd_{0.05}O_3$ (2.67 %)	10.93	0.203	0.440	2.072	0.162	3.640	0.120	56.056	0.635
$Fe_{1.95}Gd_{0.05}O_3$ (3.33 %)	10.93	0.152	0.925	0.602	0.200	1.144	0.0208	89.412	0.640
$Fe_{1.78}Gd_{0.22}O_3$	16.39	1.245	0.994	7.811	0.734	41.928	0.996	13.478	0846
$Fe_{1.73}Gd_{0.27}O_3$	21.85	1.253	0.989	1.384	0.917	24.785	0.924	17.138	0.919

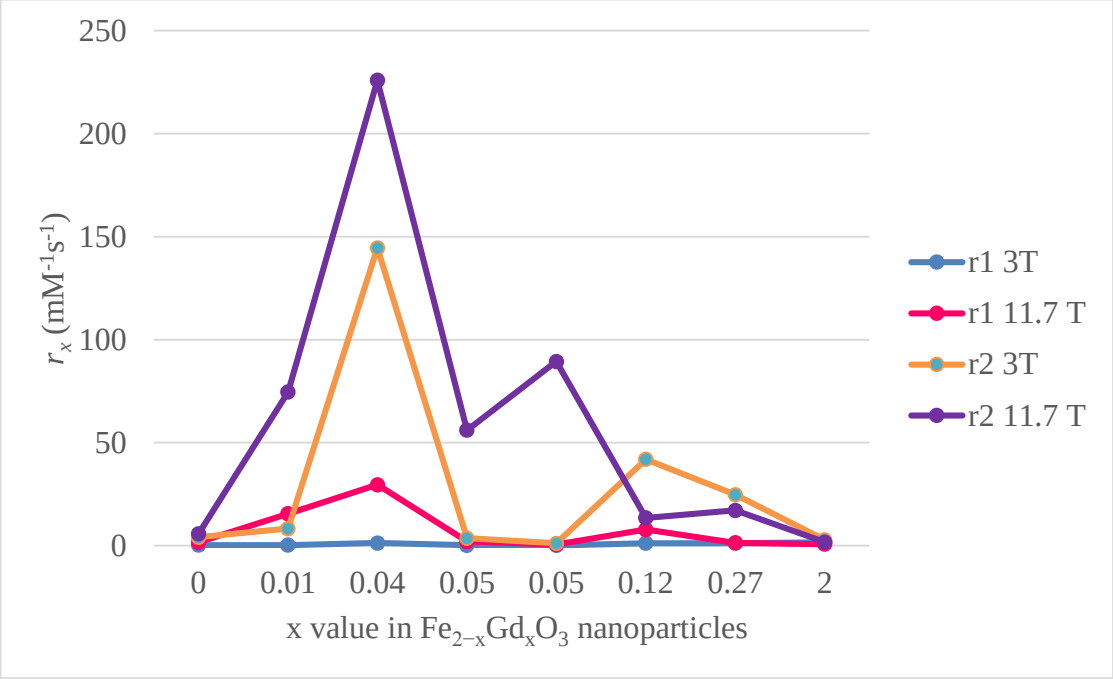

Figure 7-5 r_1 and r_2 values for $Fe_{2-x}Gd_xO_3$ nanoparticles series at 3 T and 11.7 T.

7.2.3 $Fe_{2-x}Dy_xO_3$ nanoparticle relaxivity

The relaxivity data for the $Fe_{2-x}Dy_xO_3$ nanoparticle series is shown in Table 7-5. Relaxivity measurements of these nanoparticles were difficult as the suspensions were not stable, resulting in the nanoparticles collecting at the bottom of the measuring tube. This is reflected in the poor fitting profile indicated by the R^2 values in the table. However, the relaxivity data for $Fe_{1.99}Dy_{0.01}O_3$ shows that the T_1 relaxation rate varies very little whether the nanoparticles are in the presence of a 3 T magnetic field or an 11.7 T magnetic field. The r_2 relaxivity for this compound is much higher than both γ-Fe_2O_3 and Dy_2O_3 nanoparticles at 11.7 T (51.738 $mM^{-1}s^{-1}$) as shown in Figure 7-6, indicating that this compound could be used as a high strength magnetic field contrast agent. Unfortunately due to time limitations it was not possible to repeat these measurements

with stable solutions, and further study of these compounds will be necessary to draw any definite conclusions.

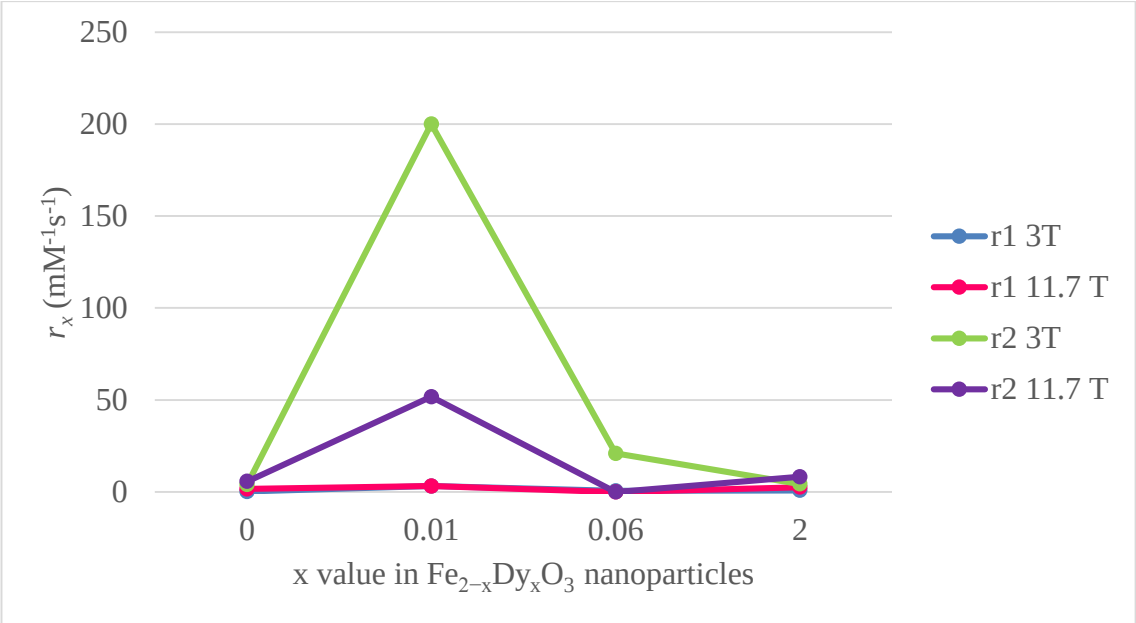

Figure 7-6 r_1 and r_2 values for $Fe_{2-x}Dy_xO_3$ nanoparticles series at 3 T and 11.7 T magnetic field strengths.

Table 7-5 Relaxivity data for $Fe_{2-x}Dy_xO_3$ nanoparticle series per mmol of compound at 3 T and 11.7 T magnetic field strengths.

Compound	Particle size estimated by the Scherrer equation from PXRD data (nm)	r_1 3T ($mM^{-1}s^{-1}$) Per mmol Compound	R-squared value	r_1 11.7 T ($mM^{-1}s^{-1}$) Per mmol Compound	R-squared value	r_2 3T ($mM^{-1}s^{-1}$) Per mmol Compound	R-squared value	r_2 11.7 T ($mM^{-1}s^{-1}$) Per mmol Compound	R-squared value
$Fe_{1.99}Dy_{0.01}O_3$	2.40	3.158	0.988	3.172	0.969	200.01	0.144	51.738	0.989
$Fe_{1.94}Dy_{0.06}O_3$	2.30	0.566	0.945	0.0007	0.2806	20.907	0.383	0.0024	0.009

7.2.4 $Gd_{2-x}Fe_xO_3$ nanoparticle relaxivity

Table 7-6 and Table 7-7 show the relaxivity data for the $Gd_{2-x}Fe_xO_3$ nanoparticle series as a function of Gd^{3+} concentration and $Gd_{2-x}Fe_xO_3$ concentration respectively. Due to poor stability of the nanoparticle solutions it was not possible to collect relaxivity data for $Gd_{2-x}Fe_xO_3$ nanoparticles with 0.61 molar % Fe content at 11.7 T.

The r_1 and r_2 relaxivity data shown in Table 7-6 does not correlate with the increase in the Fe^{3+} ion content at both magnetic field strengths. There is a general trend showing a drop in r_1 relaxivity as the magnetic field strength increases, e.g. for $Gd_{2-x}Fe_xO_3$ nanoparticles with 4.20 molar % Fe content the r_1 relaxivity changes from 4.877 $mM^{-1}s^{-1}$ to 3.574 $mM^{-1}s^{-1}$. The change in r_2 values with increasing magnetic field varies with the differing iron contents. The r_2 relaxivity for $Gd_{2-x}Fe_xO_3$ nanoparticles with 2.22 molar % Fe content roughly doubles with the increase in magnetic field strength whereas for 4.20 molar % Fe content the r_2 relaxivity decreases from 6.129 $mM^{-1}s^{-1}$ to 4.827 $mM^{-1}s^{-1}$. The same patterns are observed in Table 7-7 which shows the T_1 and T_2 relaxation times per mmol of compound. This suggests that the substitution of Gd^{3+} ions for Fe^{3+} ions has a varied impact on the magnetic properties of the nanoparticles overall.

Figure 7-7 shows the correlation between the Fe^{3+} ion content and the r_1 and r_2 relaxivities at both 3 T and 11.7 T. $Gd_{2-x}Fe_xO_3$ nanoparticles with 2.22 molar % Fe content shows the highest relaxivities of the series, however the relaxation at 3 T are must greater than at 11.7 T, suggesting that the use of these at high magnetic field strengths may not yield the best results. Another key point for this series is the r_2/r_1 ratio. A good dual probe contrast agent exhibits high r_1 relaxivity and a low r_2/r_1 ratio (close to 1). In this series the $Gd_{2-x}Fe_xO_3$ nanoparticles with 0.61 molar % Fe content and 4.20 molar % Fe content both have low r_2/r_1 ratios of 1.93 and 1.26 respectively at 3 T as well as r_1 relaxivities of

8.424 $mM^{-1}s^{-1}$ and 9.363 $mM^{-1}s^{-1}$, indicating their potential to act as dual T_1/T_2 contrast agent.

Table 7-6 Relaxivity data for $Gd_{2-x}Fe_xO_3$ nanoparticle series per mmol Gd^{3+} ions at 3 T and 11.7 T magnetic field strengths.

Molar % Fe in $Gd_{2-x}Fe_xO_3$ nanoparticles	**Particle size estimated by the Scherrer equation from PXRD data (nm)**	**r_1 3T ($mM^{-1}s^{-1}$) Per mmol Gd^{3+}**	**R-squared value**	**r_1 11.7 T ($mM^{-1}s^{-1}$) Per mmol Gd^{3+}**	**R-squared value**	**r_2 3T ($mM^{-1}s^{-1}$) Per mmol Gd^{3+}**	**R-squared value**	**r_2 11.7 T ($mM^{-1}s^{-1}$) Per mmol Gd^{3+}**	**R-squared value**
0.61	11.39	4.255	0.9953	-	-	8.199	0.9959	-	-
2.22	8.57	6.406	0.992	0.5919	0.989	13.945	0.9465	2.9369	0.9071
4.20	7.81	4.877	0.988	0.357	0.975	6.129	0.924	0.483	0.936

Table 7-7 Relaxivity data for $Gd_{2-x}Fe_xO_3$ nanoparticle series per mmol of compound at 3 T and 11.7 T magnetic field strengths.

Molar % Fe in $Gd_{2-x}Fe_xO_3$ nanoparticles	**Particle size estimated by the Scherrer equation from PXRD data (nm)**	**r_1 3T ($mM^{-1}s^{-1}$) Per mmol Compound**	**R-squared value**	**r_1 11.7 T ($mM^{-1}s^{-1}$) Per mmol Compound**	**R-squared value**	**r_2 3T ($mM^{-1}s^{-1}$) Per mmol Compound**	**R-squared value**	**r_2 11.7 T ($mM^{-1}s^{-1}$) Per mmol Compound**	**R-squared value**
0.61	11.39	8.424	0.995	-	-	16.233	0.996	-	-
2.22	8.57	12.555	0.992	1.160	0.989	27.332	0.947	5.756	0.907
4.20	7.81	9.363	0.9879	0.686	0.975	11.767	0.924	0.927	0.936

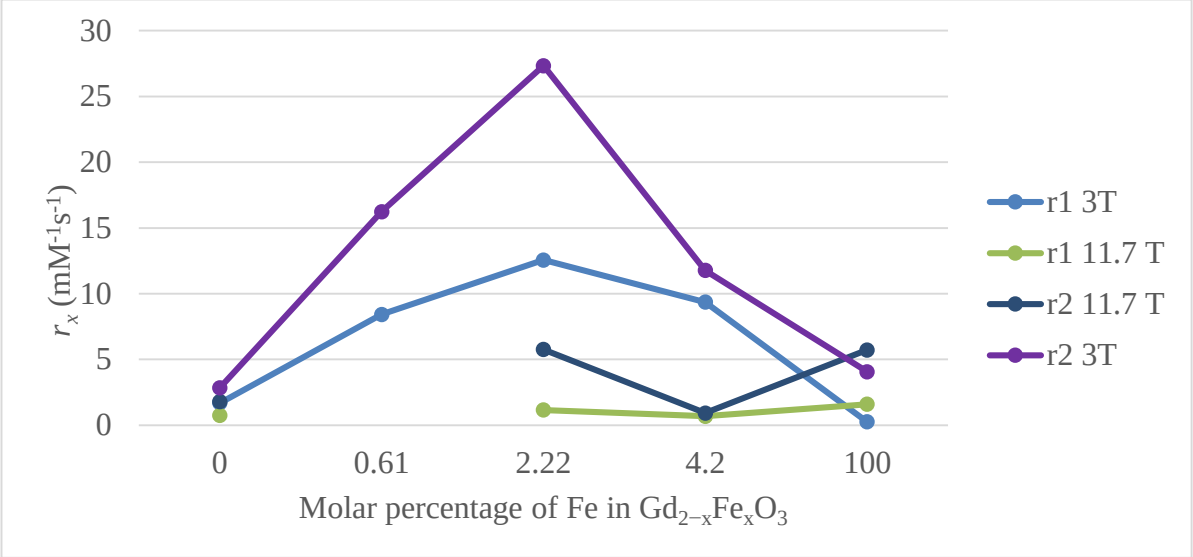

Figure 7-7 r_1 and r_2 values for $Gd_{2-x}Fe_xO_3$ nanoparticles series at 3 T and 11.7 T magnetic field strengths.

7.2.5 $Gd_{2-x}Mn_xO_3$ nanoparticle relaxivity

Table 7-9 shows the relaxivity data for the $Gd_{2-x}Mn_xO_3$ nanoparticle series. At 3 T, the r_1 values across the three compounds per mmol Gd^{3+} ions are very similar at 4.729 $mM^{-1}s^{-1}$, 5.916 $mM^{-1}s^{-1}$, and 5.496 $mM^{-1}s^{-1}$. Increasing the magnetic field strength to 11.7 T results in an increase in r_1 values to varying extents, with the highest r_1 relaxivity at 12.714 $mM^{-1}s^{-1}$ for $Gd_{1.79}Mn_{0.21}O_3$ nanoparticles. A similar trend is observed for the r_2 relaxivities per mmol Gd^{3+}ions (Table 7-8), however in this case the biggest difference in r_2 relaxivity is seen for $Gd_{1.98}Mn_{0.02}O_3$ nanoparticles.

When comparing the relaxivity data in Table 7-9 the r_1 values per mmol of $Gd_{2-x}Mn_xO_3$ nanoparticles at both 3 T and 11.7 T are consistently between 9 and 12 $mM^{-1}s^{-1}$ regardless of magnetic field strength or Mn^{2+} content. The r_2 relaxivity increases for $Gd_{1.90}Mn_{0.10}O_3$ and $Gd_{1.79}Mn_{0.21}O_3$ nanoparticles with a two-fold and three-fold increase respectively. However, for $Gd_{1.98}Mn_{0.02}O_3$ the r_2 relaxivity at 11.7 T remains similar to that of 3 T.

Figure 7-8 shows an increase in r_1 relaxivity in comparison to Gd_2O_3 nanoparticles at both 3 T and 11.7 T with the substitution of Gd^{3+} ions by Mn^{2+} ions, the changing concentration of Mn^{2+} seems to have little effect on the overall r_1 relaxivity. However, there is a general trend at both 3 T and 11.7 T showing an increase in r_2 relaxivity with increasing Mn^{2+} ion content.

At 3 T all three $Gd_{2-x}Mn_xO_3$ compounds have low r_2/r_1 ratios (1.49 for x = 0.02; 1.56 for x = 0.10; 2.18 for x = 0.21) that increase with increasing Mn^{2+} content. In addition, at 11.7 T $Gd_{1.98}Mn_{0.02}O_3$ has an r_2/r_1 ratio of 0.95 indicating that this compound has the potential to act as a dual probe T_1/T_2 contrast agent at both 3 T and 11.7 T.

Table 7-8 Relaxivity data for $Gd_{2-x}Mn_xO_3$ nanoparticle series per mmol of Gd^{3+} ions at 3 T and 11.7 T magnetic field strengths.

Compound	Particle size estimated by the Scherrer equation from PXRD data (nm)	r_1 3T ($mM^{-1}s^{-1}$) Per mmol Gd^{3+}	R-squared value	r_1 11.7 T ($mM^{-1}s^{-1}$) Per mmol Gd^{3+}	R-squared value	r_2 3T ($mM^{-1}s^{-1}$) Per mmol Gd^{3+}	R-squared value	r_2 11.7 T ($mM^{-1}s^{-1}$) Per mmol Gd^{3+}	R-squared value
$Gd_{1.98}Mn_{0.02}O_3$	21.25	4.729	0.988	6.414	0.939	5.943	0.924	10.281	0.980
$Gd_{1.90}Mn_{0.10}O_3$	28.92	5.916	0.993	9.597	0.911	9.227	0.983	10.218	0.921
$Gd_{1.79}Mn_{0.21}O_3$	40.21	5.496	0.986	12.714	0.870	11.975	0.986	14.886	0.985

Table 7-9 Relaxivity data for $Gd_{2-x}Mn_xO_3$ nanoparticle series per mmol of compound at 3 T and 11.7 T magnetic field strengths.

Compound	Particle size estimated by the Scherrer equation from PXRD data (nm)	r_1 3T ($mM^{-1}s^{-1}$) Per mmol Compound	R-squared value	r_1 11.7 T ($mM^{-1}s^{-1}$) Per mmol Compound	R-squared value	r_2 3T ($mM^{-1}s^{-1}$) Per mmol Compound	R-squared value	r_2 11.7 T ($mM^{-1}s^{-1}$) Per mmol Compound	R-squared value
$Gd_{1.98}Mn_{0.02}O_3$	21.25	10.317	0.980	12.71	0.777	15.354	0.953	12.094	0.604
$Gd_{1.90}Mn_{0.10}O_3$	28.92	11.241	0.993	10.394	0.958	17.532	0.983	41.339	0.866
$Gd_{1.79}Mn_{0.21}O_3$	40.21	9.837	0.986	10.962	0.967	21.435	0.639	58.055	0.798

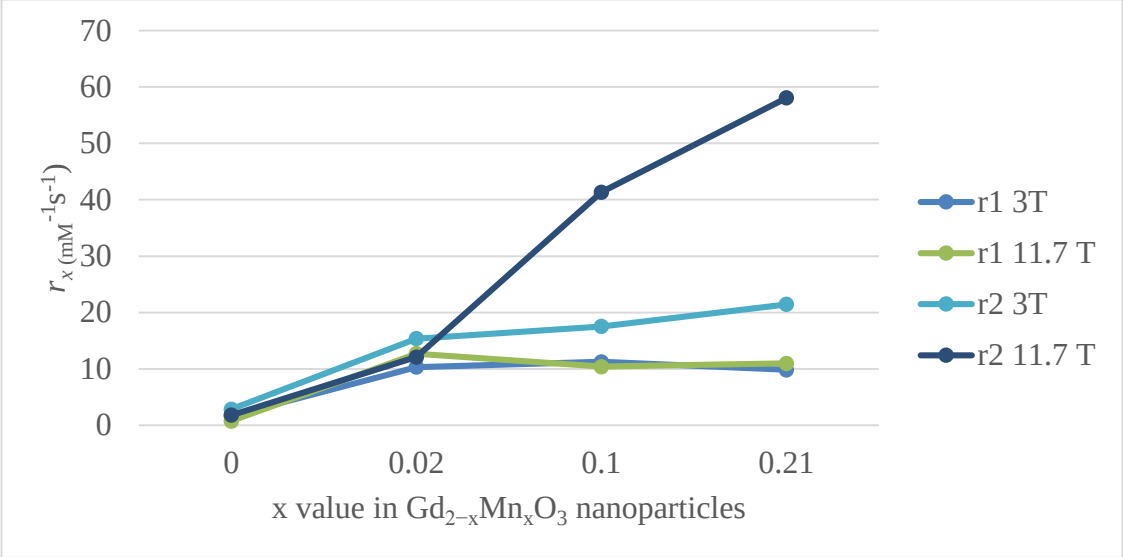

Figure 7-8 r_1 and r_2 values for $Gd_{2-x}Mn_xO_3$ nanoparticles series at 3 T and 11.7 T magnetic field strengths.

7.2.6 $Dy_{2-x}Fe_xO_3$ nanoparticle relaxivity

Table 7-10 shows the relaxivity data for the $Dy_{2-x}Fe_xO_3$ nanoparticle series at 3 T and 11.7 T. As dysprosium is generally classified as a T_2 contrast agent it is not surprising that low r_1 values are achieved at both 3 T and 11.7 T.[84] The r_2 relaxivity values at 11.7 T are roughly double those as 3 T for both compounds, however the obtained values are still lower than those obtained for Dy_2O_3 nanoparticles as shown in Figure 7-9. Although the Fe^{3+} content in the series increased from 1 % to 4.5 % there is almost no change in r_1 and r_2 relaxivity values at both 3 T and 11.7 T.

Table 7-10 Relaxivity data for $Dy_{2-x}Fe_xO_3$ nanoparticle series per concentration of compound at 3 T and 11.7 T magnetic field strengths.

Compound	Particle size estimated by the Scherrer equation from PXRD data (nm)	r_1 3T ($mM^{-1}s^{-1}$) Per mmol compound	R-squared value	r_1 11.7 T ($mM^{-1}s^{-1}$) Per mmol compound	R-squared value	r_2 3T ($mM^{-1}s^{-1}$) Per mmol compound	R-squared value	r_2 11.7 T ($mM^{-1}s^{-1}$) Per mmol compound	R-squared value
$Dy_{1.98}Fe_{0.02}O_3$	12.20	0.31	0.975	1.860	0.9001	3.483	0.964	8.650	0.900
$Dy_{1.91}Fe_{0.09}O_3$	13.40	0.31	0.975	1.511	0.757	3.483	0.964	6.696	0.986

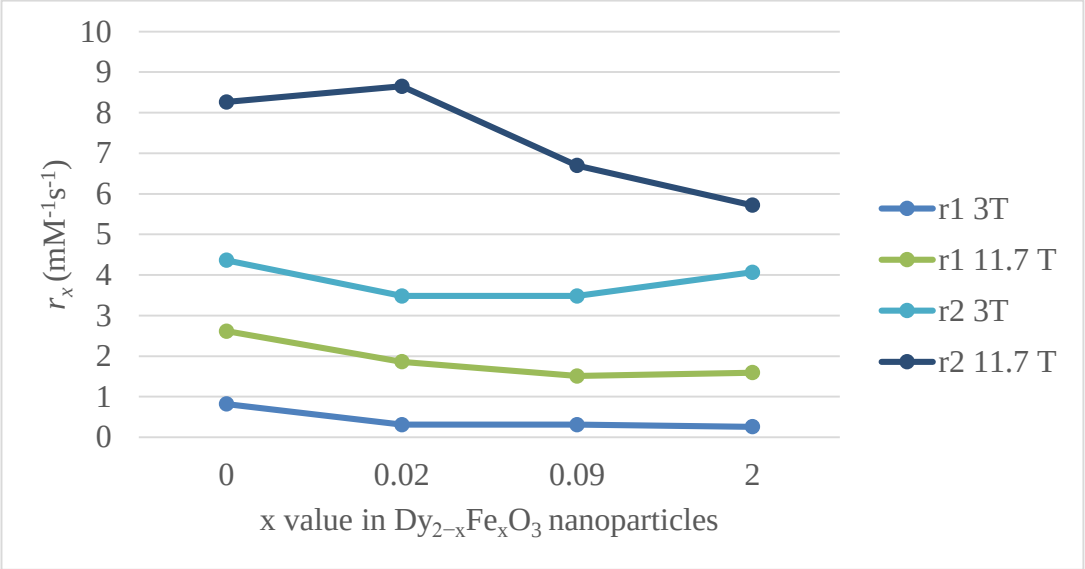

Figure 7-9 r_1 and r_2 values for $Dy_{2-x}Fe_xO_3$ nanoparticles series at 3 T and 11.7 T magnetic field strengths.

7.2.7 $Fe_2O_{3-x}F_{2x}$ nanoparticle relaxivity

The relaxivity data for $Fe_2O_{3-x}F_{2x}$ is shown in Table 7-11. At 3 T, the compound has an r_1 relaxivity of 1.735 $mM^{-1}s^{-1}$and an r_2 of 136.53 $mM^{-1}s^{-1}$. The latter of which is much higher than that of γ-Fe_2O_3 nanoparticles (r_1 = 0.522 $mM^{-1}s^{-1}$, r_2 =8.135 $mM^{-1}s^{-1}$ at 3 T; r_1 = 0.969 $mM^{-1}s^{-1}$, r_2 =11.44 $mM^{-1}s^{-1}$ at 11.7 T). Increasing the magnetic field strength to 11.7 T causes a ten-fold increase in r_1 relaxivity and an increase in r_2 relaxivity to 167.3 $mM^{-1}s^{-1}$.

Table 7-11 Relaxivity data for $Fe_2O_{3-x}F_{2x}$ nanoparticle series per mmol of compound at 3 T and 11.7 T magnetic field strengths.

Compound	**Particle size estimated by the Scherrer equation from PXRD data (nm)**	**r_1 3T ($mM^{-1}s^{-1}$)**	**R-squared value**	**r_1 11.7 T ($mM^{-1}s^{-1}$)**	**R-squared value**	**r_2 3T ($mM^{-1}s^{-1}$)**	**R-squared value**	**r_2 11.7 T ($mM^{-1}s^{-1}$)**	**R-squared value**
$Fe_2O_{3-x}F_{2x}$	13.11	1.735	0.858	18.776	0.931	136.53	0.952	167.30	0.971

7.3 DISCUSSION

In order to determine the efficacy of the prepared nanoparticles as MRI contrast agents, MR measurements were carried out at magnetic field strengths of 11.7 T and 3 T. Current clinical MRI scanners use magnetic field strengths up to 3T, however further development of the technology will result in scanners utilising much higher magnetic field strengths in routine use in the future. With this in mind it is prudent to study the relaxation properties of the prepared nanoparticles at both clinical field strengths and higher magnetic field strengths, in order to determine the compounds potential as an MRI contrast agent.

7.3.1 γ-Fe_2O_3, Gd_2O_3 and Dy_2O_3 nanoparticles

The results in Figure 7-1 to Figure 7-4 for γ-Fe_2O_3, Gd_2O_3 and Dy_2O_3 nanoparticles show the r_1 and r_2 values in a magnetic field at 3 T and 11.7 T both as a function of concentration of M^{3+} ions and concentration of the γ-Fe_2O_3, Gd_2O_3 or Dy_2O_3 compound. This is also shown in Table 7-1 and Table 7-2 for ease of comparison.

The two most common commercial contrast agents are Ferridex, an iron oxide T_2 contrast agent; and Dotarem (Gd-DOTA) a gadolinium chelate T_1 contrast agent. Typically, relaxivity measured for nanoparticles is per formula unit concentration, whereas relaxivity measured in chelated compounds is measured by the concentration of the metal ion. Therefore the data presented in this chapter follows both formats to allow for direct comparison between the commercial standard contrast agents, and the newly prepared nanoparticles presented here. Ferridex has an r_2 of 148.95 $mM^{-1}s^{-1}$ at 3 T, Magnevist (Gd-DTPA) an r_1 of 5.39 $mM^{-1}s^{-1}$ at 3 T and Dotarem an r_1 of 3.1 $mM^{-1}s^{-1}$ at 1.41 T.[91, 178, 179]

The data collected indicates the prepared γ-Fe_2O_3 nanoparticles have a greater effect on the T_2 relaxivity of water protons at both 11.7 T and 3 T, when compared against the T_1 relaxivity of water protons; which is in keeping with previously reported findings on iron oxide nanoparticles.[2, 180] Between the two different magnetic field strengths there is a noticeable change in both T_1 and T_2 relaxivity values.

At 3 T, the T_1 relaxivity (r_1) [γ-Fe_2O_3] is 0.52 $mM^{-1}s^{-1}$, in comparison to both other iron oxide nanoparticles of similar size reported in the literature, and the typical T_1 contrast agent Magnevist, this value is low. The graph indicates that change in rate of T_1 relaxation is negligible, suggesting that any T_1 effects may occur at higher concentrations. The T_2 relaxivity (r_2) [γ-Fe_2O_3] is 8.14 $mM^{-1}s^{-1}$, this is still a low value in comparison to literature reports, however the fitting of the trend line, which dictates the r_2 value, in relation to the data is poor and so the r_2 value is unreliable. Unfortunately, it has not been possible to repeat the data collection at this field strength due to limited access to the instrument.

Table 7-1 and Figure 7-1 show the r_1 and r_2 values for γ-Fe_2O_3 nanoparticles at 11.7 T. If the response matches the literature reports, the increase in the magnetic field strength would be expected to cause an increase in r_2 and a decrease in r_1 values. This is due to the higher magnetic field strength inducing stronger magnetic effects than at 3 T (see Equation 1-5), due to the high magnetic susceptibility of the nanoparticles. This causes the nanoparticles to have a higher magnetic moment at 11.7 T, inducing faster relaxation in the surrounding water protons. This reduces r_1 and increases r_2 values. For the γ-Fe_2O_3 nanoparticles prepared, the r_1 value [γ-Fe_2O_3] is 3.19 $mM^{-1}s^{-1}$ and the r_2 value [γ-Fe_2O_3] is 11.44 $mM^{-1}s^{-1}$. Both r_1 and r_2 values have increased with increasing magnetic field

strength. This indicates that the prepared γ-Fe_2O_3 nanoparticles could potentially be used as MRI contrast agents at high magnetic field strengths.

There is a large difference between the r_2 values in comparison to Ferridex, which could be associated with both the difference in particle size and the different surface functionalisation. Additionally, Ferridex consists of a mixture of Fe_3O_4 and Fe_2O_3 either as separate nanoparticles or as core-shell nanoparticles, resulting in more iron ions and thus a larger magnetic moment.

For Gd_2O_3 nanoparticles the relaxivity data is shown in Figure 7-3, Table 7-1 and Table 7-2. At 3 T, the r_1 and r_2 values per [Gd^{3+}] are 1.69 $mM^{-1}s^{-1}$ and 2.85 $mM^{-1}s^{-1}$. As expected the r_1 value is higher than that of γ-Fe_2O_3 nanoparticles (0.26 $mM^{-1}s^{-1}$) but lower than the r_2 value (4.07 $mM^{-1}s^{-1}$) as γ-Fe_2O_3 nanoparticles have dominant T_2 relaxation effects. The longitudinal relaxation rate at 3 T of the prepared Gd_2O_3 nanoparticles is lower than that of Magnevist, which has an r_1 value of 5.4 $mM^{-1}s^{-1}$ per [Gd^{3+}].

At 11.7 T, r_1 and r_2 values per [Gd^{3+}] are 0.74 $mM^{-1}s^{-1}$ and 1.79 $mM^{-1}s^{-1}$. These are both lower than the r_1 and r_2 values of γ-Fe_2O_3 suggesting that at higher magnetic field strengths γ-Fe_2O_3 nanoparticles will perform better than Gd_2O_3 as contrast agents.

7.3.2 $Fe_{2-x}Gd_xO_3$ nanoparticles

There have a few reports in recent years regarding the preparation of dual probe MRI contrast agents involving iron oxide nanoparticles with Gd^{3+} ions, either doped into the nanoparticles or attached to the surface on polymer chains.[44, 91, 128] Bae *et al.*[91] synthesized magnetite nanoparticles with Gd-DOTA attached to the surface *via* PEG chains. The overall particle diameter was 73.8±7.6 nm, which at 3 T had an r_1 value of

11.17 $mM^{-1}s^{-1}$ and an r_2 value of 30.32 $mM^{-1}s^{-1}$ compared against Magnevist (r_1 = 5.39 $mM^{-1}s^{-1}$) and Ferridex (r_2 = 148.95 $mM^{-1}s^{-1}$). The group also measured the T_2 relaxivity for the unlabelled magnetite nanoparticles at 225.81 $mM^{-1}s^{-1}$. The large difference between the r_2 values for unlabelled and Gd-labelled magnetite nanoparticles was put down to interference from the Gd-chelates in the T_2 relaxation process.

Kim *et al.*[44] synthesized Gd-doped Fe_3O_4 *via* a co-precipitation method (theoretical formula $Fe_{2.8}Gd_{0.2}O_3$) and functionalised the resulting particles with lecithin to prevent agglomeration. The group measured the T_1 and T_2 relaxation times at 3 T for a concentration of 8.3 mM contrast agent. This indicates that at the single concentration of 8.3 mM the r_1 and r_2 values of Gd-doped Fe_3O_4 nanoparticles decreased compared against control Fe_3O_4 nanoparticles.

Xiao *et al.*[128] synthesized Gd^{3+}-doped iron oxide nanoparticles of 4.64 nm, by thermal decomposition of the metal acetylacetonate salts. The group found that the r_2 based on the Fe ion concentration decreased between the control PEG – functionalised iron oxide nanoparticles and the PEG – functionalised Gd^{3+}-doped iron oxide nanoparticles, going from 73.9 $mM^{-1}S^{-1}$ to 66.9 $mM^{-1}S^{-1}$. However the r_1 based on Gd^{3+} ion concentration increased for the Gd-doped iron oxide nanoparticles when compared against Gd_2O_3 nanoparticles. The high r_1 value along with the low r_2/r_1 ratio indicate that this Gd-doped iron oxide compound has the potential to be used as a dual probe contrast agent for MRI.

The development of the $Fe_{2-x}Gd_xO_3$ series in this work was based on the use of Gd^{3+} ions for T_1 imaging and $Fe^{2+/3+}$ ions for T_2 imaging. Through combining both ions into one nanoparticle it was expected that the Fe ions would dominate during T_2 relaxation processes and the Gd^{3+} ions would dominate during T_1 relaxation processes leading to a dual-probe MRI contrast agent. In actual fact, the results show that the incorporation of

Gd^{3+} ions into the γ-Fe_2O_3 lattice results in a large increase in r_2 values at both 3 T and 11.7 T magnetic field strengths when compared against the control γ-Fe_2O_3 nanoparticles across the entire series. The r_2 value does fluctuate throughout the series, however this reflects the magnetic measurements taken for the series, presented in Chapter 3. This may be due to inhomogeneous cation distribution in the compounds, causing disruption of the coupling interactions between the metal ions. Figure 7-5 shows the r_1 and r_2 trends as the Gd^{3+} ion content increases. It is clear that the best compound from this series which improves both r_1 and r_2 values the most at all magnetic field strengths, is $Fe_{1.96}Gd_{0.04}O_3$, with the biggest effect observed for r_2 values. Further investigation is required to understand the structure of this compound, however the excellent relaxation properties observed may be due to the presence of a core-shell structure or even distribution of the cations throughout the nanoparticle, leading to co-operative coupling interaction effects.

7.3.3 $Fe_{2-x}Dy_xO_3$

Dysprosium has one of the highest magnetic moments of all the lanthanides, higher than gadolinium ions that are used as T_1 contrast agents. Gadolinium has isotropic electronic ground state containing 7 *4f* electrons. However, dysprosium has a 10 *4f* electrons, leading to an anisotropic $^6H_{5/2}$ electronic ground state and a much faster relaxation time.[81] This increased tumbling rate leads to reduced longitudinal relaxation effects and increased transverse relaxation effects. Due to this, dysprosium is classified as a T_2 contrast agent.[181]

In comparison to gadolinium chelate complexes there have been relatively few studies of dysprosium as an MRI contrast agent, focussing around Dy-DOTA and Dy_2O_3 nanoparticles.[150, 177, 181]

Cation doping of γ-Fe_2O_3 nanoparticles with Dy^{3+} ions has not previously been attempted to the best of the author's knowledge, and was carried out here in an attempt to enhance T_2 contrast agent characteristics. It was found that $Fe_{1.99}Dy_{0.01}O_3$ particles exhibited an r_2 value of 25.87 $mM^{-1}s^{-1}$, which is roughly five times greater than that of γ-Fe_2O_3 synthesised by the same method. However further doping of iron oxide with Dy^{3+} ions appears to reduce the magnetic properties of the nanoparticles as the r_2 value of $Fe_{1.94}Dy_{0.06}O_3$ was 5.77 $mM^{-1}s^{-1}$, similar to that of γ-Fe_2O_3 nanoparticles.

For $Fe_{1.99}Dy_{0.01}O_3$ nanoparticles the r_1 values were 3.16 $mM^{-1}s^{-1}$ at 3 T and 3.17 $mM^{-1}s^{-1}$ at 11.7 T, both of which are higher than those observed for γ-Fe_2O_3 nanoparticles (0.26 $mM^{-1}s^{-1}$ at 3 T and 1.59 $mM^{-1}s^{-1}$ at 11.7 T. For $Fe_{1.94}Dy_{0.06}O_3$ nanoparticles the r_1 values are 0.56 $mM^{-1}s^{-1}$ at 3 T and 0.0007 $mM^{-1}S^{-1}$ at 11.7 T.

Due to the high strength magnetic field at 11.7 T, the T_1 relaxation times are expected to be much longer than would be typically observed in a 3 T clinical MRI for both Dy-doped Fe_2O_3 compounds, and so the similarity of relaxation times between the two magnetic field strengths can only be explained by the presence of the Dy^{3+} ions having a large influence on the magnetic properties of the compounds and thus the relaxivity. These results reflect those seen in previous studies of Dy_2O_3 nanoparticles, in which the r_1 values are low and the r_2 values are of most interest. Further studies of the magnetic properties are required to fully understand the magnetic properties.

Figure 7-6 shows that in comparison to γ-Fe_2O_3, $Fe_{1.94}Dy_{0.06}O_3$, and Dy_2O_3 nanoparticles, the newly prepared compound $Fe_{1.99}Dy_{0.01}O_3$ shows the greatest potential as a T_2 imaging contrast agent.

7.3.4 $Gd_{2-x}Fe_xO_3$

Free Gd^{3+} ions can irreparably damage the central nervous system by interrupting cellular processes involving Ca^{2+} ions. In light of recent concerns for the safe use of Gd^{3+}-chelate complexes, an alternative to this popular T_1 contrast agent has been sought.[182] One of the compounds that has been the subject of interest in the last ten years is Gd_2O_3.[92, 182-184] On a nanoparticles scale Gd_2O_3 can provide similar if not more enhanced T_1 relaxation effects compared to Gd-chelate complexes such as Gd-DTPA and Gd-DOTA. Doping Gd_2O_3 nanoparticles with Fe^{3+} ions to create a dual-probe contrast agent is not something previously seen, with most dual-probes previously being developed from the SPIO perspective.

The newly prepared $Gd_{2-x}Fe_xO_3$ nanoparticles exhibited r_1 values close to those of Magnevist at 3 T, with the change in Fe^{3+} content showing no obvious trend in correlation to relaxivity.

However, when r_1 and r_2 values are measured as a function of compound concentration, there is an obvious increase in both r_1 and r_2 values observed across the series when compared against both Gd_2O_3 and γ-Fe_2O_3 nanoparticles.

Figure 7-7 clearly shows that $Gd_{2-x}Fe_xO_3$ nanoparticles with 2.22 molar % Fe content exhibit the best relaxation properties of the series, with r_1 [2.22 molar % Fe content] = 12.56 $mM^{-1}s^{-1}$ and r_2 [2.22 molar % Fe content] = 27.33 $mM^{-1}s^{-1}$ at 3 T; and r_1 [2.22 molar % Fe content] = 11.60 $mM^{-1}s^{-1}$ and r_2 [2.22 molar % Fe content] 57.56 $mM^{-1}s^{-1}$.

In addition to high r_1 values the r_2/r_1 ratios for all the compounds in this series are low, at 1.93, 2.18 and 1.96 indicating that these have the potential to be used as dual-probe T_1/T_2 contrast agents.

7.3.5 $Gd_{2-x}Mn_xO_3$

Common alternative T_1 contrast agents to Gd^{3+} are Mn^{2+} based compounds, [106, 154] such as $MnCl_2$, manganese chelates and nanoparticles.[106] Manganese is a paramagnetic element similar to gadolinium, with a $3d^5$ ground state that is generally high spin with five unpaired electrons. Whilst both gadolinium oxide and manganese oxide nanoparticles have both been studied separately for use as MRI contrast agents, only one study (to the best of the author's knowledge) has been carried out on the development of a combination manganese oxide and gadolinium oxide nanoparticle. Choi *et al.*[185] studied the relaxivity of Gd_2O_3 nanoparticles surface doped with MnO (Gd_2O_3@MnO). The group found the r_1 values of Gd_2O_3 nanoparticles and Gd_2O_3@MnO were similar, however a two-fold increase in the r_2 value was observed, with Gd_2O_3@MnO nanoparticles having relaxivity values of $r_1 = 12.8\ mM^{-1}s^{-1}$ and $r_2 = 26.6\ mM^{-1}s^{-1}$.

In the work presented here, Gd_2O_3 nanoparticles were doped with Mn^{2+} ions at different concentrations. Relaxivity data indicates that in comparison to the Gd_2O_3 nanoparticles prepared by the same method, all compounds in the $Gd_{2-x}Mn_xO_3$ series have greater r_1 and r_2 values at both 3 T and 11.7 T. In comparison to Magnevist at 3 T, the r_1 values are very similar. Interestingly, although both gadolinium and manganese are used separately as T_1 contrast agents, the results here show that when combined they exert greater influence over the T_2 relaxation process. This agrees with the finding of Choi *et al.*[185], in this case, the substitution of just a small amount of gadolinium for manganese, $Gd_{1.98}Mn_{0.02}O_3$, has resulted in a three-fold increase in r_2 relaxivity at 3 T, when compared against the control Gd_2O_3 nanoparticles. Furthermore, $Gd_{1.79}Mn_{0.21}O_3$ nanoparticles show a four-fold increase in r_2 relaxivity at 3 T.

At 3 T all three $Gd_{2-x}Mn_xO_3$ compounds have low r_2/r_1 ratios (1.49 for x = 0.02; 1.56 for x = 0.10; 2.18 for x = 0.21) that increase with increasing Mn^{2+} content. In addition, at 11.7 T $Gd_{1.98}Mn_{0.02}O_3$ has an r_2/r_1 ratio of 0.95 indicating that this compound has the potential to act as a dual probe T_1/T_2 contrast agent at both 3 T and 11.7 T.

7.3.6 $Dy_{2-x}Fe_xO_3$

As previously stated, due to the high magnetic moment and anisotropic electronic ground state for dysprosium ions, these compounds are usually classified as T_2 contrast agents. Doping of dysprosium oxide nanoparticles with iron ions was carried out in an attempt to prepare a dual probe contrast agent based around Dy_2O_3 nanoparticles. To date, no studies have been carried out on cation substitution of Dy_2O_3 nanoparticles for use as MRI contrast agents, therefore the MRI results presented here can only be compared against the control Dy_2O_3 and γ-Fe_2O_3 nanoparticles discussed in section 7.3.1.

Unfortunately, the r_1 and r_2 values for both $Dy_{1.98}Fe_{0.02}O_3$ and $Dy_{1.91}Fe_{0.09}O_3$ have decreased at both 3 T and 11.7 T, in comparison with the control Dy_2O_3 and γ-Fe_2O_3 nanoparticles. This can be explained by a decrease in the overall magnetic moment of the nanoparticles, due to the substitution of Dy^{3+} ions by Fe^{3+} ions, as iron has a lower magnetic moment (μ_{eff} = 5.6 BM) than dysprosium (μ_{eff} = 10.6 BM).

7.3.7 $Fe_2O_{3-x}F_{2x}$

A novel compound $Fe_2O_{3-x}F_{2x}$ has been prepared to study the effects of anion doping upon the magnetic properties. As no studies of this type exist that apply to either iron oxide nanoparticles or MRI contrast agents, the data can only be compared against the γ-Fe_2O_3

nanoparticles. For γ-Fe_2O_3 nanoparticles at 3 T, r_1 was measured at 0.52 $mM^{-1}s^{-1}$ and r_2 at 8.14 $mM^{-1}s^{-1}$. In comparison, for the $Fe_2O_{3-x}F_{2x}$ nanoparticles at 3 T, r_1 was measured at 1.74 $mM^{-1}s^{-1}$ and r_2 at 136.53 $mM^{-1}s^{-1}$. The new $Fe_2O_{3-x}F_{2x}$ nanoparticles show a 3-fold increase in r_1 relaxivity in comparison to the control nanoparticles, but more significantly, they show a 17-fold increase in the r_2 relaxivity. In addition, at 11.7 T the control γ-Fe_2O_3 nanoparticles exhibited an r_1 of 3.19 $mM^{-1}s^{-1}$ and an r_2 of 11.44 $mM^{-1}s^{-1}$, which was greatly improved upon by the $Fe_2O_{3-x}F_{2x}$ nanoparticles with an r_1 of 18.78 $mM^{-1}s^{-1}$, almost a 6-fold improvement; and an r_2 of 167.30 $mM^{-1}s^{-1}$, a 14-fold improvement. The exact mechanism behind this increase is unclear however, one possibility is additional coupling interaction occur due to the addition *p* electrons present in F^- ions compared with O^{2-} ions.

7.4 CONCLUSIONS

The relaxivity data presented in this chapter show that each of the seventeen prepared cation and anion doped metal oxide compounds has in most cases a positive impact on both the r_1 and r_2 relaxivity of water protons, compared to the respective undoped Fe_2O_3, Gd_2O_3 and Dy_2O_3 nanoparticles.

Currently, the most common magnetic field strengths used in clinical applications are 1.5 T and 3 T, with technological advances leading to high magnetic fields strength being used in the future.

Due to this, the development of compounds suitable for both current and high magnetic field strength applications were studied.

The nanoparticles prepared in this work that show the most potential for improving T_1 relaxation rates at 3 T are the $Gd_{2-x}Fe_xO_3$ nanoparticle series for 0.61, 2.22 and 4.20 molar % Fe content; and the $Gd_{2-x}Mn_xO_3$ nanoparticle series for x = 0.02; x = 0.10 and x = 0.21. Of these series $Gd_{1.98}Mn_{0.02}O_3$, $Gd_{1.90}Mn_{0.10}O_3$, $Gd_{1.79}Mn_{0.21}O_3$ and $Fe_{1.96}Gd_{0.04}O_3$ nanoparticles also show potential for use at 11.7 T as T_1 contrast agents.

Furthermore, $Fe_{1.96}Gd_{0.04}O_3$ exhibited excellent T_2 relaxation properties at 3 T and 11.7 T indicating its potential as a dual T_1-T_2 contrast agent.

From the $Fe_{2-x}Dy_xO_3$ nanoparticle series, $Fe_{1.99}Dy_{0.01}O_3$ nanoparticles exhibited high T_2 relaxation rates at 11.7 T compared to those of γ-Fe_2O_3 nanoparticles, however further data is required in order to study the remaining compounds in the series.

$Fe_2O_{3-x}F_{2x}$ nanoparticles exhibited high T_2 relaxation rates at both 3 T and 11.7 T compared against γ-Fe_2O_3 nanoparticles, showing their potential for use both at clinical and higher magnetic field strengths.

Various compounds exhibited high T_1 and T_2 relaxation rates at both 3 T and 11.7 T, including $Gd_{1.98}Mn_{0.02}O_3$, $Gd_{1.90}Mn_{0.10}O_3$, and $Gd_{1.79}Mn_{0.21}O_3$. Additionally the $Gd_{2-x}Fe_xO_3$ nanoparticle series indicated potential as dual T_1-T_2 contrast agents, however further optimisation of reaction conditions is required to prepare these nanoparticles without impurities.

8 CONCLUSIONS AND FURTHER WORK

The work described in this thesis demonstrates the potential of various metal oxide nanoparticles for use as MRI contrast agents, both at clinical and high magnetic field strengths.

Approximately 13 nm superparamagnetic iron oxide nanoparticles were synthesized by a co-precipitation method. The single-phase γ-Fe_2O_3 structure of the nanoparticles was confirmed by PXRD and XPS. The prepared nanoparticles were coated with citric acid to improve hydrophilicity and biocompatibility. Relaxivity values increased with increasing magnetic field strength. The relaxivity values obtained at 3 T were 0.52 $mM^{-1}s^{-1}$ and 8.14 $mM^{-1}s^{-1}$ for r_1 and r_2 respectively; and 3.19 $mM^{-1}s^{-1}$ and 11.44 $mM^{-1}s^{-1}$ for r_1 and r_2 respectively at 11.7 T. Comparison with commercial mixed Fe_3O_4/γ-Fe_2O_3 contrast agent Endorem shows lower T_2 relaxation rates, however Endorem contains nanoparticles of much larger sizes (hydrodynamic radius 120-180 nm[186]), and thus have a larger magnetic moment. There are no commercial contrast agents with similar particle size to those prepared for comparison.

Cation doping of γ-Fe_2O_3 nanoparticles with Dy^{3+} ions was carried out to synthesize a $Fe_{2-x}Dy_xO_3$ nanoparticle series, prepared *via* the same co-precipitation technique as γ-Fe_2O_3 nanoparticles. Due to the larger magnetic moment of dysprosium compared to iron, substitution of x amount of Fe^{3+} ions with Dy^{3+} ions will increase the overall magnetic moment of the nanoparticles. PXRD patterns indicate single phase nanoparticles were prepared up to x =0.06.

The T_2 relaxation rate of the prepared compound $Fe_{1.99}Dy_{0.01}O_3$ is 51.738 $mM^{-1}s^{-1}$ at 11.7 T shows an increase in the transverse relaxation times at high magnetic field strengths

compared with the T_2 relaxation rate of γ-Fe_2O_3. This suggests that these materials have the potential to be used as high magnetic field strength contrast agents. Further work is needed to study how the changing ratios of Dy^{3+}:Fe^{3+} affect the magnetic properties.

Gd^{3+} ions are used as T_1 contrast agents, whereas iron oxide is typically T_2 contrast agent. The nanoparticle series $Fe_{2-x}Gd_xO_3$ was prepared in an attempt to combine the two relaxation characteristics and create dual T_1-T_2 contrast agents.

PXRD patterns indicate single phase spinel type $Fe_{2-x}Gd_xO_3$ nanoparticles were obtained for $0 \leq x \leq 0.19$. However, the substitution of Fe^{3+} ions with Gd^{3+} ions in the γ-Fe_2O_3 lattice has varying effects on both the longitudinal and transverse relaxation properties of the nanoparticles. This may be due to inhomogeneous distribution of the Gd^{3+} throughout the octahedral sites of the iron oxide lattice. The $Fe_{2-x}Gd_xO_3$ nanoparticles for $0.01 \leq x \leq 0.27$ possess higher T_1 relaxation properties at 11.7 T when compared to both γ-Fe_2O_3 and Gd_2O_3 nanoparticles. Furthermore, significant improvements in the T_2 relaxivity have been observed at 3 T for $Fe_{1.96}Gd_{0.04}O_3$, $Fe_{1.78}Gd_{0.22}O_3$ and $Fe_{1.27}Gd_{0.73}O_3$ nanoparticles. From this series, the highest T_1 and T_2 relaxivities were obtained by the $Fe_{1.96}Gd_{0.04}O_3$ solid solution at both 3 T and 11.7 T, with a T_2 relaxivity of 144.56 $mM^{-1}s^{-1}$ at 3 T increasing to 225.93 $mM^{-1}s^{-1}$ at 11.7 T; suggesting this compound has the potential to be used as a dual T_1-T_2 contrast agent. Further study of this compound is required to determine the distribution of the cations throughout the lattice and to understand how the cation substitution affects the exchange interactions and magnetic properties.

Study of alternative metal oxide nanoparticles as potential MRI contrast agents was also performed. Initially, Gd_2O_3 nanoparticles prepared by calcination were investigated as an alternative to the more common longitudinal contrast agents, Gd^{3+} chelate complexes. At 3T, T_1 and T_2 relaxation rates for the prepared Gd_2O_3 nanoparticles were 1.691 $mM^{-1}s^{-1}$

and 2.849 $mM^{-1}s^{-1}$ respectively. Whereas Magnevist (Gd- DTPA) at 3 T, has a T_1 relaxation rate of 5.39 $mM^{-1}s^{-1}$. Improvement of the relaxation characteristics was attempted by cation doping of Gd_2O_3 nanoparticles with Mn^{2+} ions, to yield the nanoparticle series $Gd_{2-x}Mn_xO_3$.

The preparation of single phase $Gd_{2-x}Mn_xO_3$ nanoparticles was achieved up to x=0.21. After cation doping of Gd_2O_3 with Mn^{2+} ions T_1 relaxation rates tripled, obtaining r_1 values of 10.317 $mM^{-1}s^{-1}$ for x = 0.02 at 3 T. Further increase of Mn^{2+} content has limited subsequent effects on T_1 relaxation rates at 3 T, and T_1 relaxation rates at 11.7 T are almost unchanged. However, T_2 relaxation rates show a steady increase at both 3 T and 11.7 T with increasing Mn^{2+} content. $Gd_{1.79}Mn_{0.21}O_3$ possesses the highest T_2 relaxivity of this nanoparticle series at 58.055 $mM^{-1}s^{-1}$ at 11.7 T, 32 times greater than Gd_2O_3 nanoparticles. One possible reason for this is the larger nanoparticle diameter of the $Gd_{1.79}Mn_{0.21}O_3$ compound, however similar T_2 effects are seen for $Gd_{1.90}Mn_{0.10}O_3$ nanoparticles, which have a particle diameter of approximately 27 nm, similar to that of the prepared Gd_2O_3 nanoparticles. In this case, the T_2 relaxivity is roughly 23 times greater than that of the prepared Gd_2O_3 nanoparticles.

Furthermore, all three $Gd_{2-x}Mn_xO_3$ ($0.01 \leq x \leq 0.21$) compounds prepared have low r_2/r_1 ratios, indicating a potential for use as a dual T_1-T_2 contrast agent at 3 T, and also at 11.7 T for x=0.02.

Further cation doping of Gd_2O_3 nanoparticles was carried out with Fe^{3+} ions. Similarly to the $Fe_{2-x}Gd_xO_3$ nanoparticles series it was hoped that the combination of Gd^{3+} and Fe^{3+} ions would result in a dual T_1-T_2 contrast agent. The $Gd_{2-x}Fe_xO_3$ were prepared by calcination at 600 °C, although PXRD indicates that at this temperature the nanoparticles are a mixture of $Gd_{2-x}Fe_xO_3$ and unidentified impurities. Nonetheless, relaxation rates

were obtained and indicate that these nanoparticles improve T_1 relaxation rates at 3 T and T_2 relaxation rates at both 3 T and 11.7 T. Further work is needed to adequately identify the impurities present and to optimise the reaction conditions to synthesize single phase $Gd_{2-x}Fe_xO_3$ nanoparticles.

Further to the study of Gd_2O_3 nanoparticles, Dy_2O_3 nanoparticles were investigated as potential T_2 contrast agents. Synthesis by calcination provided single phase Dy_2O_3 nanoparticles, confirmed by PXRD. The relaxation properties were characterised and the Dy_2O_3 nanoparticles proved to be less effective contrast agents than γ-Fe_2O_3 nanoparticles of similar sizes. Whilst novel, single phase $Dy_{2-x}Fe_xO_3$ nanoparticles were achieved for $0.02 \leq x \leq 0.09$, cation doping of the Dy_2O_3 nanoparticles with Fe^{3+} ions only resulted in a reduction in both r_1 and r_2 values at both 3 T and 11.7 T magnetic field strengths.

The final compound described in this work is $Fe_2O_{3-x}F_{2x}$. These novel, anion doped iron oxide nanoparticles have been found to possess excellent T_2 relaxation rates at 3 T, 12 times greater than the γ-Fe_2O_3 nanoparticles of similar size presented in this work (136.53 $mM^{-1}s^{-1}$ vs. 11.44 $mM^{-1}s^{-1}$). Not only that, the nanoparticles show high relaxation rates at 11.7 T for both T_1 and T_2 relaxation indicating that these nanoparticles could be used as high magnetic field strength contrast agents.

Furthermore, the increase in relaxation rates provided by this compound will improve the detail in the MR image collected to a greater extent than those of Fe_2O_3 nanoparticles. This allows a lower dosage of the nanoparticles to be administered to the patient, lowering the risk of toxicity without compromising on the MRI sensitivity.

Due to time constraints it was not possible to completely characterise each set of solid solutions presented. Further work is required to determine the structure of the compounds, in order to understand how the magnetic properties are affected by cation and anion doping. Additionally, further optimisation of the nanoparticle surface coating is needed to improve the hydrophilic properties of the compounds. It would also be worthwhile to carry out cytotoxicity tests to understand whether the compounds prepared would be suitable for use *in vivo.*

9 REFERENCES

1. C. S. Levin, *Proc. IEEE*, 2008, **96**, 439-467.
2. Z. R. Stephen, F. M. Kievit and M. Zhang, *Mater. Today*, 2011, **14**, 330-338.
3. C. Lapa, T. Reiter, X. Li, R. A. Werner, S. Samnick, R. Jahns, A. K. Buck, G. Ertl and W. R. Bauer, *Int. J. Cardiol.*, 2015, **194**, 44-49.
4. P. Caravan, J. J. Ellison, T. J. McMurry and R. B. Lauffer, *Chem. Rev.*, 1999, **99**, 2293-2352.
5. A. Figuerola, R. Di Corato, L. Manna and T. Pellegrino, *Pharmacol. Res.*, 2010, **62**, 126-143.
6. M. A. Brown, *MRI: basic principles and applications*, Wiley-Liss, Hoboken, NJ, 2003.
7. U. I. Tromsdorf, O. T. Bruns, S. C. Salmen, U. Beisiegel and H. Weller, *Nano Lett.*, 2009, **9**, 4434-4440.
8. C. W. Jung and P. Jacobs, *Magn. Reson. Imaging*, 1995, **13**, 661-674.
9. R. M. Cornell and U. Schwertmann, *The Iron Oxides: Structure, Properties, Reactions, Occurences and Uses*, WILEY-VCH, 2003.
10. J. P. Jakubrovics, *Magnetism and Magnetic Materials*, The Institute of Materials, 1994.
11. B. Subhankar and K. Wolfgang, *J. Phys. D: Appl. Phys.*, 2009, **42**, 13001-13028.
12. H. Onishi and T. Hotta, *New J. Phys.*, 2004, **6**, 193-210.
13. L. E. Smart and E. A. Moore, *Solid State Chemistry - An introduction*, CRC Press, 2005.
14. R. J. D. Tilley, *Understanding Solids: the science of materials*, John Wiley and Sons Ltd, Chichester, 2004.
15. G. F. Dionne, *Magnetic Oxides*, Springer, 2009.
16. L. Machala, J. Tuček and R. Zbořil, *Chem. Mater.*, 2011, **23**, 3255-3272.
17. E. Tronc, C. Chaneac and J. P. Jolivet, *J. Solid State Chem.*, 1998, **139**, 93-104.
18. A. S. Teja and P.-Y. Koh, *Prog. Cryst. Growth Charact. Mater.*, 2009, **55**, 22-45.
19. R. Grau-Crespo, A. Y. Al-Baitai, I. Saadoune and N. H. De Leeuw, *J. Phys.: Condens. Matter*, 2010, **22**.
20. T. Neuberger, B. Schopf, H. Hofmann, M. Hofmann and B. von Rechenberg, *J. Magn. Magn. Mater.*, 2005, **293**, 483-496.
21. O. Veiseh, J. W. gunn and M. Zhang, *Adv. Drug Deliv. Rev.*, 2010, **62**, 284-304.
22. S. Laurent, S. Dutz, U. O. Haefeli and M. Mahmoudi, *Adv. Colloid Interface Sci.*, 2011, **166**, 8-23.
23. P. Drake, H.-J. Cho, P.-S. Shih, C.-H. Kao, K.-F. Lee, C.-H. Kuo, X.-Z. Lin and Y.-J. Lin, *J. Mater. Chem.*, 2007, **17**, 4914-4918.
24. F. Hu, Q. Jia, Y. Li and M. Gao, *Nanotechnology*, 2011, **22**, 245604.
25. A. Bjornerud and L. Johansson, *NMR Biomed.*, 2004, **17**, 465-477.
26. E. J. W. Verwey and E. L. Heilmann, *J. Chem. Phys.*, 1947, **15**, 174-180.
27. C. A. Gorski and M. M. Scherer, *Am. Mineral.*, 2010, **95**, 1017-1026.
28. D. S. Mathew and R.-S. Juang, *Chem. Eng. J.*, 2007, **129**, 51-65.
29. Y. Gossuin, P. Gillis, A. Hocq, Q. L. Vuong and A. Roch, *Wiley Interdisciplinary Reviews: Nanomedicine and Nanobiotechnology*, 2009, **1**, 299-310.
30. C. Greaves, *J. Solid State Chem.*, 1983, **49**, 325-333.
31. W. H. Bragg, *Nature*, 1915, **95**, 561.

32. J. E. Jorgensen, L. Mosegaard, L. E. Thomsen, T. R. Jensen and J. C. Hanson, *J. Solid State Chem.*, 2007, **180**, 180-185.
33. B. R. V. Narasimhan, S. Prabhakar, P. Manohar and F. D. Gnanam, *Mater. Lett.*, 2002, **52**, 295-300.
34. M. A. Gabal, A. A. El-Bellihi and S. S. Ata-Allah, *Mater. Chem. Phys.*, 2003, **81**, 84-92.
35. A. Angermann and J. Töpfer, *Journal of Materials Science*, 2008, **43**, 5123-5130.
36. B. H. Kim, N. Lee, H. Kim, K. An, Y. Il Park, Y. Choi, K. Shin, Y. Lee, S. G. Kwon, H. B. Na, J.-G. Park, T.-Y. Ahn, Y.-W. Kim, W. K. Moon, S. H. Choi and T. Hyeon, *J. Am. Chem. Soc.*, 2011, **133**, 12624-12631.
37. R. Massart, *IEEE transactions on magnetics*, 1981, **17**, 1247-1248.
38. W. Kim, C.-Y. Suh, S.-W. Cho, K.-M. Roh, H. Kwon, K. Song and I.-J. Shon, *Talanta*.
39. M. D. Carvalho, F. Henriques, L. P. Ferreira, M. Godinho and M. M. Cruz, *J. Solid State Chem.*, 2013, **201**, 144-152.
40. H. Iida, K. Takayanagi, T. Nakanishi and T. Osaka, *J. Colloid Interface Sci.*, 2007, **314**, 274-280.
41. B. R. Jarrett, M. Frendo, J. Vogan and A. Y. Louie, *Nanotechnology*, 2007, **18**, 035603.
42. E. D. Smolensky, H.-Y. E. Park, Y. Zhou, G. A. Rolla, M. Marjanska, M. Botta and V. C. Pierre, *J. Mater. Chem. B*, 2013, **1**.
43. C. Hu, Z. Gao and X. Yang, *J. Magn. Magn. Mater.*, 2008, **320**, L70-L73.
44. Jong Hee Kim, Chang Hyun Lee and Sang Kuk Lee, *Bull. Korean Chem. Soc.*, 2009, **30**, 1305-1308.
45. J. Lu, S. Ma, J. Sun, C. Xia, C. Liu, Z. Wang, X. Zhao, F. Gao, Q. Gong, B. Song, X. Shuai, H. Ai and Z. Gu, *Biomaterials*, 2009, **30**, 2919-2928.
46. S. Mohapatra, S. R. Rout and A. B. Panda, *Colloids and Surfaces A: Physicochemical and Engineering Aspects*, **384**, 453-460.
47. R. N. Panda, J. C. Shih and T. S. Chin, *J. Magn. Magn. Mater.*, 2003, **257**, 79-86.
48. C. R. De Silva, S. Smith, I. Shim, J. Pyun, T. Gutu, J. Jiao and Z. Zheng, *J. Am. Chem. Soc.*, 2009, **131**, 6336-6337.
49. S. Sun, H. Zeng, D. B. Robinson, S. Raoux, P. M. Rice, S. X. Wang and G. Li, *J. Am. Chem. Soc.*, 2004, **126**.
50. C. Barcena, A. K. Sra, G. S. Chaubey, C. Khemtong, J. P. Liu and J. Gao, *Chem. Commun.*, 2008, **0**, 2224-2226.
51. J. H. Kim;, C. H. Lee; and S. K. Lee, *Bull. Korean Chem. Soc.*, 2009, **30**, 1305-1308.
52. C. Barcena, A. K. Sra, G. S. Chaubey, C. Khemtong, J. P. Liu and J. Gao, *Chem. Commun.*, 2008, **19**, 2224-2226.
53. C. Yao, Q. Zeng, G. F. Goya, T. Torres, J. Liu, H. Wu, M. Ge, Y. Zeng, Y. Wang and J. Z. Jiang, *Journal of Phyical Chemistry C*, 2007, **111**, 12274-12278.
54. J. Liu, Y. Bin and M. Matsuo, *J. Phys. Chem. C*, 2011, **116**, 134-143.
55. J. F. Hochepied, P. Bonville and M. P. Pileni, *J. Phys. Chem. B*, 2000, **104**, 905-912.
56. J. Nam, N. Won, J. Bang, H. Jin, J. Park, S. Jung, S. Jung, Y. Park and S. Kim, *Advanced Drug Delivery Reviews*, 2013, **65**, 622-648.
57. J. Shen, L. Zhao and G. Han, *Advanced Drug Delivery Reviews*, 2013, **65**, 744-755.

58. M. R., Kjellman.P., Olsson.F., Wingardh.K., Ingvar.C., Stahlberg.F., Olsrud.J., Latt.J., Fredriksson.S., Knuttson.L. and Strand.S., *Journal of Nuclear Medicine*, 2012, **53**, 459-463.
59. H.-J. Lee, L. Li;, k. Chen, A. R. Hsu, C. Xu, J. Xie, S. Sun and X. Chen, *J Nucl Med*, 2008, **49**, 1371-1379.
60. U. I. Tromsdorf, N. C. Bigall, M. G. Kaul, O. T. Bruns, M. S. Nikolic, W. Parak, S. Forster, U. Beisiegel, G. Adam and H. Weller, *Nano Lett.*, 2007, **7**, 2422-2427.
61. E. D. Smolensky, H.-Y. E. Park, T. S. Berquo and V. C. Pierre, *Contrast Media Mol. Imaging*, 2009, **6**, 189-199.
62. L. Faucher, m. Tremblay, J. Lagueux, Y. Goussin and M.-A. Fortin, *ACS Appl. Mater. Inter.*, 2012, **4**, 4506-4515.
63. J.-L. Bridot, D. Dayde, C. Riviere, C. Mandon, C. Billotey, S. SLerondel, R. Sabattier, G. Cartron, A. Le Pape, G. Blondiaux, M. Janier, P. Perriat, S. Roux and O. Tillement, *J. Mater. Chem.*, 2009, **19**, 2328-2335.
64. S. Adachi, X. J. Wu, T. Tamura, T. Tatsuki, A. Tokiwa-Yamamoto and K. Tanabe, *Physica C: Superconductivity*, 1997, **291**, 59-66.
65. E. E. McCabe and C. Greaves, *J. Fluorine Chem.*, 2007, **128**, 448-458.
66. E. I. Ardashnikova, S. V. Lubrsky, D. I. Denisenko, R. V. Shpanchenko, E. V. Antipov and G. V. Tendeloo, *Physica C*, 1995, **253**, 259-265.
67. M. G. Francesconi, P. R. Slater, J. P. Hodges, C. Greaves, P. P. Edwards, M. Al-Mamouri and M. Slaski, *J. Solid State Chem.*, 1998, **135**, 17-27.
68. Y. J. C. Y. L. C. y. Y. Y. Z. Y. Zhao, *J Supercond Nov Magn*, 2010, **23**, 625-628.
69. H. Wang and J. P. Lewis, *J. Phys.: Condens. Matter*, 2006, **18**, 421.
70. Y. Lin, S. Lin, M. Luo and J. Liu, *Mater. Lett.*, 2009, **63**, 1169-1171.
71. M. Tang, O. Lu, J. A. Valdez, C. R. Stanek and K. E. Sickafus, *Physica Status Solidi C*, 2007, **4**, 1171-1174.
72. D. J. M. Bevan and R. L. Martin, *J. Solid State Chem.*, 2009, **181**, 2250-2259.
73. M. Tang, J. A. Valdez, K. E. Sickafus and P. Lu, *JOM*, 2007, **59**, 36-39.
74. M. Tang, J. A. Valdez, P. Lu, G. E. Gosnell, C. J. Wetteland and K. E. Sickafus, *J. Nucl. Mater.*, 2004, **328**, 71-76.
75. N. Sakai, L. Zhu, A. Kurokawa, H. Takeuchi, S. Yano, T. Yanoh, N. Wada, S. Taira, Y. Hosokai, A. Usui, Y. Machida, H. Saito and Y. Ichiyanagi, *J. Phys. Conf. Ser.*, 2011, **352**, 012008.
76. R. Bazzi, M. A. Flores, C. Louis, K. Lebbou, W. Zhang, C. Dujardin, S. Roux, B. Mercier, G. Ledoux, E. Bernstein, P. Perriat and o. Tillement, *J. Colloid Interface Sci.*, 2004, **273**, 191-197.
77. B. M. Abu-Zied and A. M. Asiri, *J Rare Earth*, 2014, **32**, 259-264.
78. M. Salavati-Niasari, J. Javidi, F. Davar and A. A. Fazl, *J. Alloys Compd.*, 2010, **503**, 500-506.
79. E. Terreno, D. D. Castelli, A. Viale and S. Aime, *Chem. Rev.*, 2010, **110**, 3019-3042.
80. C. Schweiger, P. Gil, W. Parak and T. Kissel, *J. Control. Release*, 2010, **148**, e67-68.
81. S. Cotton, *Lanthanide and Actinide Chemistry*, John Wiley & Sons, Ltd, 2006.
82. R. Mout, M. D. F., S. Rana and V. M. Rotello, *Chem. Soc. Rev.*, 2012, **41**, 2539-2544.
83. C. Fang and M. Zhang, *J. Mater. Chem.*, 2009, **19**, 6528-6266.
84. M. Bottrill, L. Kwok and N. Long, *Chem. Soc. Rev.*, 2006, **35**, 557-571.

85. J. E. Rosen, L. Chan, D.-B. Shieh and F. X. Gu, *Nanomedicine: Nanotechnology, Biology and Medicine*, 2012, **8**, 275-290.
86. B. A. Smith and B. D. Smith, *Bioconjugate Chem.*, 2012, **23**, 1989-2006.
87. M. Răcuciu, D. Creangă and A. Airinei, *The European Physical Journal E: Soft Matter and Biological Physics*, 2006, **21**, 117-121.
88. A. Ruiz, G. Salas, M. Calero, Y. Hernández, A. Villanueva, F. Herranz, S. Veintemillas-Verdaguer, E. Martínez, D. F. Barber and M. P. Morales, *Acta Biomaterialia*, 2013, **9**, 6421-6430.
89. N. T. K. Thanh and L. A. W. Green, *Nano Today*, 2010, **5**, 213-230.
90. N. Lee and T. Hyeon, *Chemistry Society Reviews*, 2012, **41**, 2575-2589.
91. K. H. Bae, Y. B. Kim, Y. Lee, J. Y. Hwang, H.-W. Park and T. G. Park, *Bioconjugate Chem.*, 2010, **21**, 505-512.
92. J. Y. Park, M. J. Baek, E. S. Choi, S. Woo, J. H. Kim, T. J. Kim, J. C. Jung, L. S. Chae, Y. Chang and G. H. Lee, *ACS Nano*, 2009, **3**, 3663-3669.
93. M. Engstrom, A. Klasson, H. Pedersen, C. Vahlberg, P.-O. Kall and K. Uvdal, *Magn. Reson. Mater. Phys., Biol. Med.*, 2006, **19**, 180-186.
94. Y.-W. Jun, J.-H. Lee and J. Cheon, *Angew. Chem. Int. Ed.*, 2008, **47**, 5122-5135.
95. Y.-W. J. Wang, *Quant. Imaging Med. Surg.*, 2011, **1**, 35-40.
96. E. V. Gopalan, I. A. Al-Omari, K. A. Malini, P. A. Joy, D. S. Kumar, Y. Yoshida and M. R. Anantharaman, *J. Magn. Magn. Mater.*, 2009, **321**, 1092-1099.
97. A. K. Gupta and M. Gupta, *Biomaterials*, 2005, **26**, 3995-4021.
98. Z. Amoozgar and Y. Yeo, *WIREs: Nanomed. Nanobio,*, 2012, **4**, 219-233.
99. D. W. McRobbie, *MRI from picture to proton*, Cambridge University Press, Cambridge, 2003.
100. M. Muthiah, I.-K. Park and C.-S. Cho, *Biotechnol. Adv.*
101. K. Donadel, M. D. V. Felisberto, V. T. Fávere, M. Rigoni, N. J. Batistela and M. C. M. Laranjeira, *Materials Science and Engineering: C*, 2008, **28**, 509-514.
102. G. Liu, R. Y. Hong, L. Guo, Y. G. Li and H. Z. Li, *Appl. Surf. Sci.*, **257**, 6711-6717.
103. P. Ja Young, D. Patel, L. Gang Ho, W. Seungtae and C. Yongmin, *Nanotechnology*, 2008, **19**, 365603.
104. R. Y. Honga, B.Fenga, L.L.Chena, G. H. Liuc, H. Z. Li, Y. Zheng and D.G.Wei, *Biochem. Eng. J.*, 2008, **42**, 290-300.
105. A. Sarawathy, S. S. Nazeer, N. Nimi, S. Arummugam, S. Shenoy and R. S. Jayasree, *Carbohydr. Polym.*, 2014, **101**, 760-768.
106. D. P. J. Pan, A. H. Schmieder, S. A. Wickline and G. M. Lanza, *Tetrahedron*, 2011, **67**, 8431-8444.
107. O. Veiseh, C. Sun, C. Fang, N. Bhattarai, J. W. Gunn, F. Kievit, K. Du, B. Pullar, D. Lee, R. G. Ellenbogen, J. olson and M. Zhang, *Clin. Cancer Res.*, 2009, **69**, 6200-6207.
108. Dann.S, *Reactions and Characterisation of Solids*, Royal Society of Chemistry, Cambridge UK, 2000.
109. H. P. Klug, *X-ray diffraction procedures for polycrystalline and amorphous materials*, Chapman and Hall, New York, 1954.
110. M. T. Weller, T. Overton, J. Rourke, F. A. Armstrong and P. W. Atkins, *Inorganic Chemistry*, Sixth edn., Oxford University Press, Oxford, 2014.
111. D. A. Skoog, F. J. Holler and S. R. Crouch, *Principles of Instrumental Analysis*, Sixth edn., Thomson Brooks/Cole, USA, 2007.

112. J. H. Newhouse, *Understanding MRI*, Little Brown, Boston USA, 1991.
113. C. Westbrook, *MRI at a glance*, Wiley-Blackwell, Chichester, UK, 2010.
114. E. Perez-Mayoral, V. Negri, J. Soler-Padros, S. Cerdan and P. Ballesteros, *European Journal of Radiology*, 2008, **67**, 453-458.
115. A. Roch, R. N. Muller and P. Gillis, *J. Chem. Phys.*, 1999, **110**, 5403-5411.
116. D. P. E. Dickson and F. J. Berry, *Mossbauer Spectroscopy*, The Press Syndicate of the University of Cambridge, Cambridge UK, 1986.
117. A. Maddock, *Mossbauer spectroscopy: principles and applications*, Albion Publishing, Chichester, 1996.
118. N. N. Greenwood and T. C. Gibb, *Mossbauer spectroscopy*, Chapman and Hall, London, 1971.
119. H. B. Na, I. C. Song and T. Hyeon, *Adv. Mater.*, 2009, **21**, 2133-2148.
120. D. L. J. Thorek, A. Chen, J. Czupryna and A. Tsourkas, *Annals of Biomedical Engineering*, 2006, **34**, 23-38.
121. A.-H. Lu, E. L. Salabas and F. Schueth, *Angew. Chem. Int. Ed.*, 2007, **46**, 1222-1244.
122. Y.-X. J. Wang, S. M. Hussain and G. P. Krestin, *European Radiology*, 2001, **11**, 2319-2331.
123. M. Gotic, G. Koscec and S. Music, *J. Mol. Struct.*, 2009, **924-926**, 347-354.
124. J. S. Salazar, L. Perez, O. De Abril, L. T. Phuoc, D. Ihiawkrim, M. Vazquez, J. M. Greneche, S. Begin-Colin and G. Pourroy, *Chem. Mater.*, 2011, **23**, 1379-1386.
125. D. Yoo, J.-H. Lee, T.-H. Shin and J. Cheon, *Acc. Chem. Res.*, 2011, **44**, 863-874.
126. M. Mahmoudi, S. Sant, B. Wang, S. Laurent and T. Sen, *Adv. Drug Deliv. Rev.*, 2011, **63**, 24-46.
127. K. Hola, Z. Markova, G. Zoppellaro, J. Tucek and R. Zboril, *Biotechnol. Adv.*, 2015.
128. N. Xiao, W. Gu, H. Wang, Y. Deng, X. Shi and L. Ye, *J. Colloid Interface Sci.*, 2014, **1**, 159-165.
129. H. Yang, Y. Zhuang, Y. Sun, A. Dai, X. Shi, D. Wu, F. Li, H. Hu and S. Yang, *Biomaterials*, 2011, **32**, 4584-4593.
130. E. Taboada, E. Rodriguez, A. Roig, J. Oro, A. Roch and R. N. Muller, *Langmuir*, 2007, **23**, 4583-4588.
131. C. Pecharronman, T. Gonzalez-Carreno and J. E. Inglesias, *Phys. Chem. Miner.*, 1995, **22**, 21-29.
132. P. B. V, *HighScore Plus*, (2012).
133. B. V. Crist, *Handbook of Monochromatic XPS Spectra, The Elements of Native Oxides*, Wiley, 2000.
134. J. B. Yang, X. D. Zhou, W. B. Yelon, W. J. James and Q. Cai, *J. Appl. Phys.*, 2004, **95**, 7540.
135. J. M. Daniels and A. Rosencwaig, *J. Phys. Chem. Solids*, 1969, **30**, 1561-1571.
136. J. S. Salazar, L. Perez, O. de Abril, T. P. Lai, D. Ihiawakrim, M. Vazquez, J. M. Greneche, S. Begin-Colin and G. Pourroy, *Chem. Mater.*, 2011, **23**, 1379-1386.
137. N.-N. Song, H.-T. Yang, H.-L. Liu, X. Ren, H.-F. Ding, X.-Q. Zhang and Z.-H. Cheng, *Sci. Rep.*, 2013, **3**, 3161-3165.
138. I. Rhee, *Journal of the Korean Physical Society*, 2009, **54**, 1721-1724.
139. R. D. Shannon and C. T. Prewitt, *Acta Crystallogr. Sect. B: Struct. Sci.*, 1969, **25**.

140. S. Chakrabarti, S. K. Mandal and S. Chaudhuri, *Nanotechnology*, 2005, **16**, 506-511.
141. H. Yang, C. Zhang, X. Shi, H. Hu, X. Du, Y. Fang, Y. Ma, H. Wu and S. Yang, *Biomaterials*, 2010, **31**, 3667-3673.
142. Y.-I. Kim, W. B. Im, M. K. Jeon, Y.-H. Lee, K.-B. Kim and K.-S. Ryu, *J. Nanosci. and Nanotechnol.*, 2011, **11**, 810-814.
143. L. B. Tahar, M. Artus, S. Ammar, L. S. Smiri, F. Herbst, M.-J. Vaulay, V. Richard, J. M. Greneche, F. Villain and F. Fievet, *J. Magn. Magn. Mater.*, 2008, **320**, 3242-3250.
144. C. E. Johnson, L. Costa, S. Gray, J. A. Johnson, A. J. Krejci, S. A. Hasan, I. Gonzaol-Juan and J. H. Dickerson, *Mossbauer Measurements on Spinel-structure Iron Oxide Nanoparticles*, Wagga Wagga, NSW, Australia, 2012.
145. Y. Goussin, A. Hocq, Q. L. Vuong, S. Disch, R. P. Hermann and P. Gillis, *Nanotechnology*, 2008, **19**, 475101-475108.
146. T. Tsuzuki, E. Pirault and P. G. McCormick, *Nanostruct. Mater.*, 1999, **11**, 125-131.
147. L. Zhou, Z. Gu, X. Liu, W. Yin, G. Tian, L. Yan, S. Jin, W. Ren, G. Xing, W. Li, X. Chang, Z. Hu and Y. Zhao, *J. Mater. Chem.*, 2012, **22**, 966-974.
148. G. Azizian, N. Riyahi-Alam, S. Hoghgoo, H. R. Moghimi, R. Zohdiagdam, B. Rafei and E. Gorji, *Nanoscale Res. Lett.*, 2012, **7**, 549-559.
149. M. Norek, E. Kampert, U. Zeitler and J. A. Peters, *J. Am. Chem. Soc.*, 2008, **130**, 5335-5340.
150. K. Kattel, J. Y. Park, W. Xu, H. G. Kim, E. J. Lee, B. A. Bony, W. C. Heo, S. Jin, J. S. Baeck, Y. Chang, T. J. Kim, J. E. Bae, K. S. Chae and G. H. Lee, *Biomaterials*, 2012, **33**, 3254-3261.
151. H. A. I. Y. Tok, F. Y. C. Boey, R. Huebner and S. H. Ng, *J. Electroceram.*, 2006, **17**, 75-78.
152. G. K. Das, Y. Zhang, L. D'Silva, P. Padmanabhan, B. C. Heng, J. S. C. Loo, S. T. Selvan, K. K. Bhakoo and T. T. Y. Tan, *Chem. Mater.*, 2011, **23**, 2439-2446.
153. H. B. Na, J. H. Lee, K. An, Y. I. Park, M. Park, I. S. Lee, D.-H. Nam, S. T. Kim, S.-H. Kim, S.-W. Kim, K.-H. Kim, K.-S. Kim, S.-O. Kim and T. Hyeon, *Angew. Chem. Int. Ed.*, 2007, **46**, 5397-5401.
154. G. H. Im, S. M. Kim, D.-G. Lee, W. J. Lee, J. H. Lee and I. S. Lee, *Biomaterials*, 2013, **34**, 2069-2076.
155. E. S. Choi, J. Y. Park, M. J. Baek, W. Xu, K. Kattel, J. H. Kim, v. Lee, v. Chang, T. J. Kim, J. E. Bae, K. S. Chae, K. J. Suh and G. H. Lee, *Eur. J. Inorg. Chem.*, 2010, 4555-4560.
156. H. Xiao, P. Li, F. jia and L. Zhang, *J. Phys. Chem. C*, 2009, **113**, 21034-21041.
157. B. Antic, P. Onnerud, D. Rodic and R. Tellgren, *Powder Diffr.*, 1993, **8**, 216-220.
158. R. Qiao, C. Yang and M. Gao, *J. Mater. Chem.*, 2009, **19**, 6274-6293.
159. J.-H. Lee, Y.-M. Huh, Y.-w. Jun, J.-w. Seo, J.-t. Jang, H.-T. Song, S. Kim, E.-J. Cho, H.-G. Yoon, J.-S. Suh and J. Cheon, *Nature Medicine*, 2007, **13**, 95-99.
160. S. Mohapatra, S. R. Rout and A. B. Panda, *Colloids and Surfaces A: Physicochemical and Engineering Aspects*, **384**, 453-460.
161. E. I. Ardashnikova, S. V. Lubrsky, D. I. Denisenko, R. V. Shpanchenko, E. V. Antipov and G. V. Tendeloo, *Physica C*, 1995, **253**, 259-265.
162. Y. J. Cui, Y. L. Chen, Y. Yang, Y. Zhang and Y. Zhao, *J Supercond Nov Magn*, 2010, **23**, 625-628.

163. H.-Y. Lee;, Z. Li;, K. Chen;, A. R. Hsu;, C. Xu;, J. Xie;, S. Sun; and X. Chen, *J Nucl Med*, 2008, **49**, 1371-1379.
164. P. R. Slater, J. P. Hodges, M. Grazia. Francesconi, C. Greaves and M. Slaski, *J. Mater. Chem.*, 1997, **7**, 2077-2083.
165. J. Sheng, K. Tang, Z. Liang, Y. Wang, D. Wang and W. Zhang, *Mater. Chem. Phys.*, 2009, **115**, 483-487.
166. J. V. Jokerst, T. Lobovkina, R. N. Zare and S. S. Gambhir, *Nanomedicine*, 2011, **6**, 715-728.
167. C. Sun, K. Du, C. Fang, N. Bhattarai, O. Veiseh, F. Kievit, Z. Stephen, D. Lee, R. G. E. bogen, B. Ratner and M. Zhang, *ACS Nano*, 2010, **4**, 2402-2410.
168. K. Kumar, A. M. Nightingale, S. H. Krishnadsan, K. N., M. Wylenzinska-Arridge, K. Zeissler, W. R. Branford, E. Ware, A. J. deMello and J. C. deMello, *J. Mater. Chem.*, 2012, **22**.
169. S. Mornet, J. Portier and E. Duguet, *J. Magn. Magn. Mater.*, 2005, **293**, 127-134.
170. A. Masoudi, H. R. Madaah, Hosseini, M. A. Shokrgozar, R. Ahmadi and M. A. Oghabian, *Int. J. Pharm.*, 2012, **433**, 129-141.
171. S. Nigam, K. C. Barick and D. Bahadur, *J. Magn. Magn. Mater.*, 2011, **323**, 237-243.
172. M. Racuciu, D. E. Creanga and A. Airinei, *The European Physical Journal E*, 2006, **21**, 117-121.
173. E. Cheraghipour, S. Javadpour and A. R. Mahdizadeh, *Journal of Biomedical Science and Engineering*, 2012, **5**, 715-719.
174. L. Li, K. Y. Mak, C. W. Leung, K. Y. Chan, W. Zhong and P. W. T. pong, *Microelectron. Eng.*, 2013, **110**, 329-334.
175. V. Azmeera, P. Adhikary and S. Krishnamoorthi, *International Journal of Carbohydrate Chemistry*, 2012, 7.
176. P. Caravan, C. T. Farrar, L. Frullano and R. Uppal, *Contrast Media Mol. Imaging*, 2009, **4**, 89-100.
177. M. Norek, E. Kampert, U. Zeitler and J. A. Peters, *J. Am. Chem. Soc.*, 2008, **130**, 5335-5340.
178. S. Laurent, L. V. Elst and R. Muller, *Contrast Media Mol. Imaging*, 2006, **1**, 128-137.
179. S. Laurent, L. V. Elst and R. N. Muller, *Contrast Media Mol. Imaging*, 2006, **1**, 128-137.
180. C. Schweiger, P. Gil, W. Parak and T. Kissel, *J. Controlled Release*, 2010, **148**, e67-68.
181. M. Norek and J. Peters, *Progress in Nucleat Magnetic Resonance Spectroscopy*, 2011, **59**, 64-82.
182. J. Fang, P. Chandraseskharan, X.-L. Liu, Y. Yang, Y.-B. Lv, C.-T. Yang and J. Ding, *Biomaterials*, 2014, **35**, 1636-1642.
183. Z. Liu, F. Pu, S.Huang, Q. Yuan, J. Rem and X. Qu, *Biomaterials*, 2013, **34**, 1712-1721.
184. J.-L. Bridot, A.-C. Faure, S. Laurent, C. Rivière, C. Billotey, B. Hiba, M. Janier, V. josserand, J.-L. Coll, L. V. Elst, R. Muller, S. Roux, P. Perriat and O. Tillement, *J. Am. Chem. Soc.*, 2007, **129**, 5076-5084.
185. E. S. Choi, J. Y. Park, M. J. Baek, W. Xu, K. Kattel, J. H. Kim, J. J. Lee, Y. Chang, T. J. Kim, J. E. Bae, K. S. Chae, K. J. Suh and G. H. Lee, *Eur. J. Inorg. Chem.*, 2010, 4555-4560.

186. S. laurent, D. Forge, M. Port, A. Roch, C. Robic, L. V. Elst and R. N. Muller, *Chem. Rev.*, 2008, **108**, 2064-2110.
187. R. W. C. Cheary, A. A. , *Programs XFIT and FOURYA*, (1996) CCP14 Powder diffraction Libary-Daresbury laboratory, Warrington, England

10 APPENDIX I - DEVELOPMENT OF CALIBRATION GRAPH

Eight samples containing different ratios of commercial Fe_3O_4 and γ-Fe_2O_3 nanoparticles were prepared according to Table 10-1. The mixtures of the two types of iron oxide were ground together before collecting PXRD patterns. The method reported by Kim *et al.*[38] utilises the 440 diffraction peak as this is the most resolved diffraction peaks in the magnetite and maghemite patterns. This eliminates the possibility of asymmetric peaks due to peak overlap.

Table 10-1 Percentages of Fe_3O_4 and γ-Fe_2O_3 in calibration samples

Sample No.	% Fe_3O_4 in prepared sample	% γ-Fe_2O_3 in prepared sample
1	10	90
2	20	80
3	30	70
4	40	60
5	50	50
6	60	40
7	70	30
8	80	20
9	90	10

Once three sets of data per sample had been collected, each set of diffraction peaks were deconvoluted using XFIT software,[187] the results averaged and a calibration curve calculated.

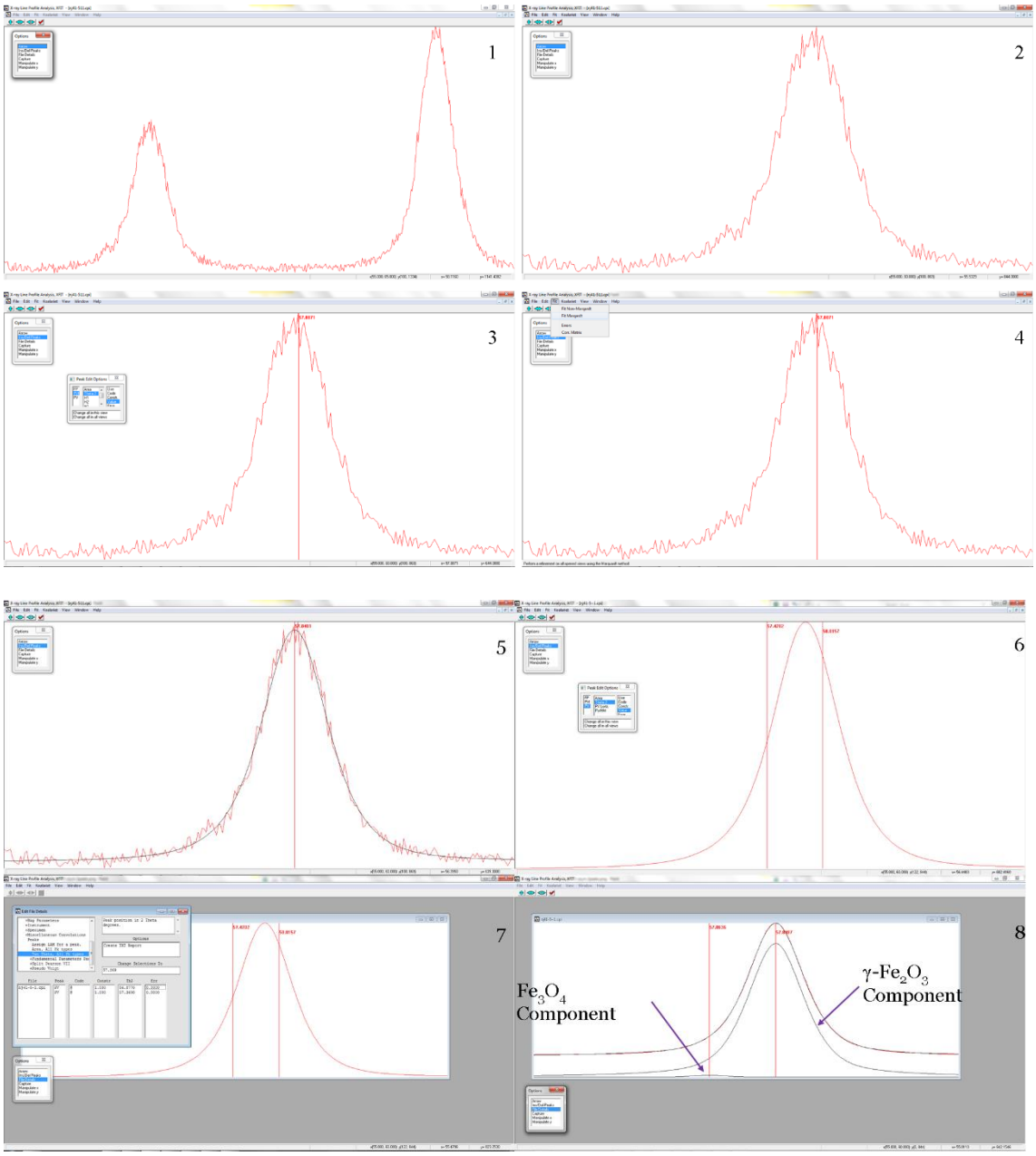

Figure 10-1 XFIT deconvolution process: ***1-2*** *PXRD diffraction patterns are collected for the 440 diffraction peak between 60-65 degrees 2 theta. The diffraction peak is isolated for deconvolution into the component parts.* ***3-5****. An asymmetric peak is fitted to the original diffraction peak data.* ***6-7****. The fitted asymmetrical peak is then deconvoluted*

*into the two symmetrical component peaks. **8**. The component peaks are resolved and the three peak areas (overall peak area, Fe_3O_4 peak area and γ-Fe_2O_3 peak area) are used to determine the phase purity.*

Initially the original data was modelled using a Pseudo-Voigt function to fit the asymmetrical diffraction peak. This calculated peak was then deconvoluted into the constituent symmetrical peaks of Fe_3O_4 and γ-Fe_2O_3. As the initial PXRD data shows no superstructure diffraction peaks at low angles (<20 2θ°) it was assumed that the cubic forms of the iron oxides were present, therefore the peak positions shown in Table 10-2 were used as starting points for the diffraction peak deconvolution process.

Table 10-2 The 440 diffraction peak positions used to calculate % constituent components in samples of iron oxide nanoparticles.

Fe_3O_4, 440 reflection (˚)	**γ-Fe_2O_3, 440 reflection (˚)**
62.455	63.001

After the peaks have been deconvoluted, the integrated peak areas were recorded as percentages of the total peak area. Equation 9-1 below was used to calculate the %Intensity for both maghemite and magnetite components in the 440 diffraction peak. This was then plotted against initial wt% in the mixtures to produces the graph in Figure 10-2. The relative mean squared error has been calculated and is shown in Table 10-3.

$$\%\mathbf{I}_{(\text{Maghemite})} = \frac{\mathbf{I}(\text{Maghemite})}{(\mathbf{I}(\text{Magnetite}) + \mathbf{I}(\text{Maghemite}))} \text{x}100 \qquad \text{Equation 9-1}$$

I = Peak intensity

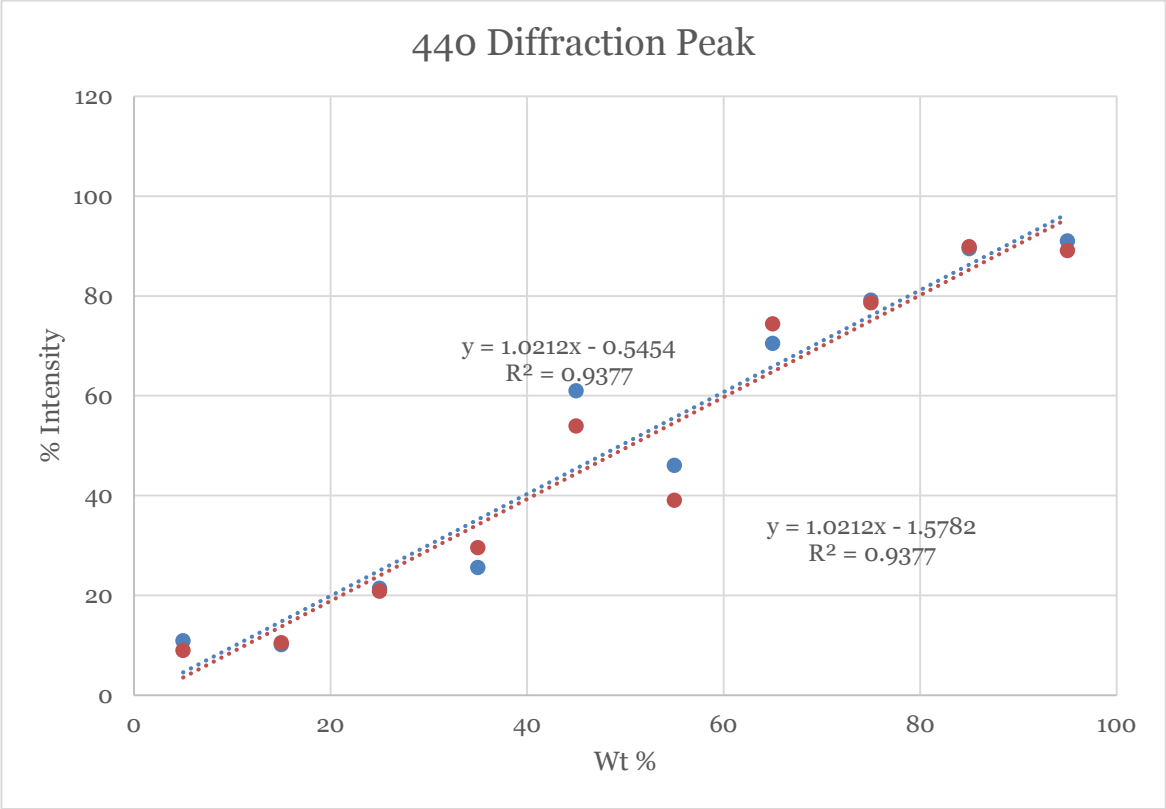

Figure 10-2 Calibration graph to quantitatively determine the magnetite (red) and maghemite (blue) components in a mixed sample using the 440 diffraction peak

Table 10-3 Calculated relative mean squared error for the 440 diffraction peak calibration graphs

Relative Mean Square Error	
Fe_3O_4, 440 reflection (˚)	**γ-Fe_2O_3, 440 reflection (˚)**
0.80	1.72

Equation 9-2 shows the calculation used to quantify the amount of Fe_3O_4 and γ-Fe_2O_3 in an unknown sample using the 440 diffraction peak intensity and the calibration graph above.

$$\frac{\mathbf{I}(\text{Maghemite})}{(\mathbf{I}(\text{Magnetite}) + \mathbf{I}(\text{Maghemite}))} \times 100 = K(\text{Wt\%Maghemite}) + C \qquad \text{Equation 9-2}$$

I= Peak Intensity

K= Gradient of slope in calibration graph

C= Intercept on calibration graph

11 APPENDIX II – RELAXIVITY DATA

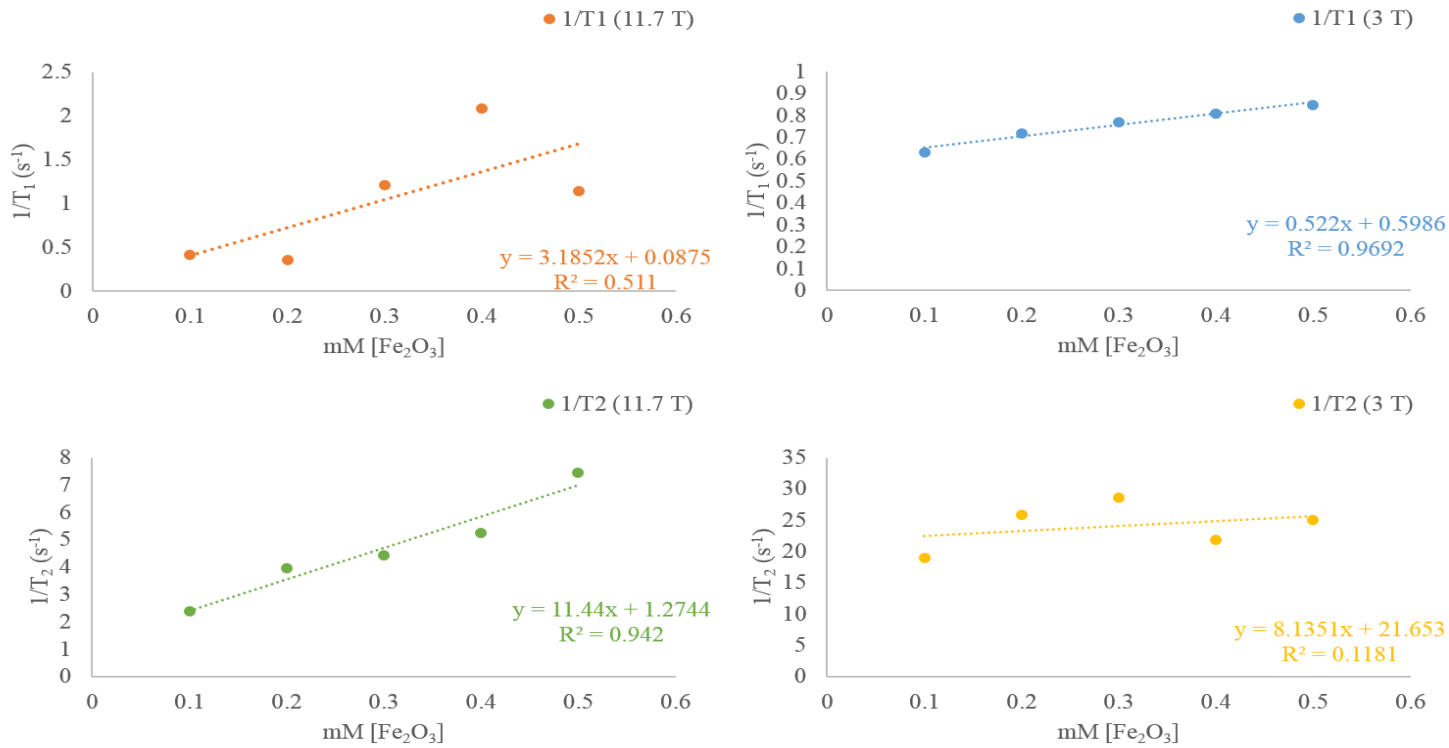

Figure 11-1 T_1 and T_2 relaxation rates per mmol of γ-Fe_2O_3 nanoparticles at 3 T and 11.7 T magnetic field strengths.

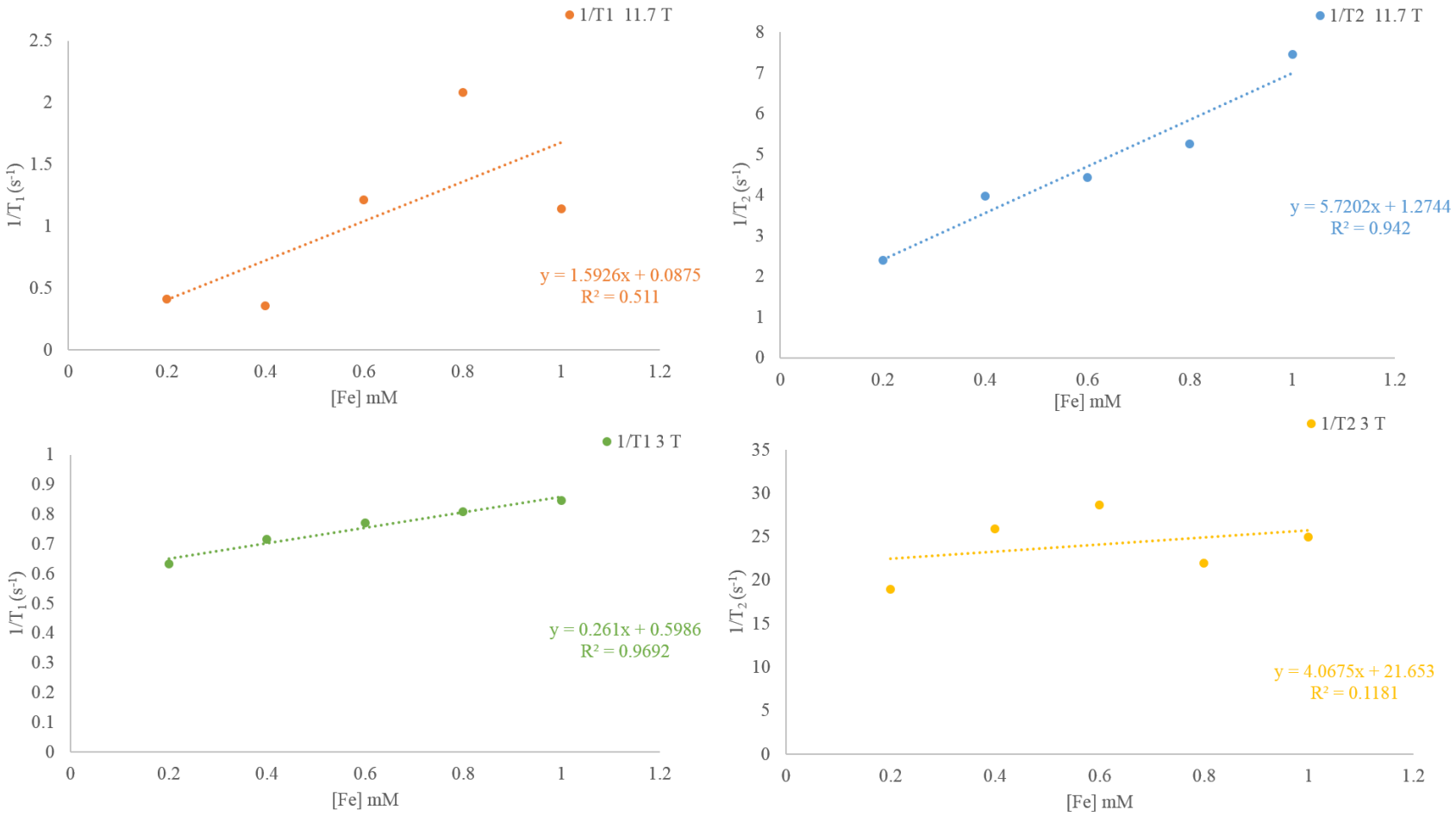

Figure 11-2 T_1 and T_2 relaxation rates per mmol of Fe^{3+} in γ-Fe_2O_3 nanoparticles at 3 T and 11.7 T magnetic field strengths.

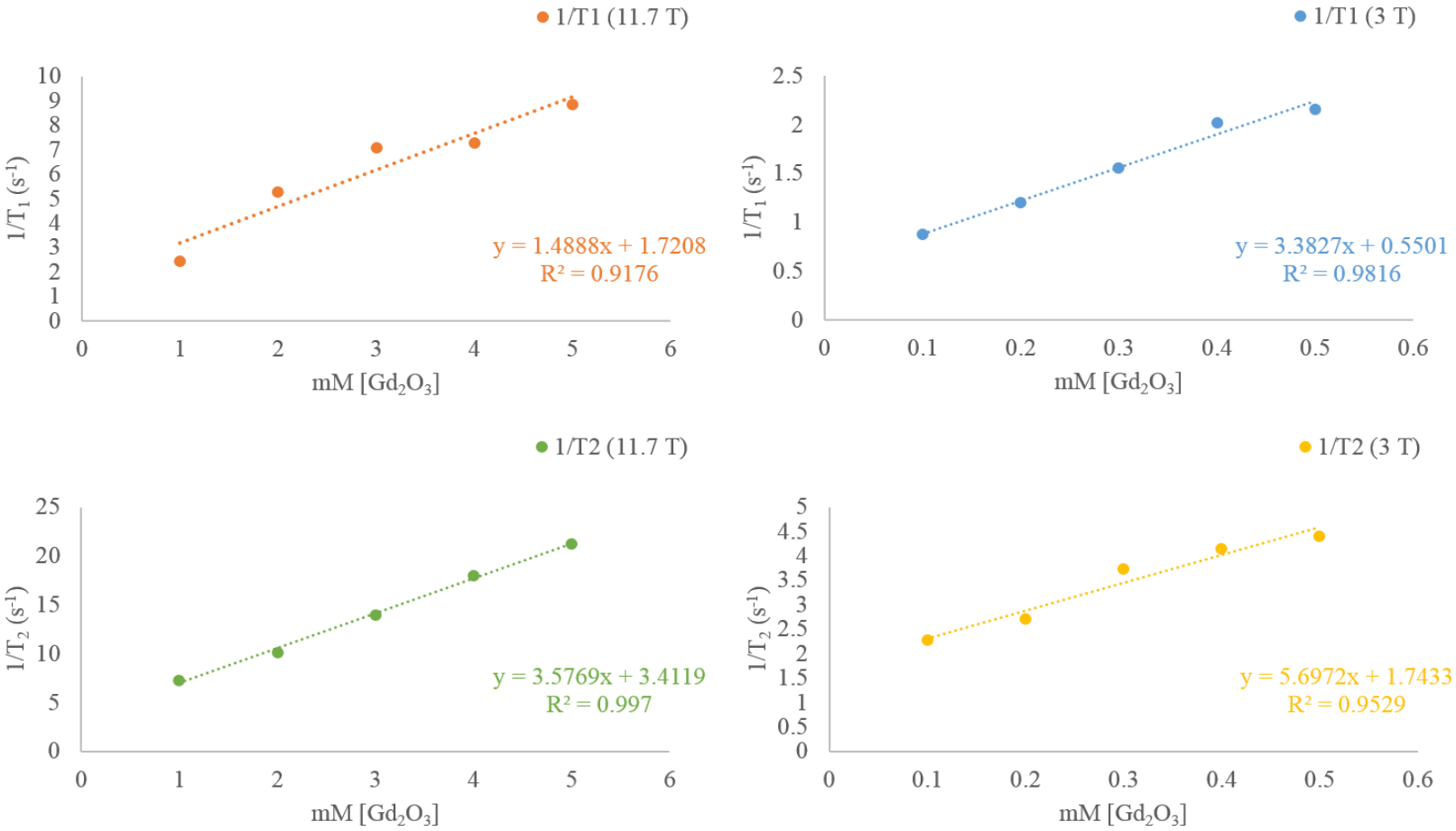

Figure 11-3 T_1 and T_2 relaxation rates per mmol of Gd_2O_3 nanoparticles at 3 T and 11.7 T magnetic field strengths.

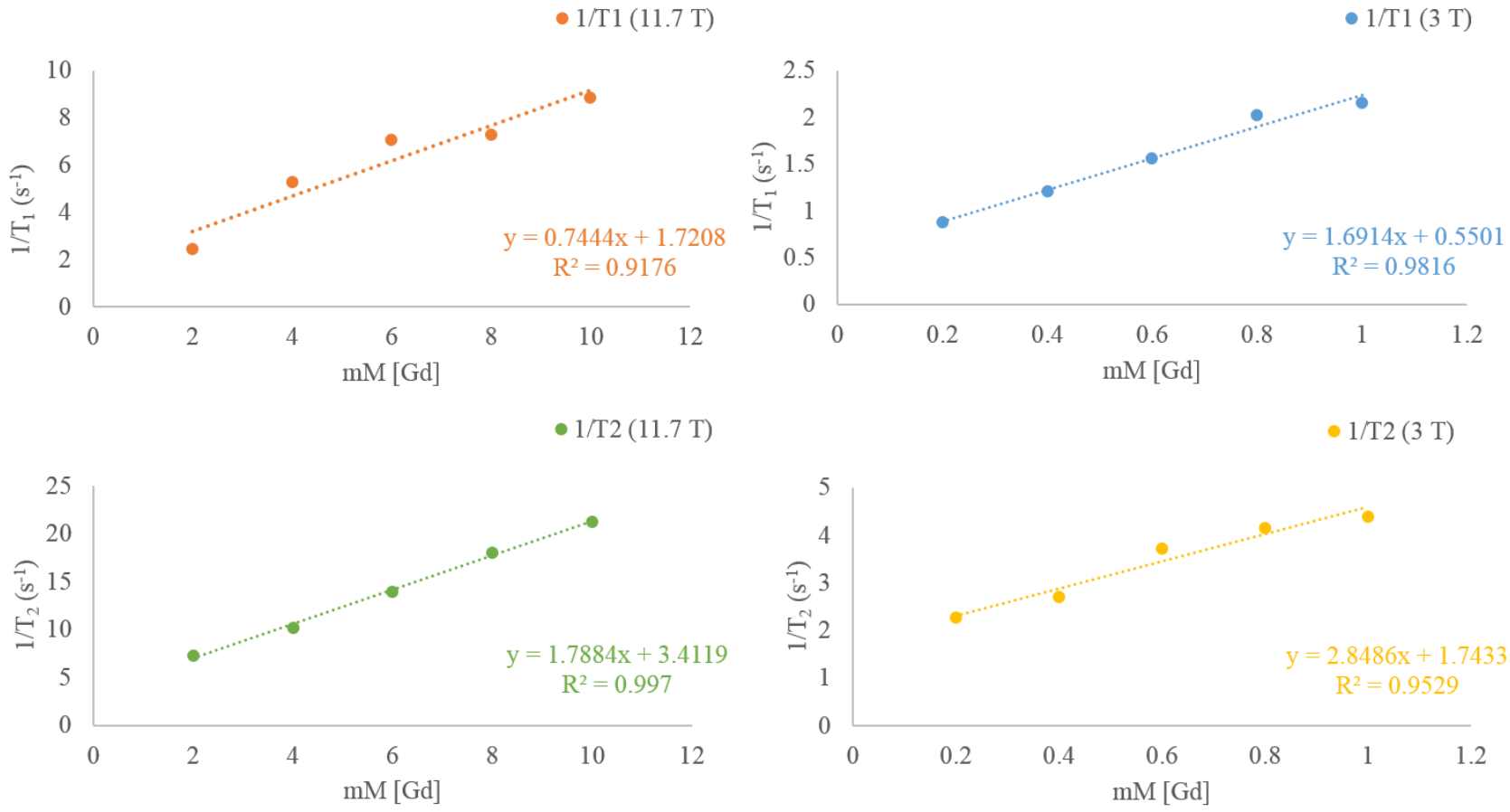

Figure 11-4 T_1 and T_2 relaxation rates per mmol of Gd^{3+} in Gd_2O_3 nanoparticles at 3 T and 11.7 T magnetic field strengths.

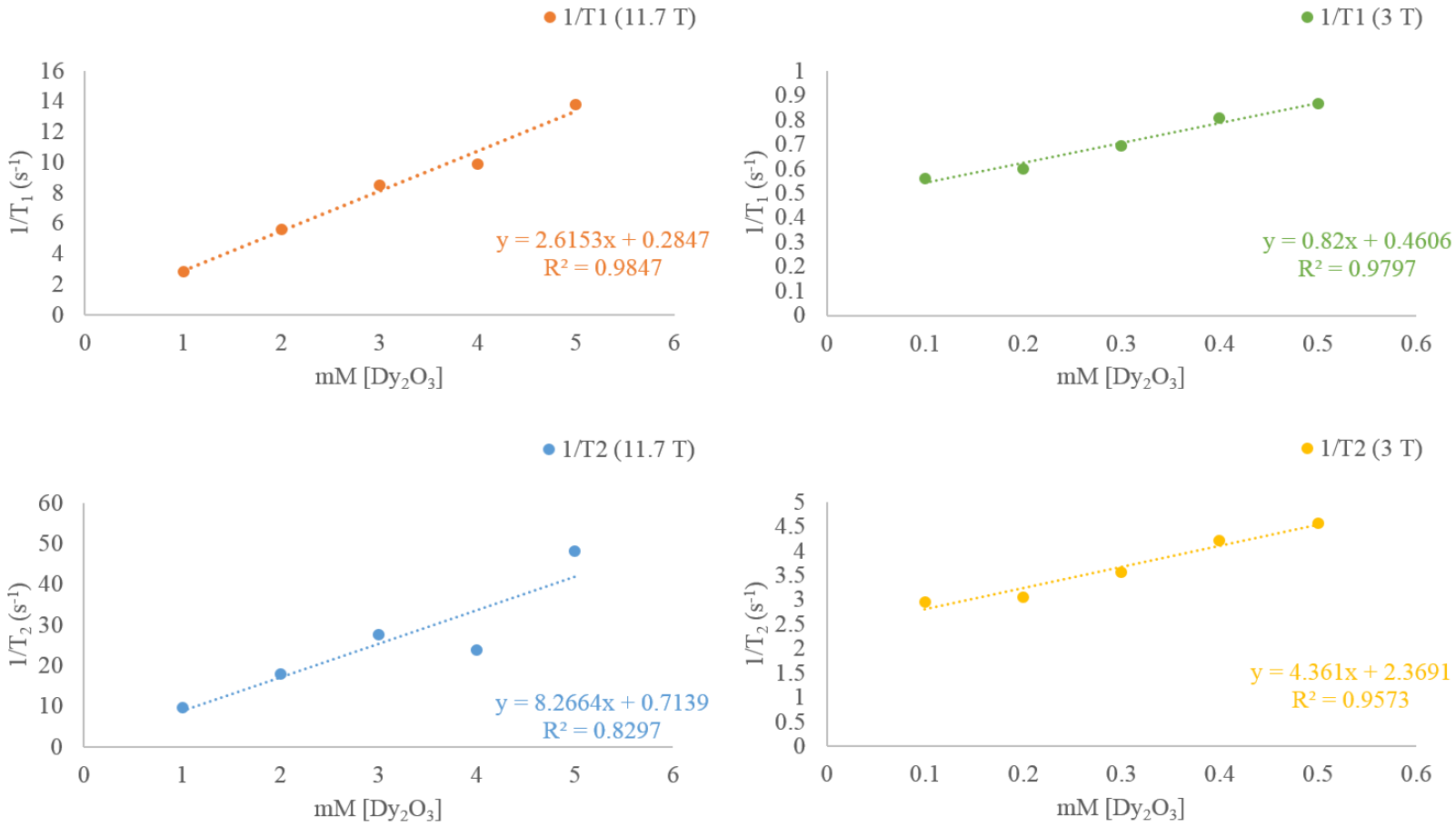

Figure 11-5 T_1 and T_2 relaxation rates per mmol of Dy_2O_3 nanoparticles at 3 T and 11.7 T magnetic field strengths.

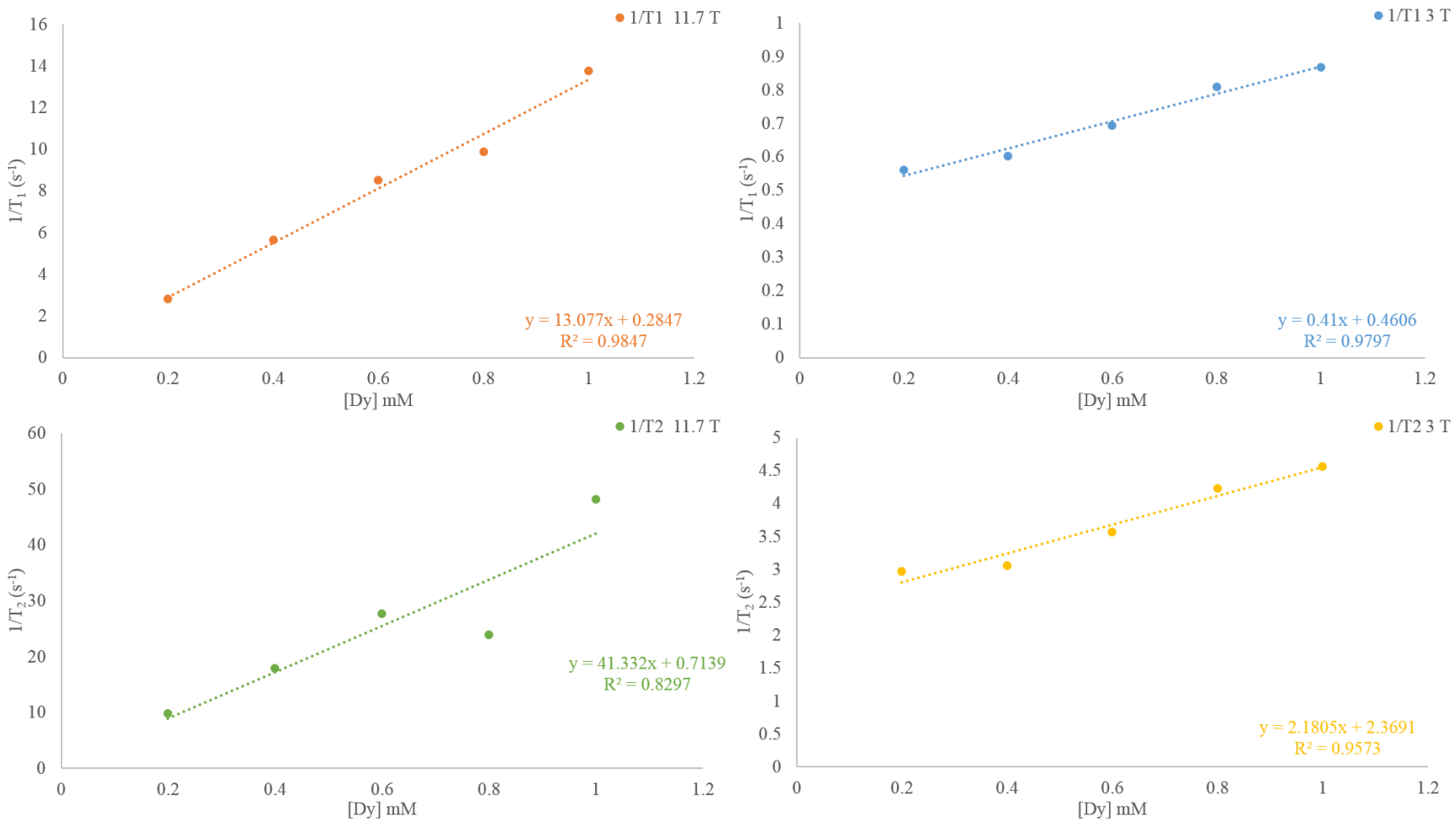

Figure 11-6 T_1 and T_2 relaxation rates per mmol of Dy^{3+} in Dy_2O_3 nanoparticles at 3 T and 11.7 T magnetic field strengths.

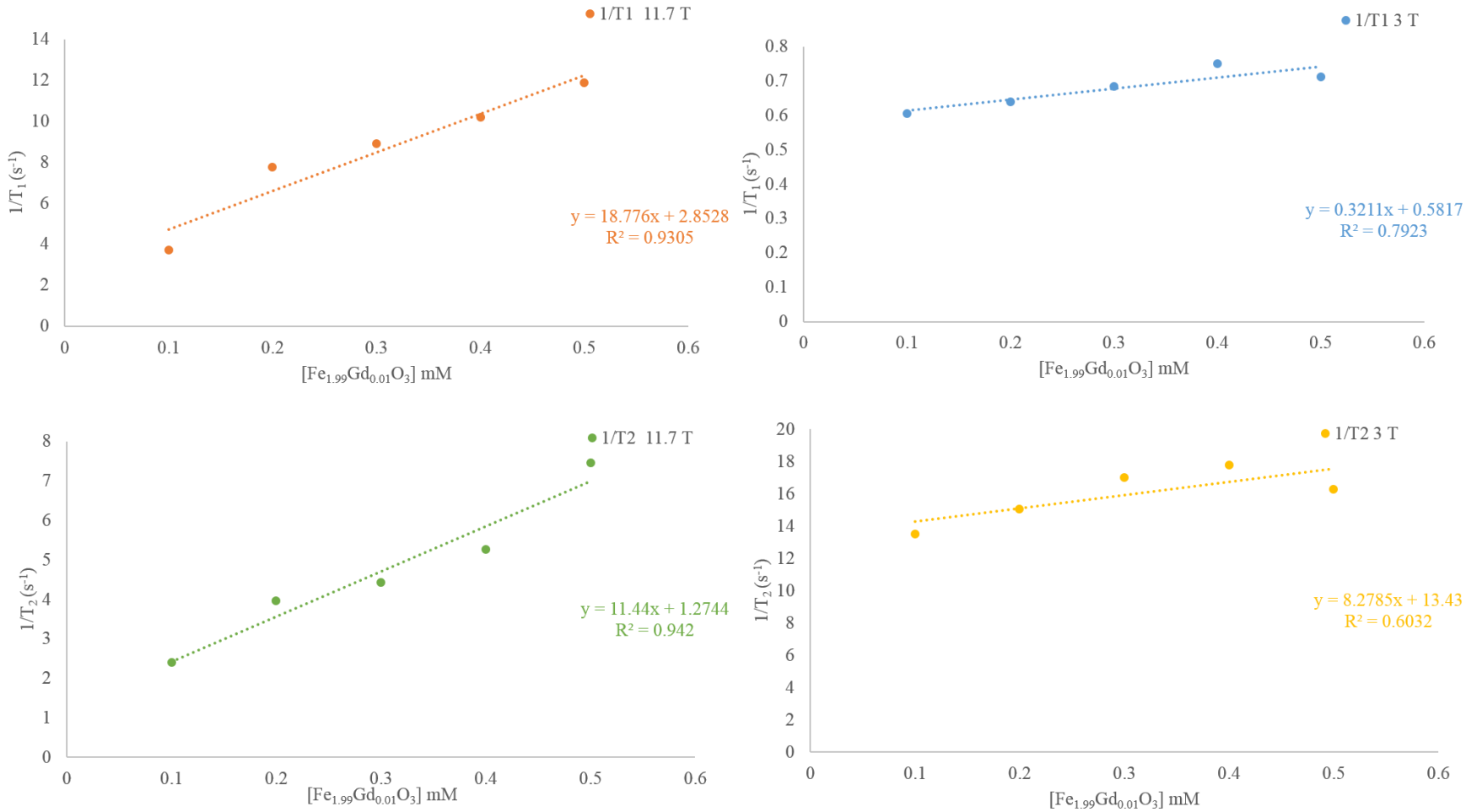

Figure 11-7 T_1 and T_2 relaxation rates per mmol of $Fe_{1.99}Gd_{0.01}O_3$ nanoparticles at 3 T and 11.7 T magnetic field strengths.

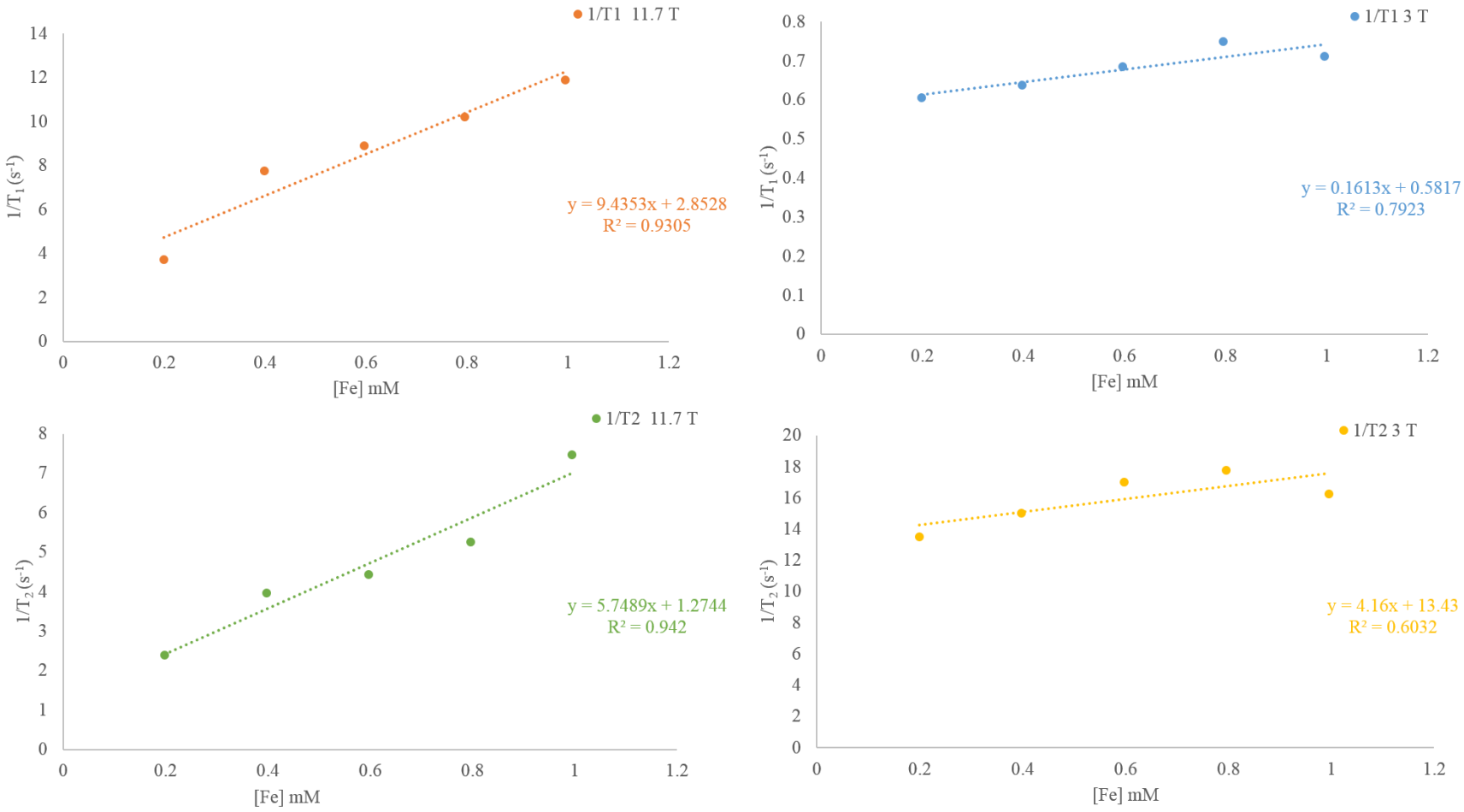

Figure 11-8 T_1 and T_2 relaxation rates per mmol of Fe^{3+} in $Fe_{1.99}Gd_{0.01}O_3$ nanoparticles at 3 T and 11.7 T magnetic field strengths.

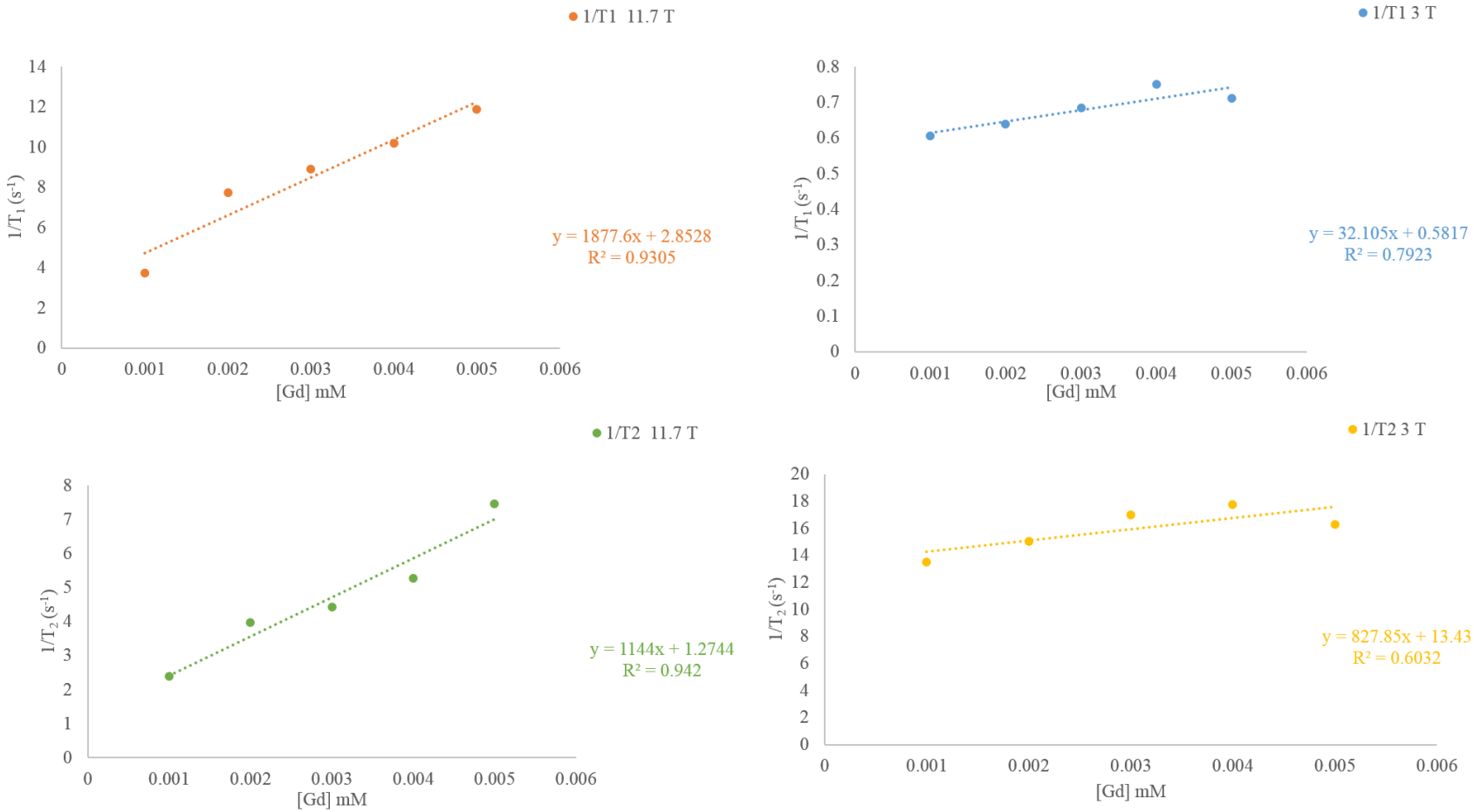

Figure 11-9 T_1 and T_2 relaxation rates per mmol of Gd^{3+} in $Fe_{1.99}Gd_{0.01}O_3$ nanoparticles at 3 T and 11.7 T magnetic field strengths.

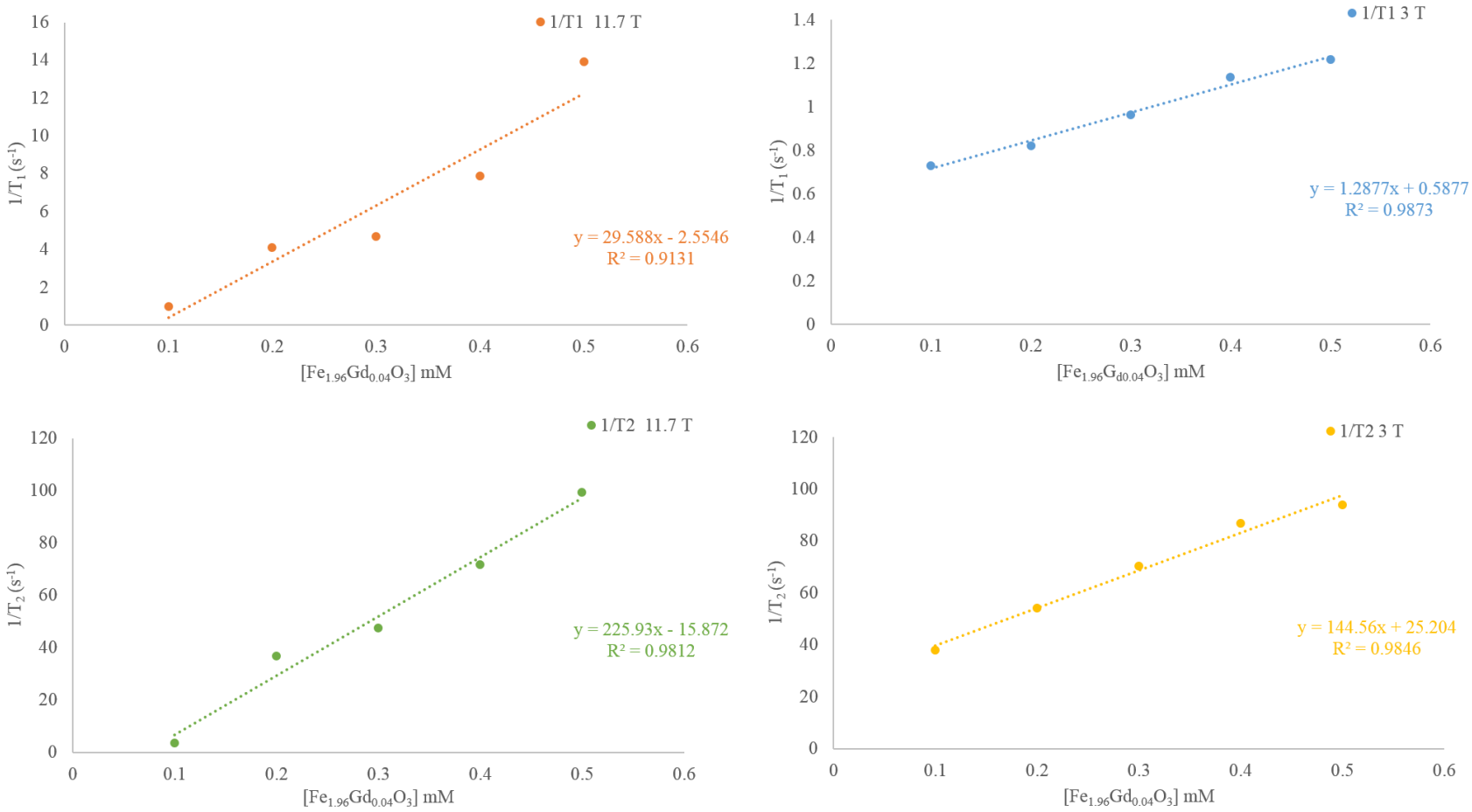

Figure 11-10 T_1 and T_2 relaxation rates per mmol of $Fe_{1.96}Gd_{0.04}O_3$ nanoparticles at 3 T and 11.7 T magnetic field strengths.

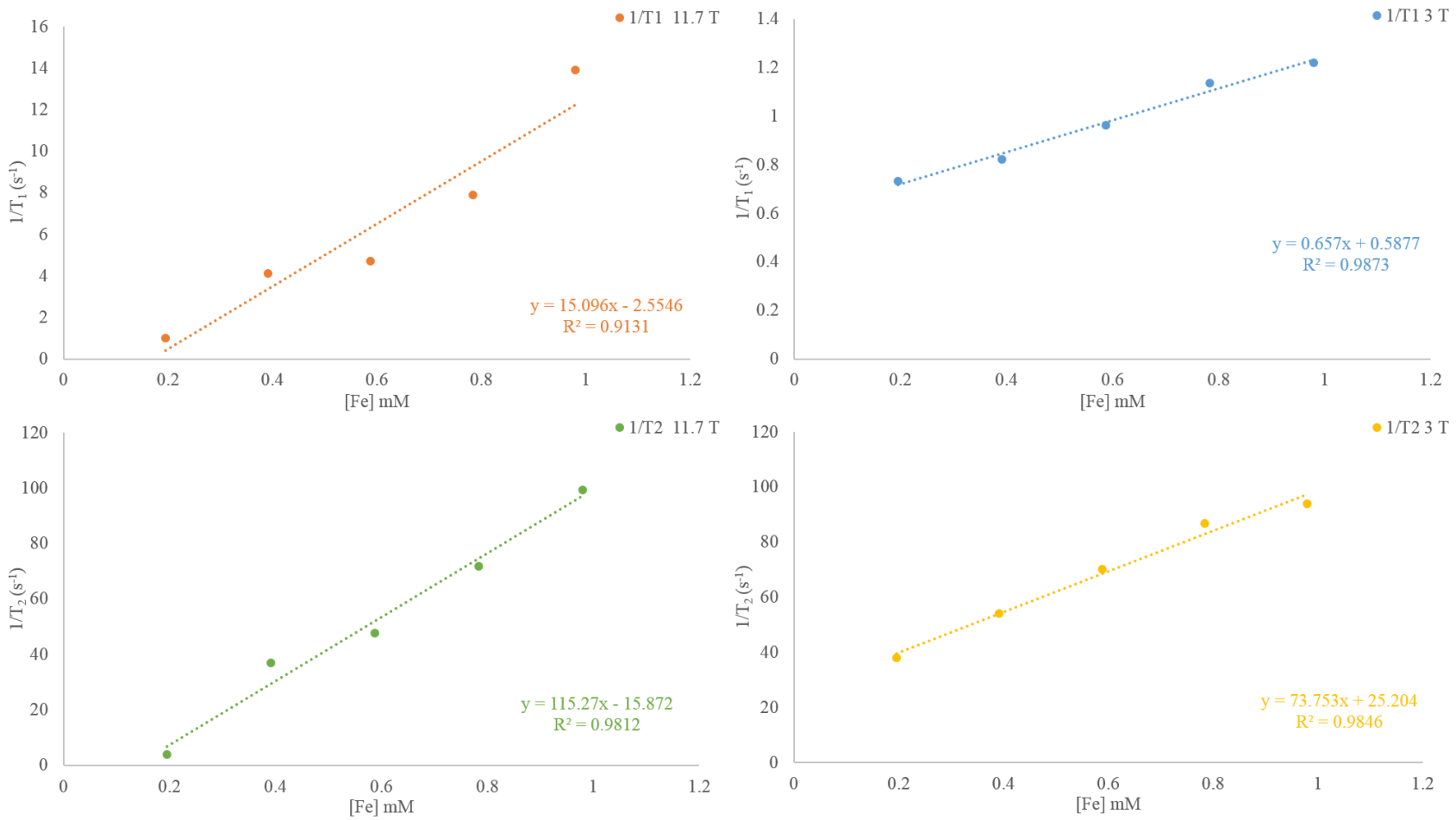

Figure 11-11 T_1 and T_2 relaxation rates per mmol of Fe^{3+} in $Fe_{1.96}Gd_{0.04}O_3$ nanoparticles at 3 T and 11.7 T magnetic field strengths.

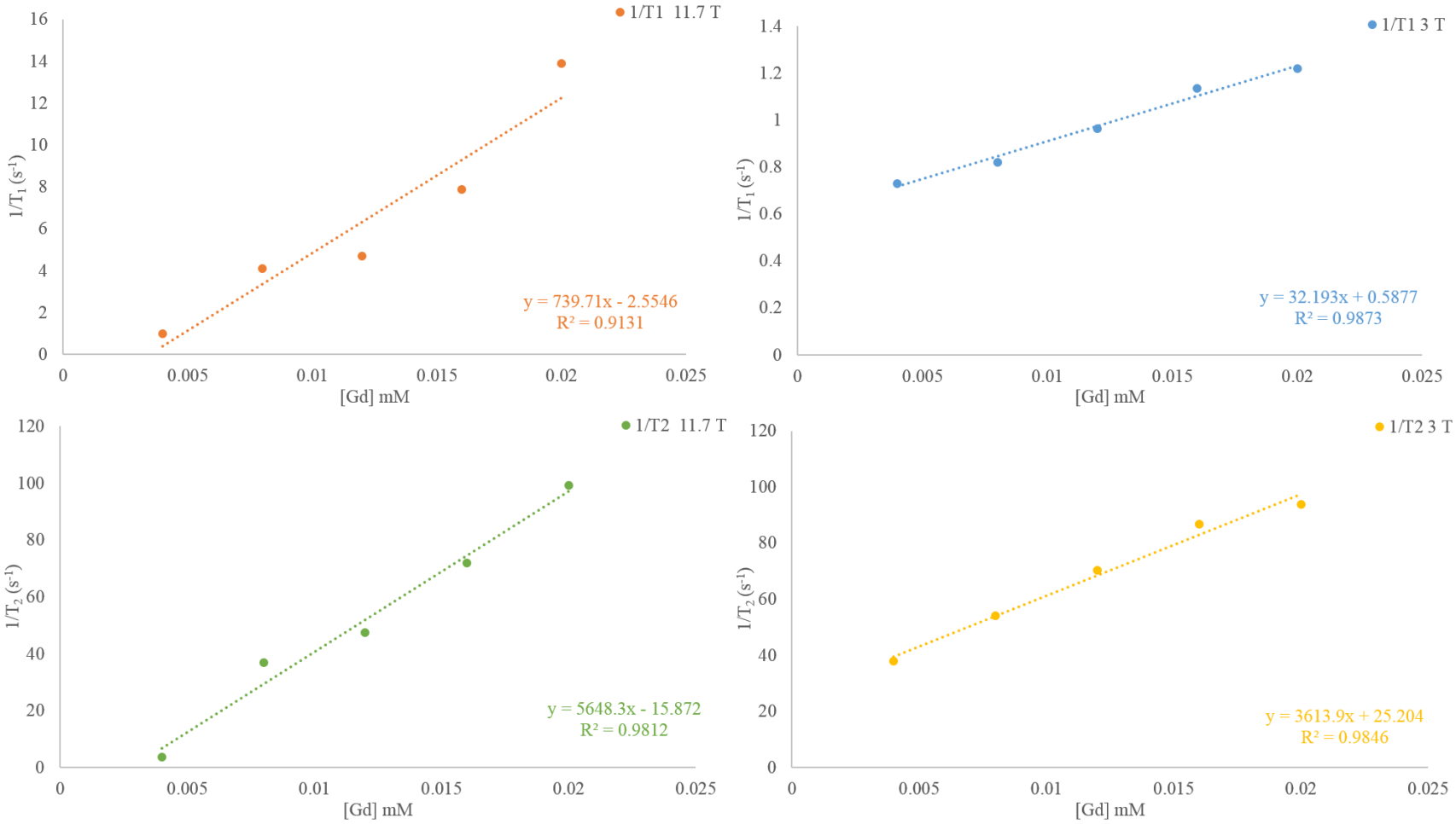

Figure 11-12 T_1 and T_2 relaxation rates per mmol of Gd^{3+} in $Fe_{1.96}Gd_{0.04}O_3$ nanoparticles at 3 T and 11.7 T magnetic field strengths.

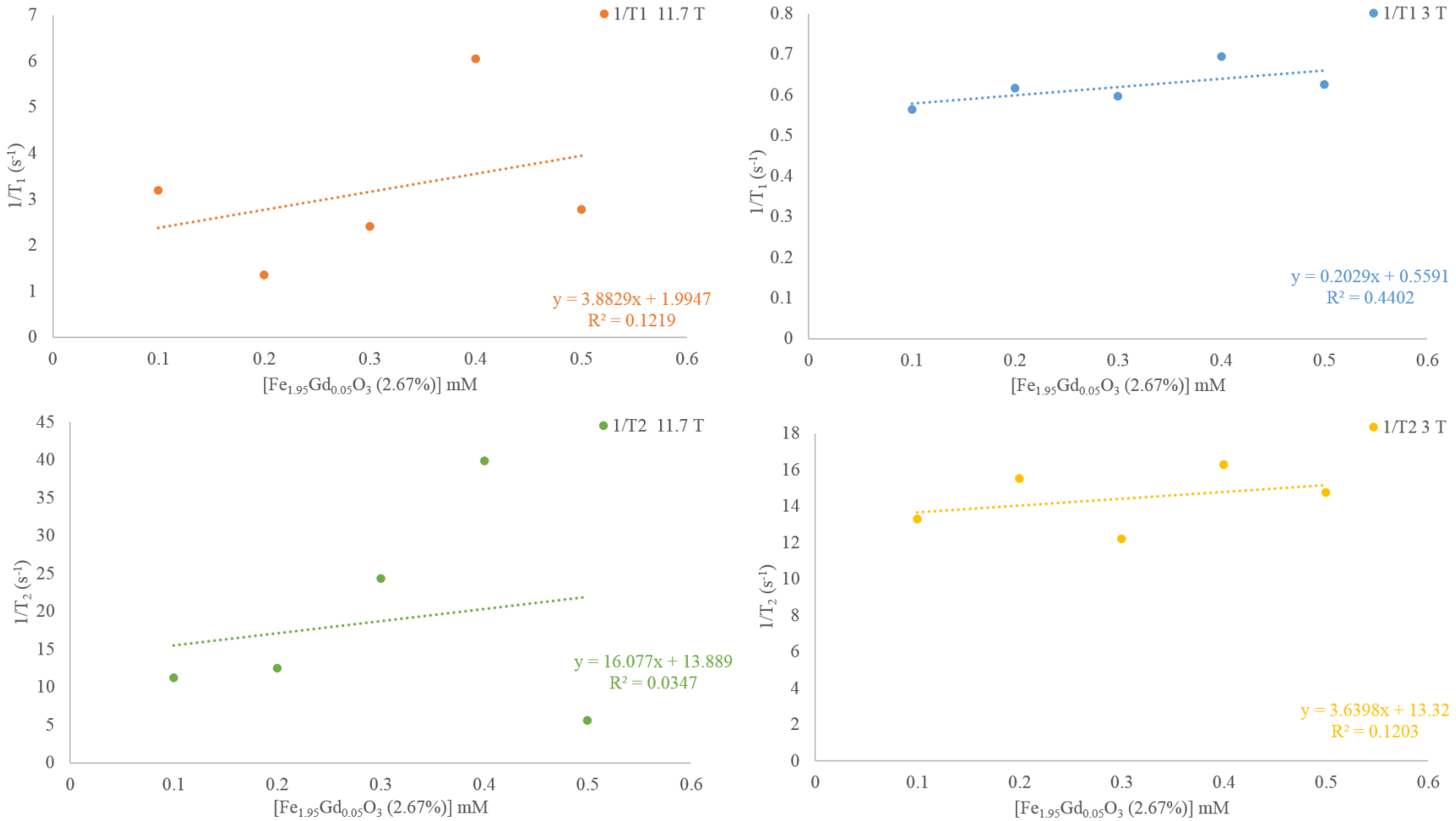

Figure 11-13 T_1 and T_2 relaxation rates per mmol of $Fe_{1.95}Gd_{0.05}O_3$(2.67%) nanoparticles at 3 T and 11.7 T magnetic field strengths.

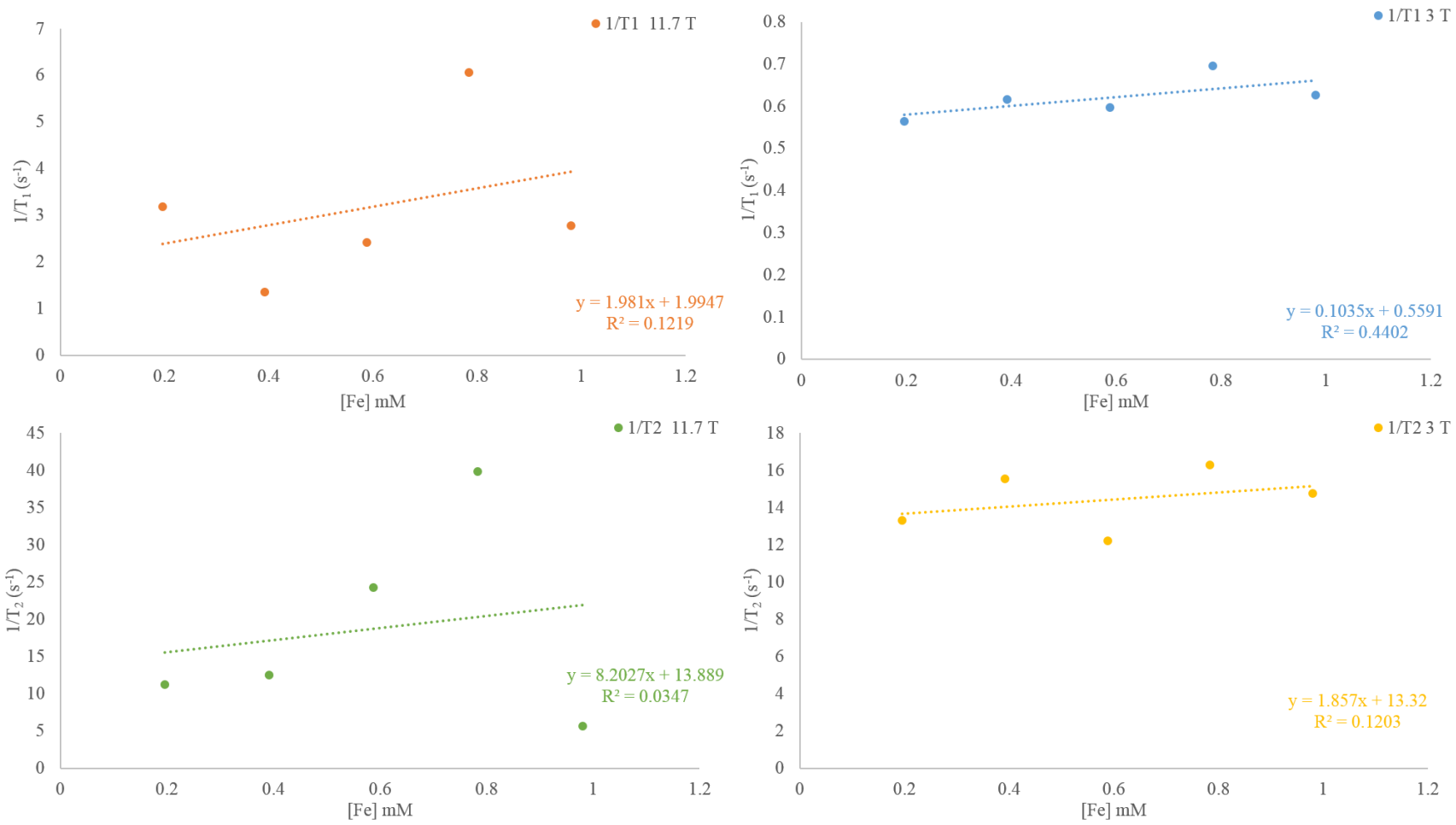

Figure 11-14 T_1 and T_2 relaxation rates per mmol of Fe^{3+} in $Fe_{1.95}Gd_{0.05}O_3$(2.67%) nanoparticles at 3 T and 11.7 T magnetic field strengths.

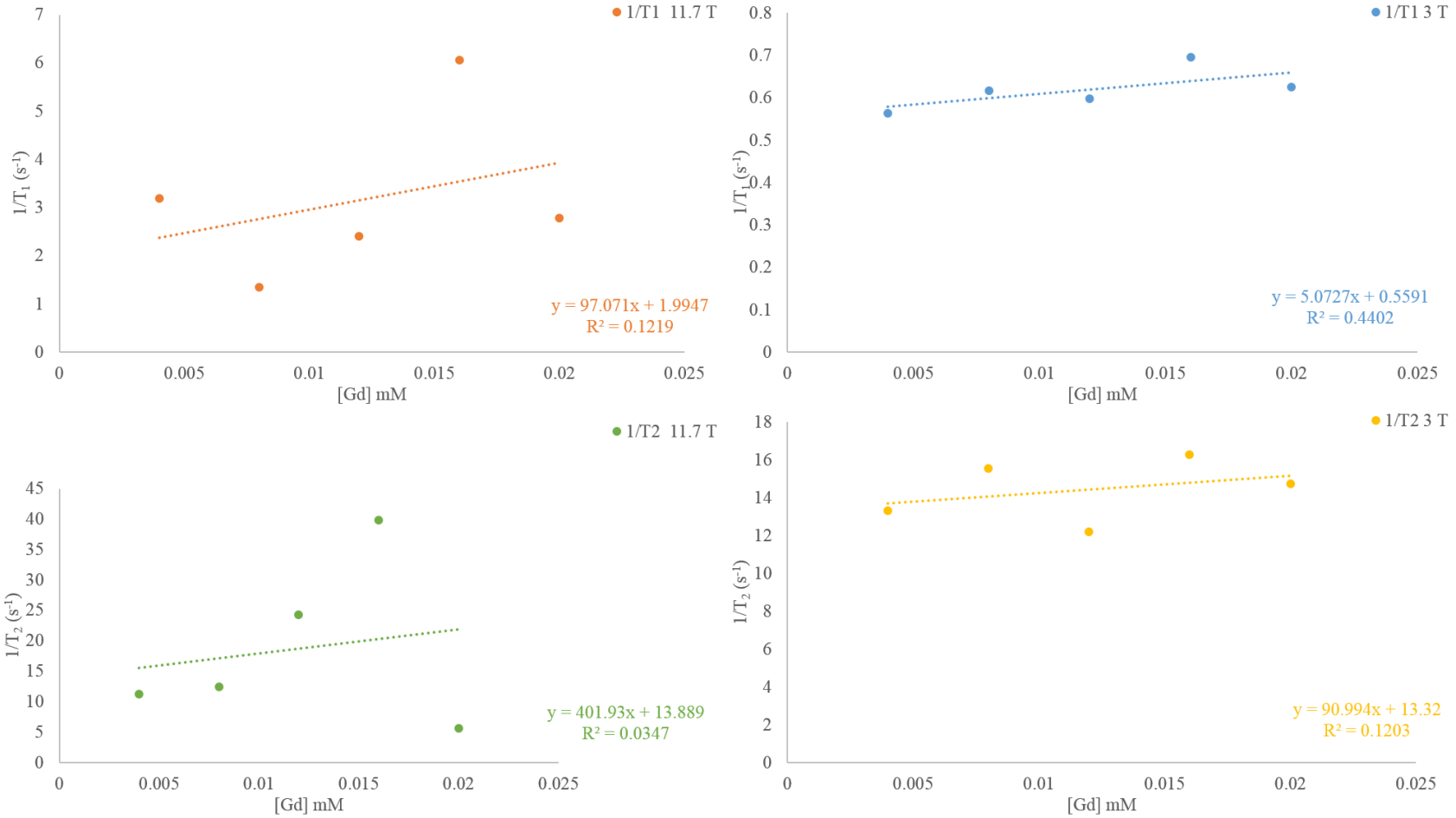

Figure 11-15 T_1 and T_2 relaxation rates per mmol of Gd^{3+} in $Fe_{1.95}Gd_{0.05}O_3$(2.67%) nanoparticles at 3 T and 11.7 T magnetic field strengths.

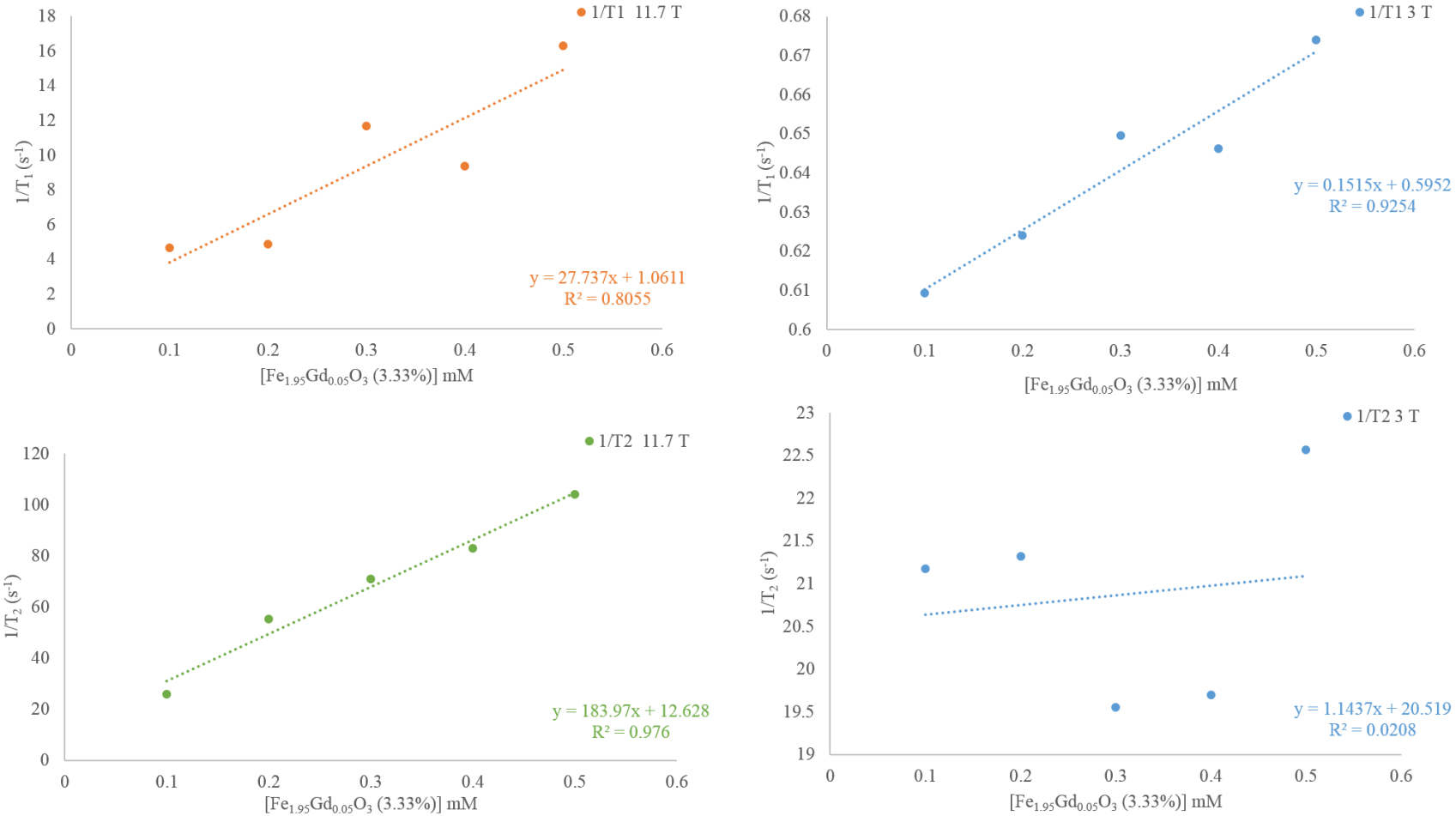

Figure 11-16 T_1 and T_2 relaxation rates per mmol of $Fe_{1.95}Gd_{0.05}O_3$(3.33%) nanoparticles at 3 T and 11.7 T magnetic field strengths.

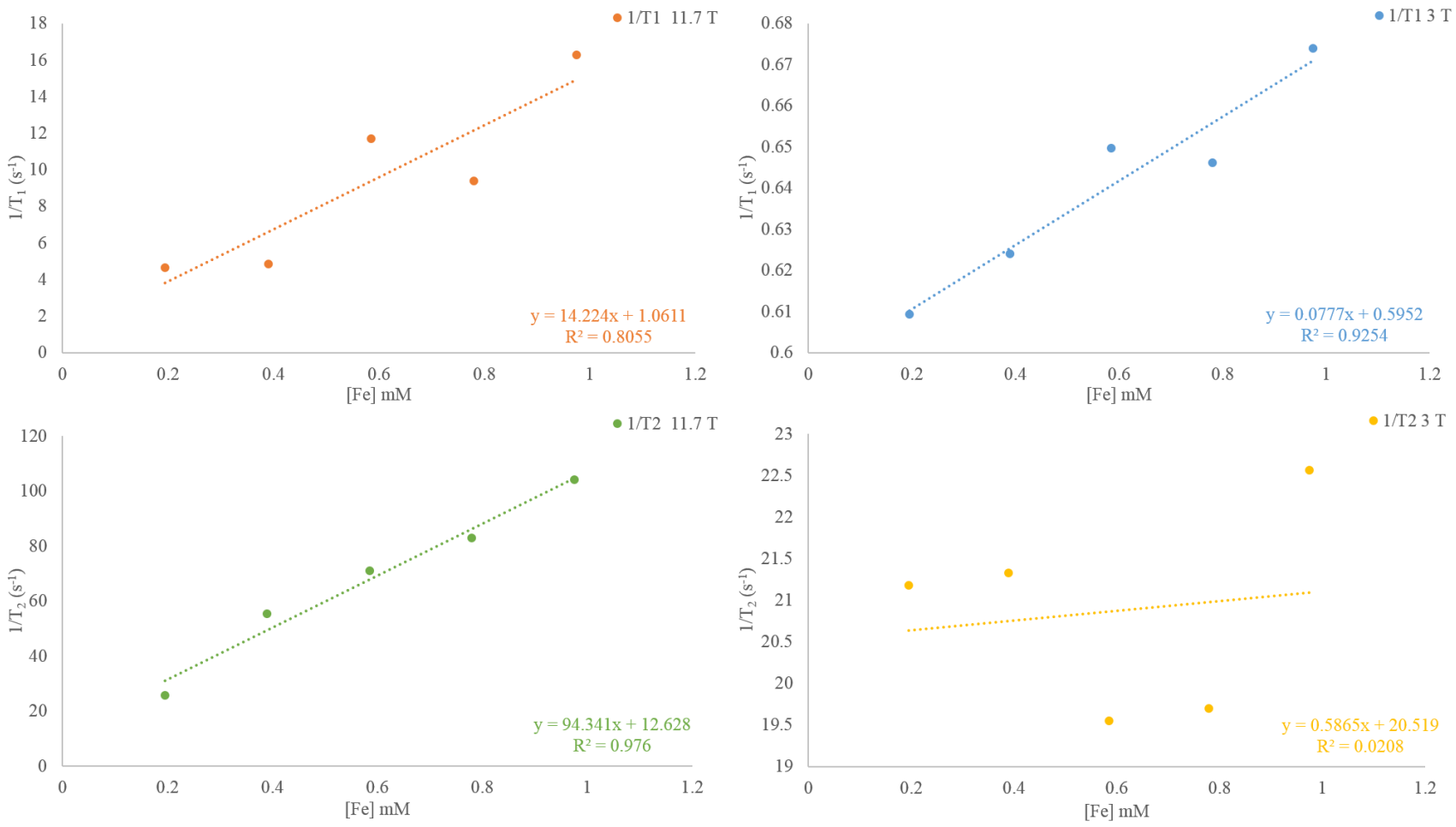

Figure 11-17 T_1 and T_2 relaxation rates per mmol of Fe^{3+} in $Fe_{1.95}Gd_{0.05}O_3$(3.33%) nanoparticles at 3 T and 11.7 T magnetic field strengths.

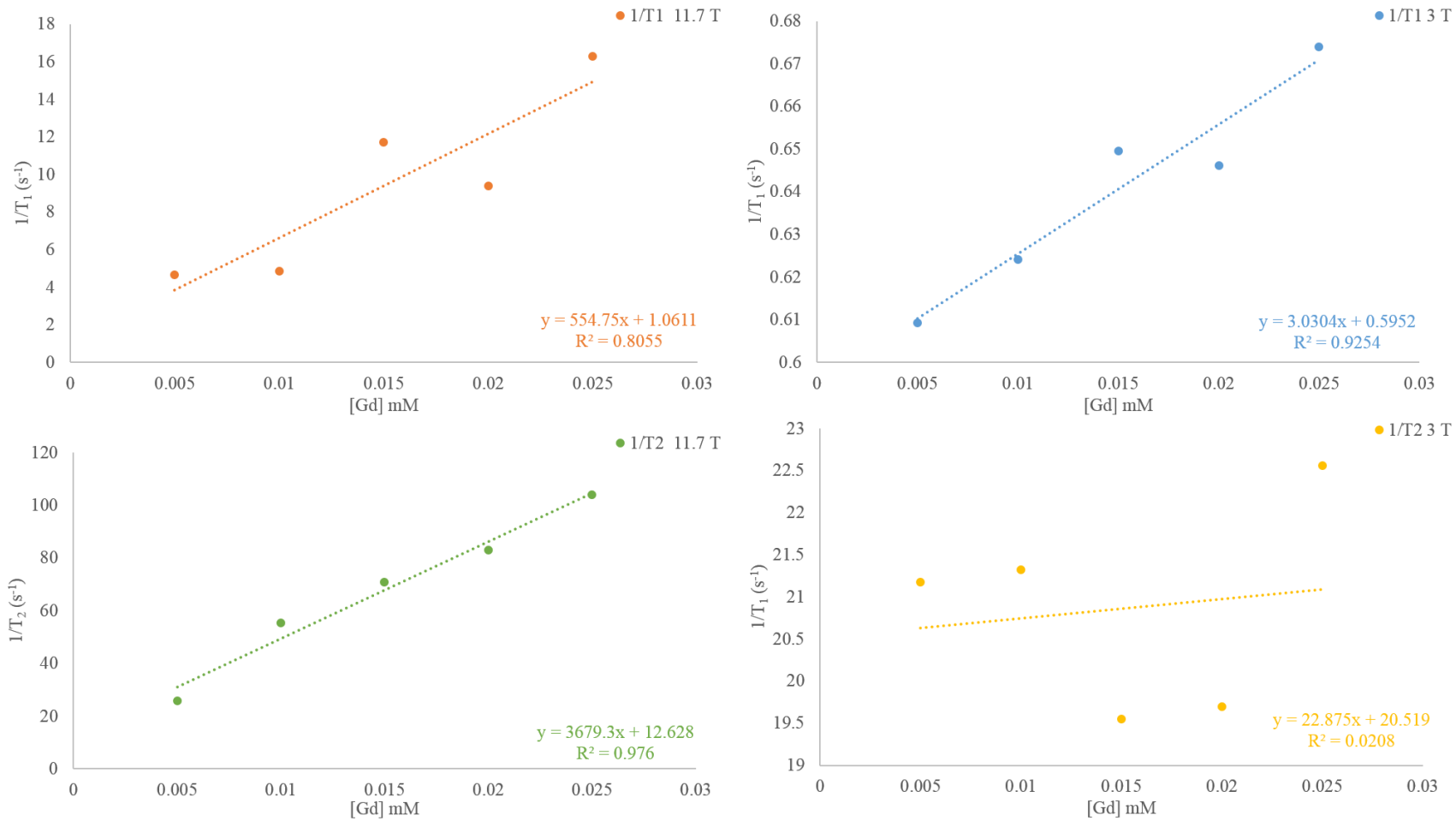

Figure 11-18 T_1 and T_2 relaxation rates per mmol of Gd^{3+} in $Fe_{1.95}Gd_{0.05}O_3$(3.33%) nanoparticles at 3 T and 11.7 T magnetic field strengths.

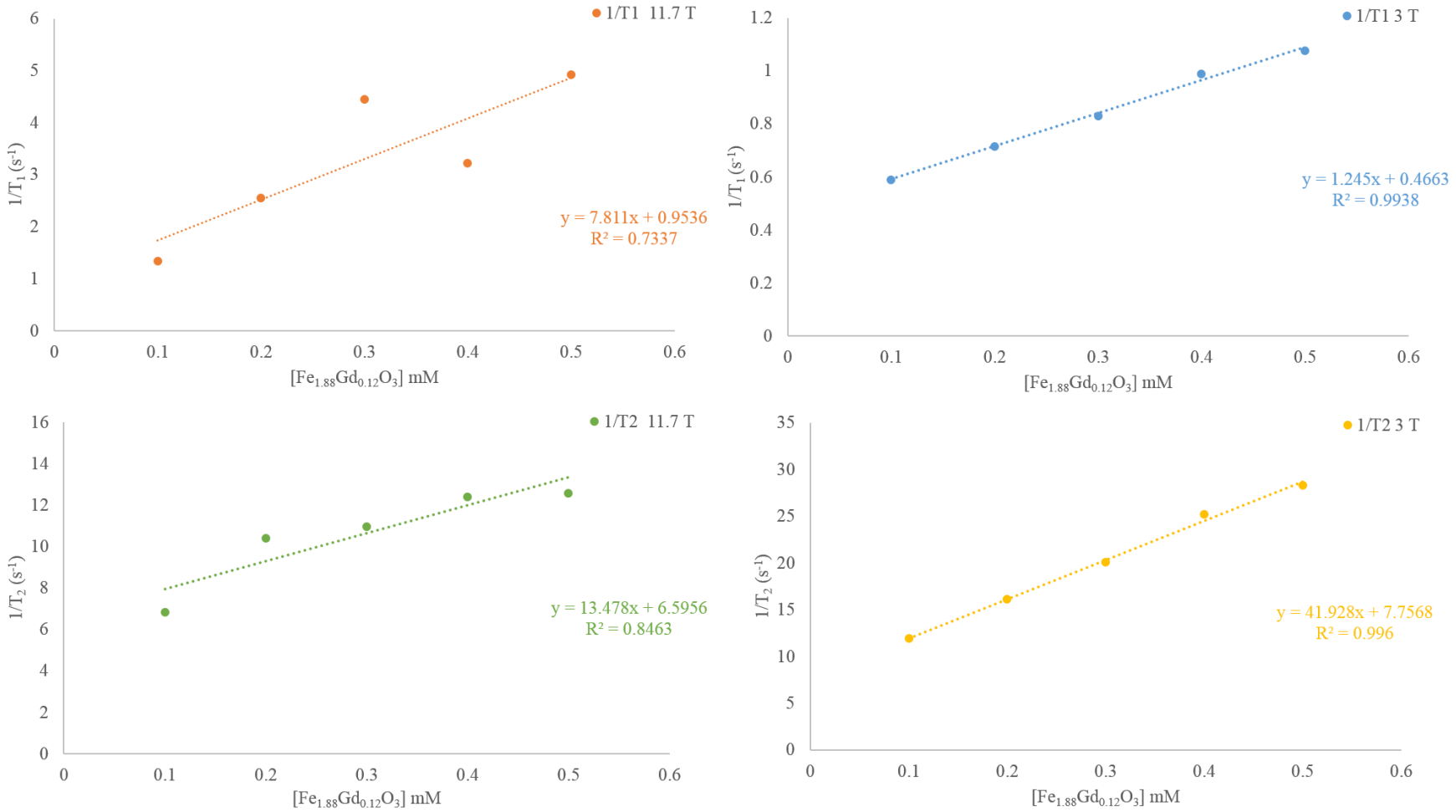

Figure 11-19 T_1 and T_2 relaxation rates per mmol of $Fe_{1.88}Gd_{0.12}O_3$ nanoparticles at 3 T and 11.7 T magnetic field strengths.

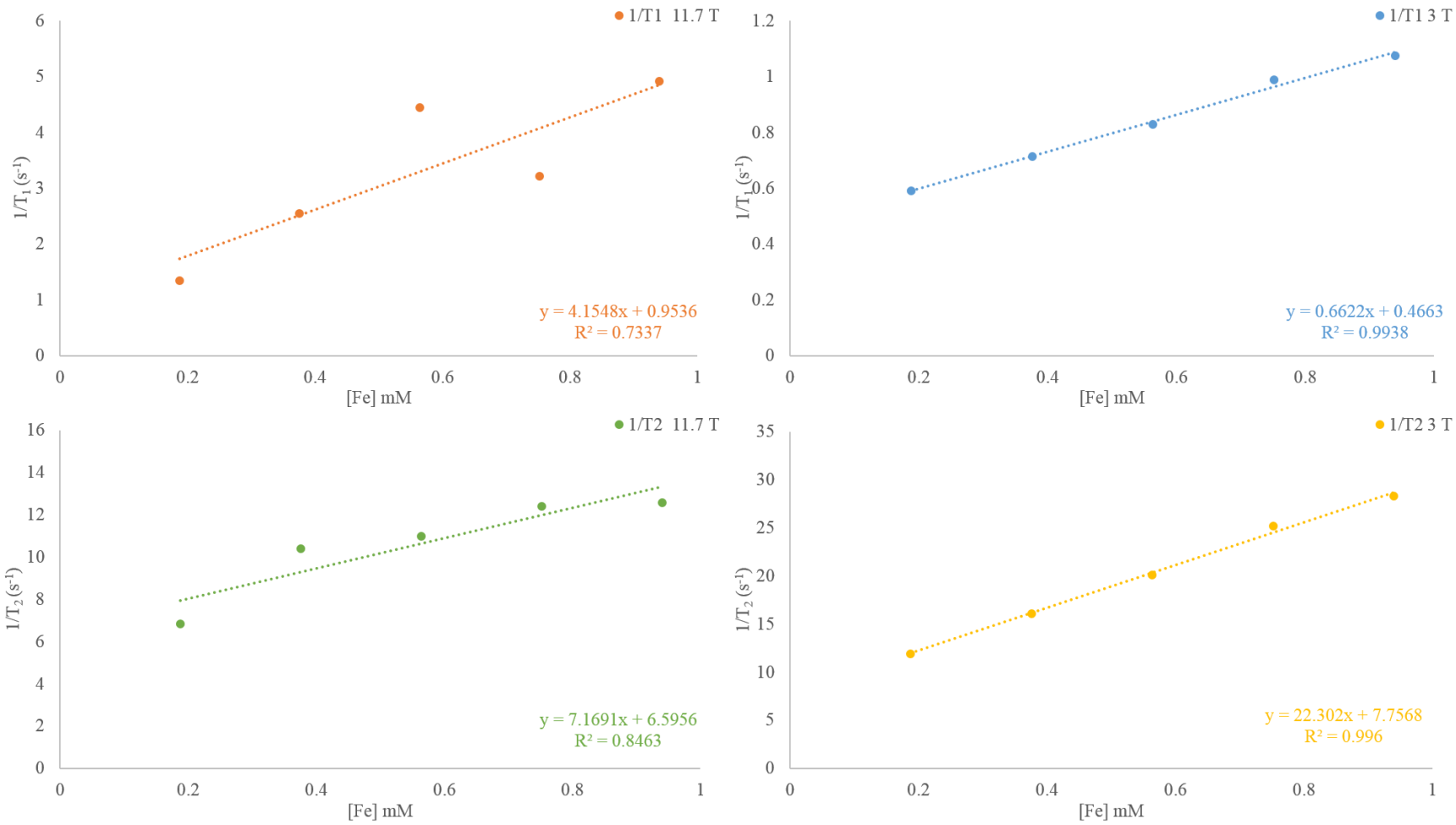

Figure 11-20 T_1 and T_2 relaxation rates per mmol of Fe^{3+} in $Fe_{1.88}Gd_{0.12}O_3$ nanoparticles at 3 T and 11.7 T magnetic field strengths.

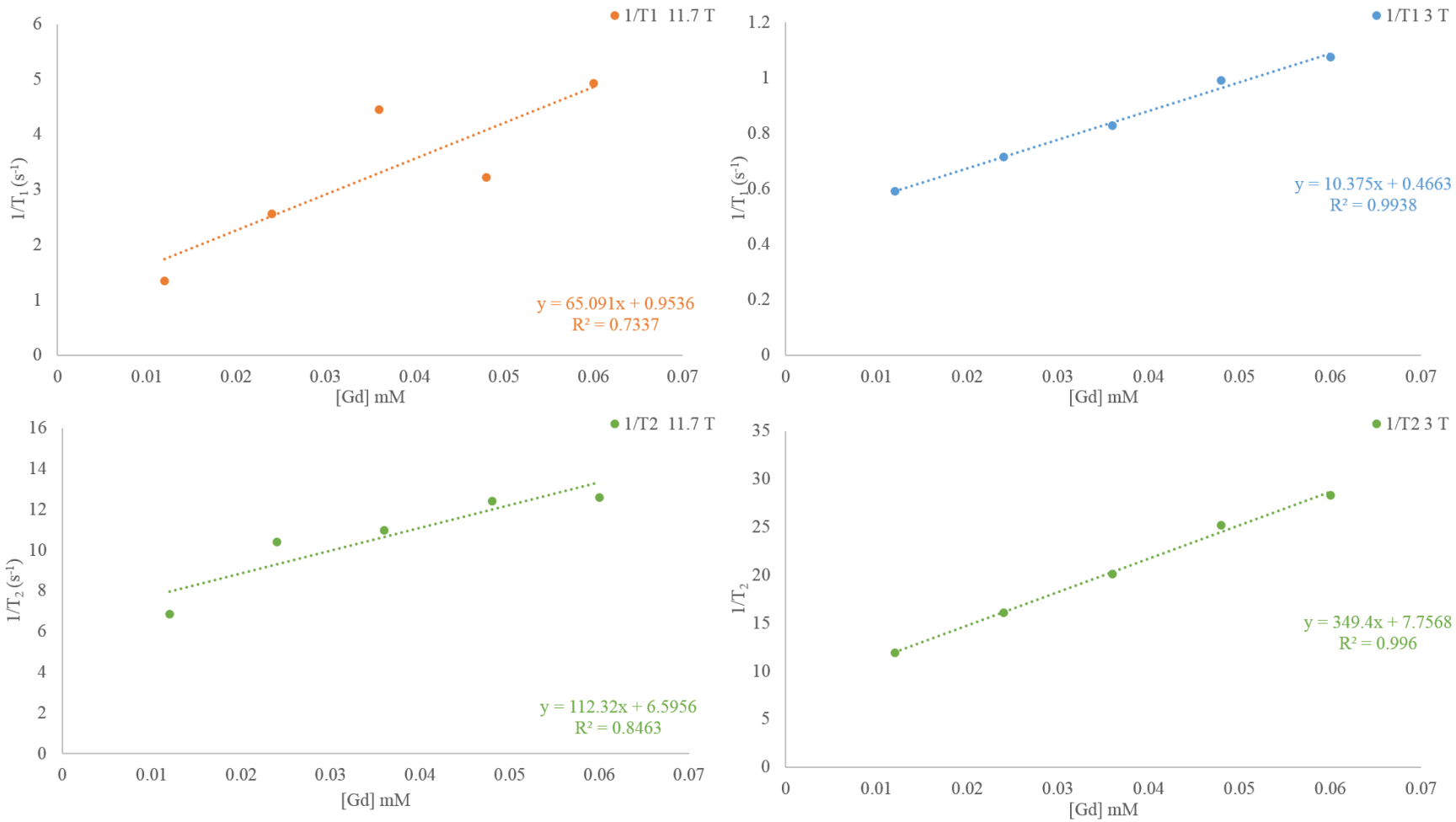

Figure 11-21 T_1 and T_2 relaxation rates per mmol of Gd^{3+} in $Fe_{1.88}Gd_{0.12}O_3$ nanoparticles at 3 T and 11.7 T magnetic field strengths.

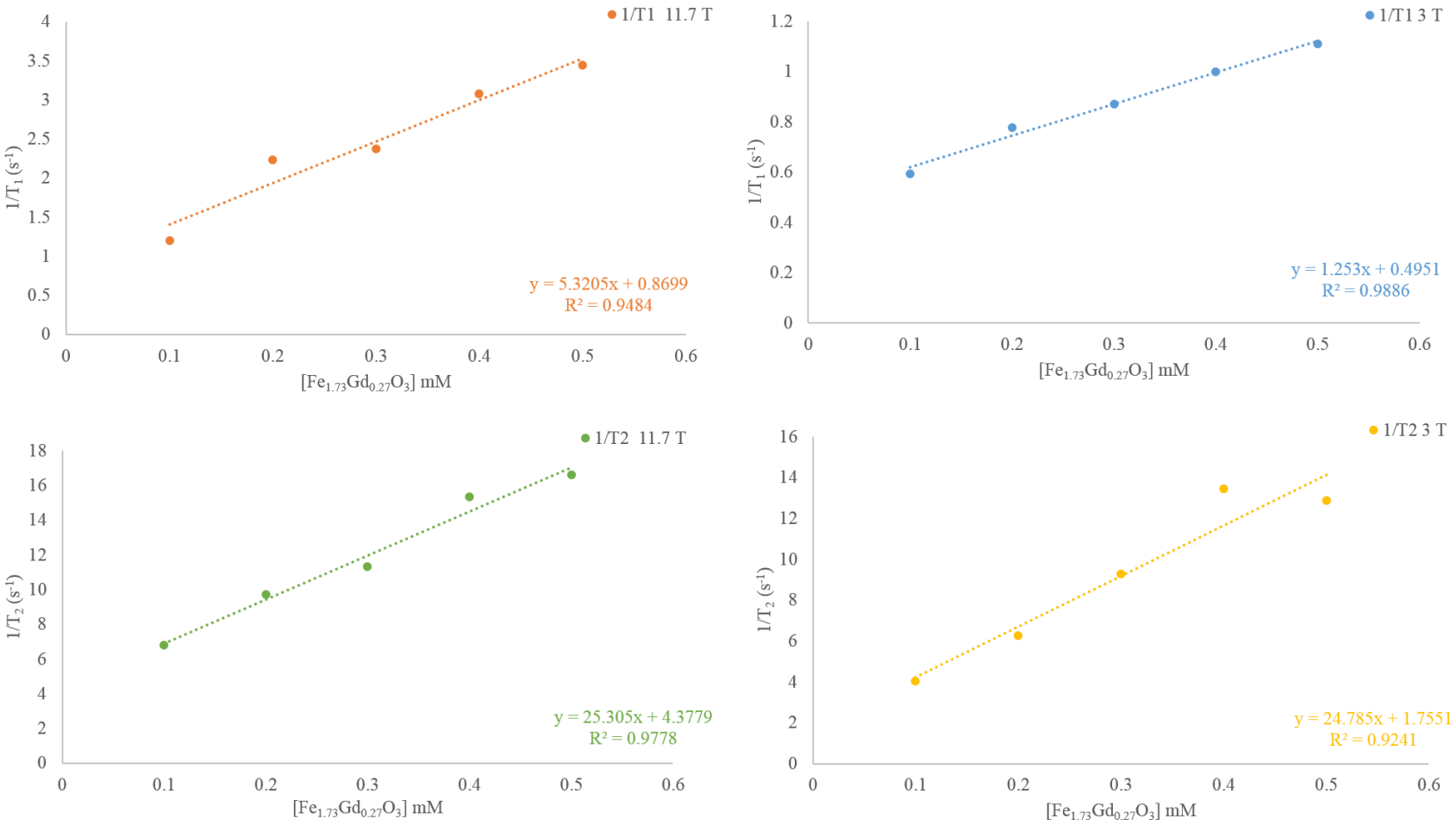

Figure 11-22 T_1 and T_2 relaxation rates per mmol of $Fe_{1.73}Gd_{0.27}O_3$ nanoparticles at 3 T and 11.7 T magnetic field strengths.

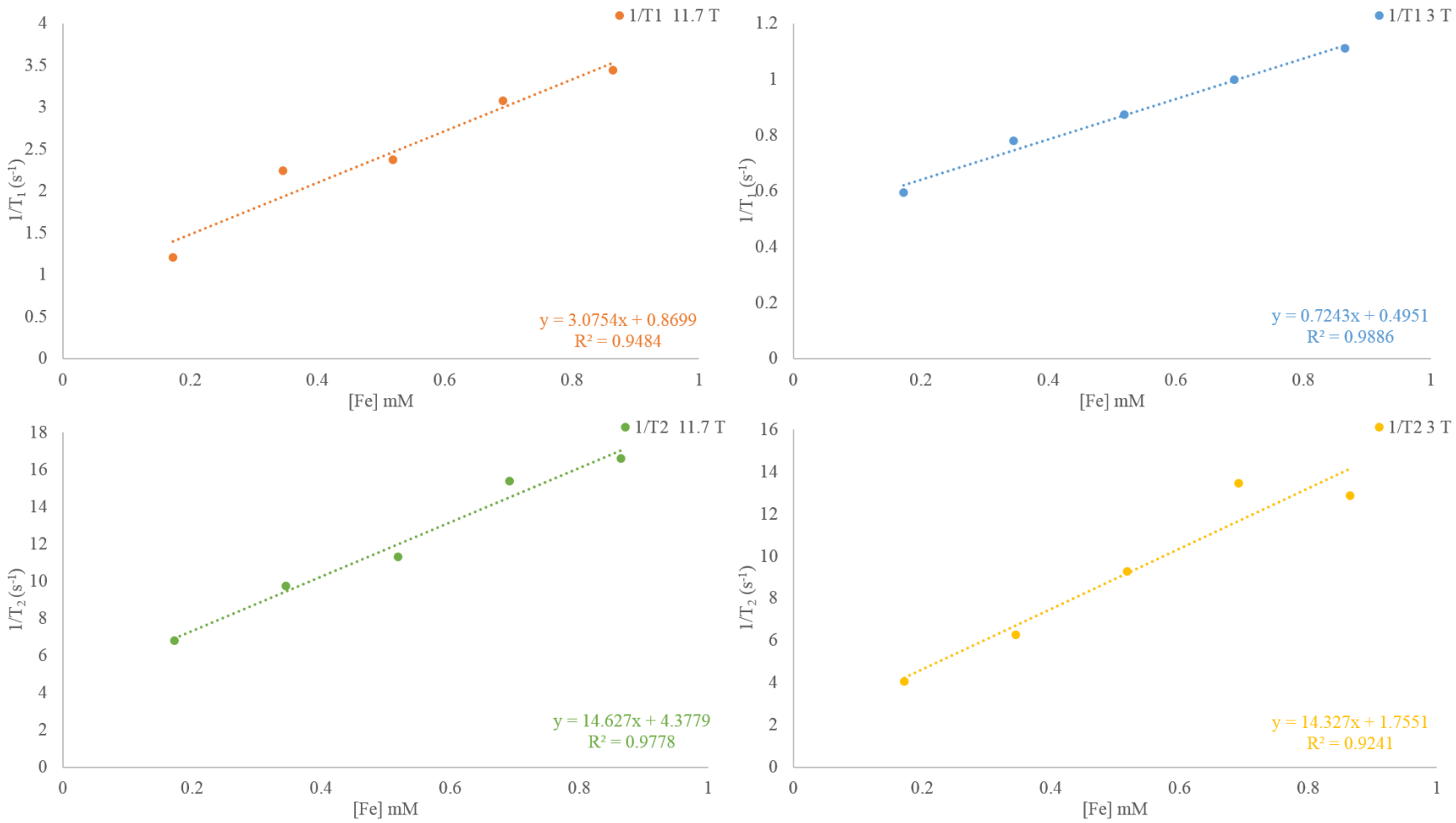

Figure 11-23 T_1 and T_2 relaxation rates per mmol of Fe^{3+} in $Fe_{1.73}Gd_{0.27}O_3$ nanoparticles at 3 T and 11.7 T magnetic field strengths.

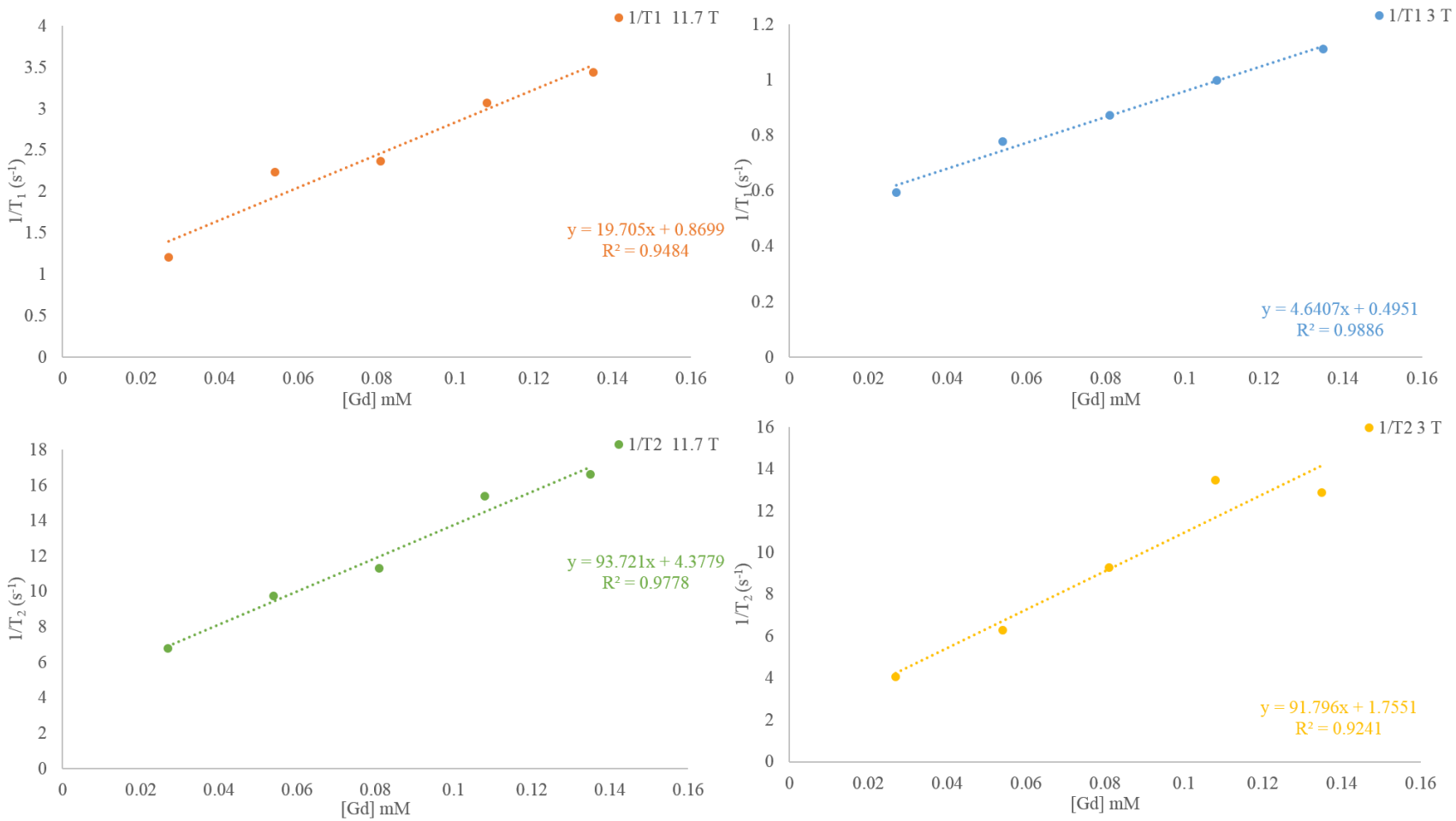

Figure 11-24 T_1 and T_2 relaxation rates per mmol of Gd^{3+} in $Fe_{1.73}Gd_{0.27}O_3$ nanoparticles at 3 T and 11.7 T magnetic field strengths.

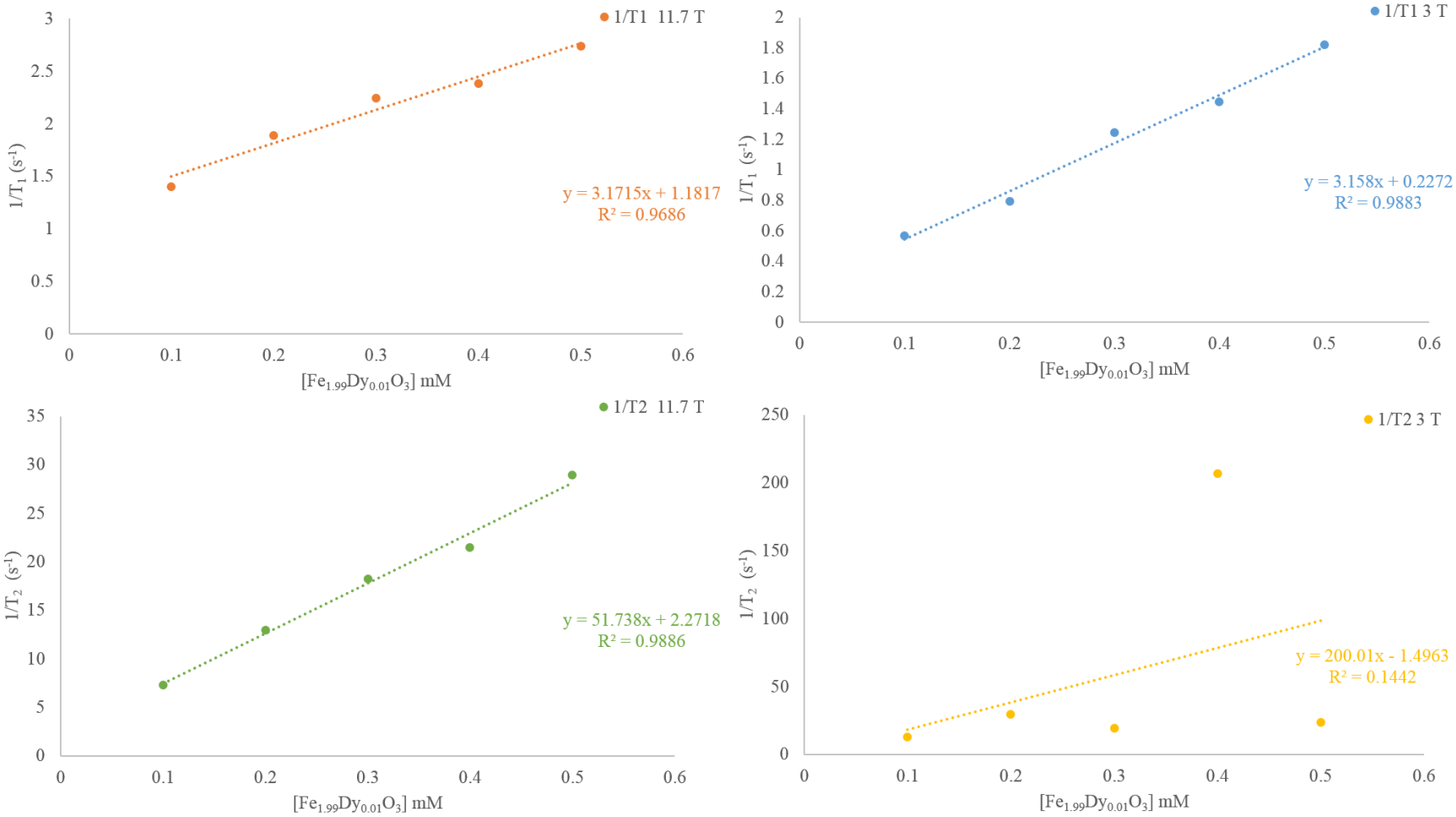

Figure 11-25 T_1 and T_2 relaxation rates per mmol of $Fe_{1.99}Dy_{0.01}O_3$ nanoparticles at 3 T and 11.7 T magnetic field strengths.

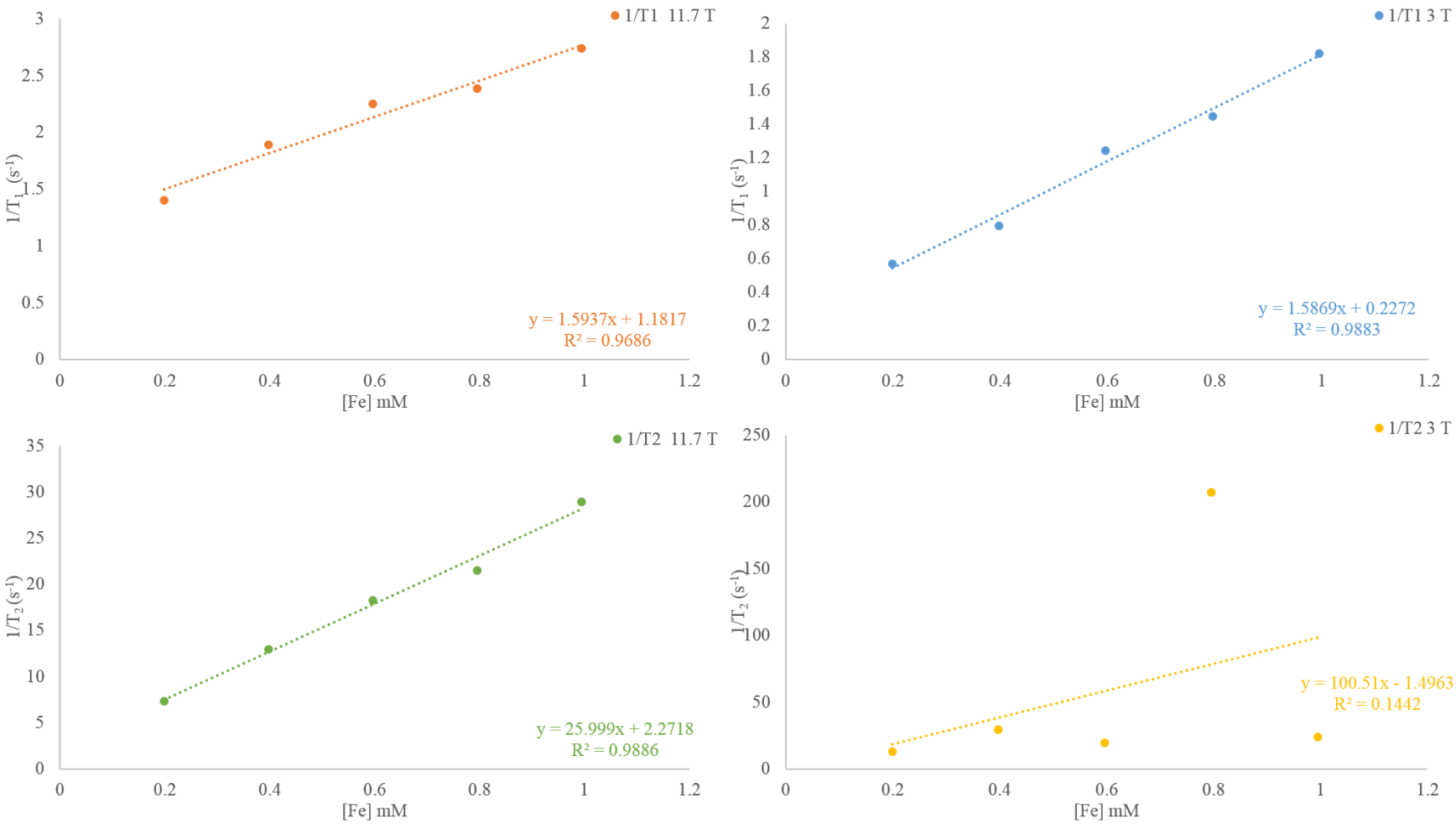

Figure 11-26 T_1 and T_2 relaxation rates per mmol of Fe^{3+} in $Fe_{1.99}Dy_{0.01}O_3$ nanoparticles at 3 T and 11.7 T magnetic field strengths.

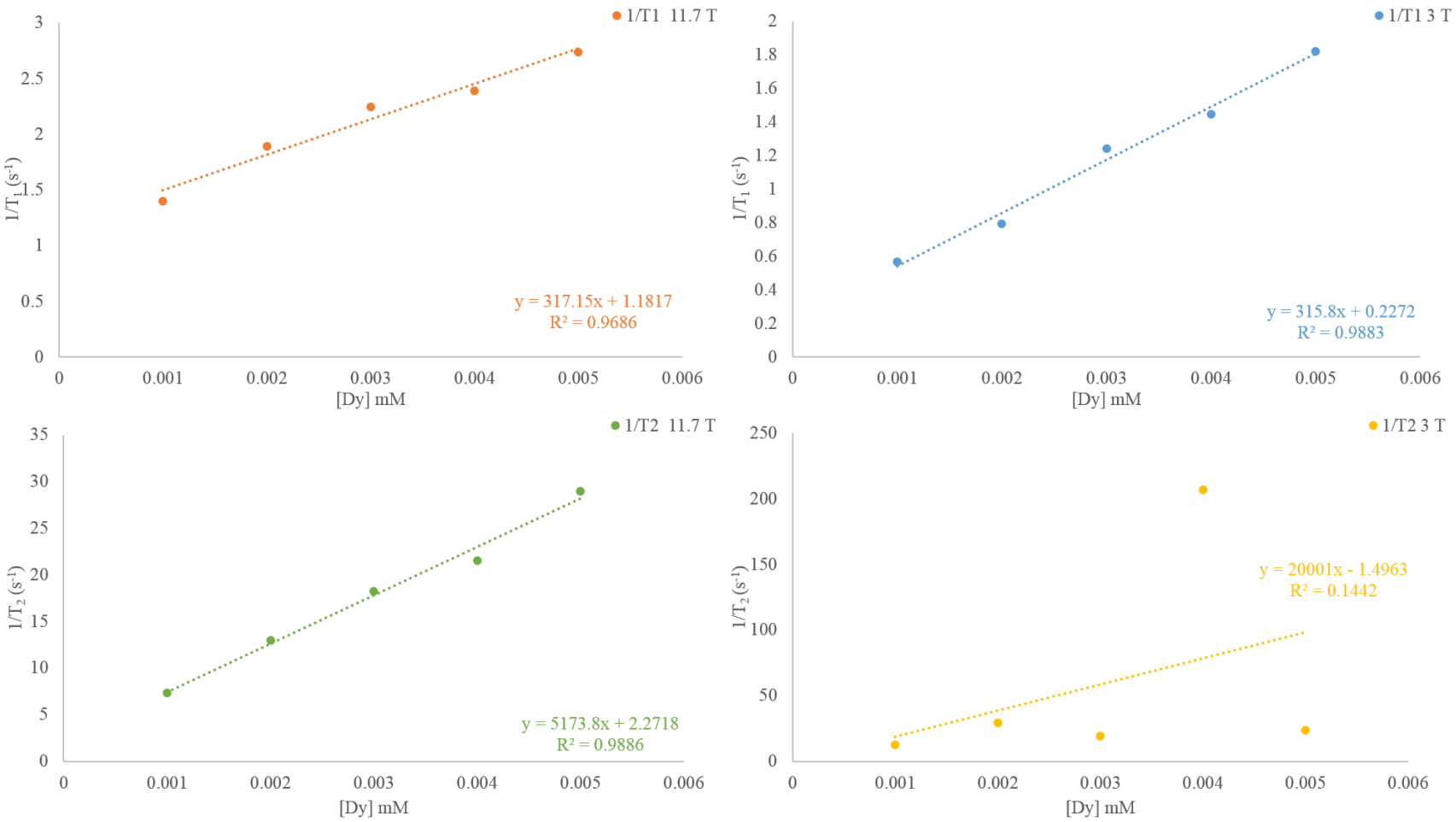

Figure 11-27 T_1 and T_2 relaxation rates per mmol of Dy^{3+} in $Fe_{1.99}Dy_{0.01}O_3$ nanoparticles at 3 T and 11.7 T magnetic field strengths.

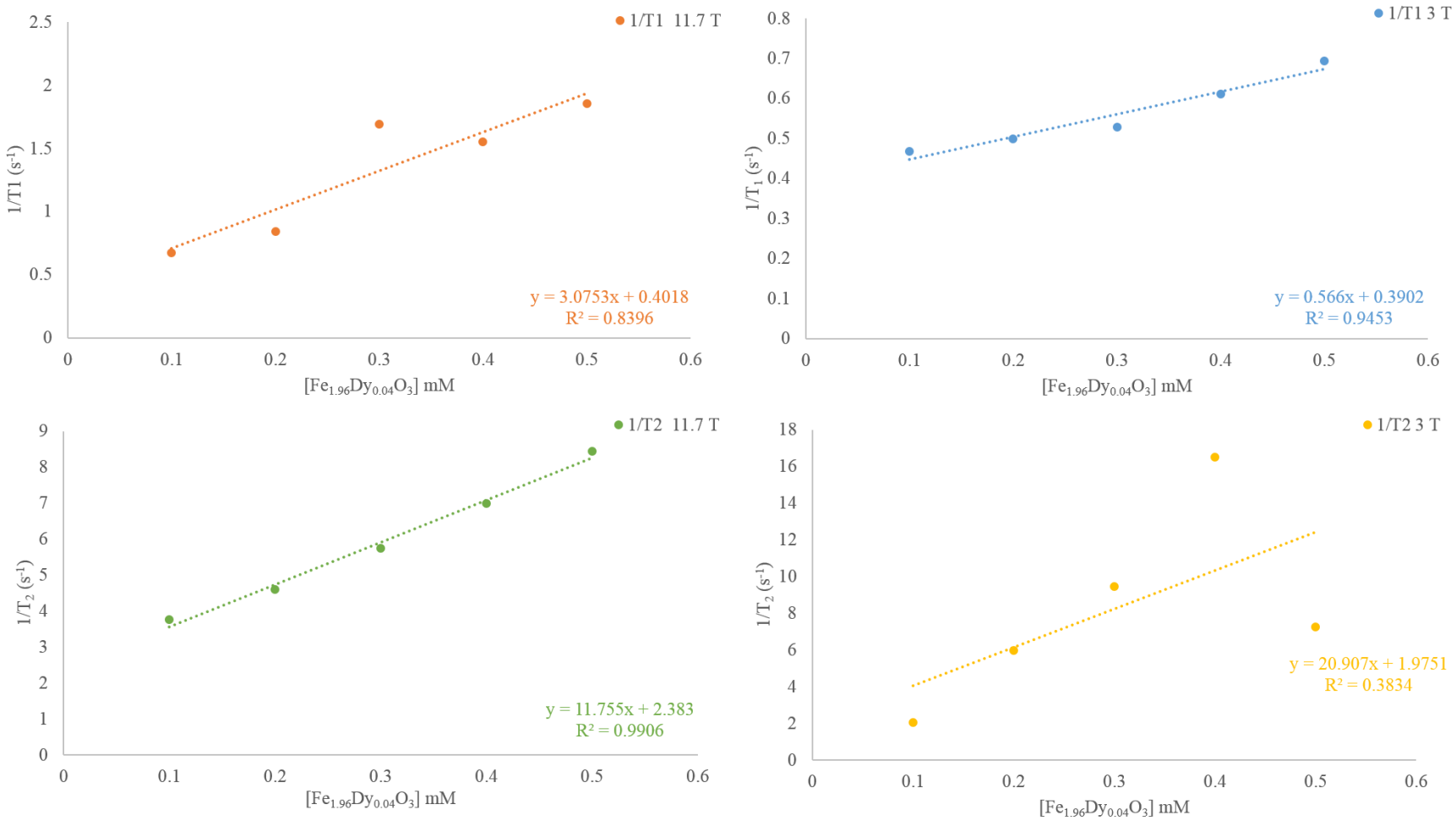

Figure 11-28 T_1 and T_2 relaxation rates per mmol of $Fe_{1.96}Dy_{0.04}O_3$ nanoparticles at 3 T and 11.7 T magnetic field strengths.

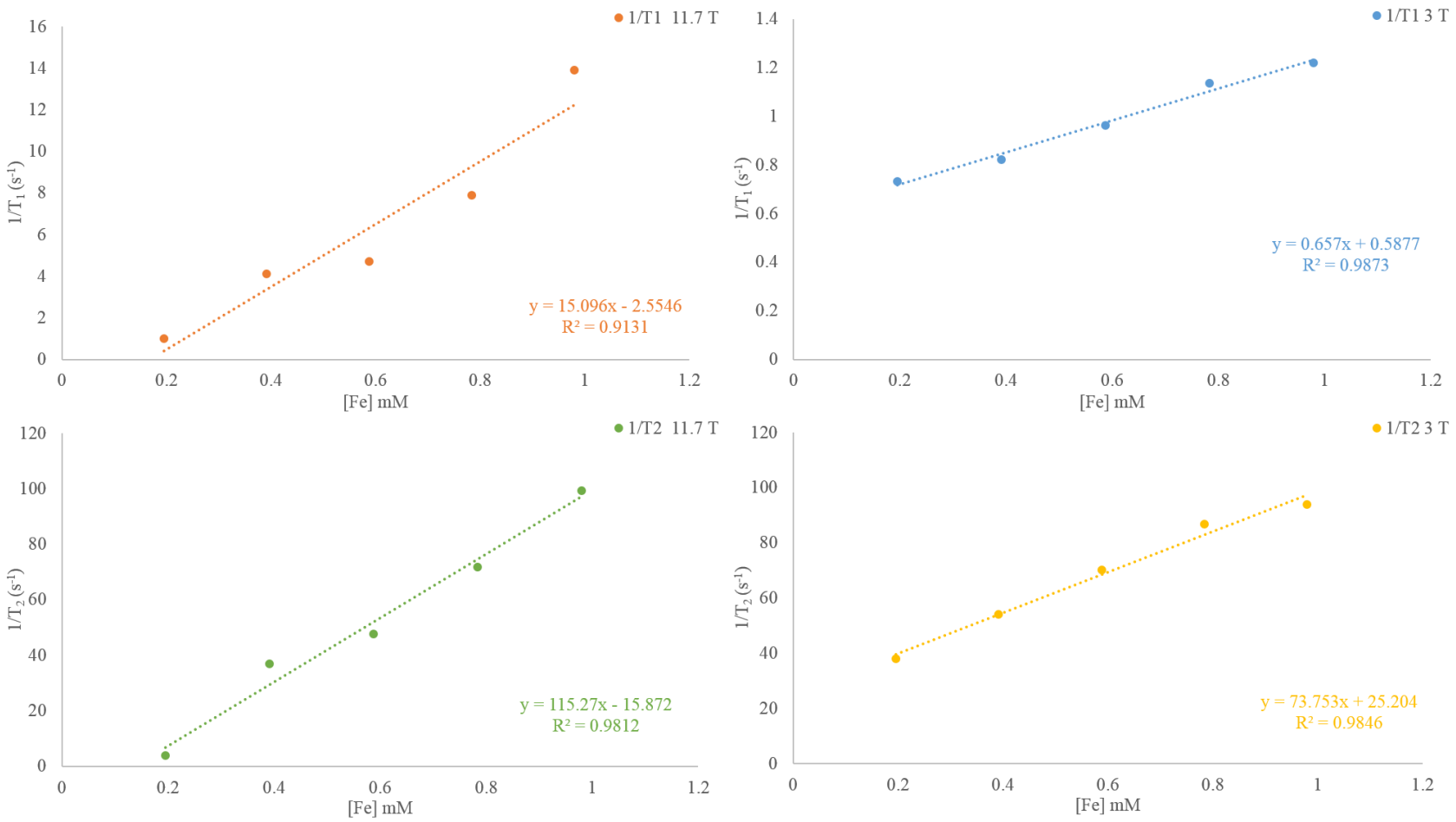

Figure 11-29 T_1 and T_2 relaxation rates per mmol of Fe^{3+} in $Fe_{1.96}Dy_{0.04}O_3$ nanoparticles at 3 T and 11.7 T magnetic field strengths.

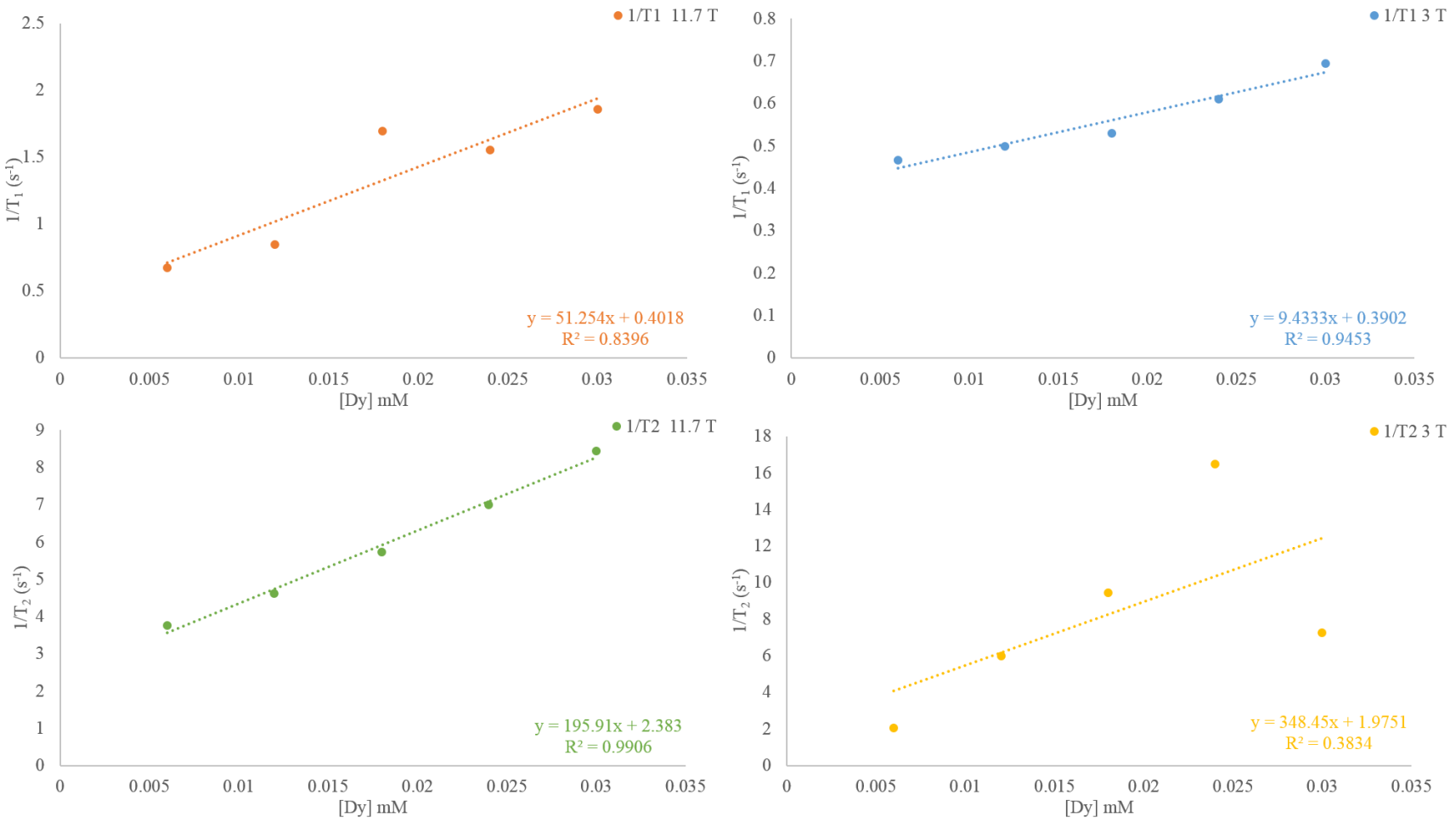

Figure 11-30 T_1 and T_2 relaxation rates per mmol of Dy^{3+} in $Fe_{1.96}Dy_{0.04}O_3$ nanoparticles at 3 T and 11.7 T magnetic field strengths.

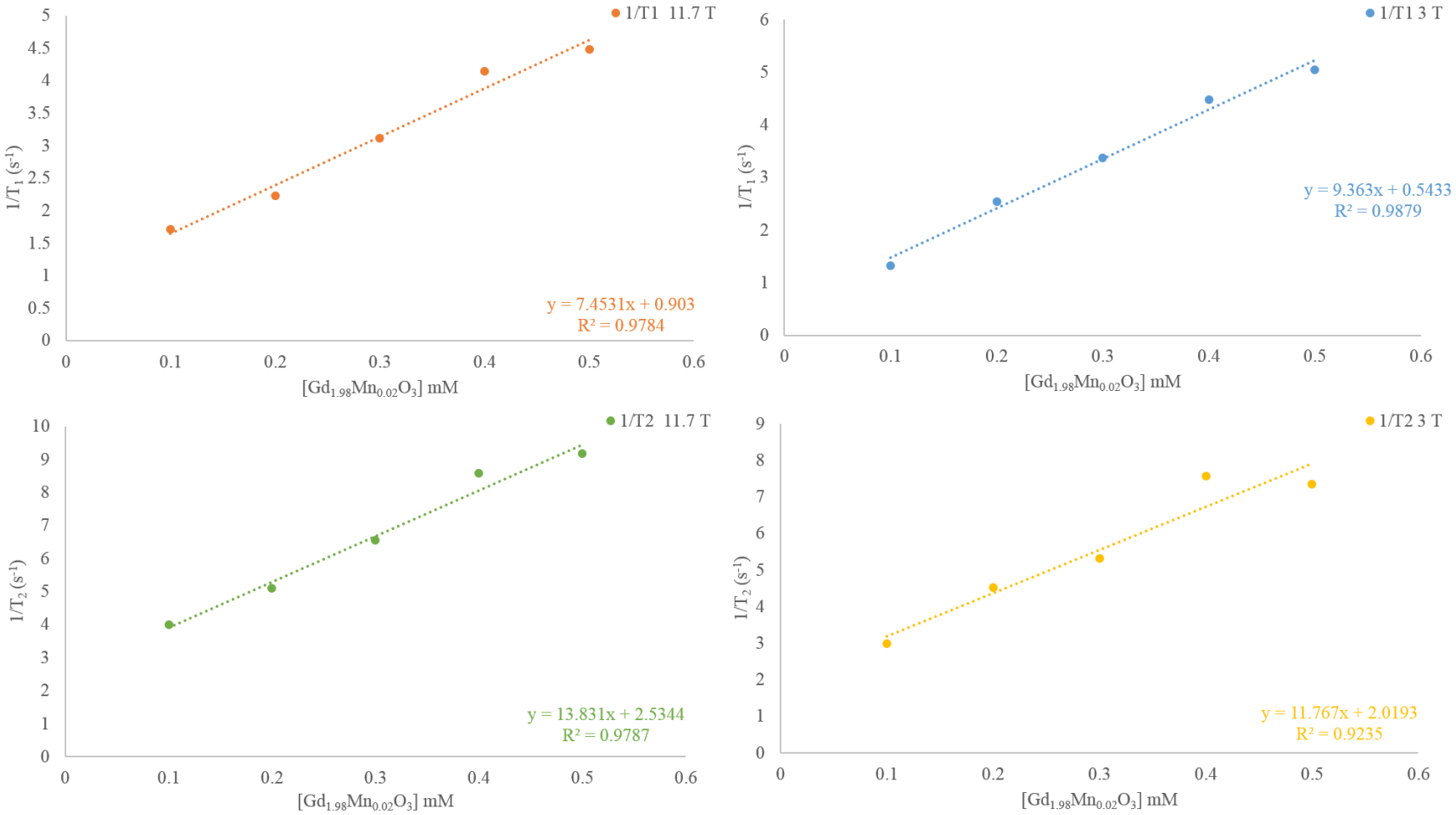

Figure 11-31 T_1 and T_2 relaxation rates per mmol of $Gd_{1.98}Mn_{0.02}O_3$ nanoparticles at 3 T and 11.7 T magnetic field strengths.

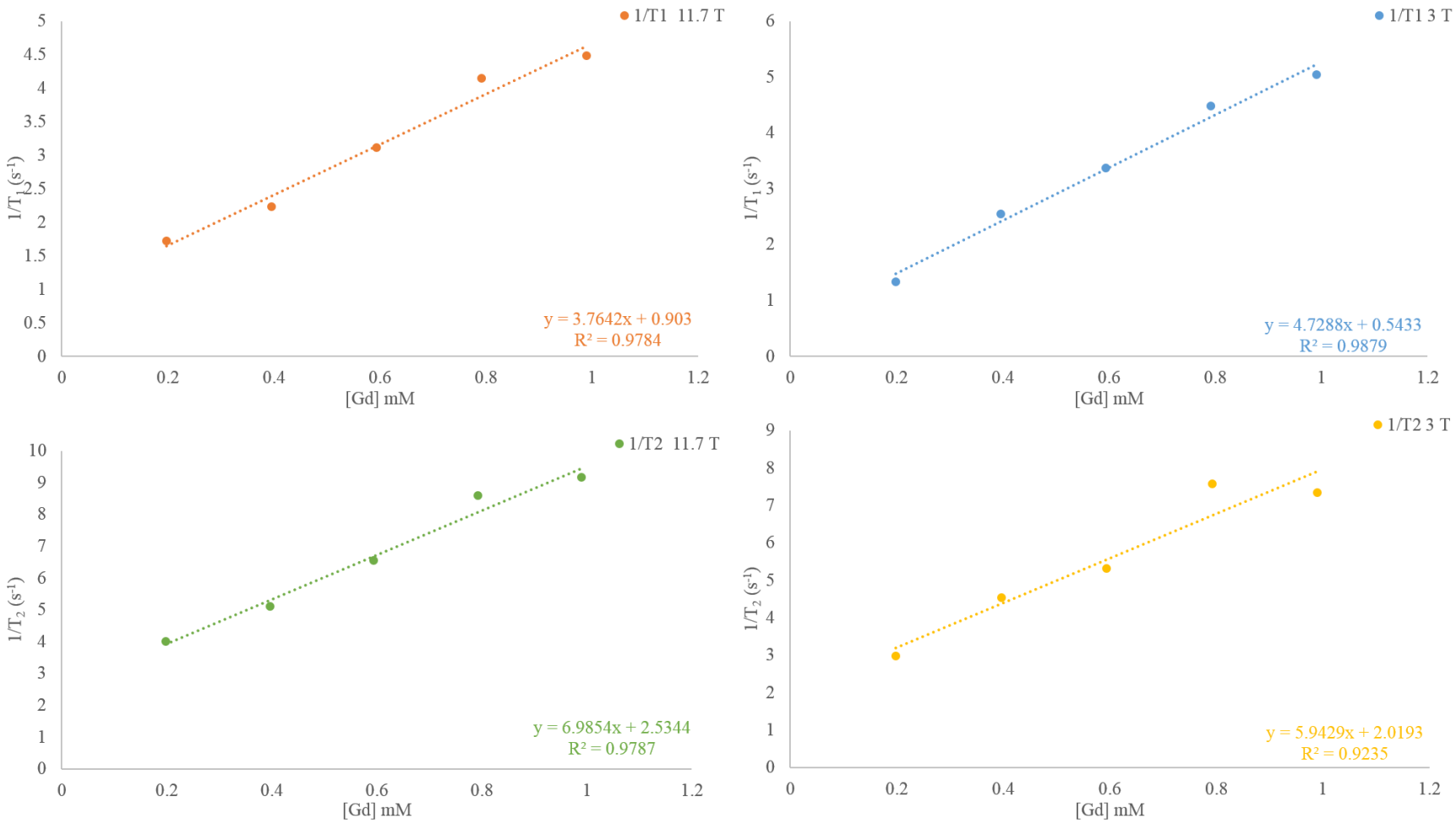

Figure 11-32 T_1 and T_2 relaxation rates per mmol of Gd^{3+} in $Gd_{1.98}Mn_{0.02}O_3$ nanoparticles at 3 T and 11.7 T magnetic field strengths.

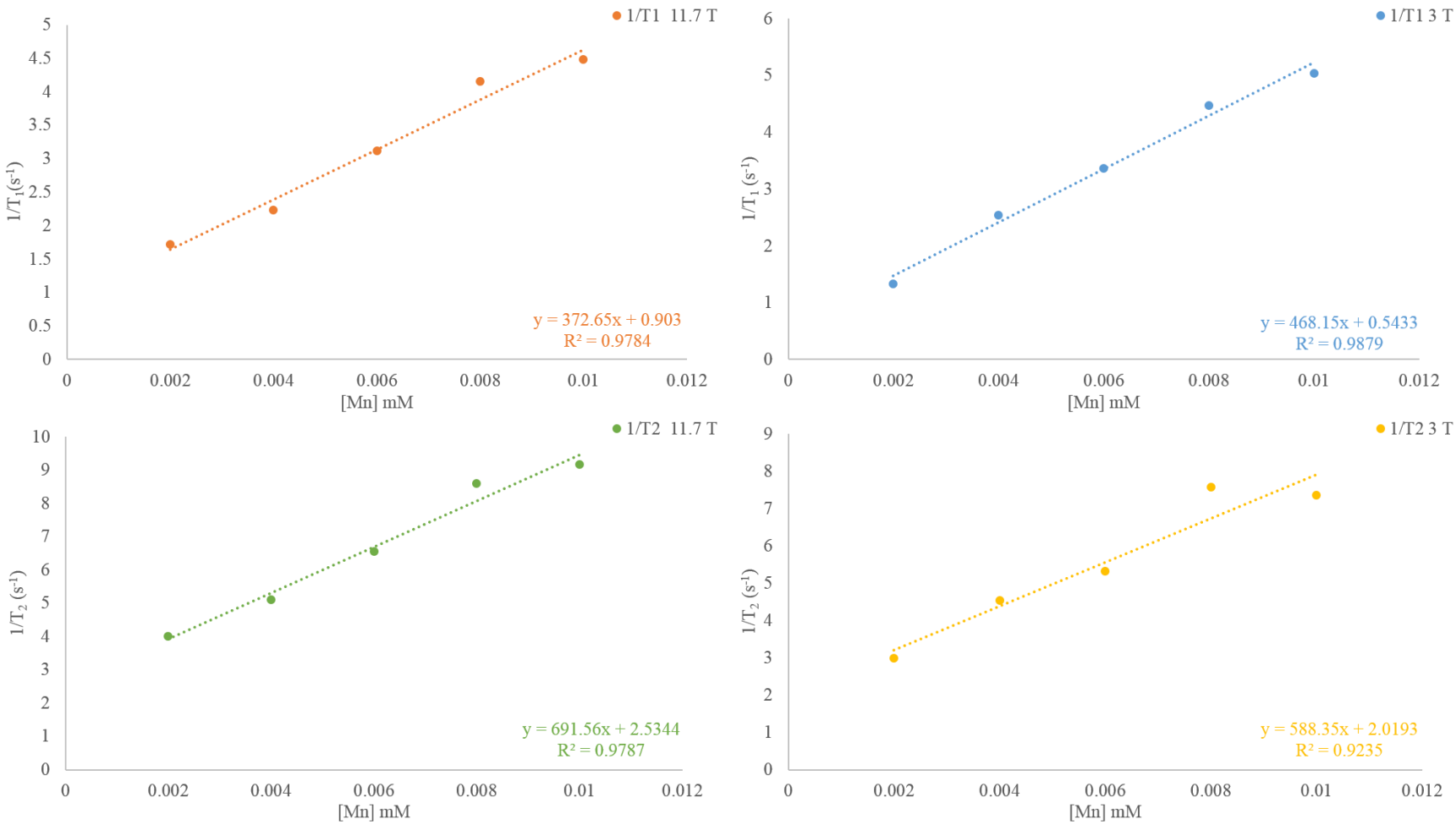

Figure 11-33 T_1 and T_2 relaxation rates per mmol of Mn^{2+} in $Gd_{1.98}Mn_{0.02}O_3$ nanoparticles at 3 T and 11.7 T magnetic field strengths.

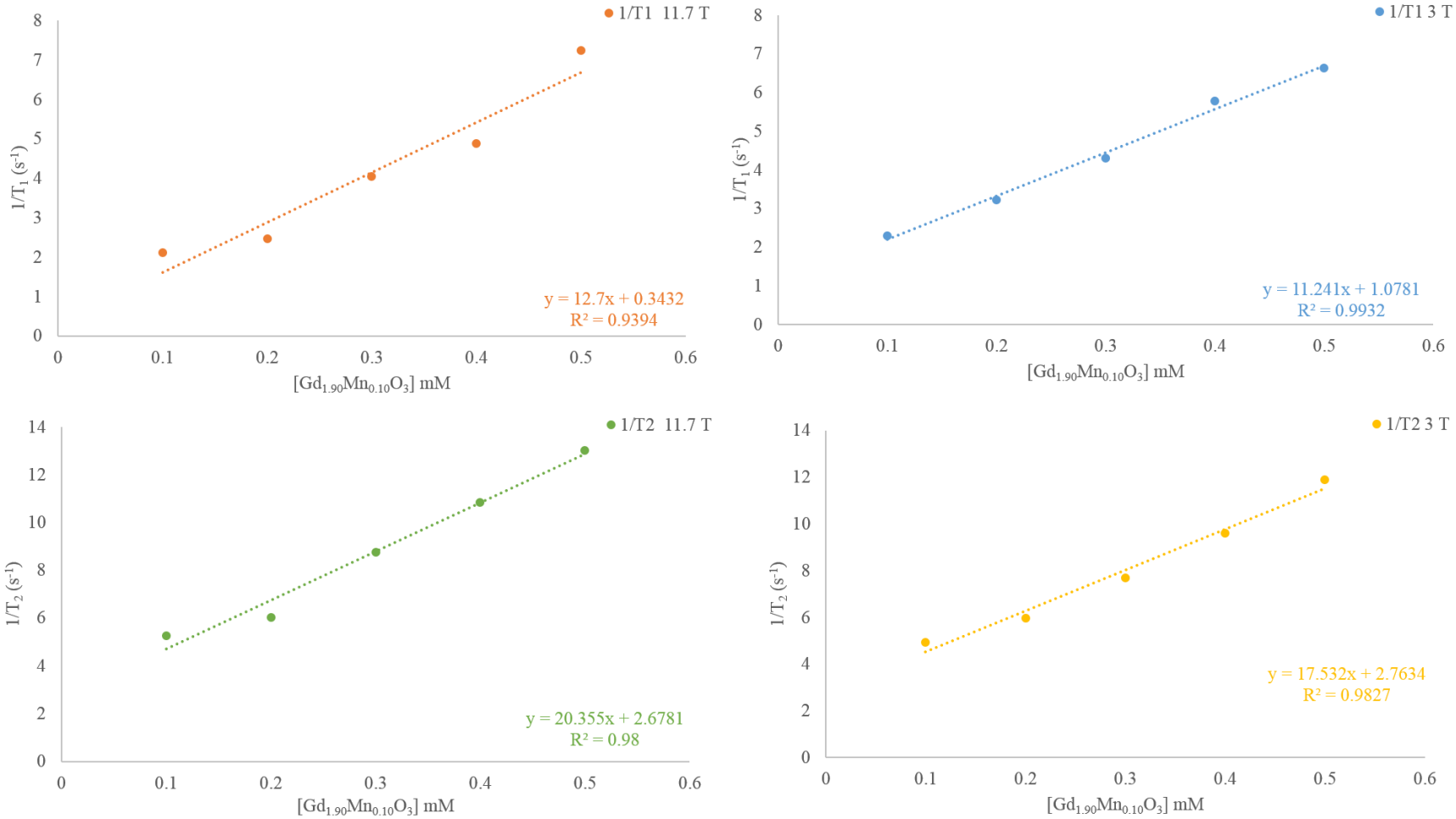

Figure 11-34 T_1 and T_2 relaxation rates per mmol of $Gd_{1.90}Mn_{0.10}O_3$ nanoparticles at 3 T and 11.7 T magnetic field strengths.

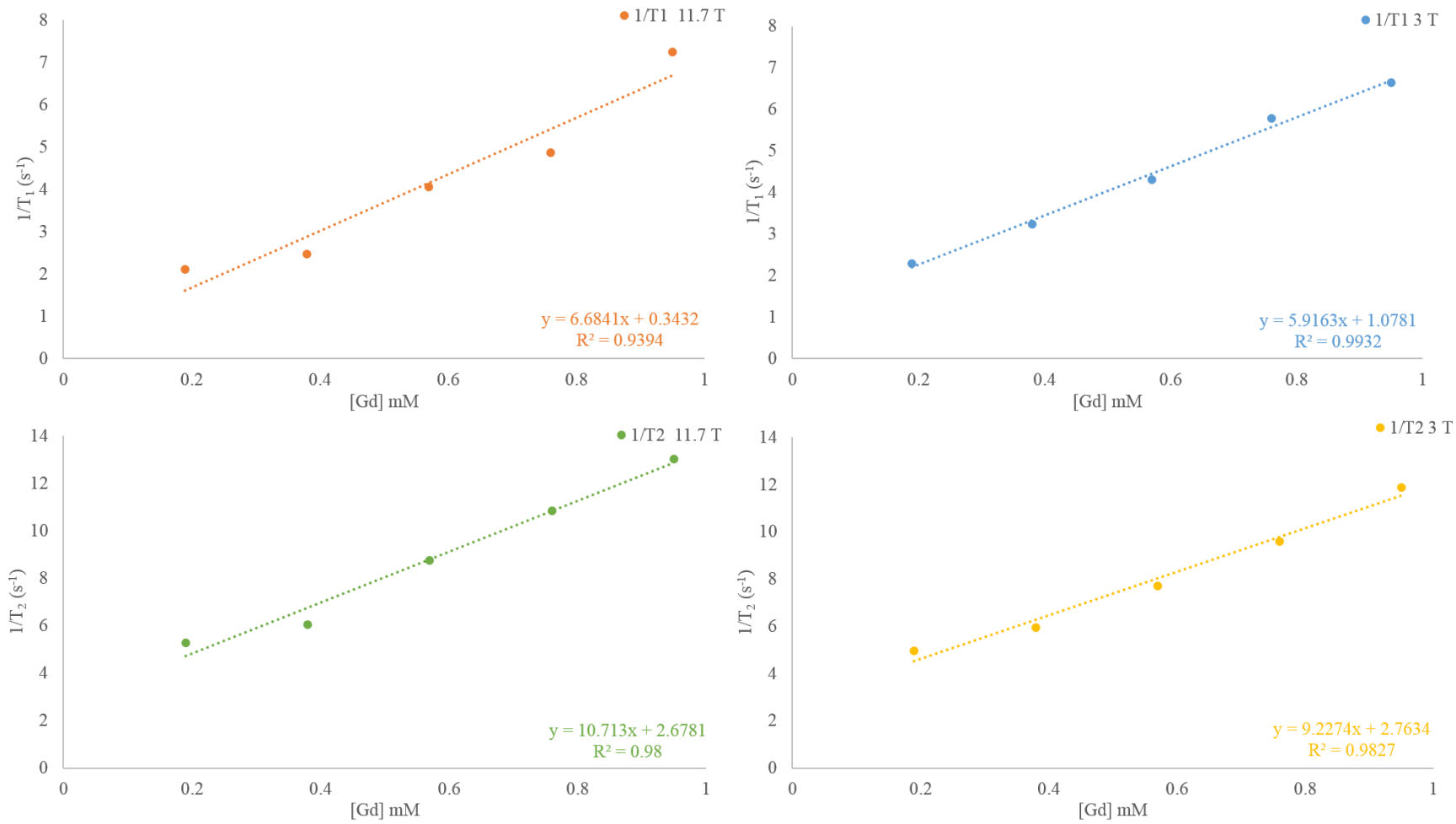

Figure 11-35 T_1 and T_2 relaxation rates per mmol of Gd^{3+} in $Gd_{1.90}Mn_{0.10}O_3$ nanoparticles at 3 T and 11.7 T magnetic field strengths.

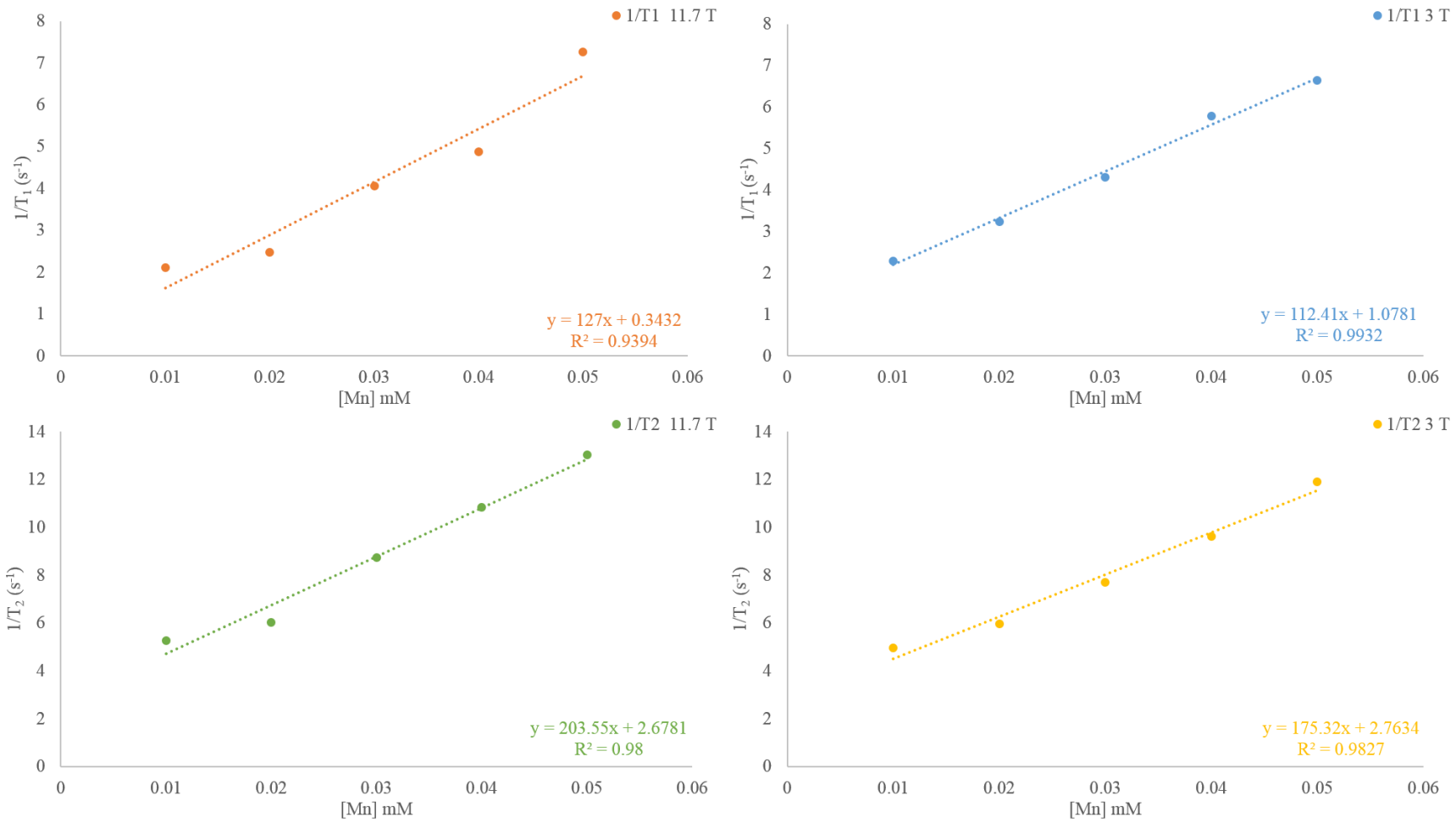

Figure 11-36 T_1 and T_2 relaxation rates per mmol of Mn^{2+} in $Gd_{1.90}Mn_{0.10}O_3$ nanoparticles at 3 T and 11.7 T magnetic field strengths.

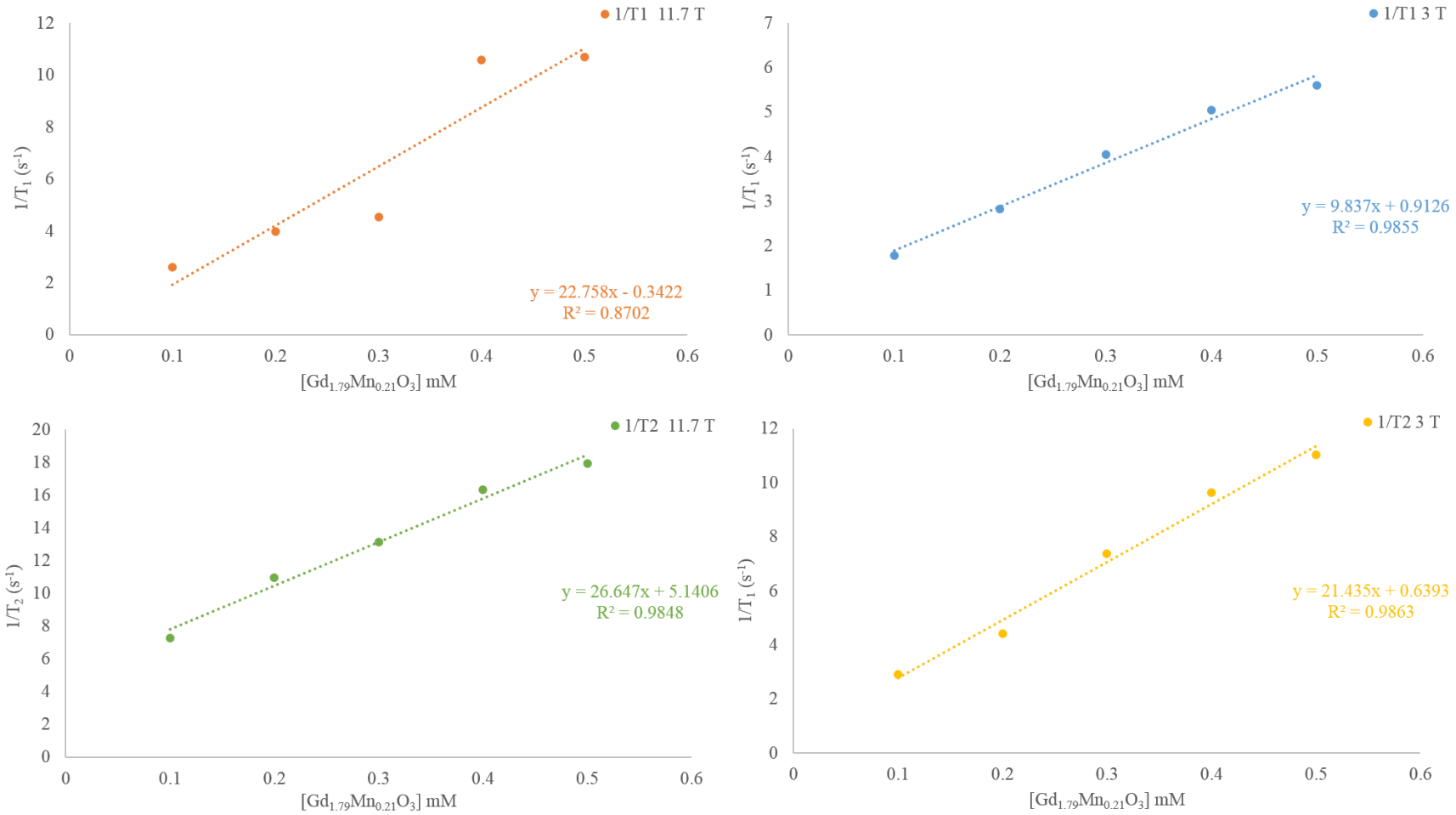

Figure 11-37 T_1 and T_2 relaxation rates per mmol of $Gd_{1.79}Mn_{0.21}O_3$ nanoparticles at 3 T and 11.7 T magnetic field strengths.

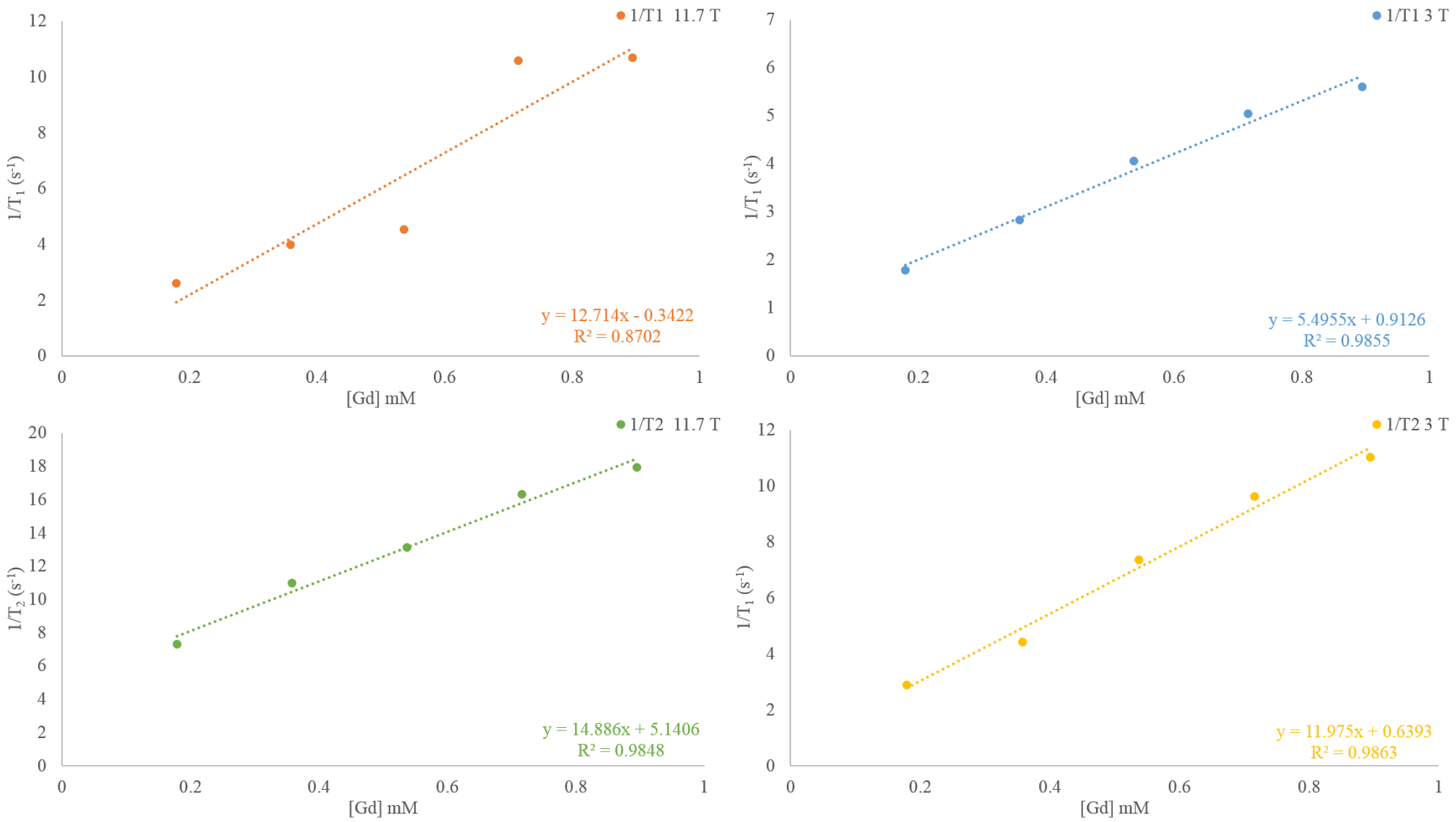

Figure 11-38 T_1 and T_2 relaxation rates per mmol of Gd^{3+} in $Gd_{1.79}Mn_{0.21}O_3$ nanoparticles at 3 T and 11.7 T magnetic field strengths.

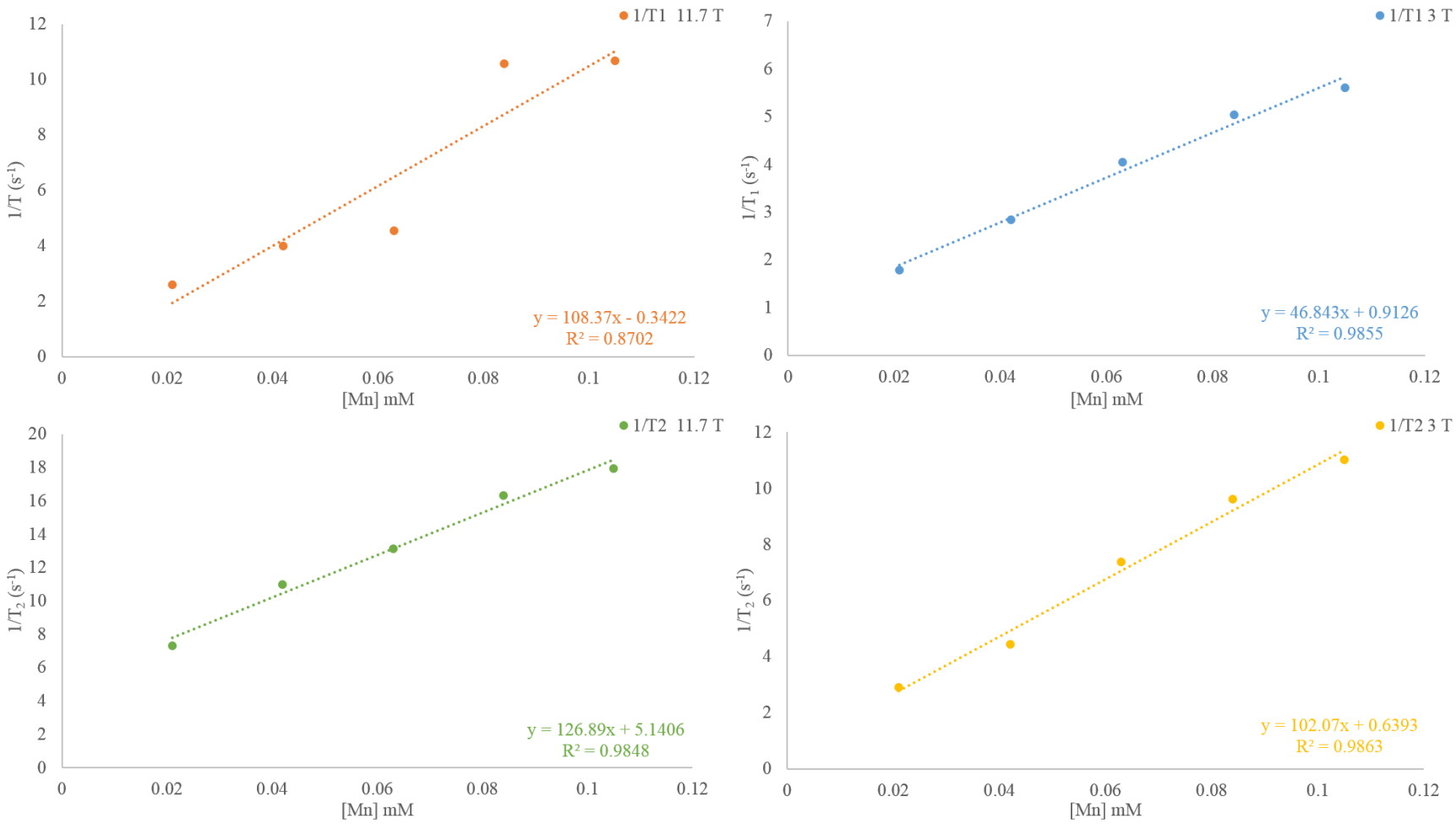

Figure 11-39 T_1 and T_2 relaxation rates per mmol of Mn^{2+} $Gd_{1.79}Mn_{0.21}O_3$ nanoparticles at 3 T and 11.7 T magnetic field strengths.

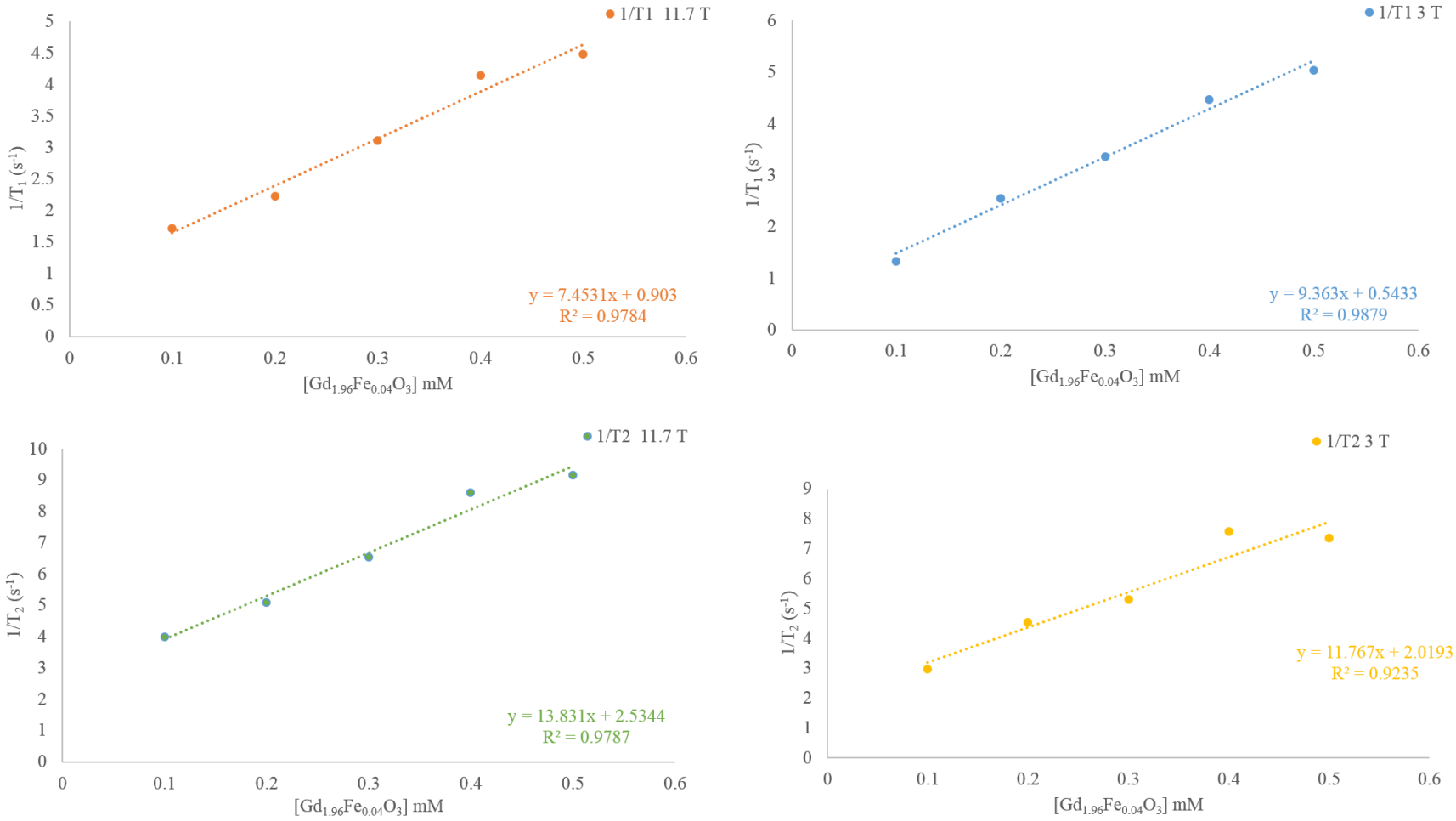

Figure 11-40 T_1 and T_2 relaxation rates per mmol of $Gd_{1.96}Fe_{0.04}O_3$ nanoparticles at 3 T and 11.7 T magnetic field strengths.

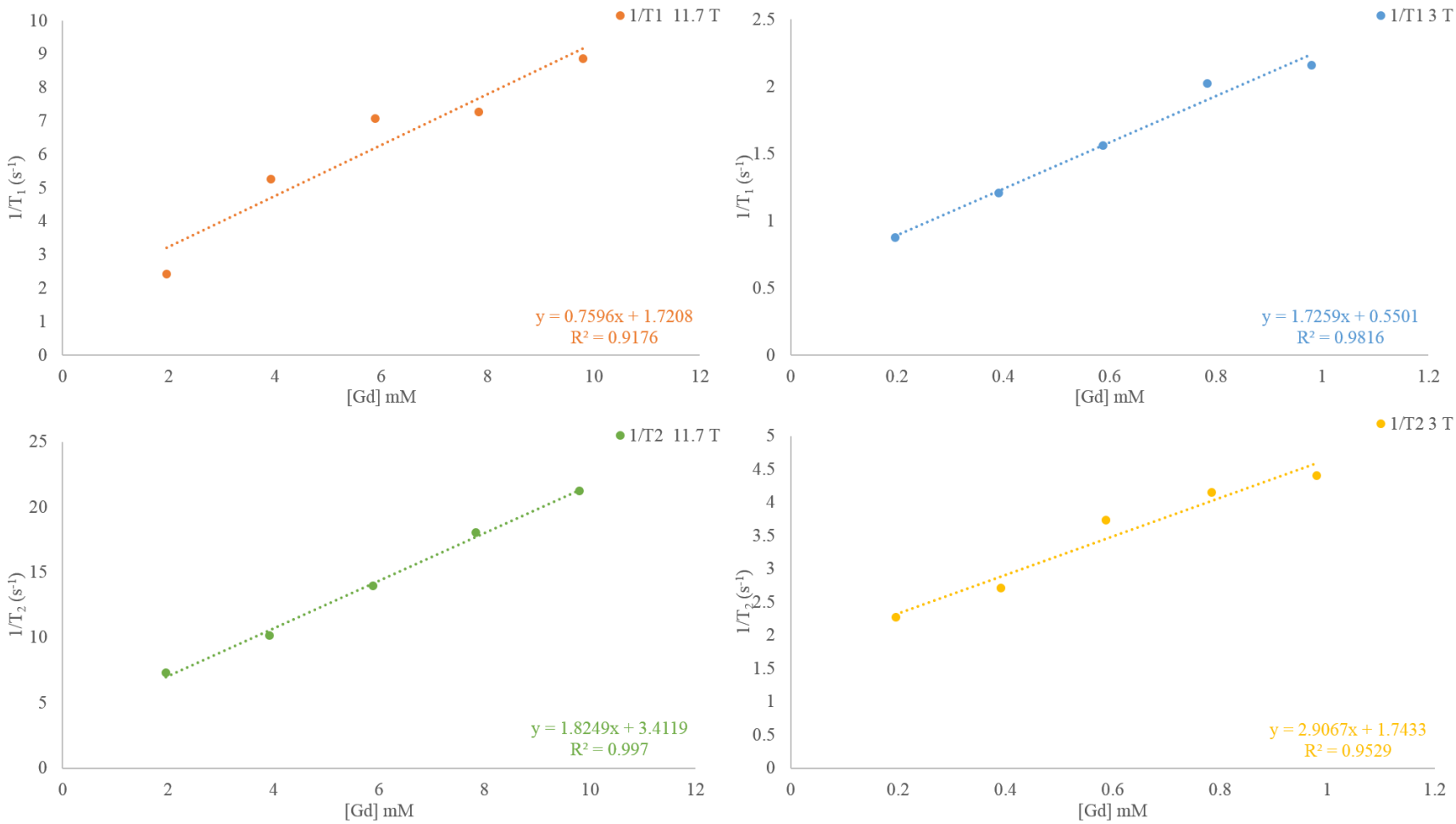

Figure 11-41 T_1 and T_2 relaxation rates per mmol of Gd^{3+} in $Gd_{1.96}Fe_{0.04}O_3$ nanoparticles at 3 T and 11.7 T magnetic field strengths.

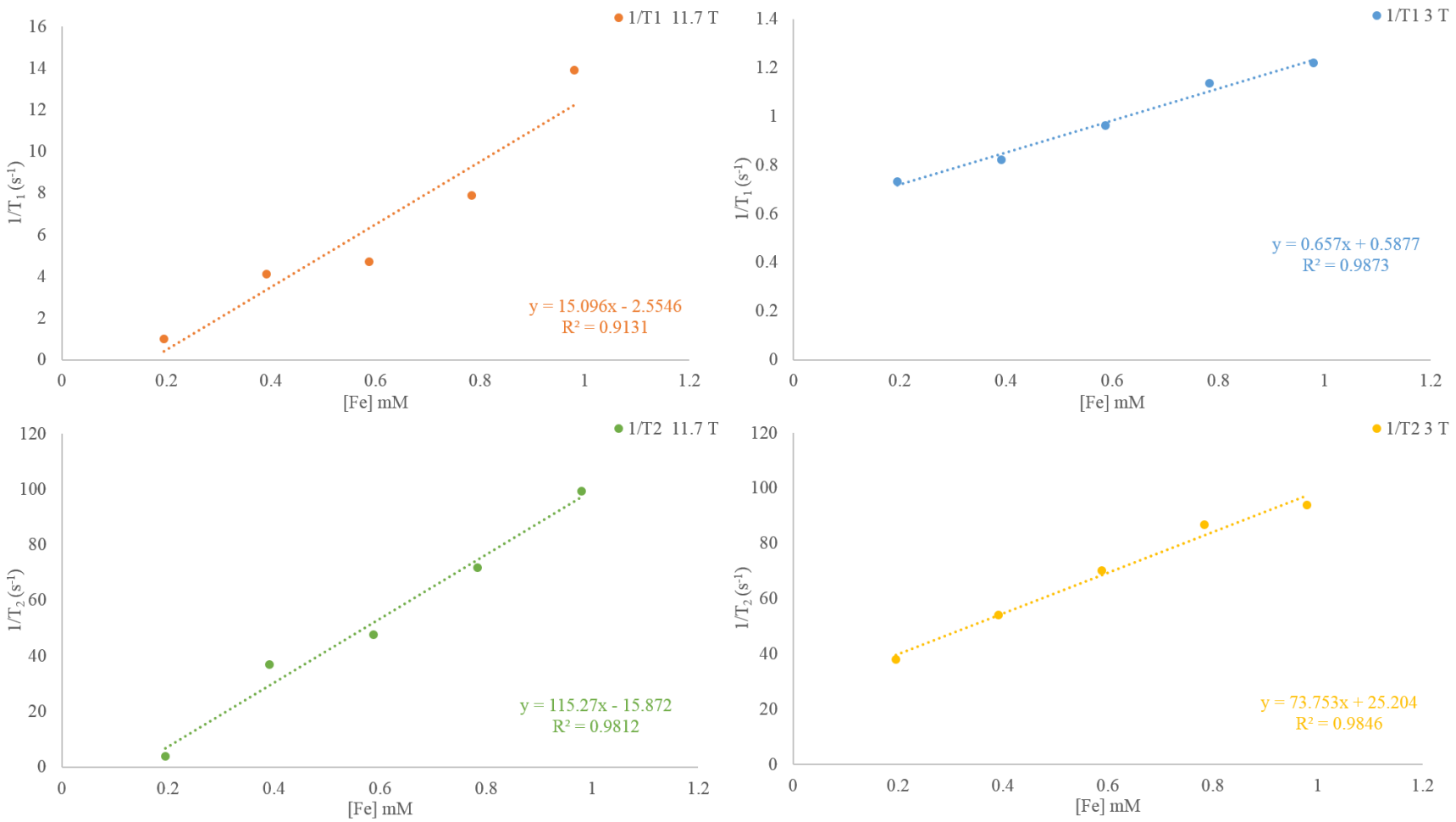

Figure 11-42 T_1 and T_2 relaxation rates per mmol of Fe^{3+} in $Gd_{1.96}Fe_{0.04}O_3$ nanoparticles at 3 T and 11.7 T magnetic field strengths.

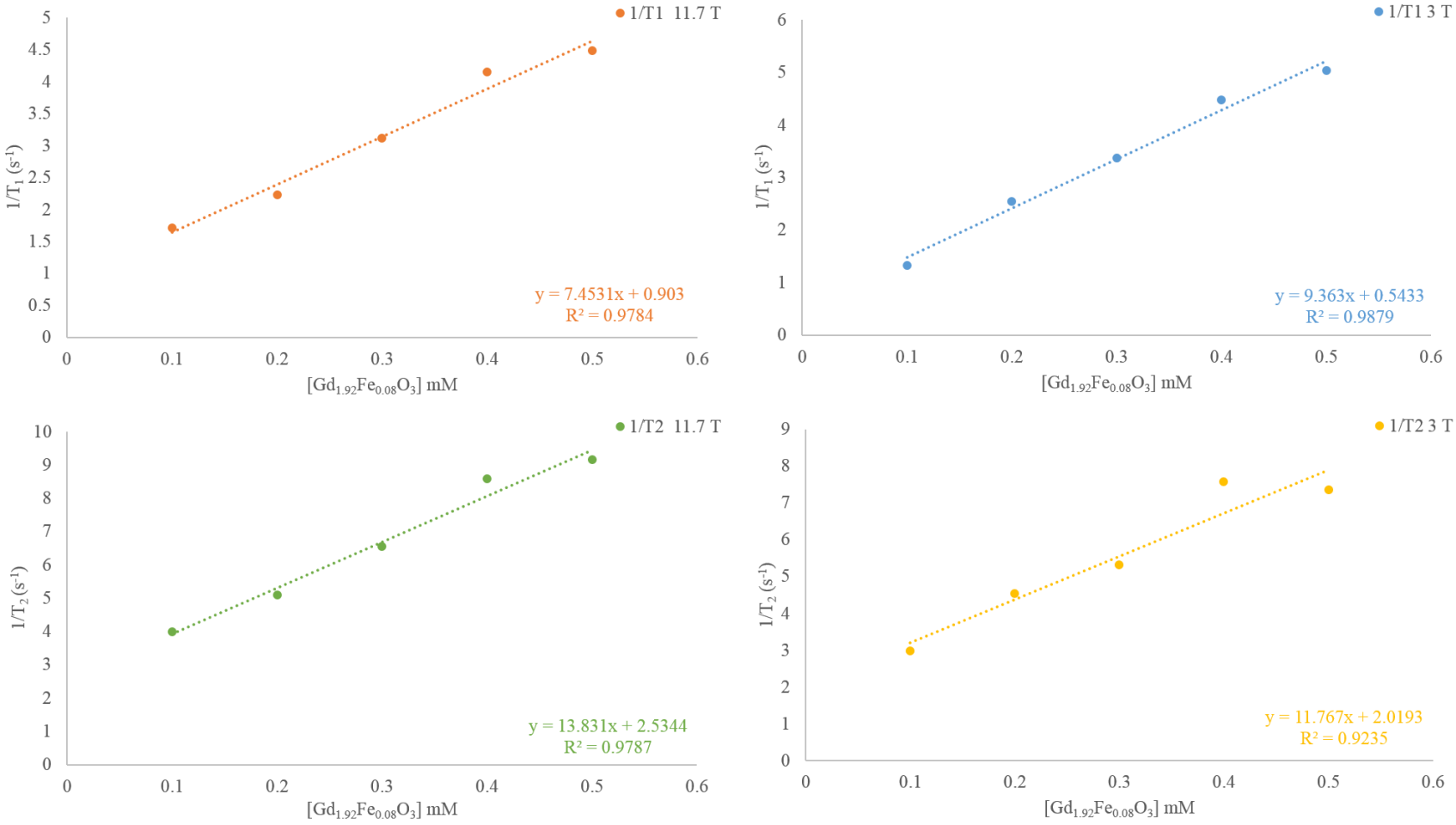

Figure 11-43 T_1 and T_2 relaxation rates per mmol of $Gd_{1.92}Fe_{0.08}O_3$ nanoparticles at 3 T and 11.7 T magnetic field strengths.

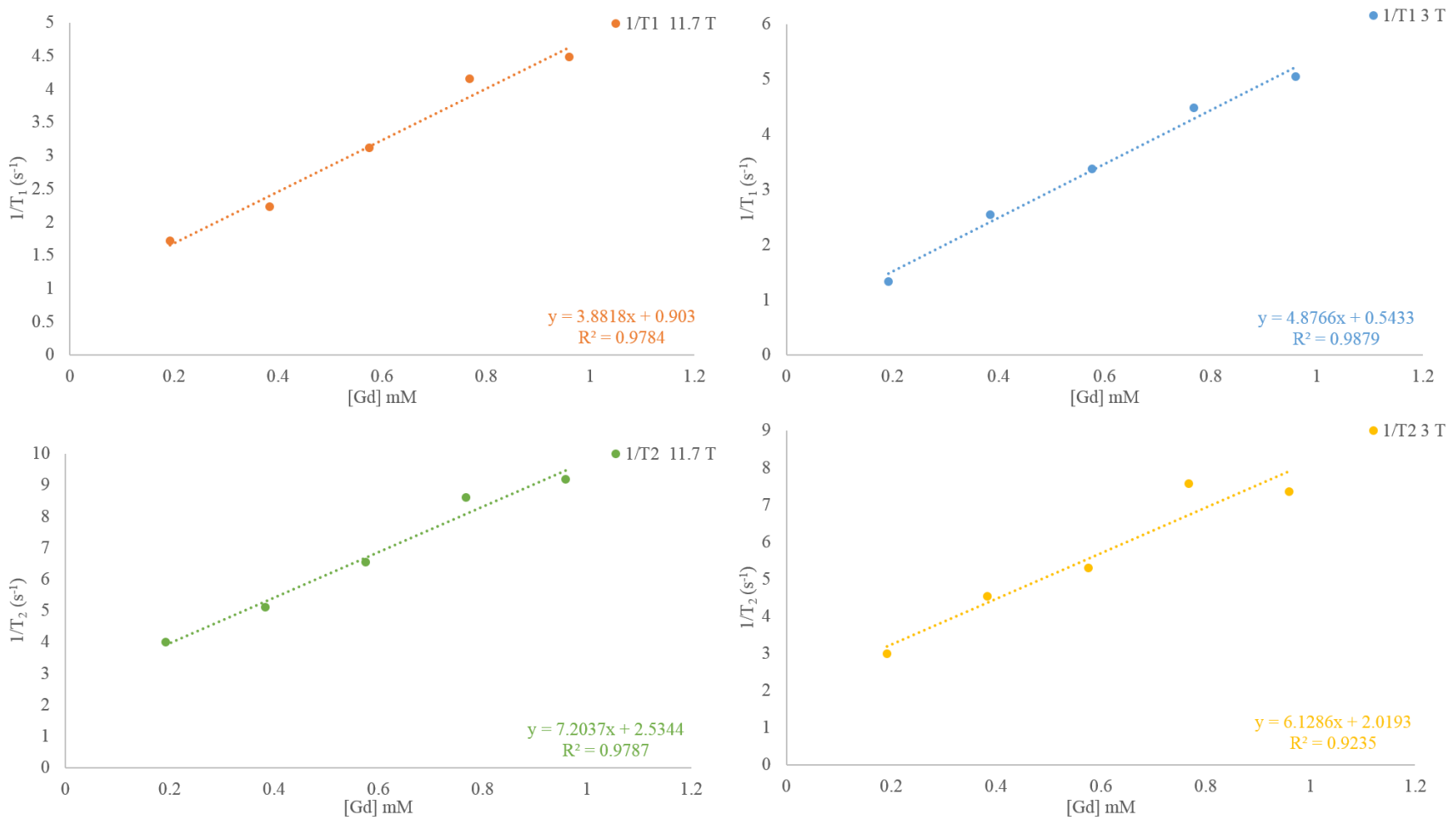

Figure 11-44 T_1 and T_2 relaxation rates per mmol of Gd^{3+} in $Gd_{1.92}Fe_{0.08}O_3$ nanoparticles at 3 T and 11.7 T magnetic field strengths.

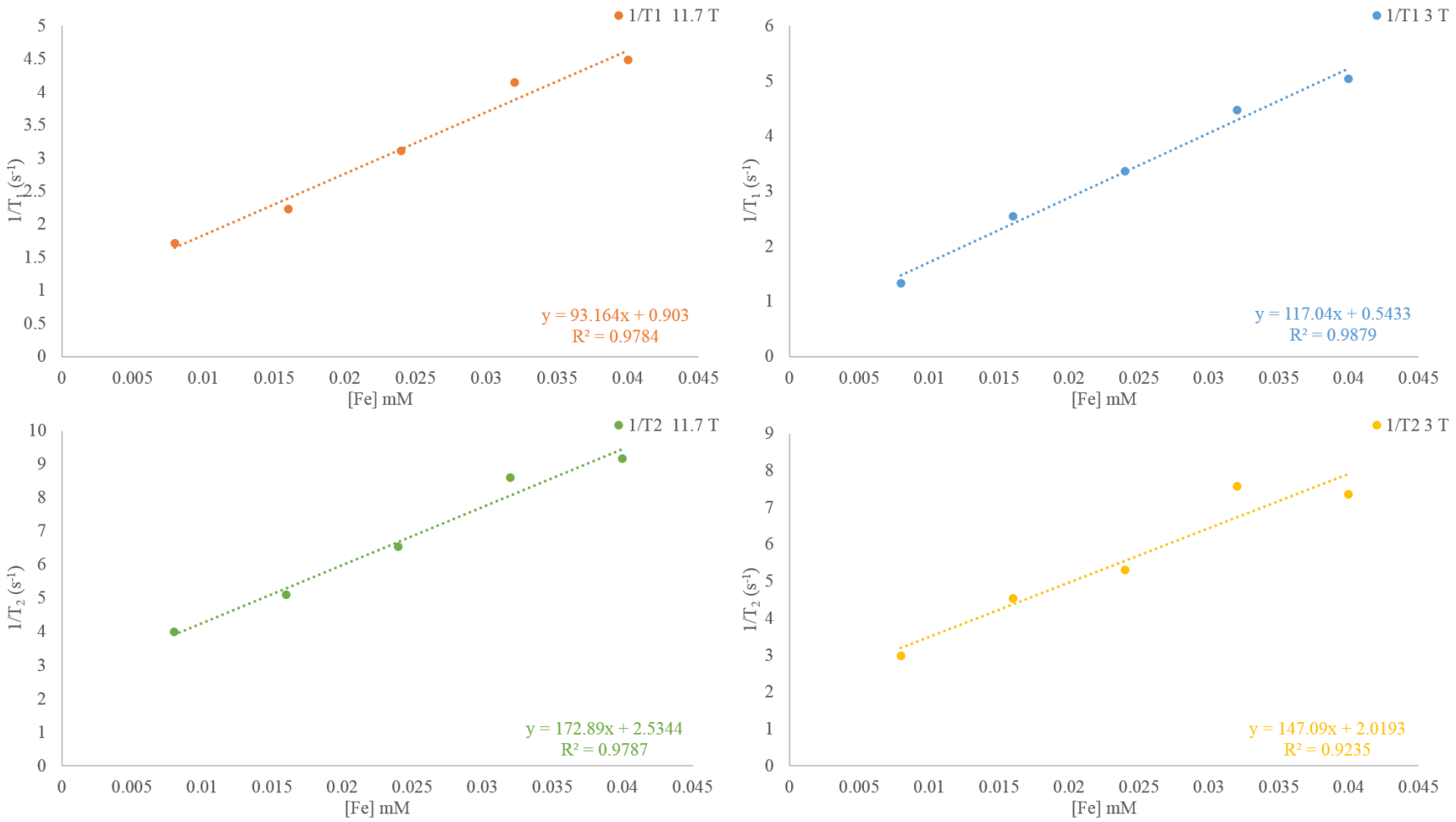

Figure 11-45 T_1 and T_2 relaxation rates per mmol of Fe^{3+} in $Gd_{1.92}Fe_{0.08}O_3$ nanoparticles at 3 T and 11.7 T magnetic field strengths.

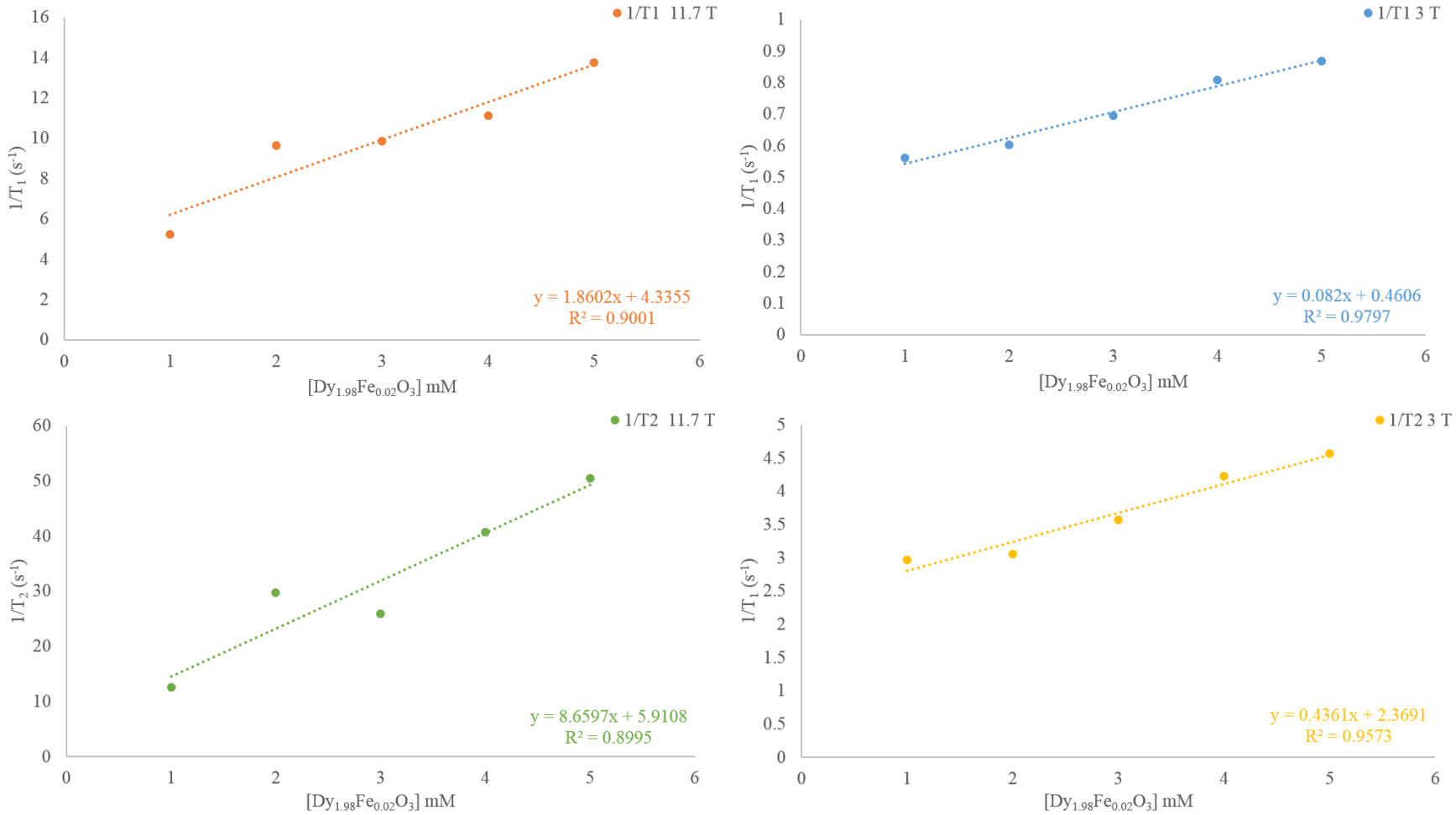

Figure 11-46 T_1 and T_2 relaxation rates per mmol of $Dy_{1.98}Fe_{0.02}O_3$ nanoparticles at 3 T and 11.7 T magnetic field strengths.

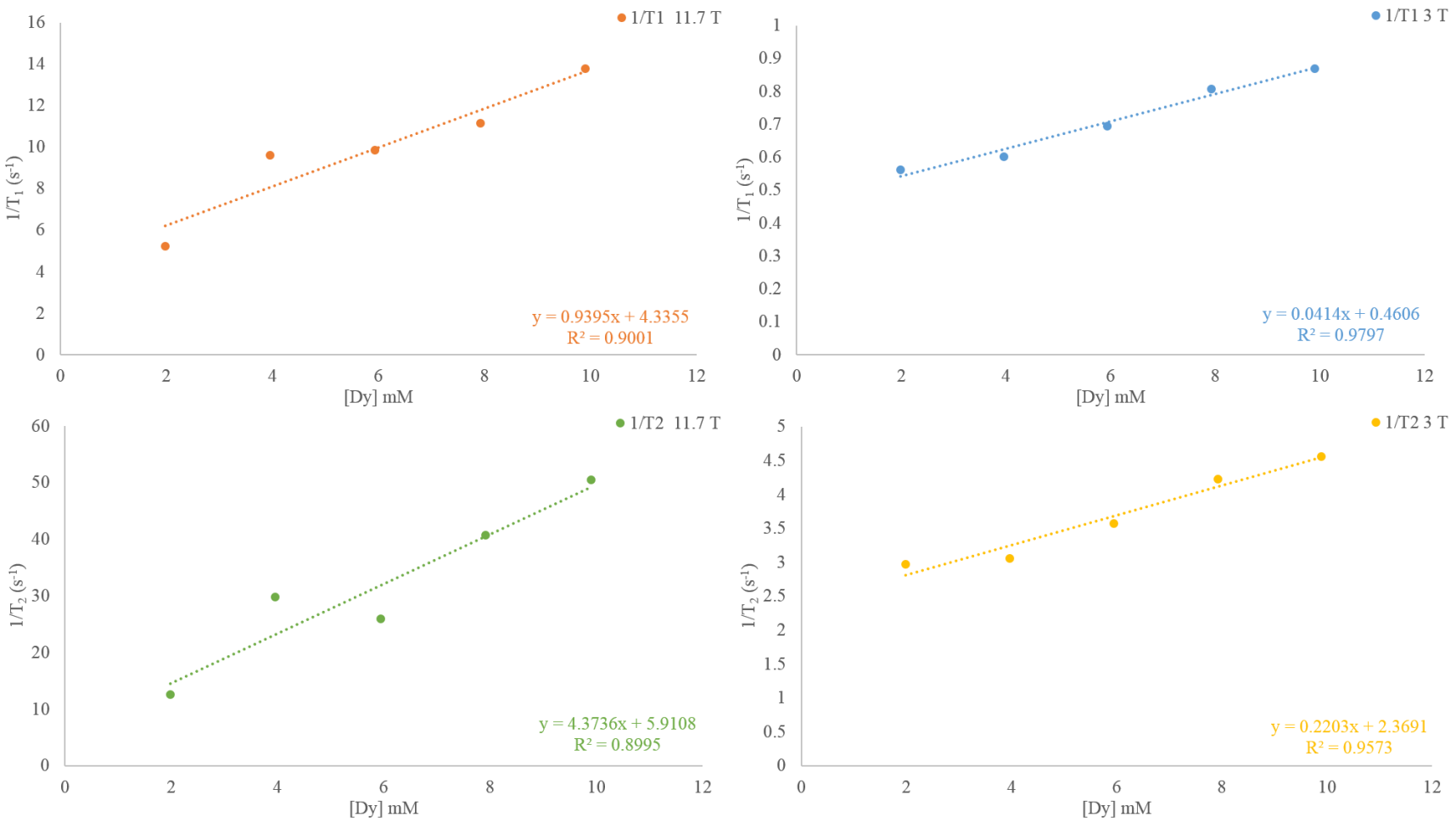

Figure 11-47 T_1 and T_2 relaxation rates per mmol of Dy^{3+} in $Dy_{1.98}Fe_{0.02}O_3$ nanoparticles at 3 T and 11.7 T magnetic field strengths.

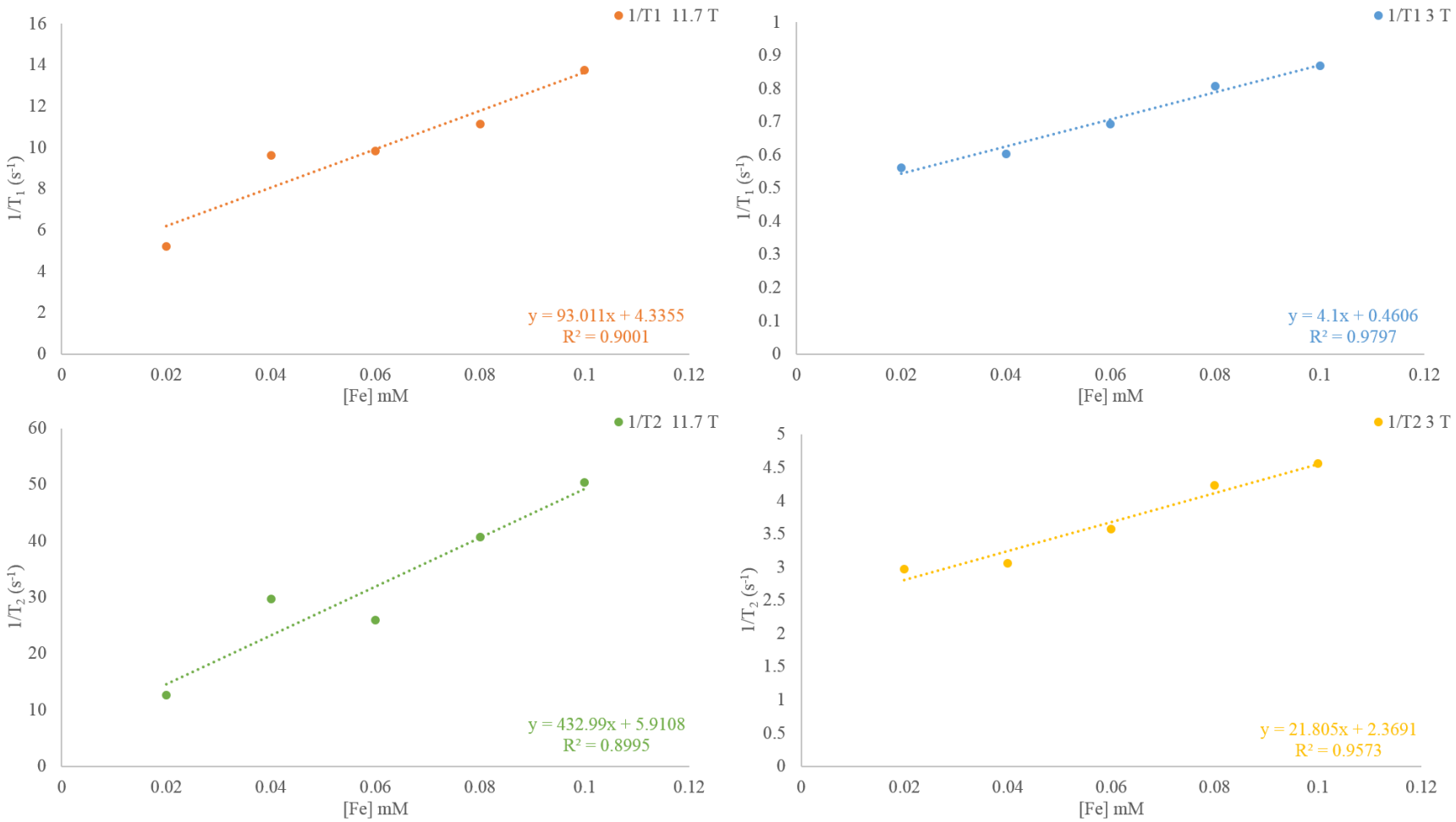

Figure 11-48 T_1 and T_2 relaxation rates per mmol of Fe^{3+} in $Dy_{1.98}Fe_{0.02}O_3$ nanoparticles at 3 T and 11.7 T magnetic field strengths.

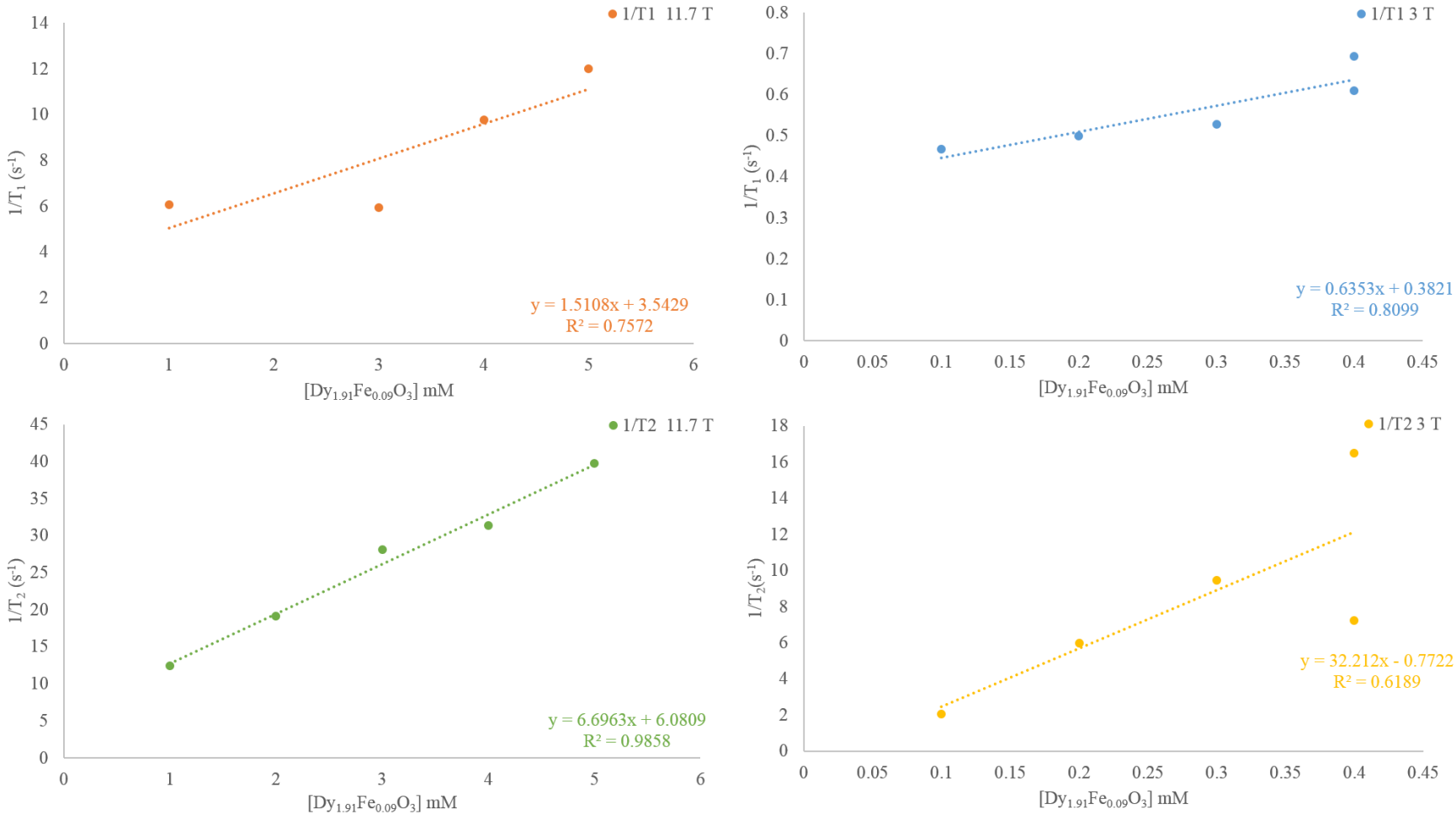

Figure 11-49 T_1 and T_2 relaxation rates per mmol of $Dy_{1.91}Fe_{0.09}O_3$ nanoparticles at 3 T and 11.7 T magnetic field strengths.

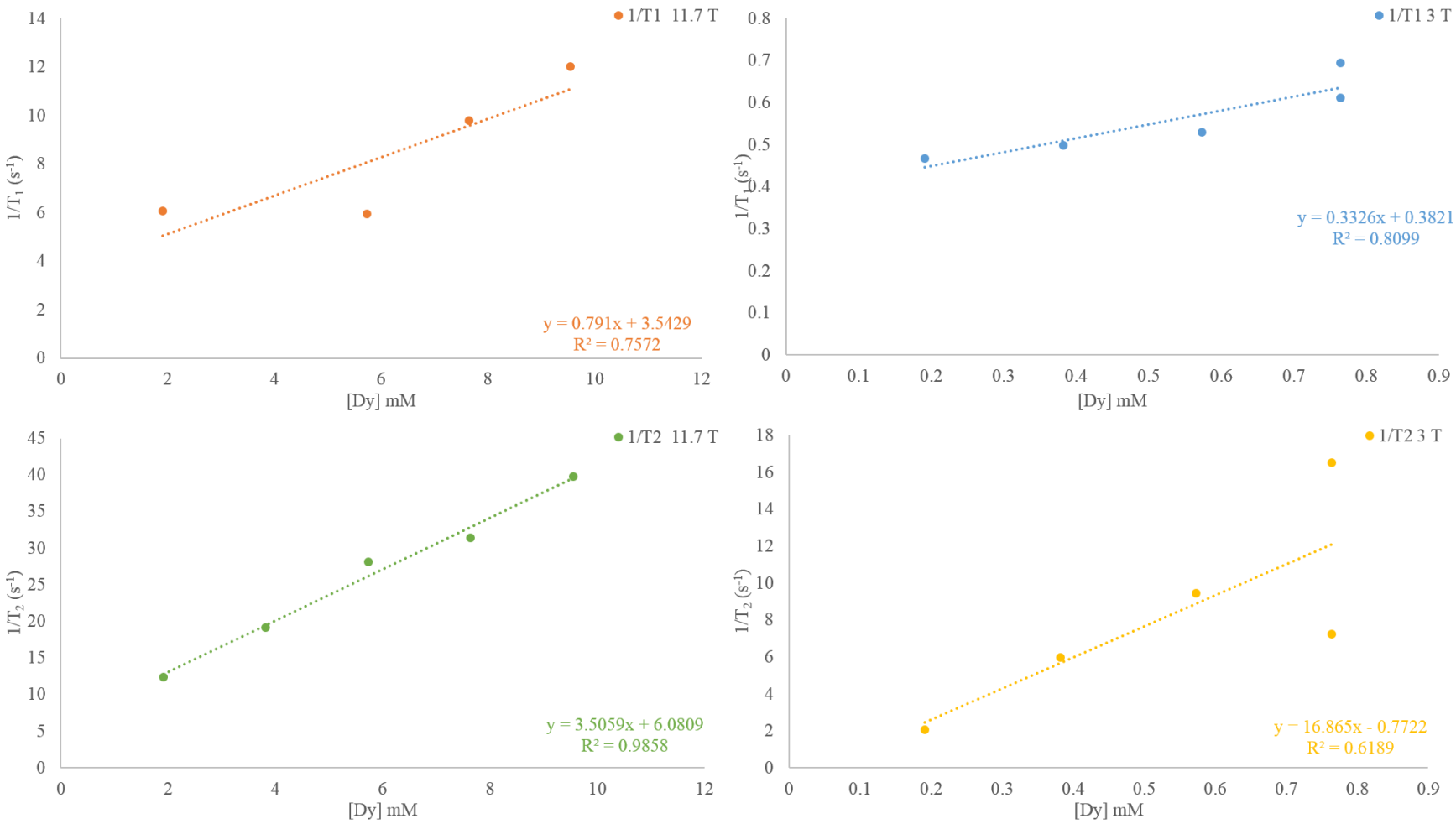

Figure 11-50 T_1 and T_2 relaxation rates per mmol of Dy^{3+} in $Dy_{1.91}Fe_{0.09}O_3$ nanoparticles at 3 T and 11.7 T magnetic field strengths.

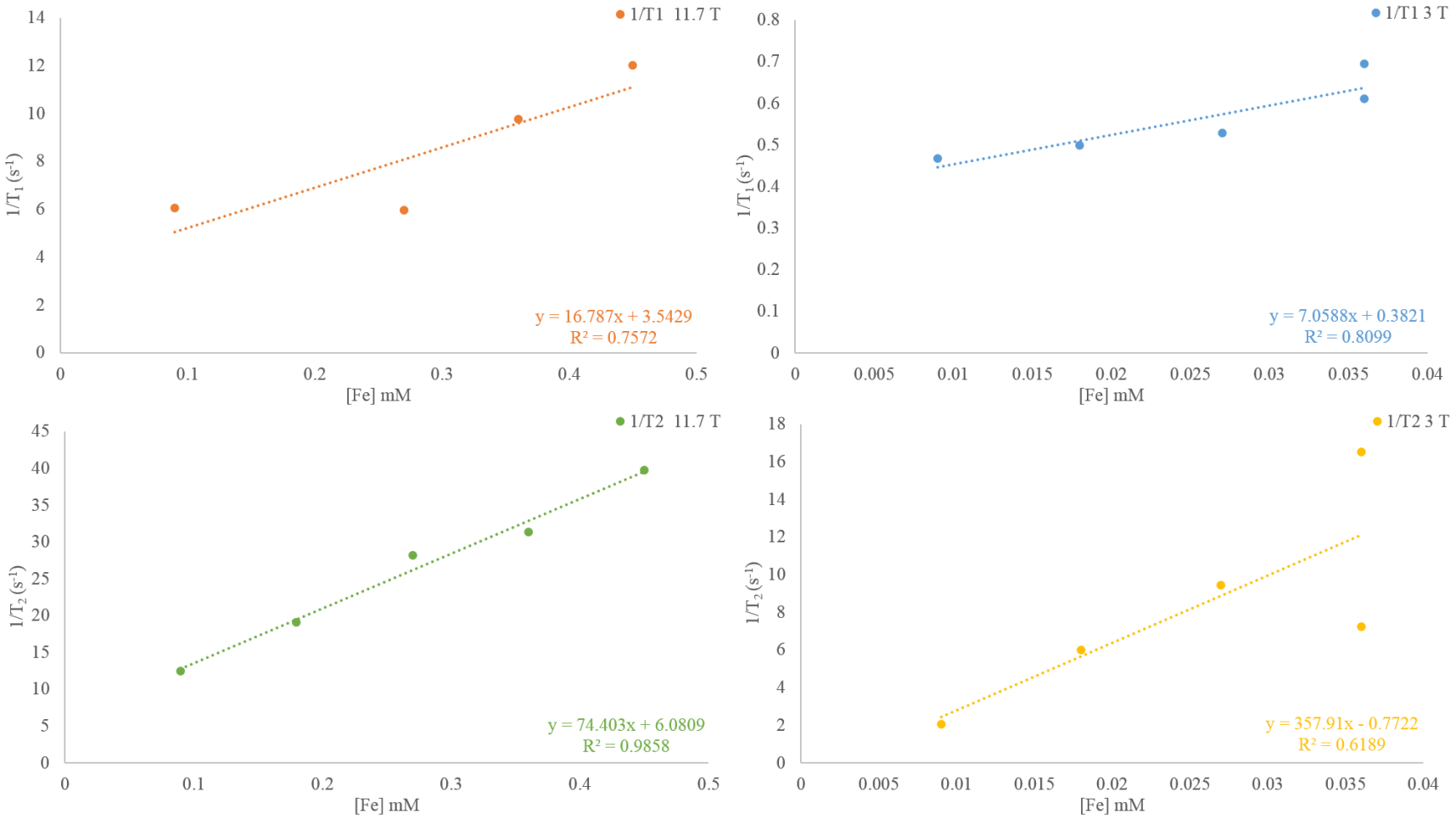

Figure 11-51 T_1 and T_2 relaxation rates per mmol of Fe^{3+} in $Dy_{1.91}Fe_{0.09}O_3$ nanoparticles at 3 T and 11.7 T magnetic field strength